Aus der Arbeitsgruppe Kardiale MRT des
Experimental and Clinical Research Centers, eine gemeinsame
Einrichtung der Charité - Universitätsmedizin Berlin und des
Max-Delbrück-Centrums für Molekulare Medizin (MDC)

DISSERTATION

Schnelle zweidimensionale Kartierung der longitudinalen Relaxationszeit T_1 bei 1.5 Tesla, 3 Tesla und 7 Tesla mittels Magnetresonanztomographie

zur Erlangung des akademischen Grades
Doctor rerum medicinalium (Dr. rer. medic.)

vorgelegt der Medizinischen Fakultät
Charité – Universitätsmedizin Berlin

von

Matthias Alexander Dieringer

aus Filderstadt

Datum der Promotion: 05.12.2014

Inhaltsverzeichnis

Zusammenfassung 3
Abstrakt (deutsch) 3
Abstract (englisch) 5
Einführung 7
Methodik 9
Ergebnisse 16
Diskussion 25
Literaturverzeichnis 28
Eidesstattliche Versicherung 30
Anteilserklärung an den erfolgten Publikationen 31
Druckexemplare 34
Lebenslauf 194
Publikationsliste 195
Artikel in wissenschaftlichen Fachzeitschriften (Peer-Review) 195
Vorträge und Poster (wissenschaftliche Kongresse) 197
Danksagung 202

Abstrakt

Die visuelle und damit subjektive Auswertung T_1 gewichteter (longitudinale Relaxationszeit) oder T_2 gewichteter (transversale Relaxationszeit) Schnittbilder gehören zur täglichen klinischen Diagnostik in der kardialen Magnetresonanztomographie (MRT). Für diese nichtquantitative Bildgebungsmethoden hängt die Qualität der Diagnostik unter anderem von Aufnahmeparametern, Gerätekonfiguration, Homogenität des Grundmagnetfeldes (B_0), vom Hochfrequenz-Sendefeld (B_1^+) sowie von der Erfahrung des Befunders ab. Die quantitative Erfassung der T_1 und T_2 Gewebeparameter birgt das Potential, sich von diesen äußeren Einflüssen unabhängig zu machen. Typischerweise sind T_1 und T_2 Akquisitions- und Quantifizierungsmethoden jedoch zeitaufwendig. Die vorgeschlagenen Techniken erzielen in der Literatur eine große Bandbreite an Normwerten, vorwiegend aufgrund technischer Hürden, unzureichenden Modellannahmen, oder physiologischen Einflussfaktoren wie Herzfrequenz, Hämodynamik als auch kardiale und respiratorische Bewegung.

Aus diesen Gründen wurde in dieser Studie eine schnelle MR Technik entwickelt, die das Grundmagnetfeld, das HF-Sendefeld und die quantitative Kartierungen der T_1 Zeit innerhalb weniger Sekunden ermitteln kann. Die entwickelte Methode wurde an einem statischen Phantom, sowie an gesunden Probanden im Gehirn bei magnetischen Feldstärken von 1.5 Tesla, 3 Tesla, und 7 Tesla getestet und gegen Referenzmessungen validiert. Exemplarisch wurde in Messungen am Patienten die klinische Anwendbarkeit demonstriert.

Ein weiterer Schwerpunkt dieser Arbeit lag im Entwurf, der Konstruktion und der Evaluierung eines MR-kompatiblen bewegten Modells einer menschlichen linken Herzkammer. Diese diente der Ermöglichung standardisierter Messungen in der Präsenz von kardialer Bewegung und Blutfluss mit dem Ziel, die T_1 Kartierung am Herzen zu ermöglichen und zu verbessern. Zum Zeitpunkt der Studie waren keine Normwerte für T_1 und T_2 Werte des Herzmuskels bei 3T vorhanden, sodass zunächst mittels eines alternativen Ansatzes bei gesunden Probanden Referenzwerte erhoben wurden.

Während Messungen bei 1.5 Tesla und 3 Tesla zur klinischen Routine gehören, sind Untersuchungen bei 7 Tesla im humanen Bereich gegenwärtig als experimentell anzusehen. Für die kardiale Bildgebung im magnetischen Hochfeld (7T) waren zum

Zeitpunkt der Entstehung dieser Arbeit notwendige Hochfrequenzspulen kommerziell nicht erhältlich. Verschiedene Spulenprototypen wurden deshalb entwickelt und auf die Machbarkeit diagnostischer Herzbildgebung geprüft und optimiert. Eine weitere Herausforderung im Hochfeld stellte die Synchronisation der Bildaufnahme mit dem Herzzyklus dar. Die konventionelle Synchronisationsmethode der Bildakquise mit dem Herzzyklus durch das Elektrokardiogramm ist in starken Magnetfeldern nicht ohne weiteres möglich. Die Ursachen wurden im Zuge dieser Arbeit untersucht, alternative Methoden entwickelt und für Humanuntersuchungen etabliert.

Abstract

Magnetic resonance imaging (MRI) is a non-invasive imaging technique free of ionizing radiation that allows medical imaging of the human body in any arbitrary orientation. Visual but subjective evaluations of longitudinal relaxation time (T_1) or transversal relaxation time (T_2) weighted images are commonly used in clinical diagnostics of cardiac MRI. For this non-quantitative measure, diagnostic quality depends on external influencing factors such as hardware configuration, sequence parameters, homogeneity of the static magnetic field (B_0) and the radio frequency transmit field (B_1^+) and the observer experience. The quantitative determination of T_1 and T_2 has the potential to offset these external influences. However, quantification is typically time consuming and can exceed clinically acceptable scan times. Different techniques described in the literature show a large scatter of normal values mainly due to insufficient model assumptions or physiological factors such as heart rate, hemodynamics, or cardiac and respiratory motion.

For these reasons, this study examines the feasibility of a rapid slice-selective T_1 quantification using variable flip angles (VFA) at magnetic field strengths of 1.5 Tesla, 3 Tesla, and 7 Tesla. For this purpose, an MR sequence was developed, which enables measurement of B_0, B_1^+ and T_1 in scan times as short as few seconds. The developed method was validated in a static phantom as well as in healthy volunteers in the brain and benchmarked against reference measurements. Exemplarily, the clinical applicability was demonstrated in patient pilot studies.

To allow measurements using this method in cardiac tissue, an MR compatible dynamic model of a human cardiac left ventricle was designed, constructed and tested. This setup resembled highly standardized physiological motion paradigms and dedicated MR signal properties to allow validation of the sequence in the presence of cardiac motion and blood flow. As no normal values for myocardium at 3T were available at the time of this study, reference values were collected in healthy volunteers using an alternative T_1 mapping approach.

Furthermore, radio-frequency (RF) coils necessary for cardiac imaging at high magnetic field strengths (7T) were not commercially available. Therefore, various multi-channel RF coil prototypes were developed, investigated, and optimized for diagnostic cardiac imaging. Another challenge in high magnetic fields was that the electrocardiogram, which is established at clinical field strengths for synchronizing the data acquisition with

the cardiac cycle, could not be used due to signal distortions. The cause of these distortions was studied and alternative approaches for data synchronization were developed and investigated.

Einführung

Die Magnetresonanztomographie (MRT) ist eine nichtinvasive Bildgebungsmethode, die frei von ionisierender Strahlung Schnittbilder des menschlichen Körpers in beliebiger Schnittorientierung erlaubt. Kardiovaskuläre MRT (CMR) bietet die Möglichkeit der Beurteilung der Morphologie, Funktion und Gewebedifferenzierung am Herzen. Neben kontrastmittelgestützten Aufnahmen bieten auch native Gewebekontraste Potential zur Detektion myokardialer Gewebeschäden. Konventionell werden neben der Wichtung der longitudinalen Relaxationszeit T_1 zur Detektion chronischer Myokardschäden auch Wichtungen der transversalen Relaxationszeit T_2 zur Detektion akuter Schäden verwendet. CMR bietet die einzigartige Möglichkeit reversible und irreversible Schäden am Gewebe zu differenzieren und akute von chronischen Ereignissen zu trennen. T_1- und T_2-gewichtete Bildgebungsverfahren sind jedoch nicht quantitativ und so unterliegt der diagnostische Wert einer Reihe von technischen und physiologischen Einflüssen. Zu den technischen Einflüssen gehören beispielsweise die Auswahl der Hochfrequenz (HF) Sende- und Empfangsspulen, die Synchronisation der Bildaufnahme mit dem Herzzyklus, räumliche und zeitliche Auflösung, die Homogenität des Grundmagnetfelds (B_0) und des HF-Sendefeldes (B_1^+), sowie die Wahl der Sequenzparameter. Physiologische Einflüsse auf die Diagnostik sind Atem-, Herz- und Blutbewegung, die begrenzte Fähigkeit der Patienten die Luft anzuhalten oder Pathologien wie Arrhythmien und Wandbewegungsstörungen, die die Bildgebung erschweren können. Die Erfahrung des Arztes gewichtete Bilder korrekt zu beurteilen spielt für eine korrekte Diagnose keine untergeordnete Rolle. Quantitative Bildgebung birgt das Potential einige dieser Fehlerquellen zu minimieren oder sogar zu eliminieren. Diese Methoden sind jedoch typischerweise zeitaufwendig und unterliegen deshalb dennoch physiologischen Einflussfaktoren wie Herzfrequenz, Hämodynamik, sowie kardiale und respiratorische Bewegung.

Aus diesen Gründen untersucht diese Studie die Durchführbarkeit einer schnellen Kartierung der Geweberelaxationszeit T_1 mit Hilfe variabler Flipwinkel (VFA) bei magnetischen Feldstärken von 1.5 Tesla, 3 Tesla und 7 Tesla. Hierzu wurde eine MR-Sequenz entwickelt, die eine Erfassung von B_0, B_1^+ und T_1 innerhalb weniger Sekunden ermöglicht [1]. Die entwickelte Methode wurde an einem statischen Phantom, sowie an gesunden Probanden im Gehirn getestet und gegen Referenzmessungen

validiert. Exemplarisch wurde in Messungen am Patienten die klinische Anwendbarkeit demonstriert.

Um eine systematische Optimierung der Sequenzen zu ermöglichen müssen technische Einflüsse von physiologischen Einflüssen separiert werden. Hierzu waren im Vorfeld hochstandardisierte Messbedingungen an statischen Phantomen und an dynamischen Modellen essentiell [2, 3]. Einflüsse konnten so gezielt untersucht und Parameter entsprechend angepasst werden. Um Messungen mit der vorgeschlagenen MR-Methode am bewegten Herzgewebe zu ermöglichen, wurde ein MR-kompatibles dynamisches Modell einer menschlichen linken Herzkammer mit hochreproduzierbaren physiologischen Bewegungsmustern und MR-Signaleigenschaften entworfen, konstruiert und getestet [4]. Dies ermöglichte eine Validierung der Sequenz unter dem Einfluss von Herzbewegung und Blutfluss. Zum Zeitpunkt der Studie waren keine Normwerte für den Herzmuskel bei 3T vorhanden, sodass als Vorarbeit zunächst mittels eines alternativen Ansatzes Referenzwerte von gesunden Probanden erhoben wurden [5]. Eine geeignete Methode zur Messung des HF-Sendefeldes am Herzen war ebenfalls nicht bekannt. Deshalb wurde als Teil dieser Arbeit eine phasenbasierte Methode realisiert und mit bereits bestehenden Methoden verglichen [6]. Als weitere Vorarbeit wurden in der vorliegenden Studie systematische Untersuchungen zu Fehlerquellen bei der Parameterkartierung durchgeführt [7].

Die Ultrahochfeldmagnetresonanztomographie bietet durch ihre intrinsisch erhöhten Signalintensitäten Potential für eine höhere zeitliche Auflösung, eine höhere räumliche Auflösung, oder eine Verkürzung der Aufnahmedauer und könnte so zu einer verbesserten Diagnose beitragen. Die technischen Unwägbarkeiten waren dato jedoch noch prävalent, sodass eine Nutzung dieser Potentiale nur bedingt möglich war. Es waren keine kommerziellen Hochfrequenzspulen für kardiale Anwendungen verfügbar, sodass diese als Teil dieser Arbeit zunächst entwickelt werden mussten. Für die kardiale Bildgebung wurden verschiedene Typen von HF-Sende- und Empfangsspulen entworfen, konstruiert, getestet und optimiert [8-12]. Das bei klinischen Feldstärken etablierte Elektrokardiogramm (EKG) zur Synchronisierung der Datenakquisition mit dem Herzzyklus konnte aufgrund von Signalverzerrungen im Hochfeld nicht verwendet werden. Die Ursache dieser Verzerrungen wurde eingehend untersucht und alternative Ansätze zur Datensynchronisation wurden entwickelt [13, 14].

Methodik

Dynamisches Modell eines linken Herzventrikels

Zur systematischen Testung von MR Sequenzen wurde ein MR kompatibles dynamisches Modell einer menschlichen linken Herzkammer erstellt [4]. Als Vorarbeit zu diesem Projekt wurde ein Prototyp-Flussmodell konstruiert und zur systematischen Untersuchungen von künstlichen Herzklappen verwendet [3]. Diese Vorarbeit war primär auf die Planimetrierbarkeit der Klappenöffnungsflächen und die Darstellung der hämodynamischen Eigenschaften ausgelegt. Kenntnisse aus weiteren vorangehenden Studien wurden für die vorliegende Arbeit genutzt, die sich mit der Quantifizierbarkeit von Blutfluss beschäftigen [2, 15]. Diese Studien legten die Grundsteine für den Entwurf und die Konstruktion des Modells einer bewegten linken Herzkammer. Das Modell umfasste drei Hauptkomponenten:

1) ein Modell der linken Herzkammer, das Elastizität und Kontraktilität sowie eine MR-Signaldynamik vergleichbar mit dem menschlichen Herzmuskel bietet

2) ein Pumpensystem, das die Kammer mit definierten pulsatilen Flussparadigmen über ein Rohrsystem versorgt

3) eine Hardwareschnittstelle zusammen mit einer eigens entworfenen Steuerungssoftware, die das Pumpsystem steuert.

Als Ausgangsmaterial wurde Silikon aufgrund der guten plastischen und elastischen Eigenschaften gewählt. Nach der Evaluierung verschiedener Produkte auf Gießbarkeit, Elastizität und MR Eigenschaften wurde ein Zweikomponentensilikon verwendet (SI 6.25, RECKLI GmbH, Herne, Deutschland). Für die Herstellung wurde eine Form auf der Grundlage der geometrischen Approximation eines Paraboloids in einem 3D-CAD - Programm (Inventor, Autodesk GmbH, München, Deutschland) entwickelt und von einem 3D - Drucker (Stratasys, Eden Prairie, USA) gedruckt. Die Abmessungen wurden von MR Schnittbildern eines gesunden Freiwilligen gewonnen und repräsentieren Normalwerte für gesunde Männer: Durchmesser 50 mm (an der Basis), Wanddicke (10 mm) und Schlagvolumen (55 ml). Die Ventrikellänge von der Basis zur Spitze betrug 75 mm. Die Relaxationszeiten T_1 und T_2 der erstarrten Ventrikelmasse wurden im 3T MRT (Verio, Siemens Healthcare, Erlangen) quantifiziert. Der Antrieb erfolgte durch einen getriebegestützten Schrittmotor, der an eine Kolbenpumpe angeschlossen war. Der Schrittmotor wurde von einer dafür eigens erstellten Steuerungssoftware in Labview (National Instruments, Austin, Texas) gesteuert. Die Steuersoftware

ermöglichte die Einspeisung beliebiger Fluss und Kontraktionsparadigmen, die der Antrieb über ein angeschlossenes Rohrsystem ausführen konnte und so das Ventrikelmodell in Bewegung setzte. Das Rohrsystem war mit einer Wasser/Glycerin-Mischung befüllt um die Viskosität von Blut zu imitieren. Flusssensordaten wurden kontinuierlich aufgezeichnet.

Da das Ventrikelphantom zur Testung von Sequenzen dienen sollte, die Pathologien darstellen können, wurde ein Modell für ein myokardiales Ödem in den Ventrikel integriert. Speziell angefertigte Silikonproben wurden mit Silikonöl vermengt und im Scanner auf Veränderungen von T_1 und T_2 untersucht. Das Silikonöl sollte fokal die myokardiale T_2 Zeit entsprechend einem myokardialen Ödem erhöhen. Die Mischung wurde fokal nach dem Befüllen der Ventrikelform, jedoch vor dem Aushärten des Silikons in die Herzkammer injiziert.

Kartierung der longitudinalen Relaxationszeit T_1 und der transversalen Relaxationszeit T_2

Um Referenzwerte für kardiale T_1 und T_2 Relaxationszeiten in gesunden Probanden zu erstellen, die bis zu diesem Zeitpunkt nicht existierten, wurden begleitend zu dieser Studie bereits bestehende T_1 und T_2 Kartierungssequenz-Prototypen an Feldstärken von 1.5T und 3T evaluiert [5, 7]. Als Ergebnis dieser Untersuchungen lässt sich ableiten, dass die Bildqualität aufgrund fehlgeschlagener Bewegungskorrektur, Suszeptibilitätsartefakten und Partialvolumeneffekten in über 8% der T_1 Messungen und in über 20% der T_2 Messungen eingeschränkt war. Dies lässt darauf schließen, dass die kardialen Kartierung von T_1 und T_2 eine schnelle und damit bewegungsunempfindliche Sequenz mit einer hohen räumlichen Auflösung erfordert [1].

Theorie

Schnelle Hochfrequenz (HF) gespoilte Gradientenecho (FLASH) Messungen mit mindestens zwei Flipwinkeln ermöglichen die Quantifizierung der longitudinalen Relaxationszeit T_1. Die allgemein anerkannte mathematische Gleichung, mit der sich FLASH Signalintensitäten S(α) im stationären Zustand (steady-state) berechnen lassen lautet

$$S_{FLASH}(\alpha) = M_0 \frac{(1-E_1)\sin(\alpha)}{1-E_1\cos(\alpha)}, \text{ mit } E_1 = e^{-\frac{TR}{T_1}}, \qquad \text{(Gleichung 1)}$$

mit M_0 als Protonendichte, TR als Repetitionszeit und α als Flipwinkel. Die Umstellung von Gleichung 1 ergibt

$$\frac{S_{FLASH}(\alpha)}{\sin(\alpha)} = E_1 \frac{S_{FLASH}(\alpha)}{\tan(\alpha)} + M_0(1-E_1) \qquad \text{(Gleichung 2)}$$

Die Darstellung der Gleichungen S(α)/sin(α) über S(α)/tan(α) ermöglicht die Extraktion von T_1 = -TR/ln(m) über die Ausgleichsgerade, wobei m die Steigung zwischen den Messpunkten darstellt.

Analog zu dieser Methode können balanced steady-state-free-precession (bSSFP) Aufnahmen mit variablen Flipwinkeln dazu verwendet werden, um die transversale Relaxationszeit T_2 zu ermitteln. Hierfür wird die linearisierte Signalgleichung verwendet:

$$\frac{S_{SSFP}(\alpha)}{\sin(\alpha)} = \frac{E_1 - E_2}{1 - E_1 E_2} \times \frac{S_{SSFP}(\alpha)}{\tan(\alpha)} + \frac{M_0(1-E_1)}{1-E_1E_2}, \text{ mit } E_2 = e^{-\frac{TR}{T_2}} \text{ (Gleichung 3)}$$

Die transversale Relaxationszeit lässt sich aus $T_2 = -TR / \ln\left(\frac{m - E_1}{mE_1 - 1}\right)$ berechnen.

Verwendung von drei Flipwinkeln

Erweiternd zum herkömmlichen Ansatz mittels zweier Flipwinkel, wurde der Vorteil der Anwendung dreier Flipwinkel für die VFA T_1 Quantifizierung untersucht. Hierbei wurde der erste Flipwinkel so gewählt, dass die maximale Signalintensität unter Berücksichtigung der jeweiligen T_1-Zeit erreicht wird. Die übrigen zwei Flipwinkel wurden von 1 ° bis 90 ° variiert. Gaußsches Rauschen wurde dem Signal hinzugefügt. Um Quantifizierungsfehler zu minimieren wurden Flipwinkeltripel berechnet, die die kleinsten Abweichungen zum theoretischen T_1 Wert aufwiesen. Diese Flipwinkel wurden für die Phantomexperimente und für die in-vivo Studien verwendet. In einem ersten Schritt wurden diese einmaligen Berechnungen für die T_1-Zeit des Phantoms durchgeführt. In einem zweiten Schritt wurden Flipwinkel für graue und weiße Substanz aus arithmetisch gemittelten Literaturwerten bei verschiedenen Feldstärken (T_1 = 950 ms bei 1.5T, T_1 = 1250 ms bei 3T, und T_1 = 1650 ms bei 7T) berechnet. Montecarlo Simulationen mit je 10000 Experimenten von T_1 = 1 ms bis T_1 = 3000 ms in Schritten von 1 ms wurden für den vorgeschlagenen Ansatz mit drei Flipwinkeln und für den herkömmlichen Ansatz mit zwei Flipwinkeln durchgeführt, um die Genauigkeit und Präzision der jeweiligen Methode zu untersuchen.

Simulationen der Bloch-Gleichungen

Gleichung 1 bis 3 gelten für Anregungen, die einen einheitlichen Flipwinkel über die gesamte Zielregion aufweisen. In schichtselektiven Aufnahmen jedoch führen nichtideale HF-Pulse zu Verformungen des Schichtprofils, welche sich in einer veränderten resultierenden Signalintensität ausdrücken. Um das Ausmaß der Deformation des Schichtprofils und ihre Auswirkungen auf die T_1 Quantifizierung mittels VFA zu untersuchen, wurde eine Simulationsumgebung in Matlab (TheMathWorks, Natick, MA, USA) erstellt, die Simulationen der Bloch-Gleichungen und die Simulation einer FLASH- und SSFP-Sequenz ermöglicht. Um die entwickelte Simulationsumgebung zu testen wurden simulierte Schichtanregungsprofile mit gemessenen Anregungsprofilen verglichen (exemplarisch am 3T Scanner mittels FLASH-Sequenz, $\alpha = 30°$). Darüber hinaus wurden simulierte und gemessene Signalintensitäten in Abhängigkeit des Flipwinkels verglichen (Echozeit (TE) = 2.5 ms; TR = 5 ms; $\alpha = 2°$-$90°$, Voxelgröße = (2x2x5) mm³).

Kartierung des Hochfrequenz-Sendefeldes (B_1^+-Mapping)

VFA-Verfahren beruhen auf genauer Vorkenntnis des im Zielbereich vorherrschenden Flipwinkels. Daher ist eine Korrektur von B_1^+-Inhomogenitäten essentiell. Grundsätzlich gibt es eine Reihe verschiedener Methoden, um das HF Sendefeld zu kartieren. Als Teil dieser Studie wurde eine Bloch-Siegert-Sequenz (TR = 100 ms, Fermi-Puls Flipwinkel = 400°, nominelles B_1^+ = 4,35 µT, Resonanzabweichung = 4 kHz) realisiert und mit anderen phasenbasierte Methoden verglichen [6]. Um gleichzeitig die Homogenität des Grundmagnetfeldes zu erfassen (B_0-Kartierung) verwendete die Sequenz Doppel-Gradientenecho-Akquisitionen mit Echozeiten, die auf die Fett/Wasser-Frequenzverschiebung angepasste wurden. Die Berechnungen der gemessenen Sendefeldverteilung normiert auf das eingespeiste B_1^+ wurden mittels Bloch-Simulationen in einer dafür entwickelten Matlabroutine unter Berücksichtigung der B_0 Resonanzverschiebungen realisiert.

MR-Hardware

Messungen am Modell und am Gehirn wurden an 1.5T/3T/7T MR Ganzkörpertomographen (Avanto/Verio/Magnetom 7T, Siemens Healthcare, Erlangen) mit identischer Software durchgeführt. Bei 1.5T und 3T wurden 12-Kanal-Kopfspulen

(Siemens Healthcare, Erlangen) für den Signalempfang verwendet werden, während bei 7T eine 24-Kanal-Kopfspule (Nova Medical, Andover, MA, USA) zum Einsatz kam. Für das Senden wurde bei 1.5T und 3T die integrierte Körperspule und bei 7T der Sendekanal der Kopfspule verwendet.

Validierung durch Experimente am Phantom

Eine ovales Phantom auf Wasserbasis (d = 10 cm, l = 20 cm, T_1 = 960 ms, T_2 = 100 ms, gemessen bei 1.5T) wurde konstruiert, um die geometrische Form und die T_1-Mittelwerte von grauer und weißer Substanz des menschlichen Gehirns bei 1.5T widerzuspiegeln. T_1 wurde mittels Zugabe von Manganchlorid und die Leitfähigkeit mittels Zugabe von Natriumchlorid eingestellt.

Als T_1 Referenzmessung diente eine Inversion-Recovery (IR) Technik (Voxelgröße = (2x2x5) mm³, TR = 10 s, α = 90°, Turbofaktor = 5, GRAPPA Beschleunigungsfaktor = 2, 8 Inversionszeiten = 60/120/240/480/750/1000/3000/5000 ms, Aufnahmedauer = 16 min) in Verbindung mit einem Spin-Echo Auslesemodul (Echoabstand = 5.5 ms). T_1 wurde in Matlab unter Verwendung einer Drei-Parameter-Kurve extrahiert.

Um die Durchführbarkeit und die Genauigkeit der 2D VFA T_1 Kartierung unter Berücksichtigung deformierter Schichtprofile zu überprüfen wurden 2D-FLASH Aufnahmen (TE/TR = 2.5/5 ms, Aufnahmezeit = 3.5 s) mit einem Satz von drei Flipwinkeln erstellt. B_1^+ Karten wurden verwendet, um die B_1^+ Inhomogenität zu berücksichtigen. T_1 des Phantoms wurde für alle Feldstärken (1.5T, 3T und 7T) quantifiziert. Zu diesem Zweck wurde eine Region in der Schicht ausgewertet, die den gesamten Querschnitt des Phantoms in einer zentralen koronaren Schicht einschloss. T_1 Mittelwerte und Standardabweichungen wurden berechnet. Um die Auswirkungen der Signaländerung aufgrund der Deformation des Schichtprofils auf die Quantifizierung von T_1 zu analysieren wurden konventionelle B_1^+ korrigierte VFA T_1 Messungen (α = 2°/13°) durchgeführt, die für 3D-Akquisitionen verwendet werden und Schichtprofildeformationen nicht berücksichtigen. Aus Gründen der Übersichtlichkeit wird im Folgenden der Ausdruck "unkorrigierte 2D VFA" für diesen Ansatz verwendet. Der vorgeschlagene Ansatz der B_1^+ korrigierten 2D VFA T_1 Kartierung, der gegenüber dem herkömmlichen Ansatz zusätzlich die Schichtprofilverformung berücksichtigt, wird als "korrigierte 2D VFA" bezeichnet.

In-vivo-Studien am Gehirn an gesunden Probanden und Patienten

Axiale 2D Bilder des Gehirns wurden mit angepassten Flipwinkel-Tripeln akquiriert (FLASH, TE/TR = 2.5/5 ms, Aufnahmezeit = 3.5 s). Die für die Phantommessungen beschriebene IR-basierte T_1 Referenzmethode wurde auch für die Probandenstudie verwendet. Graue Substanz und weiße Substanz von sechs gesunden Probanden wurden durch die Anwendung einer Kombination von Schwellenwerten in T_1-gewichteten Bildern und T_1-Karten aus der Referenzmessung segmentiert. Mittlere T_1-Zeiten und Standardabweichungen wurden für die Referenzmethode, die unkorrigierte 2D VFA und die korrigierte 2D VFA berechnet. Für die Probandenstudien wurde eine räumliche Auflösung von (2x2x5) mm³ für die Datenerfassung verwendet, die bei der Rekonstruktion auf (1x1x5) mm³ interpoliert wurde. Für Patientenstudien wurde eine räumliche Auflösung von (1.6x1.6x4) mm³ interpoliert auf (0.8x0.8x4) mm³ gewählt.

Kardiale Bildgebung im Hochfeld

Um eine Bildgebung am Herzen zu ermöglichen, mussten zunächst HF-Sende- und Empfangsspulen entwickelt werden. Bei einer magnetischen Feldstärke von 7T und höher gestaltet sich dies besonders schwierig, da HF-Wellenlängenphänomene zu Interferenzen und damit zur lokalen Verstärkungen oder Auslöschungen des Sendefeldes beitragen können. Es wurde zunächst eine Vierkanalspule entworfen, realisiert und getestet [8, 11]. Die Spule bestand aus einem anterioren und einem posterioren Element mit jeweils zwei Spulenschleifen. Dieser Entwurf war einer der ersten Versuche weltweit, die kardiale Bildgebung im Ultrahochfeld zu ermöglichen. Die Errichtung und Testung der Spule umfasste die Konstruktion, Simulationen zur Erwärmung des Gewebes, sowie Untersuchungen am Phantom und am gesunden Probanden. Aufgrund ihrer besseren Sendeeffizienz werden Oberflächenspulen bei Ultrahochfeldapplikationen bevorzugt eingesetzt. So kann mehr Leistung appliziert werden, ohne die zulässigen Erwärmungsgrenzen von Gewebe zu überschreiten. Um eine ausreichend gute Sendeleistung und Sendehomogenität zu erhalten wurden begleitend zu dieser Studie weitere Spulenkonzepte realisiert und in ähnlicher Weise evaluiert [9, 10, 12, 16].

Eine weitere Komponente der kardialen Bildgebung stellt die Synchronisation der Datenaufnahme mit dem Herzzyklus dar. Bei klinischen Feldstärken bis 3T wird ein konventionelles EKG verwendet. Bei Hochfeldapplikationen dagegen ist das EKG

aufgrund von magnetohydrodynamischen Effekten des Blutflusses gestört und kann in den meisten Fällen nicht als Synchronisationsmethode herangezogen werden. Zur Untersuchung dieser Effekte wurden eigens Studien durchgeführt. Hierzu wurden an einem für diesen Zweck entworfenen pulsatilen Flussphantom systematische Untersuchungen zur Abhängigkeit der durch Fluss erzeugten Spannungspotentiale von magnetischer Feldstärke, Elektrodenabstand, Flussrichtung relativ zu den Magnetfeldlinien, sowie Fließgeschwindigkeit unternommen. Um die magnetohydrodynamischen Effekte zu umgehen wurde eine alternative Methode zur Bildsynchronisation eingeführt und verwendet. Diese Methode beruht auf dem Prinzip des Phonokardiograms und macht sich den ersten Herzton zunutze, der beim Schließen der Atrioventrikularklappen entsteht. Eine Schnittstelle versehen mit einem Mikrokontroller erlaubt die Filterung von Störgeräuschen, die Extraktion des Herztons und die akustische Triggerung (ACT) der Bildakquisition in Echtzeit [13]. Neben der Unabhängigkeit von elektrischen Spannungspotentialen ist ein weiterer Vorteil dieser Methode direkt mit der kardialen Bewegung gekoppelt zu sein, anstatt wie beim EKG mit der elektrischen Aktivität des Herzens. Bewegte Herzbilder wurden von neun Probanden jeweils mit EKG, Pulsoxymeter, und ACT erstellt und die Bildqualität von einem erfahrenen Kardiologen begutachtet und verglichen.

Ergebnisse

Dynamisches Modell eines linken Herzventrikels

Abbildung 1 zeigt den Aufbau des Ventrikelphantoms. Um Oszillationen bei schnell wechselnden Fließgeschwindigkeiten zu vermeiden wurde eine Kombination aus Kupfer- und Plastikrohren als Verbindung zwischen Pumpe und Ventrikelmodell eingesetzt. Die Befüllung erfolgte über ein separates Befüllungssystem mittels Kunststoffschläuchen.

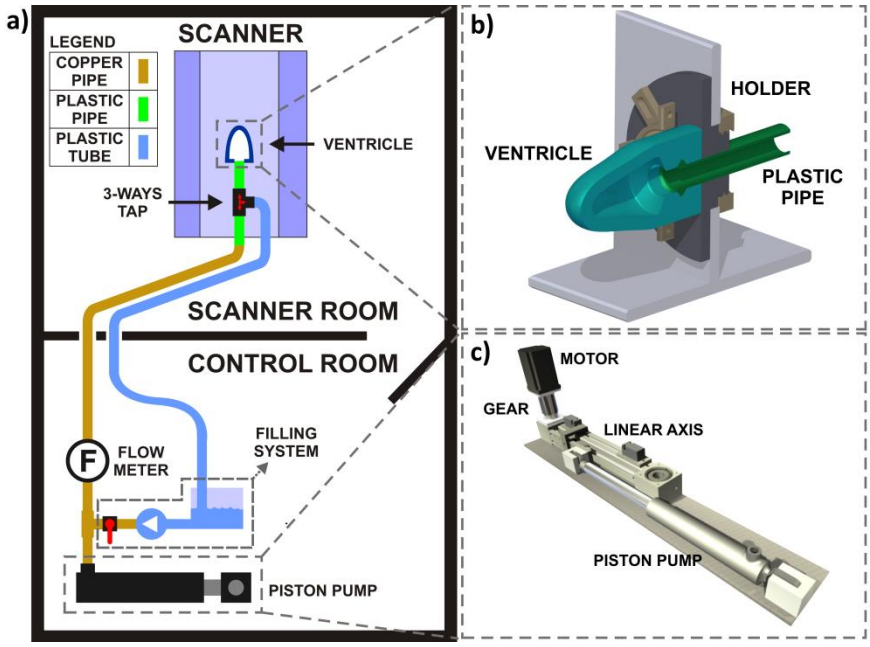

Abbildung 1: (a) Systemaufbau: Kupferrohre propagieren ein Wasser/Glycerin-Gemisch von der Pumpe im Kontrollraum in die künstliche Herzkammer im Scanner. Eine Füllpumpe mit angeschlossenem Rohrsystem vereinfacht den Füllvorgang. Strömungssensordaten wurden kontinuierlich erfasst und in der Steuereinrichtung gespeichert. **(b)** 3D-Modell (Inventor, Autodesk GmbH, München, Deutschland) der linken Herzkammer in einer Halterung. **(c)** Pumpensystem bestehend aus einem getriebegestützten Schrittmotor, einer Linearachse und einer Kolbenpumpe. Der Antrieb erfolgte über einen Labview-Schnittstelle.

Die Messung der T_1 Zeit des Ventrikels ergab 1002±8 ms, die T_2 Zeit betrug 58±1 ms. Beide Zeiten liegen in der Größenordnung von menschlichen myokardialen T_1 und T_2 Zeiten. Abbildung 2 zeigt die T_2 Kartierung eines Kurzachsenschnitts des Ventrikelmodells in der Höher der injizierten Pathologie. Das ödemartige Gemisch

befindet sich auf der unteren Seite und weißt eine T_2 Erhöhung auf, die sich in derselben Größenordnung auch in in-vivo Messungen findet [7].

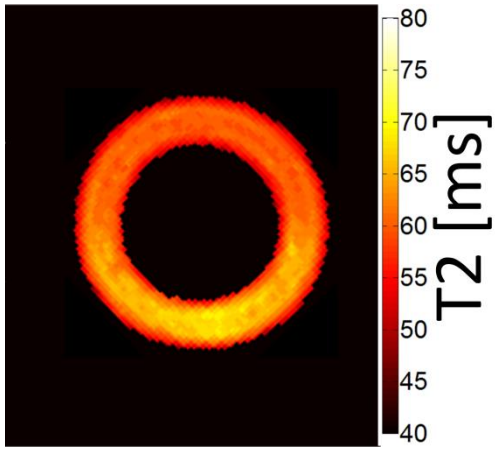

Abbildung 2: T_2-Karte einer mittventrikulären kurzen Achse in der Höhe der fokal injizierten Mischung, die T_2-Zeiten eines myokardialen Ödems widerspiegelt. T_2-Zeiten wurden um ca. 30% von 59±1 ms auf 75±2 ms erhöht. T_2-Werte variieren mit der Dispersion der Ödemmischung im Ventrikel aufgrund von Partialvolumeneffekten.

Der Antrieb zusammen mit der dafür entwickelten Steuersoftware erlaubte eine Einspeisung beliebiger Fluss- und Kontraktionsmuster, welche durch das im Scanner befindliche Ventrikelmodell ausgeführt und mittels Flusssensoren und Phasenkontrast-Flussmessungen überwacht wurden. Abbildung 3a zeigt eine sehr gute Übereinstimmung von eingespeisten gaussförmigen Flussparadigmen, den Flusssensordaten und den Phasenkontrastmessungen. Abbildung 3b zeigt die dazugehörigen Volumenkurven. Um ein repräsentatives Flussparadigma zu testen, wurde von einem gesunden Probanden das Flussparadigma aus einer Phasenkontrastmessung in der aufsteigenden Aorta extrahiert (Abbildung 3c). Abbildung 3d zeigt das Paradigma eines Patienten, der an einer Aortenklappenstenose und einer Aortenklappeninsuffizienz leidet. Auch bei diesen physiologischen Flusskurven stimmen die Messungen mit dem Paradigma sehr gut überein.

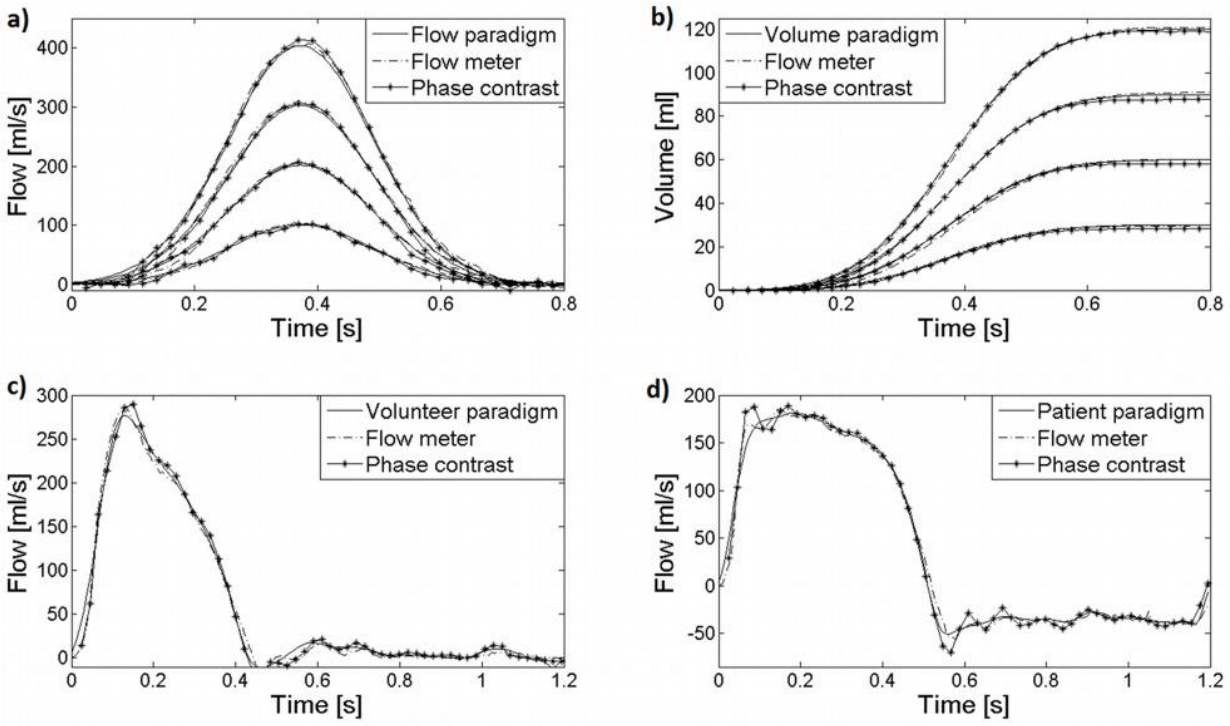

Abbildung 3: *Messwerte des Durchflussmessers (Strich-Punkt-Linie) gegenüber der MR-Phasenkontrast-Flussmessungen (Punkte) für verschiedene Flussparadigmen (durchgezogene Linie)*

Die zeitlich aufgelöste Fluss- **(a)** und Volumenmessungen **(b)** zeigten eine gute Übereinstimmung mit den Eingangsparadigmen für Schlagvolumen von 30/60/90/120 ml. **(c)** Flussparadigma von der aufsteigenden Aorta eines gesunden Probanden und **(d)** eines Patienten mit Aortenklappenstenose und Aortenklappeninsuffizienz. Auch hier stimmen Phasenkontrast-Flussmessungen und Messungen mittels Durchflussmesser gut mit den Paradigmen überein.

Kartierung des longitudinalen Relaxationsparameters T_1

Die Verwendung von drei Flipwinkeln verbesserte den Präzisionsindex ($\sigma T_1 / \overline{T}_1$) um durchschnittlich 11% gegenüber der Verwendung von nur zwei Flipwinkeln (Abbildung 4a). Abbildung 4b zeigt das Schichtprofil aus den Simulationen der Bloch-Gleichungen (blaue Linie) und der Messung im Phantom (schwarze gestrichelte Linie). Simulation und Messung zeigen sehr gute Übereinstimmung. Die Verformung des Schichtprofils wird durch die HF-Pulsform, TR, T_1 und den Flipwinkel maßgeblich bestimmt. Die Übereinstimmung spiegelt sich auch in den simulierten Signalkurven (blaue Linie)

versus den Messungen (schwarze Punkte) in Abhängigkeit vom Flipwinkel wider, wie Abbildung 4c zeigt. Als Referenz ist der theoretische Signalverlauf ohne Deformierung des Schichtprofils (grüne gestrichelte Linie) dargestellt. Die maximale Signalintensität trat bei $\alpha = 11°$ auf (unter Berücksichtigung der Schichtprofilverformungen) im Gegensatz zum theoretischen Ernst-Winkel von 6°.

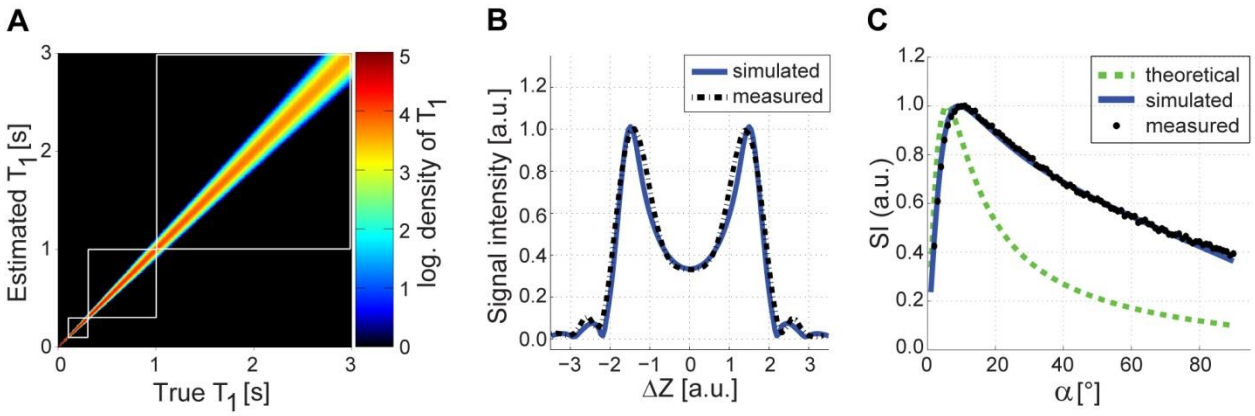

Abbildung 4: *Montecarlo Simulation, Schichtprofil und Signalintensitäten*
(a) Simulierte logarithmische Dichteverteilung der wahren T_1-Werte gegen die durch korrigierte 2D VFA berechneten T_1 Werte. Für jeden T_1-Wert wurden 10000 Experimente durchgeführt. **(b)** Simulation des Schichtprofils mittels Bloch-Gleichungen (blaue Linie) und Schichtprofilmessungen (schwarz gestrichelte Linie) in einem Wasserphantom (T_1 = 1000 ms) mittels einer FLASH-Sequenz (TR = 5 ms, $\alpha = 30°$) zeigen gute Übereinstimmung. Das Schichtprofil weicht wesentlich von einem idealen Rechteck ab.
(c) Theoretische (grün gestrichelte Linie), Bloch simulierte (blau Linie) und gemessene (schwarze Punkte) Signalintensitäten für FLASH in Abhängigkeit vom Flipwinkel.

Die Korrektur des HF-Sendefeldes zusammen mit der Korrektur der Schichtprofildeformation ermöglichte eine T_1 Kartierung im Phantom. Abbildung 5a zeigt die Verteilungen des HF-Sendefeldes bei verschiedenen Feldstärken, die zur Korrektur der 2D VFA T_1 Kartierung herangezogen wurden. Abbildung 5b zeigt die IR-Referenzmessung, die unkorrigierte 2D VFA T_1 Kartierung und die korrigierte 2D VFA T_1 Kartierung. Die Differenzen zwischen Referenzmessung und unkorrigierter bzw. korrigierter 2D VFA T_1 Kartierung ist in Abbildung 5c dargestellt. Der unkorrigierte Ansatz ergab eine Unterschätzung der T_1-Zeit um -63.0±1.5% gemittelt über alle

Feldstärken im Vergleich zur Referenzmessung. Der korrigierte Ansatz dagegen ergab eine T_1-Abweichung von lediglich 0.2±1.4%.

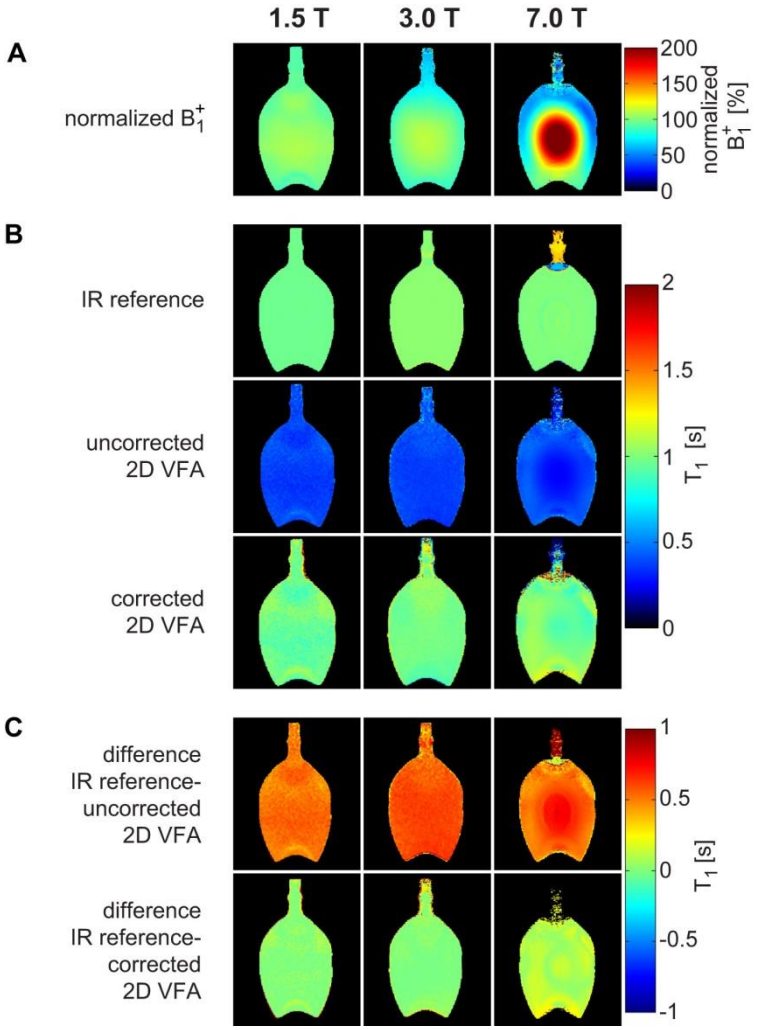

Abbildung 5: *Normierte B_1^+ Karten (a), T_1-Karten (b) und T_1-Differenzkarten im Wasserphantom (c) bei 1.5T, 3T und 7T*

(a) Gemessenes B_1^+ normiert auf nominelles B_1^+ (4,35 µT) in Prozent. **(b, obere Reihe)** T_1 aus der IR-Referenzmessung (T_1 = 963±7 ms bei 1.5T, T_1 = 1022±10 ms bei 3T, T_1 = 1002±10 ms bei 7T). **(b, mittlere Reihe)** Unkorrigierter 2D VFA Ansatz, der lediglich B_1^+ korrigiert aber Schichtprofilverformungen nicht berücksichtigt. **(b, untere Reihe)** T_1-Karte mit Korrektur von B_1^+ und der Schichtprofildeformierung. **(c, obere Reihe)** Differenzkarte zwischen IR-Referenz und unkorrigierter 2D VFA. **(c, untere Reihe)** Differenzkarte zwischen IR-Referenz und korrigierter 2D VFA.

Auch in-vivo konnte die Korrektur des HF-Sendefeldes zusammen mit der Korrektur der Schichtprofildeformation eine Verbesserung in Bezug auf die Referenzmessung

herstellen, wie Abbildung 6 demonstriert. Die angepassten Flipwinkel für die unkorrigierte 2D VFA waren 2°/13°, 2°/12° und 2°/11° für die magnetischen Feldstärken von 1.5T, 3T und 7T. Für die korrigierte 2D VFA wurden 3°/11°/26°, 3°/9°/22° und 3°/8°/25° verwendet.

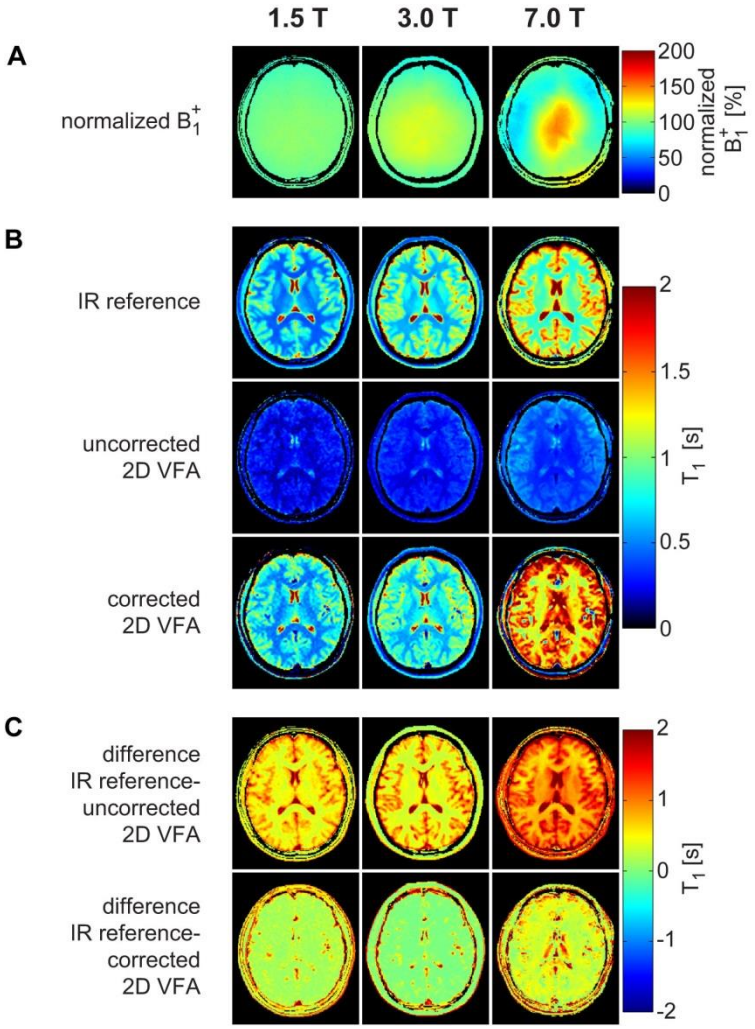

Abbildung 6: B_1^+ Karten **(a)** und T_1 Karten **(b)** vom Gehirn eines gesunden Probanden mittels IR-Referenzmessung, unkorrigierter 2D VFA und korrigierter 2D VFA bei 1.5T, 3T und 7T. **(c)** Differenz zwischen IR-Referenzkarte und unkorrigierter/korrigierter 2D VFA.

Tabelle 1 zeigt die mittels IR-Referenzmessung, unkorrigierter 2D VFA und korrigierter 2D VFA gemessenen T_1 Werte in gesunden Probanden für graue und weiße Substanz bei magnetischen Feldstärken von 1.5T, 3T und 7T.

		T_1 [ms]		
		1.5T	**3T**	**7T**
Weiße Substanz	IR Referenz	678±10	911±15	1284±22
	Unkorrigierte 2D VFA	298±14	377±25	554±21
	Korrigierte 2D VFA	791±21	969±85	1855±141
Graue Substanz	IR Referenz	1154±82	1615±149	2065±69
	Unkorrigierte 2D VFA	465±40	518±42	804±48
	Korrigierte 2D VFA	1282±78	1433±80	2524±137

Tabelle 1: T_1 Werte für graue/weiße Substanz in gesunden Probanden für IR-Referenzmessung, unkorrigierte 2D VFA und korrigierte 2D VFA bei magnetischen Feldstärken von 1.5T, 3T und 7T.

Exemplarisch wurden korrigierte 2D VFA T_1 Messungen bei einem Patienten mit Multipler Sklerose bei 7T und einem Schlaganfallpatienten bei 3T durchgeführt. Die T_1 Karten sind in Abbildung 7 dargestellt. Die Abgrenzbarkeit der Läsionen ist in den T_1 Karten sehr deutlich.

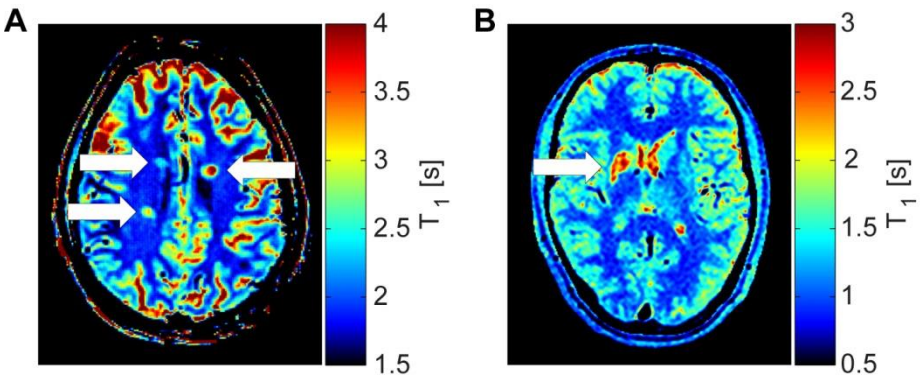

Abbildung 7: (a) T_1-Karte mittels korrigierter 2D VFA eines Multiple Sklerose Patienten bei 7T. Die Karte zeigt drei periventrikuläre Läsionen (weiße Pfeile). Gemittelte T_1 der Läsionen war 2758±615 ms im Vergleich zu 1842±62 ms in der umgebenden weißen Substanz. **(b)** Korrigierte 2D VFA T_1-Karte eines Schlaganfall-Patienten bei 3T, die eine subkortikale Läsion (weißer Pfeil) aufweist. Der Schlaganfall trat fünf Monate vor der Messung auf. T_1 der Läsion war 2554±316 ms im Vergleich zu 951±74 ms in der umgebenden weißen Substanz.

Kardiale Bildgebung im Hochfeld

Die Vierkanal-HF-Sende- und Empfangsspule (Abbildung 8) für Messungen am Herzen wurde erfolgreich entworfen, konstruiert und an gesunden Probanden getestet [8, 11]. Abbildung 9 demonstriert, dass die Spule sowohl in verschiedenen kardialen Langachsenschnitten als auch in den Kurzachsenschnitten eine hervorragende Bildqualität und Signalhomogenität mit exzellentem Blut-Myokard-Kontrast liefert und im Vergleich zu klinischen Feldstärken eine Messung mit erhöhter räumlicher Auflösung von bis zu (1x1x2.5) mm^3 unterstützt. Es konnten Schnittbilder in diagnostischer Qualität erstellt werden.

Die Untersuchungen der Signalverzerrungen im EKG ließen auf magnetohämodynamische Effekte schließen, die in Phantommessungen reproduziert werden konnten. Hierbei erzeugt das fließende Blut je nach Flussrichtung, Geschwindigkeit und Elektrodenabstand ein elektrisches Potential, das zu einer Erhöhung der T-Welle führt. Abschließend konnten diese Spannungspotentiale zur Triggerung peripherer Angiographien verwendet werden. Dies konnte am Beispiel der Karotiden demonstriert werden [14].

Die Auswertung von Signalspuren verschiedener Triggermethoden ergab eine Überlegenheit der akustische Triggerung gegenüber EKG und Pulsoximetrie [13]. EKG und Pulsoxymeter weisen im Gegensatz zu ACT eine große Streuung der Triggerzeitpunkte auf. Mittels ACT aufgenommene Herzbilder wurden von einem erfahrenen Kardiologen mit der besten Bildqualität bewertet.

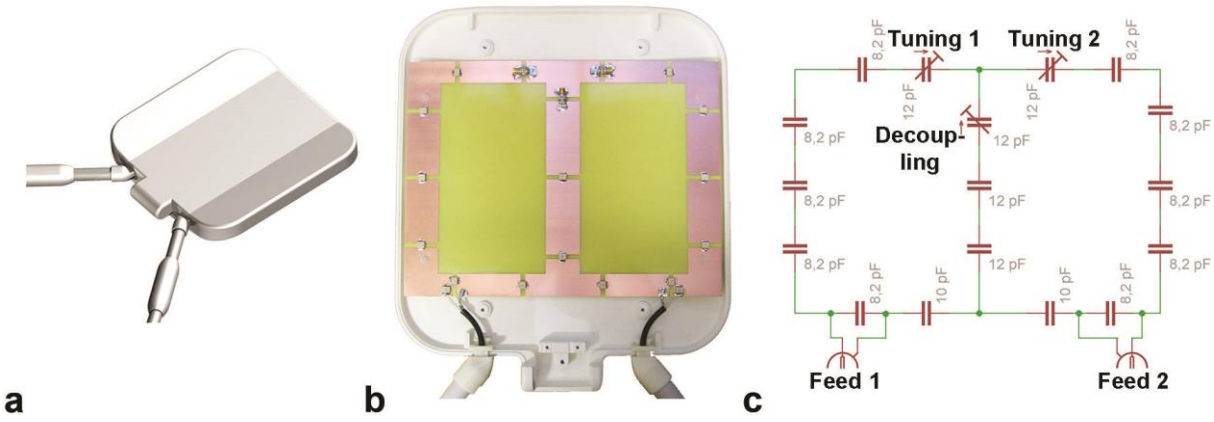

Abbildung 8: 3D-Modell eines der Körpergeometrie angepassten Spulengehäuses **(a)**, das Interieur der vorgeschlagenen Spulenkonstruktion **(b)** und das Prinzipschaltbild **(c)**.

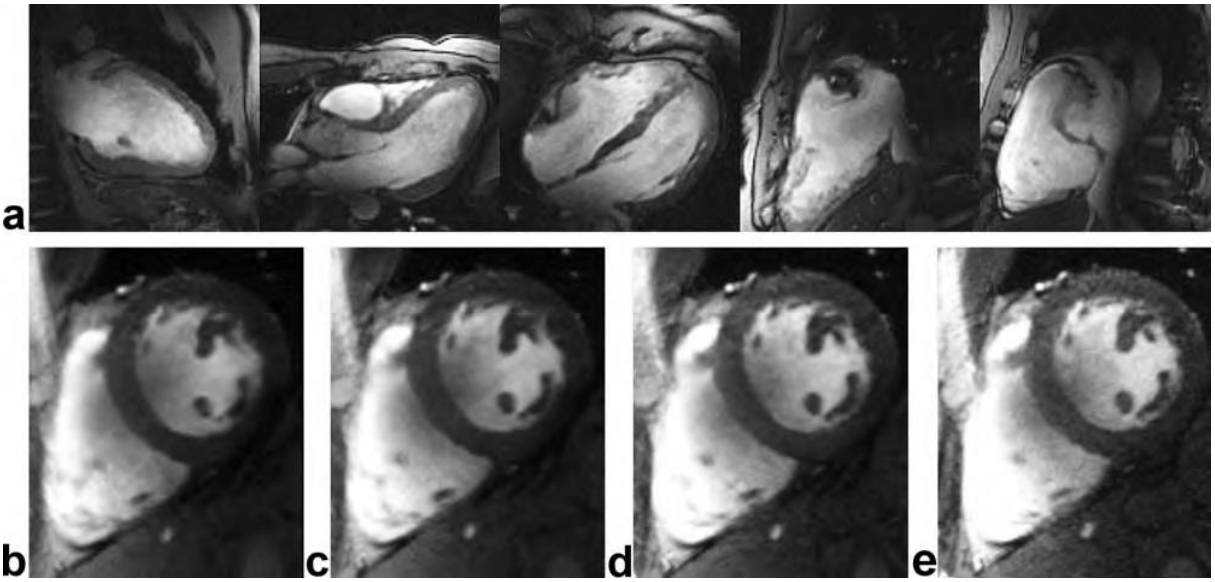

Abbildung 9: **(a)** 2D-FLASH CINE Bilder mit der Vierkanal-Sende/Empfangs-HF-Spule bei 7T in der späten Diastole in verschiedenen Ansichten (von links nach rechts: Zwei-Kammer-Blick, Drei-Kammer-Blick, Vier-Kammer-Blick, lange Achse des rechten Ventrikels, Aortenklappe). **(b)** Mittventrikulärer Kurzachsen-Blick. Der inhärente Signalgewinn von 7T wurde bei einer planaren Auflösung von 1x1mm² in eine reduzierte Schichtdicke von **(b)** 8 mm, **(c)** 6 mm, **(d)** 4 mm, und **(e)** 2.5 mm übersetzt.

Diskussion

Die vorliegende Studie demonstriert die Machbarkeit der schnellen 2D T_1 Quantifizierung mittels variabler Flipwinkel in Phantomexperimenten und in vivo im Gehirn von gesunden Probanden und Patienten bei Magnetfeldstärken von 1.5T, 3T und 7T.

Zur standardisierten Messung unter dynamischen Bedingungen wurde ein bewegtes MR-kompatibles Modell einer menschlichen linken Herzkammer entwickelt und untersucht. Das Ventrikelmodell zeigte ausreichende Signalintensitäten und wies MR Relaxationsparameter auf, die dem menschlichen Herzmuskelgewebe ähnlich sind. Fokal veränderte Materialeigenschaften wurden erfolgreich in das Herzkammermodell integriert, die akut verletztes Herzgewebe reflektieren. Die Elastizität und Standhaftigkeit des Modells ermöglichte einen Antrieb durch ein motorisiertes Pumpsystem. Die Steuereinheit erlaubte einstellbare Funktionsparameter wie Fluss-/Kontraktionsparadigma, Herzfrequenz, Schlagvolumen, Ejektionsfraktion, sowie endsystolische und enddiastolische Volumina. Das System unterstützte physiologische und pathophysiologische Kontraktions- und Relaxationsparadigmen über eine große Bandbreite an hämodynamischen Flussbedingungen. Dedizierte Flussparadigmen wurden erfolgreich ausgeführt. Die Genauigkeit und Zuverlässigkeit des Systems wurde durch den Einsatz eines Durchflussmessers, Phasenkontrastflussmessungen und Cine-Volumetrie nachgewiesen.

Um die kardiale Bildgebung bei 7T zu ermöglichen wurde eine Vierkanalspule erfolgreich entworfen, konstruiert und appliziert. Eine diagnostische Bildqualität mit ausreichender Signalhomogenität, exzellentem Blut-Myokard-Kontrast und einer räumlichen Auflösung von bis zu 1x1x2.5 mm³ konnte mithilfe der akustischen Triggerung erreicht werden. Feine anatomische Strukturen wie Perikard, Mitral-und Trikuspidalklappe und deren Apparatus, sowie Trabeculae konnten genau abgegrenzt werden. Dieser Schritt war notwendig, um die Grundlagen für die Applikation von T_1 Kartierungen am Herzen bei 7T zu schaffen.

Die entwickelte Sequenz ist in der Lage, B_0, B_1^+ und T_1 in kürzester Zeit zu akquirieren. Auswirkungen von HF-Sendefeldinhomogenitäten sowie Deformationen des Schichtprofils aufgrund nichtidealer HF-Pulse wurden zu diesem Zweck eingehend untersucht und berücksichtigt. Die durch Schichtprofilverformung induzierten Fehler im Vergleich zu Referenz konnten mittels Simulationen der Bloch-Gleichungen für alle

getesteten Feldstärken korrigiert werden. Die Verbesserung der Messgenauigkeit durch das vorgeschlagene Verfahren für angepasste Flipwinkel wurde durch Simulationen und experimentellen Daten bestätigt. Die Korrektur durch B_1^+ Karten immunisierte die korrigierte 2D VFA T_1 Kartierungsmethode gegen HF Sendefeldinhomogenitäten, die bei hohen und ultrahohen Feldstärken ausgeprägt sind.

Im Vergleich zur vorgestellten Methode wurde die Referenzmethode bereits unter Verwendung paralleler Bildgebung mit einem Beschleunigungsfaktor von R = 2 zusammen mit einem Turbo-Spin-Echo-Faktor = 5 und einem reduzierten Phasenfeld beschleunigt. Der korrigierte 2D VFA Ansatz reduziert die Datenakquisitionszeit um einen Faktor von etwa 570 gegenüber der unbeschleunigten Inversion-Recovery Referenzmethode. Offensichtlich unterstützt die korrigierte 2D VFA T_1-Kartierung moderate Beschleunigungen, die den Geschwindigkeitsvorteil gegenüber der Referenz weiter ausbauen. Die schnelle Datenerfassung reduziert zudem die Bewegungsempfindlichkeit der Methode.

Unsere Ergebnisse zeigen schwere T_1 Quantifizierungsfehler aufgrund von Schichtprofildeformierungen in der unkorrigierten 2D VFA T_1 Kartierungsmethode, die lediglich auf theoretischen Signalgleichungen beruht. Dies unterstreicht, dass die theoretische Signalberechnungen nur für ideale rechteckige Schichtprofile unter der Annahme gleichmäßiger Anregung über die gesamte Schicht gelten. In der Realität sind schnelle HF-Pulse jedoch in der Bandbreite begrenzt und führen zu einer räumlich ungleichmäßigen Flipwinkelverteilung. Der Grad der Schichtprofildeformation ist abhängig von HF-Pulsform, T_1, TR und dem angewendeten Flipwinkel. Folglich ist es wichtig Schichtprofilverformungen zu korrigieren, bevor 2D VFA T_1-Werte als korrekt betrachtet werden können.

Die T_1 Kartierung des Gehirns zeigte eine gute Übereinstimmung mit der Referenzmessung bei 1.5T und 3T sowohl für graue als auch für weiße Substanz. Mittels korrigierter 2D VFA gemessene T_1 Relaxationszeiten waren bei 7T höher in Bezug auf die Referenzmessung, obwohl die Phantommessungen eine gelungene Korrektur bestätigen. Der Grund für die Abweichung zur Referenzmessung lag vermutlich in der unzureichenden Annahme, dass Gewebe nur aus einer einzigen Komponente besteht und daher von einer monoexponentiellen Relaxation ausgegangen wurde. Im Zuge dieser Arbeit wurden auch Signalsimulationen mit Mischgewebe erstellt. Die simulierten Differenzen zwischen der IR-Referenzmessung und der

korrigierten 2D VFA Methode lagen in der Größenordnung der in in-vivo Experimenten beobachteten Abweichungen.

Für die Applikation am Herzen gibt es bereits einen Sequenzprototypen, der eine Synchronisation mit dem Herzzyklus sowie eine segmentierte Datenaufnahme erlaubt. Initiale und vielversprechende Ergebnisse konnten bereits bei 3T an gesunden Probanden aufgenommen werden. Eine systematische Optimierung der Sequenz für kardiale Applikationen an dem im Zuge dieser Arbeit erstellten dynamischen Herzkammermodells wäre der nächste logische Schritt. Die technischen Voraussetzungen für eine Erweiterung der Methode um eine Kartierung der Relaxationszeit T_2 sind bereits gegeben. Eine balanced-steady-state-free-precession Sequenz, die ähnlich der vorgestellten T_1 Kartierung auf der Applikation von variablen Flipwinkeln beruht und auf diese Weise eine T_2 Kartierung ermöglicht, ist bereits mit der T_1 Kartierungsmethode in der Sequenz vereint. Erste Ergebnisse konnten bereits am Phantom erzielt werden, die eine Übereinstimmung der T_2 Werte mit Multi-Echo-Spin-Echo Referenzmessungen zeigten. Letztlich ist eine Kombination der T_1 und T_2 Werte angestrebt, um den Dynamikbereich zu erhöhen und so die Differenzierbarkeit verschiedener Gewebearten weiter zu fördern, um abschließend den diagnostischen Wert zu verbessern.

Literaturverzeichnis

1. M.A. Dieringer, M. Deimling, D. Santoro, J. Wuerfel, V.I. Madai, J. Sobesky, F. von Knobelsdorff-Brenkenhoff, T. Niendorf, and J. Schulz-Menger, *Rapid Parametric Mapping of the Longitudinal Relaxation Time T1 Using Two-Dimensional Variable Flip Angle Magnetic Resonance Imaging at 1.5 Tesla, 3 Tesla, and 7 Tesla.* PLoS One, in press.

2. P.D. Gatehouse, M.P. Rolf, M.J. Graves, M.B. Hofman, J. Totman, B. Werner, R.A. Quest, Y. Liu, J. von Spiczak, M. Dieringer, D.N. Firmin, A. van Rossum, M. Lombardi, J. Schwitter, J. Schulz-Menger, and P.J. Kilner, *Flow measurement by cardiovascular magnetic resonance: a multi-centre multi-vendor study of background phase offset errors that can compromise the accuracy of derived regurgitant or shunt flow measurements.* J Cardiovasc Magn Reson, 2010. 12: p. 5.

3. F. von Knobelsdorff-Brenkenhoff, M.A. Dieringer, A. Greiser, and J. Schulz-Menger, *In vitro assessment of heart valve bioprostheses by cardiovascular magnetic resonance: four-dimensional mapping of flow patterns and orifice area planimetry.* Eur J Cardiothorac Surg, 2011. 40(3): p. 736-42.

4. M.A. Dieringer, J. Hentschel, T. de Quadros, F. von Knobelsdorff-Brenkenhoff, W. Hoffmann, T. Niendorf, and J. Schulz-Menger, *Design, construction, and evaluation of a dynamic MR compatible cardiac left ventricle model.* Med Phys, 2012. 39(8): p. 4800-6.

5. F. von Knobelsdorff-Brenkenhoff, M. Prothmann, M.A. Dieringer, R. Wassmuth, A. Greiser, C. Schwenke, T. Niendorf, and J. Schulz-Menger, *Myocardial T1 and T2 mapping at 3 T: reference values, influencing factors and implications.* J Cardiovasc Magn Reson, 2013. 15(1): p. 53.

6. F. Carinci, D. Santoro, F. von Samson-Himmelstjerna, T.D. Lindel, M.A. Dieringer, and T. Niendorf, *Characterization of phase-based methods used for transmission field uniformity mapping: a magnetic resonance study at 3.0 T and 7.0 T.* PLoS One, 2013. 8(3): p. e57982.

7. R. Wassmuth, M. Prothmann, W. Utz, M. Dieringer, F. von Knobelsdorff-Brenkenhoff, A. Greiser, and J. Schulz-Menger, *Variability and homogeneity of cardiovascular magnetic resonance myocardial T2-mapping in volunteers compared to patients with edema.* J Cardiovasc Magn Reson, 2013. 15: p. 27.

8. M.A. Dieringer, W. Renz, T. Lindel, F. Seifert, T. Frauenrath, F. von Knobelsdorff-Brenkenhoff, H. Waiczies, W. Hoffmann, J. Rieger, H. Pfeiffer, B. Ittermann, J. Schulz-Menger, and T. Niendorf, *Design and application of a four-channel transmit/receive surface coil for functional cardiac imaging at 7T.* J Magn Reson Imaging, 2011. 33(3): p. 736-41.

9. A. Graessl, W. Renz, F. Hezel, M.A. Dieringer, L. Winter, C. Oezerdem, J. Rieger, P. Kellman, D. Santoro, T.D. Lindel, T. Frauenrath, H. Pfeiffer, and T. Niendorf, *Modular 32-channel transceiver coil array for cardiac MRI at 7.0T.* Magn Reson Med, 2013 (epub ahead of print).

10. B. Wagenhaus, A. Pohlmann, M.A. Dieringer, A. Els, H. Waiczies, S. Waiczies, J. Schulz-Menger, and T. Niendorf, *Functional and morphological cardiac magnetic resonance imaging of mice using a cryogenic quadrature radiofrequency coil.* PLoS One, 2012. 7(8): p. e42383.

11. F. von Knobelsdorff-Brenkenhoff, T. Frauenrath, M. Prothmann, M.A. Dieringer, F. Hezel, W. Renz, K. Kretschel, T. Niendorf, and J. Schulz-Menger, *Cardiac chamber quantification using magnetic resonance imaging at 7 Tesla--a pilot study.* Eur Radiol, 2010. 20(12): p. 2844-52.

12. F. von Knobelsdorff-Brenkenhoff, V. Tkachenko, L. Winter, J. Rieger, C. Thalhammer, F. Hezel, A. Graessl, M.A. Dieringer, T. Niendorf, and J. Schulz-Menger, *Assessment of the right ventricle with cardiovascular magnetic resonance at 7 Tesla.* J Cardiovasc Magn Reson, 2013. 15: p. 23.

13. T. Frauenrath, F. Hezel, W. Renz, T.d.O. de Geyer, M. Dieringer, F.V. Knobelsdorff-Brenkenhoff, M. Prothmann, J. Schulz-Menger, and T. Niendorf, *Acoustic cardiac triggering: a practical solution for synchronization and gating of cardiovascular magnetic resonance at 7 Tesla.* J Cardiovasc Magn Reson, 2010. 12(1): p. 67.

14. T. Frauenrath, K. Fuchs, M.A. Dieringer, C. Ozerdem, N. Patel, W. Renz, A. Greiser, T. Elgeti, and T. Niendorf, *Detailing the use of magnetohydrodynamic effects for synchronization of MRI with the cardiac cycle: a feasibility study.* J Magn Reson Imaging, 2012. 36(2): p. 364-72.

15. F. von Knobelsdorff-Brenkenhoff, M.A. Dieringer, K. Fuchs, F. Hezel, T. Niendorf, and J. Schulz-Menger, *Isometric handgrip exercise during cardiovascular magnetic resonance imaging: set-up and cardiovascular effects.* J Magn Reson Imaging, 2013. 37(6): p. 1342-50.

16. T. Niendorf, A. Graessl, C. Thalhammer, M.A. Dieringer, O. Kraus, D. Santoro, K. Fuchs, F. Hezel, S. Waiczies, B. Ittermann, and L. Winter, *Progress and promises of human cardiac magnetic resonance at ultrahigh fields: a physics perspective.* J Magn Reson, 2013. 229: p. 208-22.

Eidesstattliche Versicherung

„Ich, Matthias Alexander Dieringer, versichere an Eides statt durch meine eigenhändige Unterschrift, dass ich die vorgelegte Dissertation mit dem Thema: „Schnelle zweidimensionale Kartierung der longitudinalen Relaxationszeit T_1 bei 1.5 Tesla, 3 Tesla und 7 Tesla mittels Magnetresonanztomographie“ selbstständig und ohne nicht offengelegte Hilfe Dritter verfasst und keine anderen als die angegebenen Quellen und Hilfsmittel genutzt habe.

Alle Stellen, die wörtlich oder dem Sinne nach auf Publikationen oder Vorträgen anderer Autoren beruhen, sind als solche in korrekter Zitierung (siehe „Uniform Requirements for Manuscripts (URM)“ des ICMJE -*www.**icmje**.org*) kenntlich gemacht. Die Abschnitte zu Methodik (insbesondere praktische Arbeiten, Laborbestimmungen, statistische Aufarbeitung) und Resultaten (insbesondere Abbildungen, Graphiken und Tabellen) entsprechen den URM (s.o) und werden von mir verantwortet.

Meine Anteile an den ausgewählten Publikationen entsprechen denen, die in der untenstehenden gemeinsamen Erklärung mit der Betreuerin, angegeben sind. Sämtliche Publikationen, die aus dieser Dissertation hervorgegangen sind und bei denen ich Autor bin, entsprechen den URM (s.o.) und werden von mir verantwortet.

Die Bedeutung dieser eidesstattlichen Versicherung und die strafrechtlichen Folgen einer unwahren eidesstattlichen Versicherung (§156,161 des Strafgesetzbuches) sind mir bekannt und bewusst.“

_____

Datum Unterschrift

Anteilserklärung an den erfolgten Publikationen

Matthias Alexander Dieringer hatte folgenden Anteil an den folgenden Publikationen:

Publikation 1: P.D. Gatehouse, M.P. Rolf, M.J. Graves, M.B. Hofman, J. Totman, B. Werner, R.A. Quest, Y. Liu, J. von Spiczak, **M. Dieringer**, D.N. Firmin, A. van Rossum, M. Lombardi, J. Schwitter, J. Schulz-Menger, and P.J. Kilner, *Flow measurement by cardiovascular magnetic resonance: a multi-centre multi-vendor study of background phase offset errors that can compromise the accuracy of derived regurgitant or shunt flow measurements.* J Cardiovasc Magn Reson, 2010. 12: p. 5.
Beitrag im Einzelnen: Modellbau, Datenakquisition, Auswertung der Daten, Revision des Manuskripts

Publikation 2: T. Frauenrath, F. Hezel, W. Renz, T.d.O. de Geyer, **M. Dieringer**, F.V. Knobelsdorff-Brenkenhoff, M. Prothmann, J. Schulz-Menger, and T. Niendorf, *Acoustic cardiac triggering: a practical solution for synchronization and gating of cardiovascular magnetic resonance at 7 Tesla.* J Cardiovasc Magn Reson, 2010. 12(1): p. 67.
Beitrag im Einzelnen: Datenakquisition, Interpretation der Daten, Revision des Manuskripts

Publikation 3: F. von Knobelsdorff-Brenkenhoff, T. Frauenrath, M. Prothmann, **M.A. Dieringer**, F. Hezel, W. Renz, K. Kretschel, T. Niendorf, and J. Schulz-Menger, *Cardiac chamber quantification using magnetic resonance imaging at 7 Tesla--a pilot study.* Eur Radiol, 2010. 20(12): p. 2844-52.
Beitrag im Einzelnen: Anteil an der Konzeption, Datenakquisition, Interpretation der Daten, Revision des Manuskripts

Publikation 4: **M.A. Dieringer**, W. Renz, T. Lindel, F. Seifert, T. Frauenrath, F. von Knobelsdorff-Brenkenhoff, H. Waiczies, W. Hoffmann, J. Rieger, H. Pfeiffer, B. Ittermann, J. Schulz-Menger, and T. Niendorf, *Design and application of a four-channel transmit/receive surface coil for functional cardiac imaging at 7T.* J Magn Reson Imaging, 2011. 33(3): p. 736-41.
Beitrag im Einzelnen: Anteil an der Konzeption, Datenakquisition, Auswertung der Daten, Interpretation der Daten, Entwurf des Manuskripts, Revision des Manuskripts

Publikation 5: F. von Knobelsdorff-Brenkenhoff, **M.A. Dieringer**, A. Greiser, and J. Schulz-Menger, *In vitro assessment of heart valve bioprostheses by cardiovascular magnetic resonance: four-dimensional mapping of flow patterns and orifice area planimetry.* Eur J Cardiothorac Surg, 2011. 40(3): p. 736-42.
Beitrag im Einzelnen: Anteil an der Konzeption, Modellbau, Datenakquisition, Auswertung der Daten, Interpretation der Daten, Revision des Manuskripts

Publikation 6: T. Frauenrath, K. Fuchs, **M.A. Dieringer**, C. Ozerdem, N. Patel, W. Renz, A. Greiser, T. Elgeti, and T. Niendorf, *Detailing the use of magnetohydrodynamic effects for synchronization of MRI with the cardiac cycle: a feasibility study.* J Magn Reson Imaging, 2012. 36(2): p. 364-72.
Beitrag im Einzelnen: Anteil an der Konzeption, Modellbau, Datenakquisition, Entwicklung von Auswertungsprogrammen, Auswertung der Daten, Interpretation der Daten, Revision des Manuskripts

Publikation 7: **M.A. Dieringer**, J. Hentschel, T. de Quadros, F. von Knobelsdorff-Brenkenhoff, W. Hoffmann, T. Niendorf, and J. Schulz-Menger, *Design, construction, and evaluation of a dynamic MR compatible cardiac left ventricle model.* Med Phys, 2012. 39(8): p. 4800-6.
Beitrag im Einzelnen: Konzeption, Modellbau, Datenakquisition, Entwicklung von Auswertungsprogrammen, Auswertung der Daten, Interpretation der Daten, Entwurf des Manuskripts, Revision des Manuskripts

Publikation 8: B. Wagenhaus, A. Pohlmann, **M.A. Dieringer**, A. Els, H. Waiczies, S. Waiczies, J. Schulz-Menger, and T. Niendorf, *Functional and morphological cardiac magnetic resonance imaging of mice using a cryogenic quadrature radiofrequency coil.* PLoS One, 2012. 7(8): p. e42383.
Beitrag im Einzelnen: Anteil an der Konzeption, Datenakquisition, Entwicklung von Auswertungsprogrammen, Auswertung der Daten, Interpretation der Daten, Entwurf des Manuskripts, Revision des Manuskripts

Publikation 9: T. Niendorf, A. Graessl, C. Thalhammer, **M.A. Dieringer**, O. Kraus, D. Santoro, K. Fuchs, F. Hezel, S. Waiczies, B. Ittermann, and L. Winter, *Progress and promises of human cardiac magnetic resonance at ultrahigh fields: a physics perspective.* J Magn Reson, 2013. 229: p. 208-22.
Beitrag im Einzelnen: Revision des Manuskripts

Publikation 10: F. von Knobelsdorff-Brenkenhoff, V. Tkachenko, L. Winter, J. Rieger, C. Thalhammer, F. Hezel, A. Graessl, **M.A. Dieringer**, T. Niendorf, and J. Schulz-Menger, *Assessment of the right ventricle with cardiovascular magnetic resonance at 7 Tesla.* J Cardiovasc Magn Reson, 2013. 15: p. 23.
Beitrag im Einzelnen: Interpretation der Daten, Revision des Manuskripts

Publikation 11: R. Wassmuth, M. Prothmann, W. Utz, **M. Dieringer**, F. von Knobelsdorff-Brenkenhoff, A. Greiser, and J. Schulz-Menger, *Variability and homogeneity of cardiovascular magnetic resonance myocardial T2-mapping in volunteers compared to patients with edema.* J Cardiovasc Magn Reson, 2013. 15: p. 27.
Beitrag im Einzelnen: Entwicklung von Auswertungsprogrammen, Auswertung der Daten, Interpretation der Daten, Revision des Manuskripts

Publikation 12: F. von Knobelsdorff-Brenkenhoff, M. Prothmann, **M.A. Dieringer**, R. Wassmuth, A. Greiser, C. Schwenke, T. Niendorf, and J. Schulz-Menger, *Myocardial T1 and T2 mapping at 3 T: reference values, influencing factors and implications*. J Cardiovasc Magn Reson, 2013. 15(1): p. 53.
Beitrag im Einzelnen: Anteil an der Konzeption, Datenakquisition, Entwicklung von Auswertungsprogrammen, Interpretation der Daten, Revision des Manuskripts

Publikation 13: F. von Knobelsdorff-Brenkenhoff, **M.A. Dieringer**, K. Fuchs, F. Hezel, T. Niendorf, and J. Schulz-Menger, *Isometric handgrip exercise during cardiovascular magnetic resonance imaging: set-up and cardiovascular effects.* J Magn Reson Imaging, 2013. 37(6): p. 1342-50.
Beitrag im Einzelnen: Anteil an der Konzeption, Datenakquisition, Interpretation der Daten, Revision des Manuskripts

Publikation 14: A. Graessl, W. Renz, F. Hezel, **M.A. Dieringer**, L. Winter, C. Oezerdem, J. Rieger, P. Kellman, D. Santoro, T.D. Lindel, T. Frauenrath, H. Pfeiffer, and T. Niendorf, *Modular 32-channel transceiver coil array for cardiac MRI at 7.0T.* Magn Reson Med, 2013 (epub ahead of print).
Beitrag im Einzelnen: Datenakquisition, Entwicklung von Auswertungsprogrammen, Interpretation der Daten, Revision des Manuskripts

Publikation 15 F. Carinci, D. Santoro, F. von Samson-Himmelstjerna, T.D. Lindel, **M.A. Dieringer**, and T. Niendorf, *Characterization of phase-based methods used for transmission field uniformity mapping: a magnetic resonance study at 3.0 T and 7.0 T*. PLoS One, 2013. 8(3): p. e57982.
Beitrag im Einzelnen: Entwicklung von Auswertungsprogrammen, Interpretation der Daten, Revision des Manuskripts

Publikation 16: **M.A. Dieringer**, M. Deimling, D. Santoro, J. Wuerfel, V.I. Madai, J. Sobesky, F. von Knobelsdorff-Brenkenhoff, J. Schulz-Menger, T. Niendorf, *Rapid Parametric Mapping of the Longitudinal Relaxation Time T1 Using Two-Dimensional Variable Flip Angle Magnetic Resonance Imaging at 1.5 Tesla, 3 Tesla, and 7 Tesla.* PLoS One, in press
Beitrag im Einzelnen: Konzeption, Entwicklung der Messsequenzen und der Auswertungsprogramme, Datenakquisition, Auswertung der Daten, Interpretation der Daten, Entwurf des Manuskripts, Revision des Manuskripts

Unterschrift, Datum und Stempel der betreuenden Hochschullehrerin

Unterschrift des Doktoranden

Journal of Cardiovascular Magnetic Resonance

RESEARCH Open Access

Flow measurement by cardiovascular magnetic resonance: a multi-centre multi-vendor study of background phase offset errors that can compromise the accuracy of derived regurgitant or shunt flow measurements

Peter D Gatehouse[1], Marijn P Rolf[2], Martin J Graves[3], Mark BM Hofman[2], John Totman[4], Beat Werner[5], Rebecca A Quest[6], Yingmin Liu[7], Jochen von Spiczak[8], Matthias Dieringer[9], David N Firmin[1], Albert van Rossum[10], Massimo Lombardi[11], Juerg Schwitter[12], Jeanette Schulz-Menger[13], Philip J Kilner[1*]

Abstract

Aims: Cardiovascular magnetic resonance (CMR) allows non-invasive phase contrast measurements of flow through planes transecting large vessels. However, some clinically valuable applications are highly sensitive to errors caused by small offsets of measured velocities if these are not adequately corrected, for example by the use of static tissue or static phantom correction of the offset error. We studied the severity of uncorrected velocity offset errors across sites and CMR systems.

Methods and Results: In a multi-centre, multi-vendor study, breath-hold through-plane retrospectively ECG-gated phase contrast acquisitions, as are used clinically for aortic and pulmonary flow measurement, were applied to static gelatin phantoms in twelve 1.5 T CMR systems, using a velocity encoding range of 150 cm/s. No post-processing corrections of offsets were implemented. The greatest uncorrected velocity offset, taken as an average over a 'great vessel' region (30 mm diameter) located up to 70 mm in-plane distance from the magnet isocenter, ranged from 0.4 cm/s to 4.9 cm/s. It averaged 2.7 cm/s over all the planes and systems. By theoretical calculation, a velocity offset error of 0.6 cm/s (representing just 0.4% of a 150 cm/s velocity encoding range) is barely acceptable, potentially causing about 5% miscalculation of cardiac output and up to 10% error in shunt measurement.

Conclusion: In the absence of hardware or software upgrades able to reduce phase offset errors, all the systems tested appeared to require post-acquisition correction to achieve consistently reliable breath-hold measurements of flow. The effectiveness of offset correction software will still need testing with respect to clinical flow acquisitions.

Introduction

Phase contrast cardiovascular magnetic resonance (CMR) [1] measurements of flow through planes transecting the great arteries are used clinically for calculations of cardiac output, shunt flow [2,3] or aortic or pulmonary regurgitation [4,5]. In combination with measurements of left ventricular volume or mitral inflow, measurement of aortic outflow may also allow the indirect calculation of mitral regurgitation [5-7]. Such measurements are non-invasive and require no contrast agent or ionising radiation. They represent a capability unique to CMR which can be of considerable value in clinical investigation and research. However, the derivation of cardiac output, regurgitant or shunt flow from velocity images calls for a very high standard of accuracy, requiring the minimisation of background phase offset errors, which are the focus of this paper. Note that this paper examines the offsets before any

* Correspondence: p.kilner@rbht.nhs.uk
[1]CMR Unit, Royal Brompton Hospital, London, UK

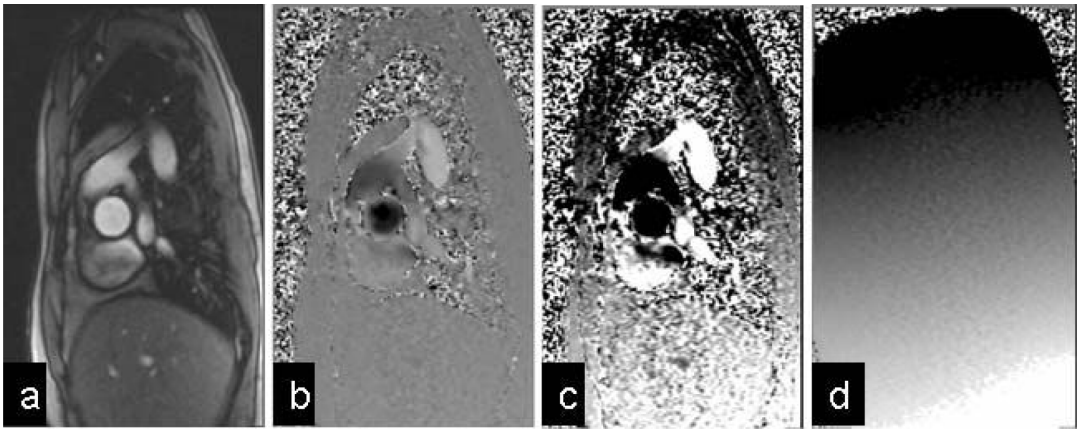

Figure 1 A systolic frame of an aortic flow acquisition. (170 ms after R-wave, at Venc = 150 cm/s). (a) Signal magnitude image, (b) Phase contrast velocity image shown at normal greyscale settings (black = -150 cm/s, white = +150 cm/s) where there apparently uniformly grey chest wall fails to reveal the background offset error. The same image is therefore reprinted in (c) with more extreme greyscale contrast to show up the background offset errors (black ≤ -15 cm/s, white ≥ +15 cm/s) (d) Phase contrast image using identical sequence protocol, but of static gelatin phantom, displayed with same greyscale as (c), demonstrating the phase offset.

correction technique has been applied, such as static tissue or static phantom baseline correction, which may generally reduce the problem subject to the reliability of the correction method itself.

As illustrated in Figure 1, clinical flow acquisitions can be subject to small positive or negative phase offset errors. They can be recognised where stationary tissue shows small apparent velocities which tend to increase with distance from the centre of the image. Phase offset errors may involve regions of flow measurement. They may vary unpredictably with slice orientation, slice shift (along the slice-select direction) and with other parameters that affect the gradient waveforms or their timings. They generally vary gradually with position over the image and are stable over all frames of a properly retro-gated cine. Although typically small, of the order of 1 or 2 cm/s, they matter because calculations of volume flow are based on the summation of velocities through the whole cross sectional areas of vessels and also through all phases of the cardiac cycle. Because of these two summations, the small background velocity offset error accumulates to give potentially significant errors in the calculated volume flow (Figure 2).

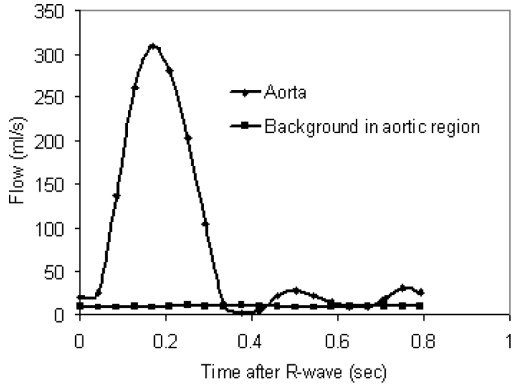

Figure 2 Aortic flow 64 ml/beat measured from Figure 1. The background in the aortic region was measured in the phantom, as in Figure 1d. The aortic flow curve includes 8.4 ml/beat due to the background offset of 1.6 cm/s in the aortic region. The true aortic flow is 56 ml/beat. The relative error in the calculated flow measurement is therefore 15%. Although the example in Figure 1 may be relatively easy to correct by correcting phase offset errors of signal across the relatively large regions of static chest wall and liver, correction is not always as straightforward in clinical acquisitions. Without such an independent correction of the background offset, it would be difficult to correct the aortic flow curve by using physiological assumptions such as negligible flow in diastole.

The background offset errors in typical cardiac flow applications have been studied previously e.g. [8-10] and their consequences can be estimated as follows. For example, consider a 5% error in a stroke volume of 80 ml/beat, which is 4 ml, which we suggest may represent a limit of acceptability. If this were measured over a great vessel of diameter 30 mm and through an R-R interval of 1 second, the 4 ml error could result from a mean velocity error of only 0.57 cm/s. This velocity offset corresponds to less than 0.4% of a typical velocity-encoding range (Venc) of 150 cm/s (or 0.3% of 200 cm/s). The high sensitivity of derived flow measurement to small errors in velocity is attributable to the double summation, over the vessel area and throughout the R-R interval. Given only 0.6 cm/s offset errors, as above, the calculation of shunt flow from the difference between pulmonary and aortic flow measurements might be affected by up to 10%, if the background errors were to

have opposing polarities in the two acquisitions [9]. The effects on measurements of valve regurgitation are harder to summarise. Considering a regurgitant fraction (RF) of 15% as an example, corresponding to a 15 ml reverse flow during 600 ms of diastole after 100 ml of forward flow during 400 ms of systole, the 0.6 cm/s offset discussed above would cause the RF to be miscalculated as either 12.5% or 17.5%, depending on the polarity of the offset. Relative to moderate and severe regurgitation the error in RF may appear less because the offset results in a smaller relative miscalculation of the larger reverse flow, although the reduction would partially be cancelled by the increased velocity encoding range that would be needed to avoid aliasing during the increased amount of forward flow. Please note that the estimates above are based on a velocity offset of 0.6 cm/s, which we propose as a theoretical limit of acceptability.

When baseline offset correction methods have been applied with proof of their *in-vivo* efficacy [9,10], the resulting CMR measurements of flow have been found to have a high accuracy, which may be hard to achieve by any other *in-vivo* modality. It should be understood that this study uses uncorrected offset data, revealing how much dependence there is on the correction methods and their routine *in-vivo* reliability.

The study reported here was initiated by members (PJK, JS, AvR, JS-M, ML) of the EuroCMR Working Group of the European Society of Cardiology (ESC). Among them, they had experience of several types of commercially available CMR system, and they shared concerns regarding possible inaccuracies in derived flow measurements. They agreed that background phase offset errors were, amongst other possible problems, likely to be the principal cause for concern. Therefore, the purpose of this study was to use static gel phantoms to investigate whether their concerns were justified, potentially motivating further optimisation of CMR velocity mapping for clinical flow measurements. The ability of CMR to rapidly and non-invasively measure flow through planes transecting the large vessels is unique, clinically valuable and worth optimising.

Methods

Static gel phantom

To eliminate the possibility of convection or motion-induced currents within fluid phantoms, an aqueous solution of gelatine was set within 10-15 litre uniform plastic tanks, with sufficient dimensions at all sites to enable measurement over the regions specified below. To reduce T1 for improved signal to noise ratio of the gelatine, 5 mmol/l of Gd-DTPA was added. These methods were adopted because the background offsets being studied were potentially very small.

CMR Systems tested

The study was limited to 1.5 T as this is currently the most widely-used main field strength for CMR. Automatic correction of concomitant gradient terms [11] was employed, whereas any other filtering or correction of background offset errors was turned off. Only CMR systems with higher gradient performance supporting breath-hold flow imaging within the range of imaging parameters specified below were included. Three 1.5 T scanner types were used, one from each of three manufacturers. We acquired static phantom phase offset datasets using twelve separate 1.5 Tesla CMR systems, four each of the three different types (See Acknowledgements section; this change was required by the publisher in final proofreading for some mysterious reason).

Phase contrast velocity acquisitions

To ensure consistent test protocols for each type of scanner, four of the investigators (PG, MPR, MJG, JT) set up an acquisition protocol for each type of system, and transferred this protocol to the other sites of that type. This protocol included the slice orientations described below.

We aimed to use similar phase-contrast sequence parameters for each of the three scanner types. The following sequence parameters were reproduced for each type (merely as a model for a typical clinical exam and not necessarily representing a recommendation of a set of optimized parameters for a breath-hold through-plane flow study). All cine phase-contrast acquisitions were by retrospectively gated pulse sequences, where the phase-encode was updated by each detected ECG R-wave. The continuous gradient activity of this approach, with no silent gap while waiting for the next R-wave, has the advantage of a more stable background offset during the cardiac cycle [12], as well as enabling late diastolic imaging. All acquisitions used an ECG simulator at 1 second R-R interval, through-plane velocity-encoding at Venc = 150 cm/s, slice thickness 6 mm, FOV = 320 mm square, uninterpolated pixels 1.25 mm (FE) by 2.5 mm(PE), flip angle 22°, 6 raw data lines per cardiac cycle, and no parallel imaging. These parameters often required "first-level" operation of the gradient system with respect to peripheral nerve stimulation. The square FOV is of course atypical for cardiac work, but was adopted to avoid centres modifying FOVs to avoid PE-wraparound of the large phantoms sometimes used. Similarly unusual, two averages were used to ensure adequate SNR for measurement of the small velocity offsets. Neither of these adaptations would be expected to modify the background offset error. Certain other aspects of the pulse sequence were beyond our control using standard clinical sequences, and these are listed below for each type of scanner. Unless stated below, the velocity encoding was asymmetric (i.e. it used phase-

subtraction of velocity-compensated and velocity-encoded sequence repetitions). For all of the sequences, the gradient-echo was asymmetric (i.e. the gradient-echo rephased early in the ADC sampling window for short TE). The TR values stated were between the RF excitation pulses, and in all cases the true flow cine temporal resolution was 12 × TR. A larger number of *temporally interpolated* cine phases was reconstructed by the Siemens and GE machines, but without consequences for the true flow acquisition.

Systems used were as follows:

Philips Achieva R2.53 (4 sites). TR5.5 ms, TE2.8 ms, pixel bandwidth 355 Hz/pixel (Fat/Water Shift 0.62). The slice-selective RF pulse used an asymmetric design with a late centre. The background phase-offset correction ("LPC filter") was switched off for this study (see Discussion). Fifteen cardiac phases were reconstructed (*i.e.* temporal interpolation was not performed during reconstruction).

Siemens Avanto VB15 TR6.6 ms (4 systems over 3 sites), TE2.8 ms, sampling bandwidth 355 Hz/pixel. The controls for RF pulse and gradient mode, which control the use of faster and stronger RF and gradient pulses, were both set to "Normal" mode in order to achieve TR and TE similar to the other scanners. Twenty-five cardiac phases were reconstructed (*i.e.* temporal interpolation was applied by reconstruction).

GE Signa Excite 14M5 (4 systems over 3 sites). This used symmetric velocity-encoding (i.e. two sequence repetitions with positive and negative velocity sensitivities around the velocity-compensated waveform, also known as "balanced" velocity-encoding). The "flow analysis" flag was on, disabling a spatial high-pass filter used for phase-contrast angiography background suppression. (In a slightly different form this filter apparently resembles the Philips approach to background correction). The GE "flow optimization" control resulted in longer TE and TR than the other scanners and was therefore not used. The readout ADC bandwidth was 41.67 kHz (pixel bandwidth 326 Hz/pixel). On the GE, the TR and TE ranged over 5.9-6.0 ms and 2.9-3.0 ms respectively for the oblique slices tested but were reproduced exactly at all 4 sites, as the sequence optimised its timings depending on image plane orientation. Twenty cardiac phases were reconstructed (*i.e.* temporal interpolation was applied by reconstruction).

Each centre acquired the same two planes (3 acquisitions), as defined in the transferred protocol files (Figure 3). Again, we emphasise that these were defined for scanner comparison rather than making any form of recommendation. The 'aortic' (Ao) plane was 45° oblique between transverse and sagittal planes, with anterior-posterior phase-encoding. The 'main pulmonary artery' (MPA-LR and MPA-HF) plane was 45° oblique between transverse and coronal planes, the two acquisitions using left-right and head-foot phase-encoding, respectively. All three acquisitions were centered on the isocentre.

Analysis of phantom 'velocity' map data

All images were analyzed independently by two sites using independent software written at each site in Matlab (The MathWorks, Natick, USA). The software reported the most extreme mean velocity offset measured in a circular 'great vessel' region, 30 mm diameter [13], centered within specified distances (see below) from the centre of each velocity map. It aimed to record the 'worst-case' error that might affect typical great vessel flow measurements. The relevant extent of regions interrogated was estimated from the locations of the ascending aorta and MPA in a survey of clinical flow studies. For the Ao plane the maximum distance was set at 50 mm from the image centre (Figure 4) and for both MPA planes, 70 mm from the image centre, which was located at the magnet isocentre in all cases. The larger span of regions for MPA analysis reflected the more anterior location of the MPA in patient studies. Working on the averaged image of all the frames of the cine, the largest mean apparent velocity in cm/s found by any of the 30 mm diameter circular regions centred within the defined spatial limits was recorded for each plane studied. The result reported was temporally averaged over all of the cine frames. The uncertainty in the results was assessed using the standard deviation across the cine frames (i.e. temporal rather than spatial standard deviation) of the region's mean value. The study did not aim to compare the signal to noise ratio of velocity measurements between systems. The uncertainty was a combination of random noise of any frame-to-frame variations during the retro-gated velocity cine, and was stated as an indicator of the offset assessment's reliability.

Results

Table 1 shows the average of the two independent analyses, for all three planes at all 12 scanners. As an overall indication of the amount of offset, the average, ignoring the polarity of the offset, over all 12 scanners for the Aortic, MPA(head-foot phase-encoding) and MPA(left-right phase-encoding) planes gave 1.6 cm/s, 2.9 cm/s and 3.7 cm/s, respectively. The results of the two image analyses agreed with an uncertainty range of less than ± 0.2 cm/s, as defined above.

The data of Table 1 is plotted in Figure 5 in comparison with the 0.6 cm/s suggested in the Introduction as an acceptable error level (displayed in green).

Since the MPA plane results appeared larger than the Ao plane on average, the question arises whether this was due to the larger analysis region used (MPA 70 mm

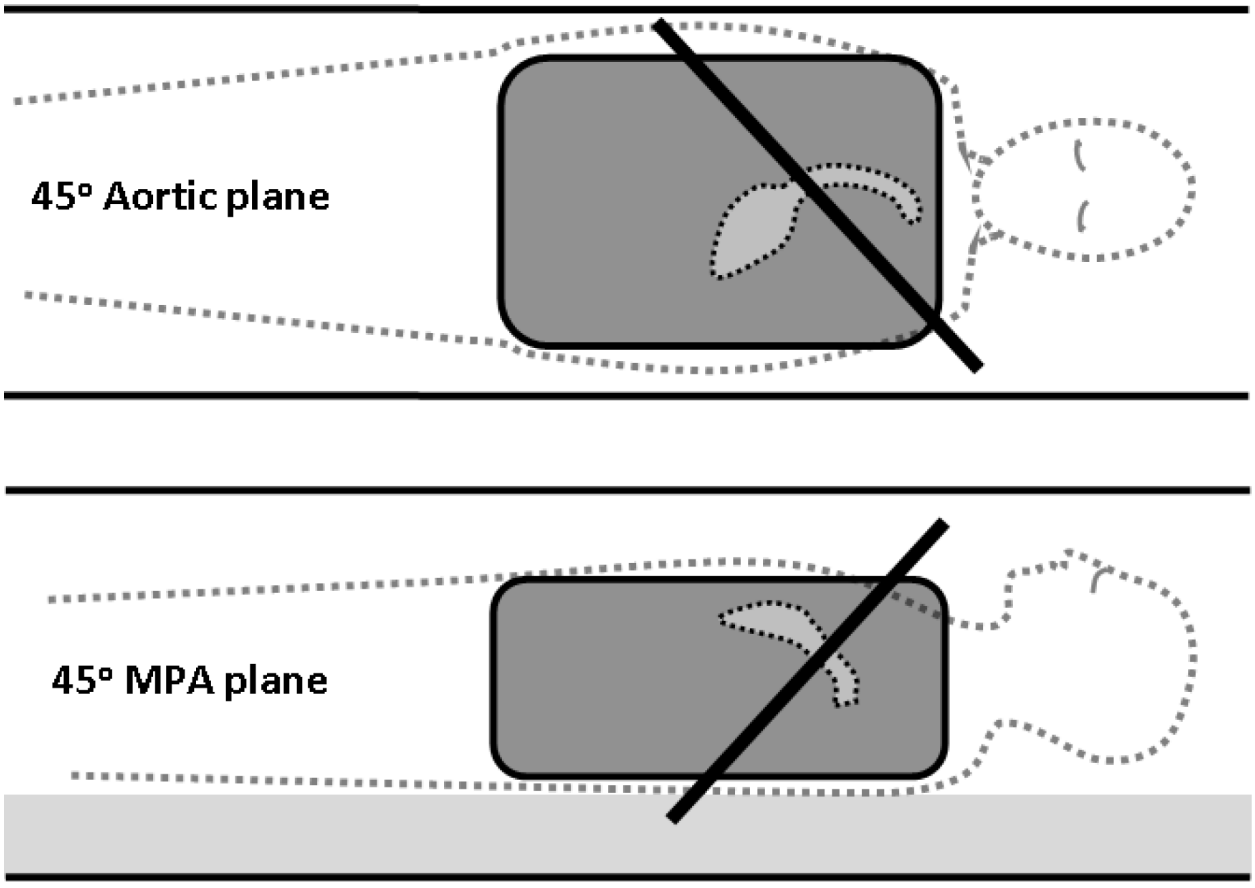

Figure 3 Coronal (upper) and sagittal (lower) illustrations of the oblique planes of velocity acquisition (thick black lines). The Aortic plane, for which an antero-posterior phase-encode direction was always chosen, was at 45° between transverse and sagittal. The main pulmonary artery (MPA) plane, which was acquired twice, either with left-right or head-foot phase-encode directions, was at 45° between transverse and coronal. Each plane passed through the isocentre. The dark grey region represents the uniform gelatin phantom, with dotted lines indicating a corresponding patient position with typical orientations of the aorta and MPA in which flows are typically measured through slices similar to those of this study.

vs Ao 50 mm). Analysis was therefore repeated over a central region of up to 50 mm from isocentre for all three plane orientations, giving 1.6 cm/s, 2.2 cm/s and 2.6 cm/s for the Aortic, MPA (head-foot) and MPA (left-right phase-encode) respectively.

Discussion

Implications of the study

In 35 of the 36 results, the uncorrected offset exceeded a 0.6 cm/s limit of acceptability which we explained in the Introduction. This implies that all 12 scanners would need to rely on accurate *in-vivo* post-processing correction of velocity offsets for the breath-hold protocol that was used. Referring to the 0.6 cm/s threshold of acceptability defined in the Introduction, the velocity offsets actually measured in the current study were on average *four* times greater than 0.6 cm/s, which could measure the 15% regurgitant fraction example given above as anywhere between 5% and 25%. In some clinical applications, for example in straightforward measurements of peak jet velocity for the assessment of a stenosis, such offsets remain insignificant. But in other situations, the effect may be magnified further, for example if a great vessel is significantly dilated, if stroke volume is reduced, or the R-R interval is increased due to bradycardia.

From Figure 5, it is apparent that all four scanners of type 3 usually showed less severe offsets than most of the data from the others. In spite of the efforts to replicate the imaging parameters on all 3 types, inevitable differences in the gradient waveforms of the three pulse sequences might have caused this difference. It would be unsafe to conclude that scanner type 3 has better eddy-current correction than the other types. The only certain proof would be in a careful comparison of residual eddy currents (i.e. pre-emphasis errors) between scanner types, which would require specialised sequence

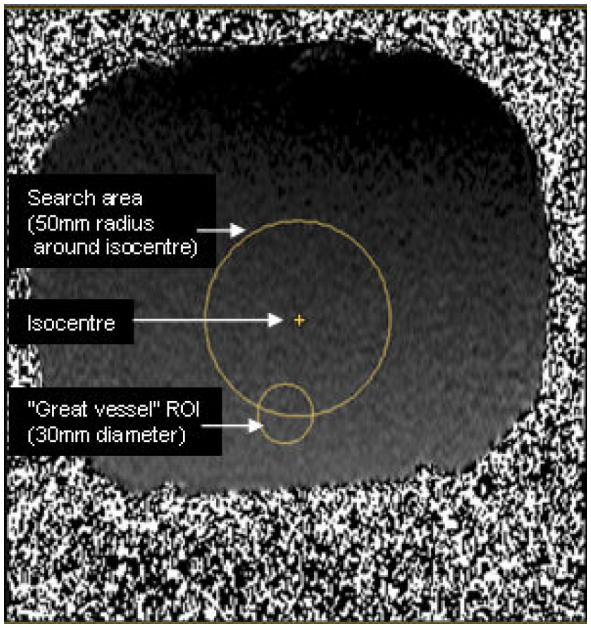

Figure 4 The flow offset analysis method. The mean phase offset over the smaller 30 mm diameter circle, which represents a typical "great vessel" ROI, was calculated for all positions of such ROIs with their centres located up to 50 mm from the isocentre of the magnet (up to 70 mm for MPA planes). The largest ROI value found was taken as the 'worst case' result for that plane of acquisition. All image planes passed through the isocentre. In this example, the largest error was found in the mean ROI positioned at the lower edge of the search region.

expertise on each scanner type. To the best of our knowledge this has not been performed.

Velocity offsets caused by Maxwell (concomitant) gradients in phase-contrast imaging are calculable allowing automatic correction during reconstruction [11]. The remaining offset is caused mainly by residual eddy current errors due to small inaccuracies in the pre-emphasis [14] and also any small errors in the concomitant gradient correction. Post-processing to reduce the background offsets was not used in this study for two reasons. First, we wished to see if post-processing was necessary for accurate flow measurements. Second, post-processing might be highly effective in the phantoms used, but could potentially be less effective in-vivo during routine cardiovascular investigation. Of course, there are several other well-recognised sources of error which may compromise the accuracy of breath-hold flow measurements. Examples might arise from reduced spatial or temporal resolution and lower signal to noise ratio using fast acquisition protocols. There may also be physiological effects of breath-holding on flow [15]. However, these are beyond the scope of this study.

Lessons and Limitations of the study

The methods reported here, which aimed to implement comparable phase contrast acquisitions across CMR sites and systems, turned out to be more challenging than had been anticipated. An initial attempt to invite data collection from different sites resulted in unacceptably wide variations of acquisition parameters, in spite

Table 1 Largest mean uncorrected velocity offset (cm/s) in regions centred within 50 mm of isocentre for the aortic plane, and within 70 mm for the MPA plane (head-foot or left-right phase-encoding). The twelve rows are from the four sites using each scanner type. The scanner types are not identified.

cm/s	Scanner Site	Aorta	MPA (HF phase-enc)	MPA (LR phase-enc)
Scanner type 1	1	-2.2 cm/s	-3.8 cm/s	-5.6 cm/s
	2	-2.8	-3.1	-5.5
	3	-0.7	-3.2	-5.3
	4	-1.3	-3.5	-4.7
Scanner type 2	5	-2.2	-3.4	-5.4
	6	-1.1	-3.9	-3.1
	7	1.6	-4.0	-3.6
	8	-2.7	-4.9	-4.9
Scanner type 3	9	1.6	1.2	1.8
	10	1.2	-0.7	0.4
	11	0.9	1.6	2.1
	12	1.1	-1.7	2.0
Mean of all 12 absolute values		1.6 cm/s	2.9 cm/s	3.7 cm/s
Range of all 12 absolute values		0.7 to 2.8 cm/s	0.7 to 4.9 cm/s	0.4 to 5.6 cm/s

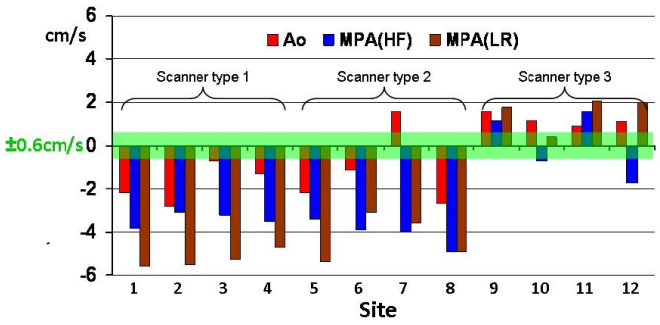

Figure 5 Uncorrected velocity offset results from all 12 sites. The largest mean value of the ROI found anywhere up to 5 cm inplane from isocenter for the aortic slice (up to 7 cm for the two MPA slices). The green zone represents the 0.6 cm/s offset described in the Discussion section.

of the careful work undertaken by colleagues at several sites. It became clear that the phantom studies would require pre-set acquisition protocols, transferred digitally between systems. This necessitated cross-system planning and collaboration, which brought to light important variables between systems. Certain variables precluded complete standardisation of acquisition parameters, using clinically available software (For example, the Siemens system did not allow symmetric velocity encoding, whereas the GE system did not allow asymmetric velocity encoding). A further limitation of the study lies in the analysis method of searching for the largest offset in regions displaced in in-plane directions, while the main pulmonary artery tends to have an anterior offset. Taking that example, slices acquired through the isocenter of the magnet may not be optimal for MPA flow measurement. The couch move facility should in this case have been used to relocate the vessel region rather than the centre of the slice. We nevertheless believe that the results recorded give a reasonable indication of the offsets that might be expected in clinical practice.

This study was not designed to find out if any particular plane had greater offsets, but used 45° oblique 'aortic' and 'MPA' planes to test orientations that might typically be used in acquisitions for cardiac output, shunt or regurgitant flow measurement. The apparently larger offset in most MPA planes compared to the aortic planes was not necessarily regarded as representative as orientations might vary in clinical practice, so the significance of this was not tested. Although most of the results have negative polarity, this was not investigated further. Opposite polarities from the same scanner have been reported previously [9].

Future work

Two obvious questions arise from this work. First, how could a phase-contrast protocol be optimised to minimise the background error in clinical routine? Due to the variability between different scanner types general advice cannot be given beyond the following. Most current CMR systems support automatic couch positioning for flow imaging, aiming to bring the vessel of interest for flow measurement into the isocenter plane (i.e. z = 0 plane, zero head-foot offset) as possible to minimise velocity offset errors. However, implementation of this facility varies between systems and it is important to be aware that the vessel region of interest, not necessarily the centre of the slice, should be positioned with zero offset along the head-foot direction. (For the ascending aorta, transverse imaging can solve this difficulty). Beyond this basic step, any further optimisation of sequence waveforms to minimise background offsets is highly sensitive to residual errors in the correction of eddy currents. The term "residual errors" refers to the difference between the eddy current-related field distortion and the pre-calibrated compensation for eddy-currents (known as "pre-emphasis") applied to the gradient waveforms. The accumulation of this residual phase error during the time between velocity encoding and the echo may be positive or negative, leading to positive or negative offsets in the phase-subtraction velocity image. It can be estimated that a velocity offset of 0.6 cm/s in a 200 cm/s VENC scan may arise from a residual error (of time-constant ≈ Te) of ≈ 0.01% of the amplitude of the gradient change made for velocity-encoding, which is extremely challenging for manufacturers to achieve. This is around ten times more demanding of accurate pre-emphasis than balanced SSFP cine imaging, and it remains uncertain whether this could ever be improved reliably so that offset post-processing correction techniques will not be needed.

The second question that arises from the work is, how reliable are velocity offset correction techniques *in-vivo* since it appears that most systems require them? This study did not use any correction methods which might have appeared unrealistically effective when applied to images from the large uniform, gelatin phantoms. Correction software may be less reliable *in-vivo*, particularly if there is insufficient stationary tissue in the acquisition plane, or if signal from it is poor. Furthermore, phase-

encode wraparound and possible spatial non-linearity of the offset may be problematic. An alternative but more time-consuming approach to offset correction requires identical flow acquisitions using a stationary phantom after a patient study, subtracting the corresponding apparent phantom velocities from the clinical acquisition [9] (with smoothing to avoid SNR reduction by the subtraction). This approach should correct all background offsets precisely, even if non-linearly distributed, provided that the offsets are stable as a function of time. More work is required to evaluate the *in-vivo* reliability of correction methods, for example using post-acquisition phantom scans as a temporary gold standard [10].

For use in clinical routine, the results imply that sites should be cautious about potential inaccuracy unless they have proved otherwise for the protocols and correction methods used there.

In conclusion, all of the 12 systems tested (without offset correction methods) showed velocity offset values larger than the 0.6 cm/s shown necessary for <10% error in the most sensitive cardiac applications. It is therefore necessary to have a reliable background offset correction method for images acquired by a typical breath-hold flow protocol. The reliability of background velocity offset correction techniques needs to be tested with respect to clinical flow acquisitions.

Potentially Competing interests

Peter Gatehouse: Research agreement with Siemens.
David Firmin: Research agreement with Siemens.
John Totman: Research agreement with Philips.
Martin Graves: Research support from GE.
All other authors: None.

Acknowledgements

The authors thank Dr Jason Polzin (GE), Dr Marc Kouwenhoven (Philips) and Dr Andreas Greiser (Siemens) for useful discussions during this work. We also acknowledge the assistance of Filomena Santarelli at Pisa in the initial work on GE machines, before software version issues excluded her site among others. Philip Kilner is supported by the British Heart Foundation.
Sites of CMR systems tested:
GE Signa Excite: Addenbrooke's Hospital, Cambridge, UK (two machines); VU University Medical Center, Amsterdam, NL; Kinderspital, Zurich, CH
Philips Achieva: Guy's Hospital, London, UK; St Thomas' Hospital, London, UK; Hammersmith Hospital, London, UK; ETH Zurich, CH
Siemens Avanto: Royal Brompton Hospital, London, UK (two machines); Charité Universitätsmedizin Berlin, DE; University of Auckland, Auckland, NZ

Author details

[1]CMR Unit, Royal Brompton Hospital, London, UK. [2]Department of Physics and Medical Technology, VU University Medical Center, Amsterdam, the Netherlands. [3]University Department of Radiology, Addenbrooke's Hospital, Cambridge, UK. [4]Division of Imaging Sciences, King's College, London, UK. [5]Division of Neuroradiology and Magnetic Resonance, University Children's Hospital, Zurich, Switzerland. [6]Radiological Sciences Unit, The Hammersmith Hospitals NHS Trust, London, UK. [7]Auckland MRI Research Group, University of Auckland, Auckland, New Zealand. [8]Institute for Biomedical Engineering, University and ETH Zurich, Zurich, Switzerland. [9]Franz-Volhard-Klinik, Charité Universitätsmedizin, Berlin, Germany. [10]Department of Cardiology, VU University Medical Center, Amsterdam, the Netherlands. [11]Magnetic Resonance Laboratory, Italian National Research Council (CNR), Pisa, Italy. [12]Cardiac MRI Center, University Hospital Zurich, Zurich, Switzerland. [13]Franz-Volhard-Klinik, Charité Universitätsmedizin, Berlin, Germany.

Authors' contributions

PJK, JS, AvR, JS-M, ML forming the EuroCMR Working Group of the European Society of Cardiology (ESC) conceived the study. PG designed the study with the assistance of MPR, MH, MG, JT. All other authors installed the designated test protocol, made appropriate test phantoms and ran the tests.

Received: 8 October 2009
Accepted: 14 January 2010 Published: 14 January 2010

References

1. Nayler GL, Firmin DN, Longmore DB: **Blood flow imaging by cine magnetic resonance.** *J Comput Assist Tomogr* 1986, **10(5)**:715-22.
2. Petersen SE, Voigtlander T, Kreitner KF, Kalden P, Wittlinger T, Scharhag J, Horstick G, Becker D, Hommel G, Thelen M, Meyer J: **Quantification of shunt volumes in congenital heart diseases using a breath-hold MR phase contrast technique–comparison with oximetry.** *Int J Cardiovasc Imaging* 2002, **18(1)**:53-60.
3. Colletti PM: **Evaluation of intracardiac shunts with cardiac magnetic resonance.** *Curr Cardiol Rep* 2005, **7(1)**:52-8.
4. Rebergen SA, Chin JGL, Ottenkamp J, Wall van der EE, de Roos A: **Pulmonary regurgitation in the late post-operative follow-up of tetralogy of Fallot: volumetric quantification by nuclear magnetic resonance velocity mapping.** *Circulation* 1993, **88**:2257-66.
5. Gelfand EV, Hughes S, Hauser TH, Yeon SB, Goepfert L, Kissinger KV, Rofsky NM, Manning WJ: **Severity of mitral and aortic regurgitation as assessed by cardiovascular magnetic resonance: optimizing correlation with Doppler echocardiography.** *J Cardiovasc Magn Reson* 2006, **8(3)**:503-7.
6. Hundley WG, Li HF, Willard JE, Landau C, Lange RA, Meshack BM, Hillis LD, Peshock RM: **Magnetic resonance imaging assessment of the severity of mitral regurgitation.** *Circulation* 1995, **92**:1151-1158.
7. Fujita N, Chazouilleres AF, Hartiala JJ, O'Sullivan M, Heidenreich P, Kaplan JD, Sakuma H, Foster E, Caputo GR, Higgins CB: **Quantification of mitral regurgitation by velocity-encoded cine nuclear magnetic resonance imaging.** *JACC* 1994, **23**:951-958.
8. Miller TA, Landes AB, Moran AM: **Improved accuracy in flow mapping of congenital heart disease using stationary phantom technique.** *J Cardiovasc Magn Res* 2009, **11**:52.
9. Chernobelsky A, Shubayev O, Comeau CR, Wolff SD: **Baseline correction of phase contrast images improves quantification of blood flow in the great vessels.** *J Cardiovasc Magn Reson* 2007, **9(4)**:681-5.
10. Lankhaar JW, Hofman MB, Marcus JT, Zwanenburg JJ, Faes TJ, Vonk-Noordegraaf A: **Correction of phase offset errors in main pulmonary artery flow quantification.** *J Magn Reson Imaging* 2005, **22(1)**:73-9.
11. Bernstein MA, Zhou XJ, Polzin JA, King KF, Ganin A, Pelc NJ, Glover GH: **Concomitant gradient terms in phase contrast MR: analysis and correction.** *Magn Reson Med* 1998, **39(2)**:300-8.
12. Søndergaard L, Ståhlberg F, Thomsen C, Spraggins TA, Gymoese E, Malmgren L, Müller E, Henriksen O: **Comparison between retrospective gating and ECG triggering in magnetic resonance velocity mapping.** *Magn Reson Imaging* 1993, **11(4)**:533-7.
13. Mao SS, Ahmadi N, Shah B, Beckmann D, Chen A, Ngo L, Flores FR, Gao YL, Budoff MJ: **Normal thoracic aorta diameter on cardiac computed tomography in healthy asymptomatic adults: impact of age and gender.** *Acad Radiol* 2008, **15**:827-34.
14. Bernstein , King , Zhou : **Chapters 10.3 and 15.2 in "Handbook of MRI pulse sequences".**, ISBN 0-12-092861-2.
15. Johansson B, Babu-Narayan SV, Kilner PJ: **The effects of breath-holding on pulmonary regurgitation measured by cardiovascular magnetic resonance velocity mapping.** *J Cardiovasc Magn Reson* 2009, **11**:1.

doi:10.1186/1532-429X-12-5
Cite this article as: Gatehouse *et al.*: Flow measurement by cardiovascular magnetic resonance: a multi-centre multi-vendor study of background phase offset errors that can compromise the accuracy of derived regurgitant or shunt flow measurements. *Journal of Cardiovascular Magnetic Resonance* 2010 **12**:5.

Journal of Cardiovascular Magnetic Resonance

RESEARCH Open Access

Acoustic cardiac triggering: a practical solution for synchronization and gating of cardiovascular magnetic resonance at 7 Tesla

Tobias Frauenrath[1*], Fabian Hezel[1], Wolfgang Renz[1,2], Thibaut de Geyer d'Orth[1], Matthias Dieringer[1,3,4], Florian von Knobelsdorff-Brenkenhoff[3,4], Marcel Prothmann[3], Jeanette Schulz-Menger[1,3,4], Thoralf Niendorf[1,4]

Abstract

Background: To demonstrate the applicability of acoustic cardiac triggering (ACT) for imaging of the heart at ultrahigh magnetic fields (7.0 T) by comparing phonocardiogram, conventional vector electrocardiogram (ECG) and traditional pulse oximetry (POX) triggered 2D CINE acquisitions together with (i) a qualitative image quality analysis, (ii) an assessment of the left ventricular function parameter and (iii) an examination of trigger reliability and trigger detection variance derived from the signal waveforms.

Results: ECG was susceptible to severe distortions at 7.0 T. POX and ACT provided waveforms free of interferences from electromagnetic fields or from magneto-hydrodynamic effects. Frequent R-wave mis-registration occurred in ECG-triggered acquisitions with a failure rate of up to 30% resulting in cardiac motion induced artifacts. ACT and POX triggering produced images free of cardiac motion artefacts. ECG showed a severe jitter in the R-wave detection. POX also showed a trigger jitter of approximately $\Delta t = 72$ ms which is equivalent to two cardiac phases. ACT showed a jitter of approximately $\Delta t = 5$ ms only. ECG waveforms revealed a standard deviation for the cardiac trigger offset larger than that observed for ACT or POX waveforms.
Image quality assessment showed that ACT substantially improved image quality as compared to ECG (image quality score at end-diastole: ECG = 1.7 ± 0.5, ACT = 2.4 ± 0.5, p = 0.04) while the comparison between ECG vs. POX gated acquisitions showed no significant differences in image quality (image quality score: ECG = 1.7 ± 0.5, POX = 2.0 ± 0.5, p = 0.34).

Conclusions: The applicability of acoustic triggering for cardiac CINE imaging at 7.0 T was demonstrated. ACT's trigger reliability and fidelity are superior to that of ECG and POX. ACT promises to be beneficial for cardiovascular magnetic resonance at ultra-high field strengths including 7.0 T.

Background

The challenge of synchronization of data acquisition with the cardiac cycle constitutes a practical impediment of cardiovascular magnetic resonance (CMR). Cardiac motion has been addressed by synchronization strategies exploiting (i) finger plethysmography [1], (ii) cardiac activity related esophageal wall motion [2], (iii) invasive left ventricular blood pressure gating [3], (iv) Doppler ultrasound [4], (v) motion induced changes in the impedance match of RF-coils [5], (vi) self gating techniques [6-10] and optic acoustic methods [11] including human and animal studies. In current clinical CMR, cardiac motion is commonly dealt with using electrocardiographic (ECG) or finger pulse oximetry (POX) triggering/gating techniques [12-14] to synchronize data acquisition with the cardiac cycle. At higher magnetic field strengths the artifact sensitivity of ECG recordings and even of advanced vector ECG increases [13,15]. ECG, being an inherently electrical measurement with electrically active components [12], does carry a risk of surface heating of patients' skin and even of skin burns resulting from induction of high voltages in ECG hardware [16-19]. As ultrahigh field CMR becomes more widespread, the propensity of ECG recordings to

* Correspondence: Tobias.Frauenrath@mdc-berlin.de
[1]Berlin Ultrahigh Field Facility (B.U.F.F.), Max-Delbrueck Center for Molecular Medicine, Berlin, Germany
Full list of author information is available at the end of the article

interference from electromagnetic fields and to magneto-hydrodynamic effects is further pronounced [20-22].

Realizing the constraints of conventional ECG, a MR-stethoscope which uses the phonocardiogram has been proposed. Its feasibility for the pursuit of/prospectively triggered and retrospectively gated cardiac imaging has been demonstrated for field strengths up to 3.0 T [20,21,23] The applicability and clinical efficacy of acoustic cardiac triggering (ACT) has not been demonstrated for imaging of the heart at ultrahigh magnetic fields yet due to the lack of appropriate RF coils and other practical obstacles of CMR at 7.0 T. Recently, R-wave mis-registration has been consistently reported for ECG triggered CMR at 7.0 T [24-26]. Consequently, in one study approximately 20% of the healthy subjects needed to be excluded from left ventricular function assessment [24,25]. In another study 80% of the acquisitions were gated using pulse oximetry due to ECG-triggering problems [26]. Driven by the limitations and motivated by the challenges of conventional ECG together with the advantages of ACT, this study compares phonocardiogram triggered, conventional vector electrocardiogram triggered and traditional pulse oximetry triggered CMR cine imaging at 7.0 T in a pilot study as precursor to a larger clinical study.

To accomplish this goal, the suitability, accuracy and reproducibility of each cardiac triggering approach for the assessment of left ventricular parameter at 7.0 T is explored. For this purpose, breath-held 2D CINE imaging in conjunction with a retrospective triggering regime is conducted paralleled by real time logging of the ECG, POX and ACT signal waveforms to track (mis)synchronization between the cardiac cycle and data acquisition. A qualitative and quantitative analysis of 2D CINE images and signal waveforms is performed. The merits and limitations of the acoustic cardiac gating approach are discussed and its implications for other ultrahigh field MR imaging applications are considered.

Materials and methods

Acoustic Noise Measurements at 7.0 T

During CMR, recordings of a phonocardiogram inside of the magnet bore are paralleled by acoustic noise due to gradient coil switching consisting of several very sharp harmonic components, which are related to the echo time TE and the repetition time TR. For this reason, acoustic measurements were conducted to assess the acoustic signal-to-noise ratio between the sound pressure level induced by the cardiac activity and the sound-pressure level generated by the gradient noise. Acoustic measurements were conducted inside the 7.0 T magnet bore. Two series of acoustic signals were acquired. The first series was designed to record and characterize the noise generated in the MR environment by a 2D CINE FLASH sequence (TE = 2 ms, TR = 4 ms, pixel bandwidth = 445 Hz, FOV = (32 × 32) cm^2 using an optical microphone (MO 2000 set, Sennheiser, Wedemark, Germany). For this purpose, the optical microphone was positioned at the same position with respect to the scanning table and the magnet bore as it was used in the volunteer study. The second series was setup to collect and analyze the phonocardiogram derived from the heart sound of healthy subjects superimposed by the environmental noise generated by the same 2D CINE FLASH technique. For this purpose, an acoustic sensor (diameter = 5 cm) covered by a membrane to generate a pressure wave in a waveguide was attached to the optical microphone. The acoustic signal was recorded by means of an USB-soundcard chip (PCM2903; Texas Instruments, Dallas, TX, USA). The optical microphone was calibrated with a 94 dB test tone provided from a pistonphone (Voltcraft SLC-100, Conrad electronics, Germany). After connecting the membrane to the microphone the set-up was calibrated manually to correct for the minor attenuation induced by the acoustic sensor's membrane. With this set-up absolute sound pressure levels were obtained. Furthermore, this approach offers the benefit that the characteristics of the acoustic signal measurements are given by the environment and not by the signal processing unit. Due to the use of this linear time invariant network approach frequency-shifts between the acoustic signal obtained from the MR environment and the final power spectrum can be avoided. Also, the sound pressure level can be normalized to the auditory threshold.

Pulse Oximetry, ECG and Acoustic Triggering

For pulse oximetry, a commercial sensor (Siemens, Erlangen, Germany) was placed on the tip of the right index finger to track changes in the absorbance due to the pulsing arterial blood. A wireless connection linked the sensors output to the internal physiological signal controller circuitry of the MR scanner.

For ECG recording and triggering, a commercial vector ECG module (Siemens, Erlangen, Germany) was used. The electrodes (ConMed, Corp., Utica, NY, USA) of the vector ECG were carefully placed at the anterior chest wall, with one electrode on the sternum, one on the left thorax, and one below the sternum following the manufacturer's patient preparation instructions. For the vector ECG's training period the patient table was placed in the home position to eliminate major interferences with the fringe field. The waveform was delivered to the internal physiological signal controller circuitry of the clinical MR scanner.

Unlike traditional ECG-triggering the acoustic approach employs the phonocardiogram's first heart

tone for triggering instead of electrophysiological signals [23]. The acoustic gating device comprises four main components: an acoustic sensor made of synthetic material placed on the subject's anterior chest for phonocardiogram detection, an acoustic wave guide for signal transfer and to ensure galvanic decoupling, a signal processing unit and a coupler unit to the MR system. The two former aspects have also safety implications since the ACT approach galvanically isolates the subject and hence eliminates the risk for patient burns. Signal processing and conversion were conducted outside the magnet room using dedicated electronic circuit [23]. Short rectangular shaped trigger pulses were generated to provide an output trigger signal. This waveform was delivered to the internal physiological signal controller circuitry of the clinical MR scanner. This design was chosen to meet the needs of cardiac gated/triggered CMR: (i) maximum latency of 35 ms between the ECG's R-wave and phonocardiogram based trigger output pulse, (ii) free of interference with electromagnetic fields and (iii) immunity to magneto-hydrodynamic effects. The current implementation connects the trigger signal to the MR-scanner's standard external trigger signal input. Hence, no changes to the MR system's hardware or software are required [23]. The acoustic sensor was positioned directly on the subject's chest at the anterior left fifth intercostals space and gently fixed with a strap incorporated in the MR patient table. Note that neither the limited ECG in the MR scanner nor the acoustic waveforms reported here should be treated as reliable indicators of patient emergency conditions.

Three patient table positions were selected to examine the signal waveform as a function of the magnetic field strength: (i) patient table in home position so that the magnetic field strength at the ECG, POX and ACT sensor position was approximately 0.3 T, (ii) ECG, POX and ACT sensor position aligned with the front end of the magnet with a fringe field of approximately 1.0 T and (iii) ECG, POX and ACT sensor in the magnet's isocenter (B_0 = 7.0 T).

Logging and Analysis of Signal Waveforms at 7.0 T

For all subjects vector ECG, POX and ACT were connected at the same time to record traces of waveforms along with the trigger information simultaneously. This information was extracted from the scanners central physiological monitoring unit (CPMU) and simultaneously stored in log files with a sampling rate of 400 Hz (ECG), 50 Hz (POX) and 200 Hz (ACT). Also, the trigger detection tickmarks generated for Vector ECG, POX or ACT triggering by the scanners CPMU were written into log files. This logging procedure was paralleled by storing the respiratory trace simultaneously using a sampling rate of 50 Hz.

The recorded data were processed to analyze the trigger information and to assess triggering efficiency and temporal fidelity of synchronization with the cardiac cycle for each trigger technique. Off-line analysis of the log-files was performed using LabVIEW (National Instruments, Austin, TX, USA). For this purpose a customized post-processing algorithm was developed. The post-processing procedure includes the following features:

• Identification of breath hold periods: Only portions of the trigger signal traces which were acquired during breath-held 2D CINE FLASH imaging were included into the waveform analysis. For this purpose, the respiratory trace was used.

• Segmentation and temporal realignment: The ECG waveform is segmented into individual R-R intervals by using cross correlation between R-R intervals. For this purpose, one R-R interval acquired at the one breath-held CINE series is taken as a reference while all other R-R intervals are shifted along the time axis to achieve maximum correlation with the reference. This R-R wave segmentation mask is applied to the segmentation of the POX and ACT waveforms, which were acquired simultaneously to the ECG waveform. Temporal realignment was used to overcome the potential bias of (erroneous) trigger detection provided by the scanners internal real-time circuitry.

• Reassignment of the trigger detection tickmarks derived from the scanners central physiological monitoring unit to the realigned ECG, POX and ACT traces and assessment of the trigger jitter across the cardiac cycle.

• Calculation of the mean value and the standard deviation of the cardiac cycle for ECG, POX and ACT as an objective measure for trigger reliability.

• Calculation of the offset between the ECG's R-wave and the trigger detection moment derived from the ECG, POX and ACT waveform as an objective measure for trigger reliability.

Cine CMR at 7.0 T

End-expiratory breath-hold short axis views of the heart ranging from the atrioventricular ring to the apex were acquired using retrospectively gated 2D FLASH CINE on a 7.0 T whole body MR systems (Magnetom, Siemens, Erlangen, Germany). A 4 element transmit/receive coil was used for RF excitation and signal reception [27]. The coil was connected to the 7.0 T system via 4 transmit/receive (T/R) switches and a 1 to 4 radio frequency power splitter and combiner with a CP-like phase setting for the four individual channels. The coil setup consists of two identical coil subsets - one placed on the subject's anterior torso and one positioned posterior - each containing two transmit/receive loop coil elements.

For breath-held 2D CINE FLASH imaging field of view (FOV) was set to (340 × 308) mm^2, data

acquisition matrix size was set to 256 × 186 elements (reconstruction matrix size 256 × 232 elements). 30 cardiac phases (temporal resolution = 33 ms for a heart rate of 60 bpm) were acquired using typically 18 slices (slice thickness = 4 mm, slice gap = 2 mm). Slice order was reversed from apex-base to base-apex throughout the set of subjects to eliminate patient discomfort or training effects. Image acquisition was confined to a single slice per breath-hold. The flip angle was set to α = 35 for all subjects, resulting in TR = 5.5 ms and TE = 2.7 ms. Parallel imaging was applied (R = 2) using sensitivity encoding based reconstruction.

Three sets of breath-held 2D CINE FLASH acquisitions were performed. In one set ACT was employed. For comparison, the other set made use of vector ECG based cardiac triggering while another set used POX for cardiac triggering. The use of ACT, ECG and POX was swapped randomly to avoid systematic errors.

Image Analysis

For LV chamber quantification end-diastolic and end-systolic volume (EDV, ESV), and left ventricular mass (LVM) were calculated using commercial evaluation software (CMR42®, Circle Cardiovascular Imaging, Calgary, Canada) from images of all subjects using all three triggering methods. CMR reading was performed by one cardiologist with very profound expertise in clinical CMR (>3000 CMR examinations), who was not involved in the image acquisition at all.

For CINE image quality assessment two independent observers reviewed and scored the images in a randomized, blinded reading session. For this purpose, overall image quality of end-diastolic and end-systolic images was rated using a scale ranging from 0 to 3 for each slice. The following scale was used for the blinded reading:

0 - images with poor and non-diagnostic quality due to cardiac motion induced blurring,
1 - image quality impaired by cardiac motion which may lead to misdiagnosis,
2 - good image quality, cardiac motion artifacts hard to recognize and
3 - excellent image quality, no cardiac motion artifacts observed.

After the independent image quality assessment was completed both readers exchanged their rankings for each case-, slice- and cardiac phase, and agreed on a consensus score.

Endocardial border sharpness (EBS) of the 2D CINE FLASH images derived from ACT, ECG POX triggered acquisitions was determined through an objective measurement of acutance using a dedicated algorithm [21].

Study Population

The study was designed as a comparative volunteer study using healthy adult subjects with no history of cardiovascular disease (n = 9). The mean age was 32 ± 10 years ranging 23-52 years. The average body surface area was (2.0 ± 0.3) m^2 ranging from 1.8 m^2 to 2.7 m^2. The average body mass index was 24.8 ± 4.4 kg/m^2 (range 20.9-35.9 kg/m^2). Volunteers with contraindications to CMR were excluded. The study was carried out according to the principles of the Declaration of Helsinki and was approved by the local institutional ethics committee. Informed written consent was obtained from each volunteer prior to the study, in compliance with the local institutional review board guidelines.

Statistical Analysis

All data are presented as mean ± standard deviation (SD) unless stated otherwise. Statistical significance in the difference of the image scores was analyzed using Wilcoxon matched pairs test for the consensus scores for ACT vs ECG, ACT vs POX and ECG vs POX triggered data. Statistical significance in the difference of the parameter derived from LV function assessment was analyzed using t-test. A probability $p \leq 0.05$ was considered statistically significant. All computations were performed with Microsoft Excel (Microsoft, Redmond, USA) and R (R Foundation for Statistical Computing, Vienna, Austria). Comparison of the different triggering techniques was carried out using the Bland and Altman method [28] (GraphPad Software, Inc., La Jolla, CA, USA). The confidence interval was set to the mean value ± 1.96 of the standard deviation.

Results

Acoustic Signal-to-Noise Measurements at 7.0 T

Recordings of phonocardiograms inside the magnet bore are paralleled by acoustic noise due to gradient coil switching. High sound pressure levels (SPL) of up to 120 dB were induced by magnetic field gradients driven by the switching scheme of a 2D FLASH CINE imaging technique. Figure 1 illustrates the spectrogram which shows the sound pressure level spectrum over time obtained from a subject positioned at the magnet's isocenter during 2D CINE FLASH imaging (TE = 2.0 ms, TR = 4.0 ms) at 7.0 T. In this case of the phonocardiogram being paralleled by the gradient switching noise the sound pressure level (SPL) was tracked over a series of 6 heartbeats. The power spectra show numerous noise peaks including several very sharp harmonic components at 1/TR, 2/TR, 3/TR and 1/TE which are related to the gradient switching scheme of 2D FLASH with maximum SPL close to 120 dB. The spectrogram also revealed that the heart sound encompasses low-frequencies.

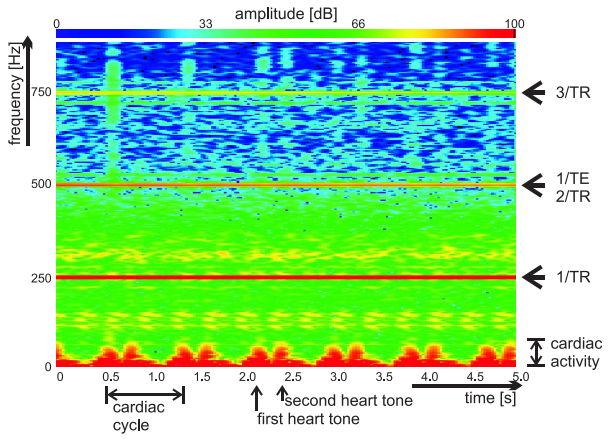

Figure 1 Acoustic Spectrogram obtained at 7.0 T. Spectrogram obtained from a subject positioned at the 7.0 T magnet's isocenter during 2D CINE FLASH acquisitions (TE = 2.0 ms, TR = 4.0 ms). The graphs show signal contributions from gradient switching superimposed on the cardiac signals. The gradient switching manifests itself by several very sharp harmonic components at 1/TR, 2/TR, 3/TR and 1/TE with maximum sound pressure level close to 120 dB. The spectrogram also shows the 1st and the 2nd heart tone which are of low-frequency nature. Acoustic signal-to-noise ratio, which is defined as the ratio between the sound pressure level due to cardiac activity and the gradient switching induced sound pressure level is approximately 30 dB for the frequency range between 10 Hz and 70 Hz.

SNR was defined as the ratio between the sound pressure level due to cardiac activity and the gradient switching induced sound pressure level. For example, for the frequency range between 10 Hz and 50 Hz a minimum signal to noise ratio of SNR = 30 dB was found for 2D CINE FLASH imaging at 7.0 T. To make acoustic triggering immune to interference from acoustic noise generated by gradient switching, separation of the acoustic cardiac activity from the higher frequency gradient noise was carried out by means of a third order inverse Chebychev filter using a UAF42 chip (Burr Brown Products by TI, Dallas, Texas, USA). The cut off frequency was set to f_c = 105 Hz since the energy of the first heart tone is mainly covered by frequencies ranging from 1 to 100 Hz. With this filtering no gradient noise peaks or peaks due to environmental noise were found within the relevant frequency range between 0 Hz to 105 Hz. The filtering yielded an attenuation of the gradient noise peaks found for frequencies above the cut-off frequency f_c = 105 Hz by at least 30 dB.

Assessment of ECG, POX and ACT Waveforms at 7.0 T

Off-line analysis of the log-files revealed that ECG waveforms were susceptible to severe distortions. Adverse signal elevation was found for cardiac phases where normally the T-wave occurs; a magneto-hydrodynamic effect which was pronounced at the isocenter of the magnet as illustrated in Figure 2, which shows ECG, POX and ACT traces derived from an individual subject over 18 cardiac cycles. ECG waveform distortions yielded an amplitude reaching the same order of magnitude or even larger than that of the R-wave. Pulse oximetry waveforms were free of interference from electromagnetic fields and magneto-hydrodynamic effects. A rather flat plateau and a significant scatter in the amplitude and width were observed for the peak in the POX trace. The peak in the POX trace showed a mean latency of approximately 350 ms with respect to the R-wave of the ECG trace. The acoustic approach provided waveforms free of interferences from electromagnetic fields or from magneto-hydrodynamic effects even in the isocenter of the 7.0 T magnet as illustrated in Figure 2. Off-line analysis of ECG and ACT traces yielded an average delay of Δt = 29.65 ms ± 4.43 ms between the R-wave and the first heart tone. This delay is not detrimental for whole R-R coverage 2D CINE FLASH using retrospective triggering.

Cardiac 2D CINE FLASH Imaging at 7.0 T

In the case of correct R-wave detection, ECG-gated 2D CINE FLASH imaging was found to be immune to cardiac motion effects as illustrated in figure 3 for one of the 9 subjects (subject 1). However, frequent R-wave mis-registration occurred in ECG-triggered acquisitions with a failure rate of up to 30% which manifests itself in a severe jitter of the R-wave detection tickmarks. Consequently, ECG triggered 2D CINE FLASH imaging was prone to severe cardiac motion artifacts if R-wave mis-registration occurred. For example, an ECG cardiac triggered whole heart coverage 2D CINE FLASH dataset obtained at diastole is shown in the top row of Figure 4 for one subject of the 9 subjects (subject 2). Images suffering from cardiac motion induced blurring are marked with dotted lines. Unlike ECG, ACT triggering produced images free of cardiac motion artefacts as illustrated in the bottom row of Figure 4 for the same subject. POX triggering 2D CINE FLASH acquisitions obtained from the same subject also produced images free of blood pulsation and cardiac motion artefacts as demonstrated in the middle row of Figure 4.

Assessment of the Trigger Detection Variance

Figure 5 shows mid-ventricular short axis views of the heart together with whole R-R interval time series of one-dimensional projections, trigger detection tickmarks and signal waveforms obtained at 7.0 T using ECG, POX and ACT triggered 2D CINE FLASH acquisitions for a midventricular slice derived from subject 1. In this example of almost correct recognition of the onset of cardiac activity, ECG, POX and ACT triggered 2D CINE FLASH imaging were found to be rather immune to the

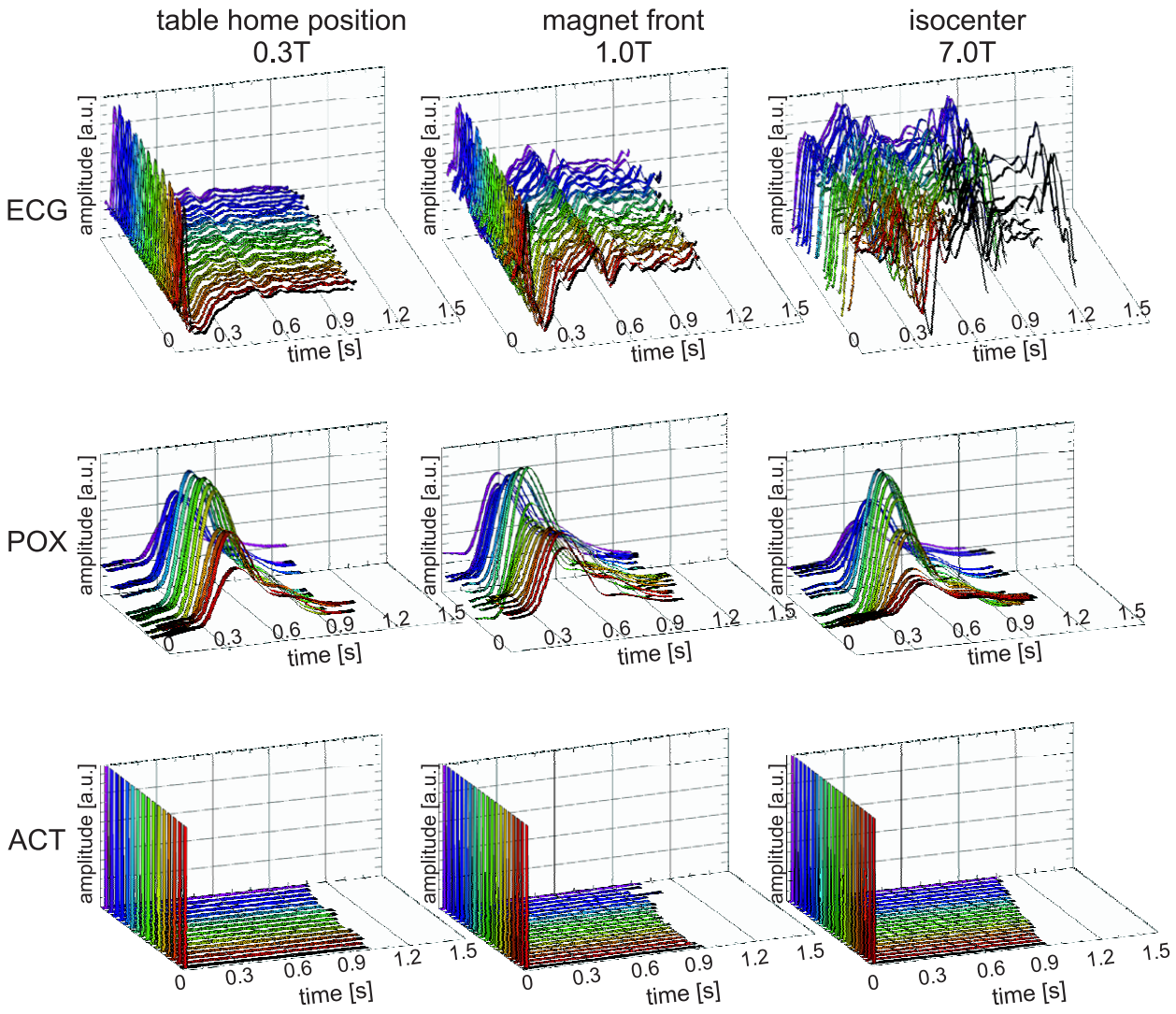

Figure 2 ECG, pulse oximetry and acoustic trigger signal traces acquired at three different field strengths. ECG **(top)**, pulse oximetry **(middle)** and acoustic trigger **(bottom)** signal traces derived from a healthy subject. Signal traces were recorded with the ECG, ACT and POX sensors located at the patient table home position **(left)**, at the front end of the 7.0 T magnet **(center)** and in the isocenter of the 7.0 T magnet **(right)** and post-processed and filtered by the scanners central physiological monitoring unit. Severe signal distortion occurred in the vector ECG signal obtained at the magnet's isocenter. A scatter in the amplitude and width was observed for the peak in the pulse oximetry trace. ACT is free of interferences with electromagnetic fields and magneto-hydrodynamic effects.

effects of cardiac motion. Consequently, the 2D CINE FLASH images derived from ECG, ACT and POX acquisitions together with the M-mode like whole R-R interval time series of one-dimensional projections along the cardiac phases safeguard recognition and delineation of the ventricular blood/myocardium interface. In spite of ECG's severe signal distortion faultless ECG triggering was observed for this example, with the exception of a scatter in the ECG trigger detection of approximately Δt = 60 ms which might compromise the temporal fidelity and hence might constitute a synchronization problem. Please note that a variance was also observed for the peak amplitude and peak width of the POX waveform as pointed out in Figure 5. This variance resulted in a trigger detection jitter of approximately Δt = 65 ms, which is equivalent to two cardiac phases. In comparison, ACT showed a 5 ms jitter which can be attributed to the ACT waveform sampling rate of 200 Hz.

Figure 6 shows an example of erroneous ECG triggering for a midventricular slice derived from subject 2. In this case, ECG triggered 2D CINE FLASH imaging was prone to severe cardiac motion artifacts due to R wave mis-registration. Trigger detection was found to be scattered across several cardiac phases including early

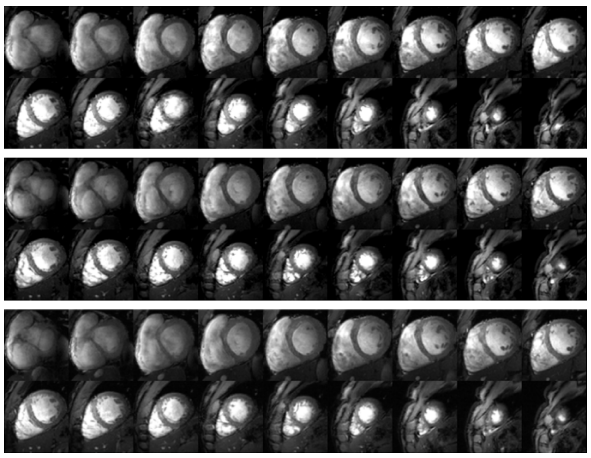

Figure 3 Short axis diastolic views free of cardiac motion effects. Short axis diastolic views obtained from breath-held base-to-apex 2D CINE FLASH acquisitions using **(top)** vector ECG, **(middle)** ACT and POX **(bottom)** gating. In this case of correct R-wave detection (subject 1), ECG-gated 2D CINE FLASH imaging was found to be immune to cardiac motion effects, as were ACT and POX gated acquisitions.

systole and diastole as demonstrated by the tickmarks depicted in Figure 6. R-wave mis-registration induced reduction in myocardium/blood contrast and image sharpness as illustrated by the short axis views together with whole R-R interval time series of one-dimensional projections. In comparison, ACT triggered 2D CINE FLASH imaging provided faultless trigger detection, accurate to the peak induced by the 1st heart tone and hence produced images free of motion artifacts. Please note the scatter in the POX peak amplitude and peak width, causing a jitter (Δt = 72 ms) in the pulse-oximetry trigger detection.

Mean R-R interval lengths deduced from the signal waveforms of ECG, POX and ACT triggered acquisitions are surveyed for each subject in Table 1 together with the standard deviation of the R-R interval length, which is a measure of the trigger detection accuracy. A close match in the mean R-R interval length and in the standard deviation of the R-R interval length derived from the assessment of the ECG, ACT and POX waveforms signifies correct trigger detection. A significant difference in the standard deviation of the R-R interval length deduced from ECG, ACT and POX waveforms indicates trigger (mis)registration at cardiac phases other than that which mark the onset of cardiac activity. Four out of nine healthy subjects showed a standard deviation for the cardiac cycle derived from ECG waveforms which was at least 1.5 times larger ($SD_{ECG} \geq 1.5 * SD_{ACT}$) than that obtained from ACT or POX waveforms.

Table 1 also surveys the standard deviation of the offset between the ECG's R-wave and the trigger detection moment which was derived from the ECG, POX and ACT waveforms and which was applied for synchronization. Four out of nine healthy subjects showed a standard deviation for the cardiac trigger offset derived from ECG waveforms which was at least four times larger ($SD_{ECG} \geq 4 * SD_{ACT}$) than that observed for ACT or POX waveforms.

Left Ventricular Parameter Assessment

Left ventricular volumes, mass and ejection fraction deduced from ECG, POX and ACT triggered acquisitions are surveyed in Figure 7. For each subject, the mean of the two measurements (ACT vs. ECG and ACT vs. POX) and the difference between the LV parameter obtained for ECG, POX and ACT triggered 2D CINE FLASH acquisitions are shown using Bland-Altman plots. The mean LV parameter derived from ECG triggered 2D CINE FLASH acquisitions were ESV = 74 ± 22ml, EDV = 170 ± 43ml, LVM = 130 ± 17) g, EF = 57 ± 8%. The mean LV parameter obtained from POX triggered 2D CINE FLASH acquisitions showed ESV = 67 ± 19 ml, EDV = 168 ± 44 ml, LVM = 130 ± 15g, EF = 60 ± 5%. In comparison, the ACT-triggered acquisitions yielded: ESV = 66 ± 20 ml, EDV = 173 ± 43 ml, LVM = 130 ± 15g, EF = 62 ± 3%. T-test revealed no significant differences for LV parameter derived from ACT, POX and ECG triggered acquisitions (all $p > 0.05$).

Image Quality Assessment

The application of acoustic triggering substantially improved the 2D CINE FLASH image quality as compared to the conventional approach. The blinded reading yielded a mean image quality score of 1.7 ± 0.5 for end-diastolic and 1.3 ± 0.6 for end-systolic cardiac images derived from ECG gated acquisitions. In comparison POX gated acquisitions yielded a mean image quality score of 2.0 ± 0.5 for end-diastolic and of 1.6 ± 0.5 for end-systolic cardiac phases. ACT triggered images showed a mean image quality score of 2.4 ± 0.5 for end-diastolic and of 2.0 ± 0.5 end-systolic cardiac phases as summarized in Table 2. A comparison between the image quality score obtained for ACT, POX and ECG gating using Wilcoxon paired test revealed significant differences between ACT vs. ECG gated acquisitions ($p = 0.10$ for endsystole, $p = 0.04$ for enddiastole) and for ACT vs. POX gated acquisitions ($p = 0.03$ for endsystole, $p = 0.01$ for enddiastole). The image quality comparison between ECG vs. POX gated acquisitions showed no significant differences in image quality ($p = 0.40$ for endsystole, $p = 0.34$ for enddiastole).

In case of faultless gating the EBS analysis revealed similar results for all synchronisation techniques. ECG

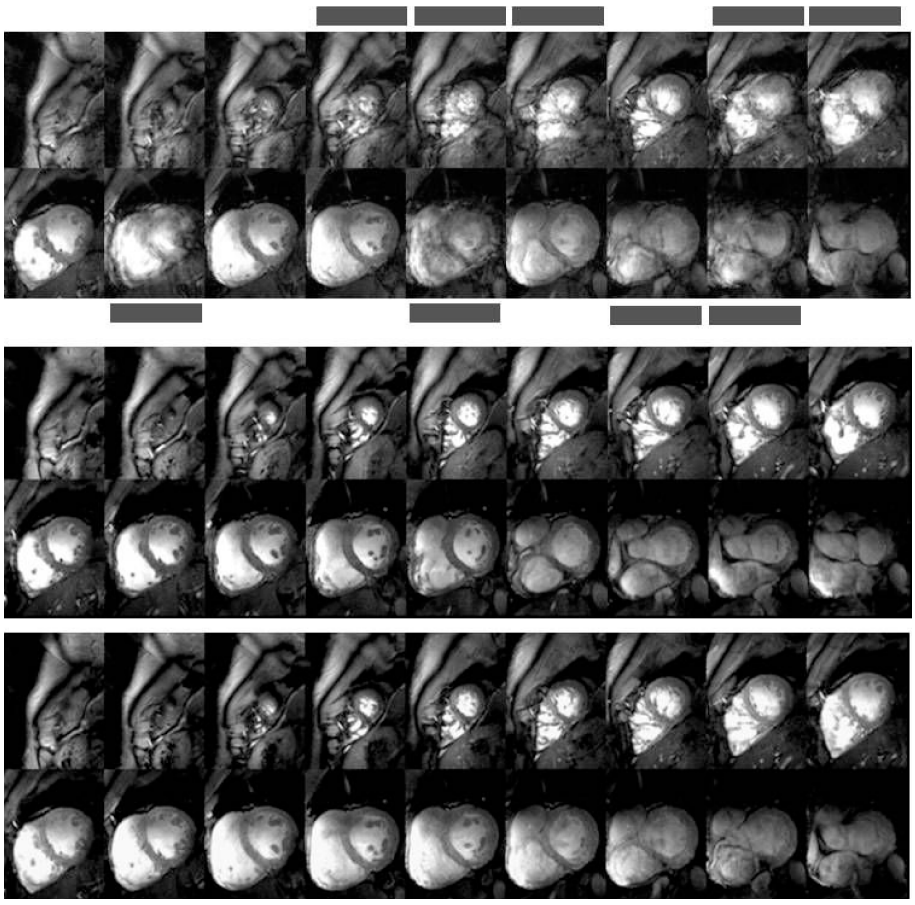

Figure 4 Short axis diastolic views showing cardiac motion artifacts when using ECG gating. Short axis diastolic views obtained from breath-held apex-to-base 2D CINE FLASH acquisitions using **(top)** vector ECG, **(middle)** ACT and POX **(bottom)** gating. In this subject (subject 2) vector ECG triggered 2D CINE FLASH imaging was prone to severe cardiac motion artifacts if R-wave mis-registration occurred. Images suffering from cardiac motion induced blurring are marked with grey bars. Acoustic triggering and POX provided image quality free of interferences from cardiac motion effects.

gated acquisitions showed an average EBS of (2.2 ± 0.3) pixels. ACT gated acquisitions yielded an average EBS of (2. 1 ± 0.2) pixels, and POX gated acquisitions showed an average EBS of (2.1 ± 0.2) pixels. In case of erroneously ECG gated acquisitions EBS analysis was challenging due to heavily reduced contrast to noise ratio (CNR) between blood and myocardium. The CNR degradation was caused by severe signal blurring across the endocardial border, as demonstrated in Figure 4.

Discussion

CMR at 7.0 T is still in its infancy and needs to continue to be very carefully validated against CMR applications very well established at 1.5 T and 3.0 T [29]. In current basic and clinical research practice some of the traits of ultrahigh field CMR are offset by challenges intrinsic to the use of ultrahigh magnetic field strength such as the synchronization of data acquisition with cardiac motion using traditional electrocardiographic (ECG) techniques. To address this issue, this study examines the applicability of acoustic cardiac triggering for CMR at 7.0 T in healthy volunteers, as a precursor to a larger clinical study. The acoustic approach was found to be immune to interference from environmental and gradient switching induced acoustic fields plus to be free of interference from electromagnetic fields and magneto-hydrodynamic effects. The efficacy and reliability of acoustic triggering is demonstrated by eliminating the frequently-encountered difficulty of mis-triggering due to ECG-waveform distortions or temporal jittering in the pulse-oximetry synchronization. R-wave mis-registration occurred in ECG-triggered acquisitions with a failure rate of up to 30% which manifest itself in severe cardiac motion induced image blurring.

It should be noted, that ECG trigger mis-registration was not equally distributed across the entire cardiac cycle but occurred at cardiac phases with large amplitude or up-slope in the ECG waveform including (i) an

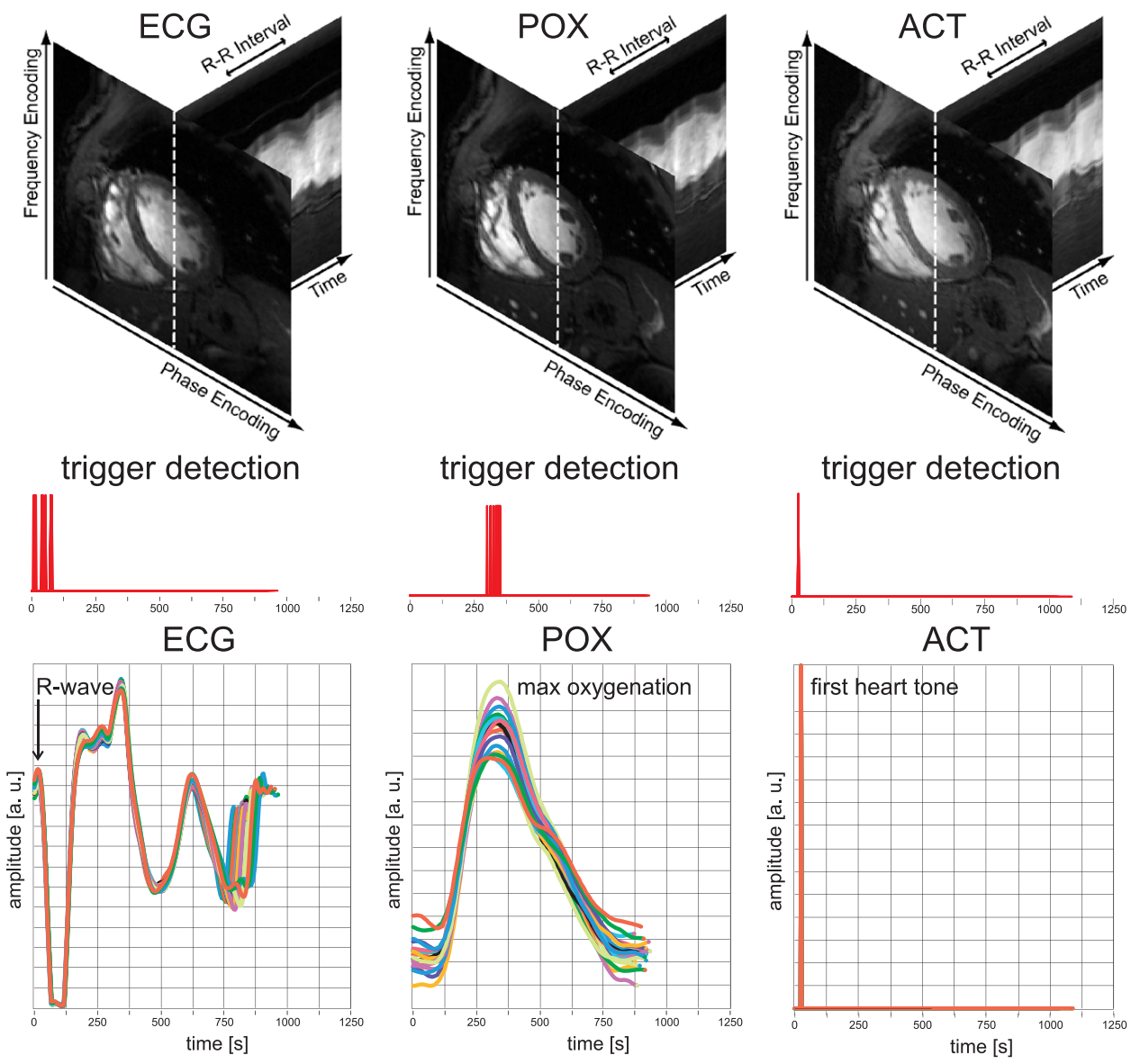

Figure 5 Example of correct ECG trigger detection. Cardiac images, trigger detection tickmarks and signal waveforms obtained at 7.0 T using vector ECG (left), pulse oximetry (center) and acoustically triggered (right) 2D CINE FLASH acquisitions. All signal waveforms show the output of the scanners central physiological monitoring unit (including processing of the ECG, POX and ACT signal) as displayed at the scanners user interface. Top: Mid-ventricular, short axis views of the heart together with whole R-R interval time series of one-dimensional projections along the profile (dotted line) marked in the short axis view. Middle: Trigger detection tickmarks obtained from a single subject over 18 cardiac cycles after temporal realignment using cross correlation and reassignment. Bottom: Signal waveforms obtained from a single subject (subject 1) over 18 cardiac cycles. In spite of vector ECG's severe signal distortion faultless vector ECG triggering was observed for this example. Hence, in this example of correct recognition of the onset of cardiac activity, vector ECG, POX and ACT triggered 2D CINE FLASH imaging were found to be immune to the effects of cardiac motion. Please note the jitter in the vector ECG (Δt = 60 ms) and in the pulse oximetry trigger (Δt = 65 ms) detection.

initial peak which covers the R-wave and (ii) major waveform distortions at systole and end-diastole. This mis-triggering behavior forces the k-space segmentation and retrospective reconstruction strategy to combine and assign k-space data which were acquired at different phases of myocardial contraction and relaxation to the same cardiac phase used to form a final image. This out-of-sync assignment causes severe degradation in image quality and image sharpness. Please note that this study did not yield missed ECG triggers. Missed triggers

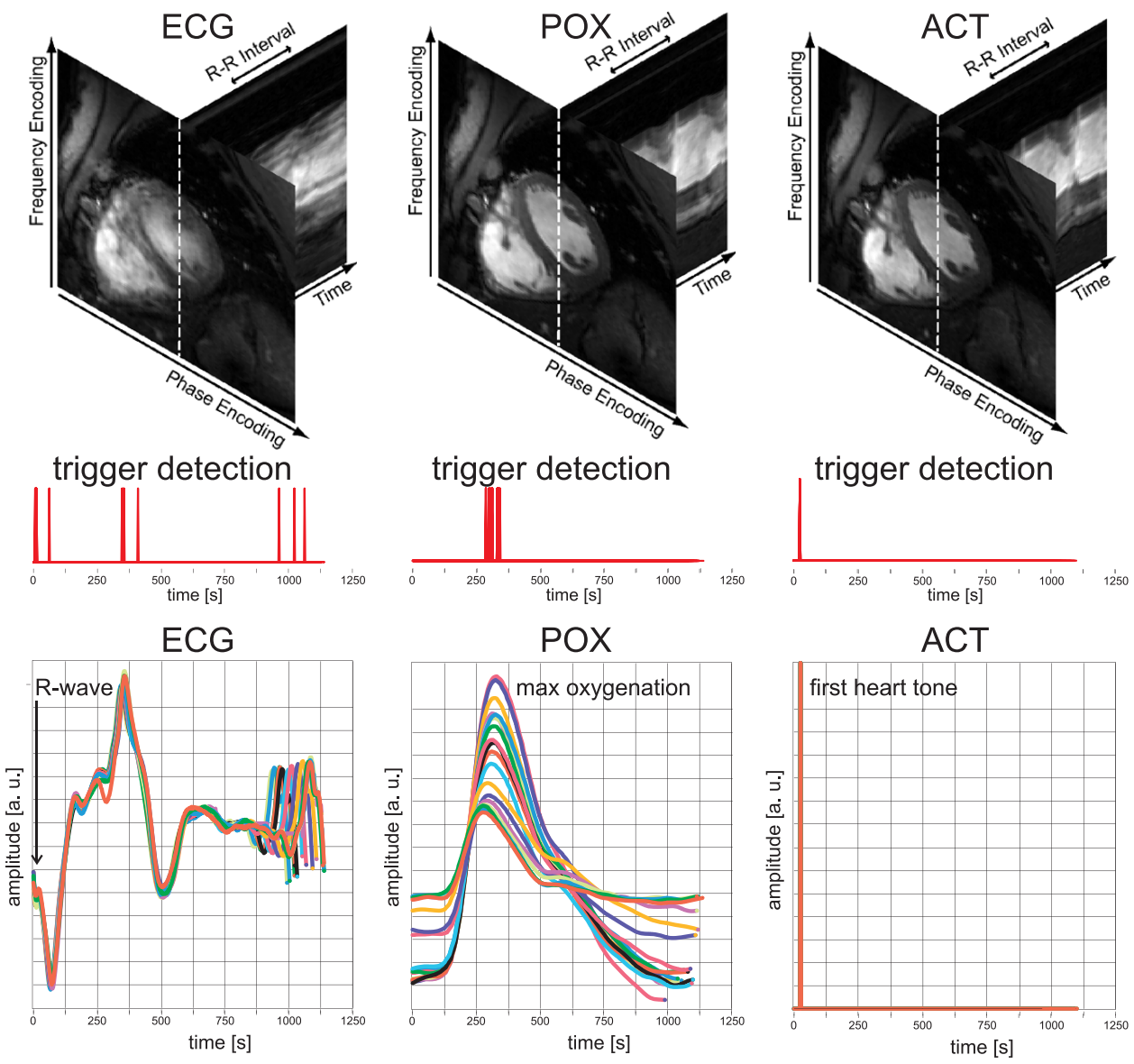

Figure 6 Example of erroneous ECG trigger detection. Cardiac images, trigger detection tickmarks and signal waveforms obtained at 7.0 T using vector ECG **(left)**, pulse oximetry **(center)** and acoustically triggered **(right)** 2D CINE FLASH acquisitions. All signal waveforms show the output of the scanners central physiological monitoring unit (including processing of the ECG, POX and ACT signal) as displayed at the scanners user interface. **Top**: Mid-ventricular, short axis views of the heart together with whole R-R interval time series of one-dimensional projections along the profile (dotted line) marked in the short axis view. **Middle**: Trigger detection tickmarks obtained from a single subject over 18 cardiac cycles after temporal realignment using cross correlation and reassignment. **Bottom**: Signal waveforms obtained from a single subject (subject 2) over 18 cardiac cycles. In this example vector ECG triggered CINE imaging was prone to severe cardiac motion artifacts due to R wave mis-registration which induced reduction in myocardium/blood contrast and image sharpness. ACT triggered 2D CINE FLASH imaging provided faultless trigger detection and hence produced images free of motion artifacts. Please note the scatter in the POX peak amplitude and peak width, causing a jitter (Δt = 72 ms) in the pulse oximetry trigger detection which constituted a synchronization problem.

would not compromise image quality but lengthen the acquisition time. Acoustically triggered 2D CINE FLASH imaging at 7.0 T produced images free of motion artifacts, as did pulse oximetry triggered 2D CINE FLASH imaging. The latter showed a scatter in the POX peak amplitude and peak width, causing a jitter of approximately Δt = 72 ms in the pulse-oximetry based trigger detection. This might be tolerable for a temporal resolution of 30 ms to 50 ms commonly used in conventional CINE imaging since data acquisition is distributed over several cardiac cycles which might result in averaging of motion effects. However, it stands

Table 1 Synopsis of the trigger detection variance assessment

Subject	Mean cardiac interval length (ms)			Standard deviation of the mean cardiac interval length (ms)			Standard deviation of the cardiac trigger offset (ms)		
	ACT	ECG	POX	ACT	ECG	POX	ACT	ECG	POX
1	869	865	840	89	54	45	78	10	11
2	870	795	1103	83	126	87	76	477	101
3	875	845	834	48	28	34	13	3	19
4	1064	999	1079	76	143	52	44	456	456
5	926	990	923	49	54	31	14	56	23
6	841	939	898	95	69	35	149	52	15
7	848	839	876	79	62	48	75	257	67
8	1110	886	1091	37	174	33	1	1047	14
9	762	576	660	81	168	144	112	488	331

Synopsis of the mean R-R interval lengths, standard deviation of the mean R-R interval lengths and standard deviation of the cardiac trigger detection offset deduced from the signal waveforms of ECG, POX and ACT triggered acquisitions. A significant difference in the standard deviation of the R-R interval length deduced from ECG, ACT and POX waveforms indicates trigger misregistration. A large standard deviation of the offset between the ECG's R-wave and the trigger detection which was derived from the ECG, POX and ACT waveforms indicates trigger misregistration.

to reason that the enhanced temporal resolution of CINE imaging facilitated by the signal-to-noise benefit at high and ultra-high fields [30] combined with the speed gain of parallel cardiac imaging [31] can be used to generate highly accurate time-series curves for wall motion tracking (i) to determine the exact time point of maximal systolic contraction and diastolic filling including assessment of mechanical dyssynchrony and (ii) to visualize small rapidly moving structures. Taking the underlying physiological temporal resolution into account it is fair to assume that a jitter in the POX trigger detection larger than 2-3 cardiac phases might diminish the temporal fidelity needed to characterize those physiologic phenomena within the cardiac cycle. Hence, the trigger detection jitter observed for pulse oximetry can constitute a challenge for reliable synchronization of data acquisition with the cardiac cycle. Another drawback of pulse oximetry is the latency between cardiac activity and trigger registration caused by the travel time of blood between the heart and the sensor position which can be in the order of several hundreds of milliseconds but which can also depend on (patho)physiology.

Acoustic triggering presents no risk of high voltage induction and patient burns, patient comfort and ease of clinical use, which all have, patient comfort, safety and practical implications. With reliable ACT triggering available, a positively-inclined practitioner might envisage using the merits of ACT to further simplify clinical CMR. For example, LV assessment is routinely conducted using 2D CINE imaging encompassing a stack of end-expiratory breath-held short axis views of the heart ranging from the atrioventricular ring to the apex. In current clinical practice, it is common to plan and scan each slice in an independent series instead of scanning all slices in a single series because of the frequently encountered risk of mis-triggering. This practical work around bears the advantage that only the most recently acquired slice needs to be re-scanned in case of non-diagnostic image quality due to mis-synchronization. Overcoming the hassle of ECG triggering, reliable triggering using ACT holds the promise to obviate the need for creating an independent series for each slice. Hence ACT, may help to streamline CINE imaging by using a single series for the entire stack of slices which has practical, data storage, data handling and data mining implications.

Admittedly, acoustic cardiac gating shares an apparent drawback of conventional ECG and pulse oximetry based cardiac triggering/gating that extra hardware is required for signal detection and processing, although the current ACT setup does not disturb the scanners certification. To overcome the constraint of using ancillary hardware various self-gating methods have been proposed and it's feasibility has been demonstrated for CMR [7,8,10,32]. However, self-gated CMR of small displacements such as vessel wall motion or MR angiography (MRA) remains a challenge due to the small changes in blood volume, low changes in vessel size and small vessel displacements throughout the cardiac cycle. The acoustic cardiac gating approach reported here is conceptually appealing for the pursuit of vascular CMR since the acoustic sensor can be used to directly detect vessel pulsation from larger vessels included in the target vessel territory.

It should be noted that the work reported here is limited to using vector ECG recordings and retrospective reconstruction techniques implemented on a clinical platform. Further fine-tuning of the post-processing and image reconstruction procedures used in current clinical

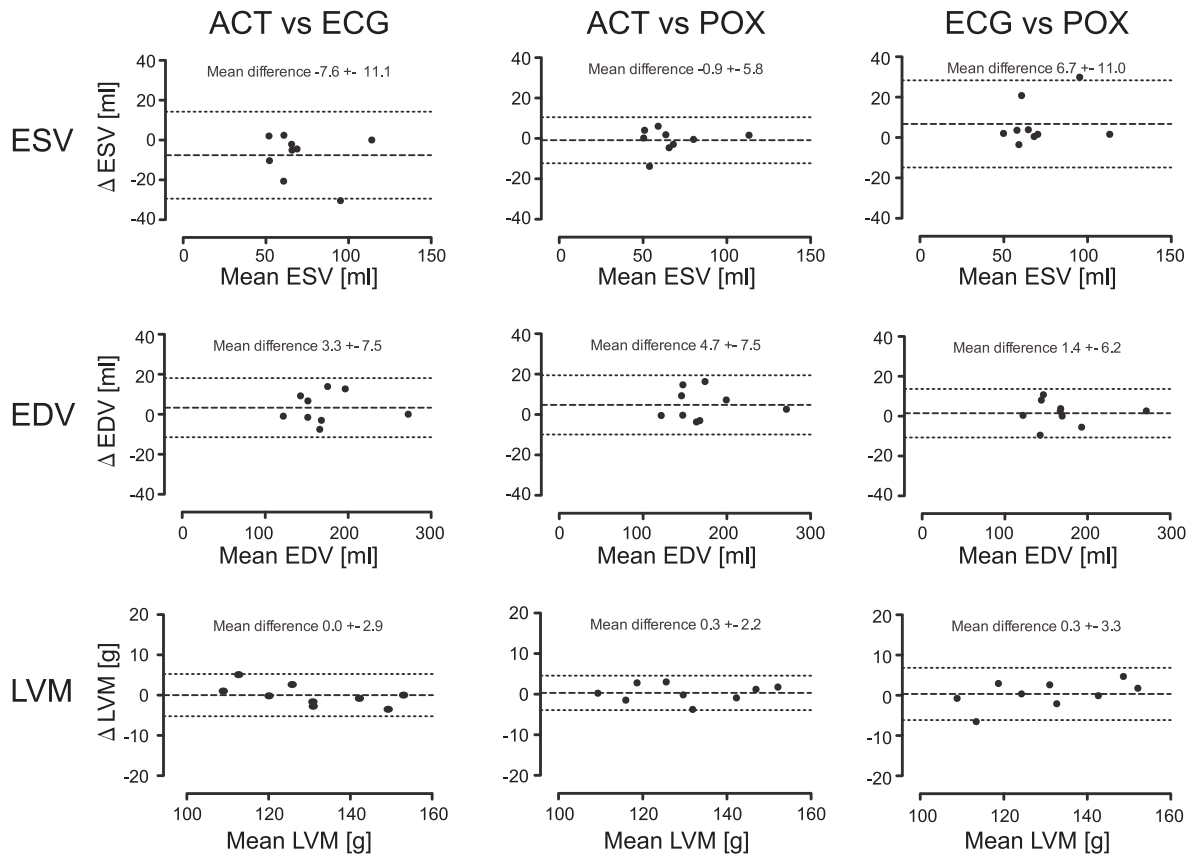

Figure 7 Comparison of cardiac chamber quantification parameters obtained for three triggering methods. Bland-Altman plots showing for each subject the mean of two measurements (ACT vs ECG, ACT vs POX and ECG vs POX) and the difference in the left ventricular parameter derived from vector ECG, ACT and POX gated 2D CINE FLASH acquisitions at 7.0 T. Dashed black lines in the Bland-Altman plots represent the mean difference while the dotted lines embody the confidence interval which was set to the mean value ± 1.96 of the standard.

Table 2 Synopsis of the image quality assessment

	End-diastolic Phase			End-systolic Phase		
Subject	**ACT**	**ECG**	**POX**	**ACT**	**ECG**	**POX**
1	2,4	2,2	1,8	1,5	1,6	1,7
2	2,6	0,9	1,9	2,1	0,5	1,6
3	2,9	2,7	2,5	2,6	2,4	2,1
4	2,9	1,7	2,8	2,6	1,2	2,4
5	2,5	1,9	1,9	2,1	1,7	1,7
6	1,6	2,1	1,8	1,5	1,5	1,4
7	1,5	1,6	1,1	1,1	1,6	1,0
8	2,8	1,1	2,4	2,4	0,8	1,5
9	2,1	0,7	1,3	1,9	0,5	0,9
Mean	**2,4**	**1,7**	**2,0**	**2,0**	**1,3**	**1,6**
SD (+/-)	**0,5**	**0,7**	**0,5**	**0,5**	**0,6**	**0,5**

Mean values of image quality scores for each subject and trigger approach. Overall image quality of end-diastolic and end-systolic images was rated using a scale ranging from 0 to 3 for each slice (0 - images with poor and non-diagnostic quality due to cardiac motion induced blurring, 1 - image quality impaired by cardiac motion which may lead to misdiagnosis, 2 - good image quality, cardiac motion artifacts hard to recognize and 3 - excellent image quality, no cardiac motion artifacts observed). Please note that the poor scores obtained for subject 7 are due to respiration induced motion artifacts.

practice including cross-correlation of ECG signals obtained for different R-R intervals together with retrospective image reconstruction is conceptually appealing to enhance ECG's trigger detection accuracy, albeit this change in the manufacturers ECG processing/reconstruction methodology is beyond the scope of the work reported here.

Conclusion

The applicability of acoustic triggering for cardiac CINE imaging at 7.0 T was shown. The intrinsic insensitivity of the MR-stethoscope to interference from electromagnetic fields renders it suitable for left ventricular parameter assessment at 7.0 T due to its excellent trigger reliability, which is superior to that of traditional ECG, VCG and conventional pulse oximetry. Acoustic cardiac triggering promises to be beneficial for ultra-high field strengths including 7.0 T and beyond, which is an important but challenging development looming on the pre-clinical research horizon. Although the full

range of ultrahigh field CMR is untapped yet, it is expected to drive future technological developments. With appropriate ancillary triggering hardware, RF-coil design and imaging techniques/protocols customized for 7.0 T applications, LV assessment and other CMR applications are feasible. While this is, for the moment, merely a start, it continues to motivate new basic and clinical research on ultrahigh field CMR, including extra efforts towards the development of a wireless signal transmission version of the acoustic triggering approach.

Author details
[1]Berlin Ultrahigh Field Facility (B.U.F.F.), Max-Delbrueck Center for Molecular Medicine, Berlin, Germany. [2]Siemens Healthcare, Erlangen, Germany. [3]Working Group on Cardiovascular Magnetic Resonance, Medical University Berlin, Charité Campus Buch, HELIOS-Klinikum Berlin-Buch, Dept. of Cardiology and Nephrology, Berlin, Germany. [4]Experimental and Clinical Research Center, Charité - Campus Buch, Humboldt-University, Berlin, Germany.

Authors' contributions
TF build the acoustic cardiac triggering device, performed the experiments, collected the data and was significantly involved in writing the manuscript. FH performed data evaluation and statistical analysis and was involved in editing the manuscript.TGO conducted analysis of the waveforms obtained for ACT, ECG and POX and was involved in editing the manuscript. MD has setup the CMR protocols for this study. FvK was responsible for the volunteer care, data documentation, left ventricular function analysis and image quality assessment. He was involved in editing the manuscript. MP performed image quality assessment. He was involved in editing the manuscript. JSM was significantly involved in the study and imaging protocol design. She was involved in editing the manuscript. TN was responsible for the overall concept, was significantly involved in the study and protocol design. He was also significantly involved in writing the manuscript.

Competing interests
Wolfgang Renz is a full-time employee of Siemens (Erlangen, Germany).

Received: 25 June 2010 Accepted: 16 November 2010
Published: 16 November 2010

References

1. Lanzer P, Botvinick EH, Schiller NB, Crooks LE, Arakawa M, Kaufman L, Davis PL, Herfkens R, Lipton MJ, Higgins CB: **Cardiac imaging using gated magnetic resonance.** *Radiology* 1984, **150**:121-127.
2. Brau AC, Wheeler CT, Hedlund LW, Johnson GA: **Fiber-optic stethoscope: a cardiac monitoring and gating system for magnetic resonance microscopy.** *Magn Reson Med* 2002, **47**:314-321.
3. Pattynama PM, van der Velde ET, Steendijk P, Lamb HJ, Baan J, de Roos A: **Cardiovascular MR imaging: pressure-gating using the arterial pressure signal from a conventional ferromagnetic micromanometer-tip catheter.** *Magn Reson Imaging* 1994, **12**:531-534.
4. Rubin JM, Fowlkes JB, Prince MR, Rhee RT, Chenevert TL: **Doppler US gating of cardiac MR imaging.** *Acad Radiol* 2000, **7**:1116-1122.
5. Buikman D, Helzel T, Roschmann P: **The rf coil as a sensitive motion detector for magnetic resonance imaging.** *Magn Reson Imaging* 1988, **6**:281-289.
6. Buehrer M, Curcic J, Boesiger P, Kozerke S: **Prospective self-gating for simultaneous compensation of cardiac and respiratory motion.** *Magn Reson Med* 2008, **60**:683-690.
7. Larson AC, White RD, Laub G, McVeigh ER, Li D, Simonetti OP: **Self-gated cardiac cine MRI.** *Magn Reson Med* 2004, **51**:93-102.
8. Larson AC, Kellman P, Arai A, Hirsch GA, McVeigh E, Li D, Simonetti OP: **Preliminary investigation of respiratory self-gating for free-breathing segmented cine MRI.** *Magn Reson Med* 2005, **53**:159-168.
9. Nijm GM, Sahakian AV, Swiryn S, Carr JC, Sheehan JJ, Larson AC: **Comparison of self-gated cine MRI retrospective cardiac synchronization algorithms.** *J Magn Reson Imaging* 2008, **28**:767-772.
10. Crowe ME, Larson AC, Zhang Q, Carr J, White RD, Li D, Simonetti OP: **Automated rectilinear self-gated cardiac cine imaging.** *Magn Reson Med* 2004, **52**:782-788.
11. Rengle A, Baboi L, Saint-Jalmes H, Sablong R, Beuf O: **Optical cardiac and respiratory device for synchronized MRI on small animal.** *Conf Proc IEEE Eng Med Biol Soc* 2007, 2046-2049.
12. Lanzer P, Barta C, Botvinick EH, Wiesendanger HU, Modin G, Higgins CB: **ECG-synchronized cardiac MR imaging: method and evaluation.** *Radiology* 1985, **155**:681-686.
13. Fischer SE, Wickline SA, Lorenz CH: **Novel real-time R-wave detection algorithm based on the vectorcardiogram for accurate gated magnetic resonance acquisitions.** *Magn Reson Med* 1999, **42**:361-370.
14. Chia JM, Fischer SE, Wickline SA, Lorenz CH: **Performance of QRS detection for cardiac magnetic resonance imaging with a novel vectorcardiographic triggering method.** *J Magn Reson Imaging* 2000, **12**:678-688.
15. Stuber M, Botnar RM, Fischer SE, Lamerichs R, Smink J, Harvey P, Manning WJ: **Preliminary report on in vivo coronary MRA at 3 Tesla in humans.** *Magn Reson Med* 2002, **48**:425-429.
16. Kugel H, Bremer C, Puschel M, Fischbach R, Lenzen H, Tombach B, Van Aken H, Heindel W: **Hazardous situation in the MR bore: induction in ECG leads causes fire.** *Eur Radiol* 2003, **13**:690-694.
17. Shellock FG, Kanal E: **Burns associated with the use of monitoring equipment during MR procedures.** *J Magn Reson Imaging* 1996, **6**:271-272.
18. Shellock FG, Crues JV: **MR procedures: biologic effects, safety, and patient care.** *Radiology* 2004, **232**:635-652.
19. Lange S, Nguyen QN: **Cables and electrodes can burn patients during MRI.** *Nursing* 2006, **36**:18.
20. Frauenrath T, Hezel F, Heinrichs U, Kozerke S, Utting JF, Kob M, Butenweg C, Boesiger P, Niendorf T: **Feasibility of cardiac gating free of interference with electro-magnetic fields at 1.5 Tesla, 3.0 Tesla and 7.0 Tesla using an MR-stethoscope.** *Invest Radiol* 2009, **44**:539-547.
21. Becker M, Frauenrath T, Hezel F, Krombach GA, Kremer U, Koppers B, Butenweg C, Goemmel A, Utting JF, Schulz-Menger J, Niendorf T: **Comparison of left ventricular function assessment using phonocardiogram- and electrocardiogram-triggered 2D SSFP CINE MR imaging at 1.5 T and 3.0 T.** *Eur Radiol* 2009.
22. Snyder CJ, DelaBarre L, Metzger GJ, van de Moortele PF, Akgun C, Ugurbil K, Vaughan JT: **Initial results of cardiac imaging at 7 Tesla.** *Magn Reson Med* 2009, **61**:517-524.
23. Frauenrath T, Niendorf T, Kob M: **Acoustic Method for Synchronization of Magnetic Resonance Imaging (MRI).** *Acta Acustica united with Acustica* 2008, **94**:148-155.
24. Brants A, Versluis M, de Roos A, Westenberg J, Webb A: **Quantitative comparison of left ventricular cardiac volume, mass and function obtained at 7 Tesla with "gold standard" values at 1.5 Tesla.** *Proc Intl Soc Mag Reson Med; Stockholm, SE* 2010, 1299.
25. Brandts A, Westenberg JJ, Versluis MJ, Kroft LJ, Smith NB, Webb AG, de Roos A: **Quantitative assessment of left ventricular function in humans at 7 T.** *Magn Reson Med* 2010.
26. Maderwald S, Nassenstein K, Orzada S, Schäfer LC, Oehmigen M, Bitz AK, Kraff O, Brote I, Ladd SC, Ladd ME, Quick HH: **MR imaging of cardiac wall-motion at 1.5T and 7T: SNR and CNR comparison.** *Proc Intl Soc Mag Reson Med; Stockholm, SE* 2010, 1299.
27. Renz W, Lindel T, Seifert F, Hoffmann W, Schulz-Menger J, Ittermann B: **A 4 channel TX/RX decoupled loop array for cardiac/body imaging at 7T.** *26th Annual Scientific Meeting of the European Society for Magnetic Resonance in Medicine and Biology; Antalya, TR* 2009, 476.
28. Bland JMAD: **Statistical method for assessing agreement between two methods of clinical measurement.** *Lancet* 1986, 307-310.
29. von Knobelsdorff-Brenkenhoff F, Frauenrath T, Prothmann M, Dieringer MA, Hezel F, Renz W, Kretschel K, Niendorf T, Schulz-Menger J: **Cardiac chamber quantification using magnetic resonance imaging at 7 Tesla-a pilot study.** *Eur Radiol* 2010, **20(12)**:2844-52.
30. Gutberlet M, Noeske R, Schwinge K, Freyhardt P, Felix R, Niendorf T: **Comprehensive Cardiac Magnetic Resonance Imaging at 3.0 Tesla: Feasibility and Implications for Clinical Applications.** *Invest Radiol* 2006, **41**:154-167.

31. Niendorf T, Sodickson DK: **Highly accelerated cardiovascular MR imaging using many channel technology: concepts and clinical applications.** *Eur Radiol* 2008, **18**:87-102.
32. Nijm GM, Sahakian AV, Swiryn S, Carr JC, Sheehan JJ, Larson AC: **Comparison of self-gated cine MRI retrospective cardiac synchronization algorithms.** *Journal of magnetic resonance imaging: JMRI* 2008, **28**:767-772.

doi:10.1186/1532-429X-12-67
Cite this article as: Frauenrath *et al.*: Acoustic cardiac triggering: a practical solution for synchronization and gating of cardiovascular magnetic resonance at 7 Tesla. *Journal of Cardiovascular Magnetic Resonance* 2010 **12**:67.

Cardiac chamber quantification using magnetic resonance imaging at 7 Tesla—a pilot study

http://dx.doi.org/10.1007/s00330-010-1888-2

Design, construction, and evaluation of a dynamic MR compatible cardiac left ventricle model

http://dx.doi.org/10.1118/1.4736954

Detailing the Use of Magnetohydrodynamic Effects for Synchronization of MRI With the Cardiac Cycle: A Feasibility Study

http://dx.doi.org/10.1002/jmri.23634

In vitro assessment of heart valve bioprostheses by cardiovascular magnetic resonance: four-dimensional mapping of flow patterns and orifice area planimetry

http://dx.doi.org/10.1016/j.ejcts.2010.12.040

Design and application of a four-channel transmit/receive surface coil for functional cardiac imaging at 7T

http://dx.doi.org/10.1002/jmri.22451

OPEN ACCESS Freely available online

PLoS one

Functional and Morphological Cardiac Magnetic Resonance Imaging of Mice Using a Cryogenic Quadrature Radiofrequency Coil

Babette Wagenhaus[1☯], Andreas Pohlmann[1*☯], Matthias Alexander Dieringer[1,2], Antje Els[1], Helmar Waiczies[1,3], Sonia Waiczies[1,3], Jeanette Schulz-Menger[2], Thoralf Niendorf[1,3]

1 Berlin Ultrahigh Field Facility (B.U.F.F.), Max-Delbrück Center for Molecular Medicine, Berlin, Germany, **2** Charité Working Group Cardiac MRI, Experimental and Clinical Research Center and HELIOS Clinics, Berlin, Germany, **3** Experimental and Clinical Research Center, a joint cooperation between the Charité Medical Faculty and the Max-Delbrück Center for Molecular Medicine, Berlin, Germany

Abstract

Cardiac morphology and function assessment by magnetic resonance imaging is of increasing interest for a variety of mouse models in pre-clinical cardiac research, such as myocardial infarction models or myocardial injury/remodeling in genetically or pharmacologically induced hypertension. Signal-to-noise ratio (SNR) constraints, however, limit image quality and blood myocardium delineation, which crucially depend on high spatial resolution. Significant gains in SNR with a cryogenically cooled RF probe have been shown for mouse brain MRI, yet the potential of applying cryogenic RF coils for cardiac MR (CMR) in mice is, as of yet, untapped. This study examines the feasibility and potential benefits of CMR in mice employing a 400 MHz cryogenic RF surface coil, compared with a conventional mouse heart coil array operating at room temperature. The cryogenic RF coil affords SNR gains of 3.0 to 5.0 versus the conventional approach and hence enables an enhanced spatial resolution. This markedly improved image quality – by better deliniation of myocardial borders and enhanced depiction of papillary muscles and trabeculae – and facilitated a more accurate cardiac chamber quantification, due to reduced intraobserver variability. In summary the use of a cryogenically cooled RF probe represents a valuable means of enhancing the capabilities of CMR of mice.

Citation: Wagenhaus B, Pohlmann A, Dieringer MA, Els A, Waiczies H, et al. (2012) Functional and Morphological Cardiac Magnetic Resonance Imaging of Mice Using a Cryogenic Quadrature Radiofrequency Coil. PLoS ONE 7(8): e42383. doi:10.1371/journal.pone.0042383

Editor: Ryuichi Morishita, Osaka University Graduate School of Medicine, Japan

Received April 2, 2012; **Accepted** July 4, 2012; **Published** August 1, 2012

Funding: This study was funded by the Max Delbrück Center for Molecular Medicine. The funders had no role in study design, data collection and analysis, decision to publish, or preparation of the manuscript.

Competing Interests: The authors have declared that no competing interests exist.

* E-mail: andreas.pohlmann@mdc-berlin.de

☯ These authors contributed equally to this work.

Introduction

Genetically modified animal models have evolved into protagonists in cardiac research. Alongside the established surgically and pharmacologically induced animal models, they are valuable for studying the pathogenesis of cardiovascular diseases. Adequate characterization, rapid phenotyping, assessment of gender effects, evaluation of novel therapeutics and long-term follow-up studies are still challenging. To this end there is an ever growing need for non-invasive *in vivo* imaging that (i) provides excellent spatial and temporal resolution (a prerequisite for cardiovascular research), (ii) has a high reproducibility and (iii) is suitable for longitudinal studies. Cardiovascular magnetic resonance (CMR) and echocardiography are widely used in clinical and preclinical studies, with CMR being accepted as the more accurate modality. Cardiac morphology and function assessment is the workhorse of CMR and is of increasing interest for a variety of mouse models in pre-clinical cardiac research, such as myocardial infarction models or myocardial injury/remodeling in genetically or pharmacologically induced hypertension.

The small size of the mouse heart and its rapid motion with typical heart rates of 400 to 600 beats per minute pose substantial challenging demands on CMR in mice. Together with signal-to-noise ratio (SNR) limitations, these challenges bear the potential to deteriorate image quality severely. Cardiac morphology and function assessment requires imaging techniques that provide excellent delineation of myocardial borders - hence the need for high ventricular blood to myocardium contrast -, full coverage of the cardiac cycle with high temporal resolution, but also coverage of the entire heart with high spatial resolution to facilitate reliable segmentation of the endo- and epicardial borders.

Realizing these competing constraints assessment of cardiac morphology, cardiac chamber quantification and cardiac function assessment require imaging protocols and hardware that are tailored for CMR. The hardware used in current experimental CMR of mice affords images with a typical in-plane spatial resolution of 100–200 μm, heart coverage of 6–13 slices of 1.0 mm thickness and measurement of 10–20 cardiac phases [1,2,3,4,5,6,7,8,9,10]. Although these studies provide acceptable image quality for the quantitative assessment of the left ventricle (LV), assessment of the right ventricle (RV) remains challenging due to the limited image quality of the RV. RV assessment is of increasing interest since remodelling and myocardial injury are not restricted to the left ventricle [11] and the RV is a primary target

of diseases including RV dysfunction or RV hypertrophy as a result of pulmonary hypertension or RV-thinning in case of dysplasia, such as arrhythmogenic right ventricular cardiomyopathy (ARVC) [12]. For preclinical research of these diseases numerous mouse models are available, such as pulmonary arterial constriction [13] (for the RV aspects of pulmonary hypertension) or plakoglobin deficient mice [14] (for ARVC). For all these reasons it is conceptually appealing to improve image quality for CMR in mice. To meet this goal enhancements in the spatial resolution are essential, which in turn built on SNR improvements.

Strategies for improving SNR are i) signal averaging, which comes at the expense of prolonged measurement times, ii) moving to higher magnetic field strengths, which are associated with practical impediments, such as increased magnetic field inhomogeneities and RF power deposition, or iii) perfecting radio frequency (RF) coil technology, which holds the promise to offer significant gains in SNR. RF coils tailored for CMR are dedicated birdcage volume coils or surface coil arrays with the geometry adjusted to the size of a mice (25–35 mm inner diameter or 15–26 mm side length respectively) [2,4,5,6,7,8,10]. An emerging RF coil technology for MRI of small rodents is the cryo-cooling of RF coils, which reduces the electronic noise. Such cryogenic RF probes are widely used in vertical NMR spectroscopy systems, but have only recently become available for horizontal small bore MR imaging systems. Significant gains in SNR with a cryogenic probe have been shown for MRI of the mouse brain [15,16,17,18]. The application of cryogenic RF coils for CMR in mice has, as of yet, untapped potential. No reports that exploit cryogenic RF coil technology for CMR in mice have been published yet.

Realizing this opportunity, this study examines the feasibility of cardiac MRI in mice employing a 400 MHz cryogenic transceive RF surface coil and demonstrates its suitability for high spatial resolution functional and structural CMR in mice. Image quality, SNR, and cardiac function are assessed. For comparison a conventional mouse heart receive-only coil array operating at room temperature is used.

Materials and Methods

Ethics Statement

Animal experiments were carried out in accordance with the guidelines provided and approved by the Animal Welfare Department of the *Landesamt für Gesundheit und Soziales* Berlin (Berlin State Office of Health and Social Affairs, Permit Number: G0019/12). All imaging experiments were performed under isoflurane anesthesia, and all efforts were made to minimize suffering.

MRI System and Coil Setup

All imaging experiments were carried out on a 9.4T small animal MR system (Biospec 94/20, Bruker Biospin, Ettlingen, Germany) operating at 400 MHz. Two RF coil set-ups were used:

a) conventional linear polarized birdcage resonator (Bruker Biospin, Ettlingen, Germany; inner diameter of 72 mm) for transmission in conjunction with a curved four channel receive only mouse cardiac coil array (Bruker Biospin, Ettlingen, Germany) at room temperature (RT) and

b) a cryogenic transceive quadrature RF surface coil (CryoProbe, CP, Bruker Biospin, Ettlingen, Germany) of similar coil geometry as the RT surface coil (overlapping coils bent to a cylinder surface; inner diameter: 20 mm, length: 85 mm) operating at around 30 K (preamplifiers at 77 K) cooled by a closed-cycle refrigeration system.

The CryoProbe's surface (which is in direct contact with the animal) is equipped with a temperature sensor and can be temperature regulated using a resistive heater unit (Bruker, BioSpin AG, Fällanden, Switzerland). This approach was used to maintain the surface temperature of the Cryoprobe at 37°C.

Animal Preparation

3-month-old C57BL/6N mice were obtained from a commercial breeder (Charles River, Sulzfeld, Germany) and kept under controlled conditions for temperature, humidity and light, with chow and water ad libitum. Mice were anesthetized in a warmed anesthetic chamber using 2.5% isoflurane in an oxygen/air mixture (2:1) with a flow rate of 750 ml/min for induction and then maintained at 1.5%. When using the CryoProbe the forepaws of the mouse were held in a caudal position by adhesive tape in order to keep the distance between mouse chest and coil elements as small as possible. The mouse was placed supine on the animal bed of the CryoProbe, in contrast to the prone position (with cranial forepaw placement) required for use of the RT-coil.

A body temperature of 37°C was maintained by warming the animal beds using a circulating heated water system (Thermo Haake GmbH, Karlsruhe, Germany) and monitoring by a rectal temperature probe throughout the measurements. Respiratory signals were continuously monitored using a commercial monitoring and gating system (SA Instruments, Inc., New York, USA) and kept between 50–70 respiration cycles per minute by regulating the isoflurane dose. Ten mice were imaged twice, once with the RT-coil and once with the CryoProbe in an interval of two weeks. The first and second MRI was performed at the same time of the day to avoid physiological variations due to circadian rhythm.

B_1 Field of the CryoProbe in vivo

Relative maps of the transmit component of the RF electromagnetic field (B_1^+) were calculated from pulse oximetry triggered FLASH acquisitions ($\alpha = 30°/60°$, TE/TR = 1.4/5000 ms, BW = 75 kHz, slice thickness = 2 mm, spatial resolution: $0.23 \times 0.71 \times 2$ mm^3 interpolated to $0.12 \times 0.23 \times 2$ mm^3, averages = 2, partially parallel imaging (PPI) acceleration = 2, acquisition time per angle = 7 min) of standard short axis and four chamber views of the mice heart using the double angle method [19,20].

In vivo Coil Comparison

To obtain a stack of cardiac short axis (SAX) views covering the whole heart, ten slices were consecutively acquired using a self-gated [4] bright-blood cine fast low angle shot technique (IntraGate-FLASH, slice thickness = 0.8 mm). For each coil two imaging protocols were conducted using:

a) conventional spatial resolution protocol (spatial resolution = $156 \times 234 \times 800$ μm^3, TE/TR = 1.4/8.5 ms, $\alpha = 15°$, BW = 75 kHz, NR = 100, cardiac frames = 20, TA ~2 min) and

b) high spatial resolution protocol (spatial resolution = $69 \times 115 \times 800$ μm^3, TE/TR = 1.3/8.5 ms, $\alpha = 20°$, BW = 75 kHz, NR = 170, cardiac frames = 20, TA ~4.5 min).

For both protocols the navigator parameters used for motion tracking and cardiac gating were: FA = 2°, BW = 2740 Hz, thickness = 2 mm in oblique slice location. The navigator slice was always aligned with the long axis of the left ventricle and crossed the apex and the center of the mitral valve. Since volume resonators and surface coils have different B_1^+ efficiency

and characteristics, the RF power adjustment slice (thickness = 2 mm) was adapted to the respective coil configuration. For the RT-coil the adjustment slice was positioned in axial orientation whereas the adjustment slice for the CryoProbe experiments was placed in the coronal orientation through the center of the heart.

For SNR comparison between both imaging protocols the mean SNR of left ventricular myocardium was estimated for a midventricular slice. The high-resolution protocol was used for in-depth SNR analysis and cardiac function assessment. SNR values were obtained by determining signal intensities from regions of interest (ROI) positioned in an end diastolic short axis view on the level of the papillary muscles using a six segment model [21]. Mean myocardium SNR values were estimated for all slices covering the heart from the base to the apex. Noise was given by the standard deviation of the signal obtained from a ROI placed in the background (air) anterior to the thorax on the midventricular level. SNR was estimated by dividing mean signal intensity of the left ventricular myocardium by the noise. Cardiac function assessment was performed twice by an experienced observer in a blinded manner using CMR42 (Circle CVI, Calgary, Canada). For this purpose endo- and epicardial borders were contoured in end-systole and end-diastole using a stack of short axis cine views. Stroke volumes (SV), end-diastolic volumes (EDV), end-systolic volumes (ESV), ejection fractions (EF), and myocardial masses (EDM) were calculated for both left and right ventricle. Intraobserver and interobserver variability for the EDV, ESV and EDM of the left and right ventricle was evaluated using Bland-Altman analysis.

To further put the SNR gain inherent to the CryoProbe to use CINE images were acquired with an exquisite spatial resolution of ($43\times138\times300$) μm^3 using short axis views (TE/TR = 1.6/12.5 ms, $\alpha = 22^\circ$, partial Fourier acceleration = 2, BW = 119 kHz, NR = 340, cardiac frames = 20, TA ~19 min, called *ultra-high resolution* in the following).

Results

Transmit Component RF Field ($B1^+$) in vivo

Relative B_1^+-maps of a four chamber view and a short axis view obtained for the CryoProbe are shown in *Figure 1*. A linear B_1^+ profile was found for a midventricular short axis view. A change in realtive B_1^+ of approximately 65% was observed in the coil sensitivity profile ranging from the anterior chest wall to the inferior myocardium. The long axis view revealed a rather constant B_1^+ distribution due to an almost parallel alignment of the slice with the coils sensitivity profile. B_1^+ values in the region of the myocardium were found to be above 100%.

In vivo Imaging of Mice Heart

Cardiac cine imaging of the mouse heart in the short axis and four chamber view was feasible for both protocols and coil configurations. The high-resolution images derived from CryoProbe acquisitions revealed an enhanced anatomical detail and myocardial border sharpness versus the RT-coil acquisitions as illustrated in Figures 2 and 3. Figure S1 shows a short axis view CINE data set of 20 cardiac phases acquired with the CryoProbe. For the four chamber view (*Figure 2*), the CP image afforded an accurate delineation of the left ventricular outflow tract including the aortic valve and the aortic vessel wall. In comparison, identifying the closing of the aortic valve in the CINE images derived from RT acquistions is elusive. For the CP images the lateral right ventricle blood myocardium border was well defined especially at the level of the apex. In contrast, subtle anatomic structures were severly blurred by noise in the RT images: a close examination of the short axis views (*Figure 3*) revealed an enhanced depiction of anatomic details of the left ventricular papillary muscles and right ventricular trabeculae in the CP images compared to the RT images, for both diastole and systole. Coronary arteries were more pronounced in the CP-images. In particular, the lateral and inferior right endocardial boundary was better delineated in the CP images. Although the shape of the right ventricle differed between the prone position (RT coil) and supine position (CP) (*Figures 2+3*), the end-diastolic volumes (EDV) or end-systolic volumes (ESV) did not differ significantly: $\Delta EDV = -2.13\pm11.37$ µl, $\Delta ESV = 3.98\pm4.95$ µl.

The SNR assessment showed that SNR derived from the lower resolved images acquired with the RT coil (SNR = 47 ± 9) was comparable to that obtained from the higher resolved images acquired with the CryoProbe (SNR = 54 ± 7). In contrast, the SNR of the higher resolved images acquired with the RT coil was only 15 ± 2, and that of the lower resolved images acquired with the CP was 221 ± 16.

Both slicewise and segmented analysis of the mean SNR in the myocardium demonstrated superior SNR for the CP compared to the RT coil (*Figure 4*). The gain in SNR (CP vs RT) ranged from 3.0 to 5.0. Highest SNR gains were observed for the region located closest to the coil. The SNR gain was less pronounced for regions more distant to the CP/RT coil. Segmental SNR analysis resulted in: SNR_{CP}/SNR_{RT} = 3.0, 3.2, 3.7, 4.3, 4.3, 3.2 for segments 1–6. The slice by slice SNR analysis revealed a minor reduction in the SNR gain from base to apex for both coils, with the exception of the apical slice in the CP images, where SNR increased again. For slices 1–6 a comparable mean SNR gain was observed: $SNR_{CP}/SNR_{RT} = 3.6\pm0.1$. A peak SNR gain of 5.0 was achieved in the apical slice.

Bland-Altman analysis of intraobserver comparison for end-diastolic volumes (EDV), end-systolic volumes (ESV), and end-diastolic myocardial masses (EDM) for the left and right ventricle is shown in *Figure 5*. Standard deviations of the mean differences for EDV, ESV and masses were found to be smaller using the CryoProbe for both left and right ventricle. The LV-EDV and RV-ESV showed the largest impact, followed by the LV-EDM and the RV-EDM.

The analysis of the interobserver comparison yielded the following mean differences (± standard deviations, RT/CP): LV-EDV 0.0 ± 1.4 µl/1.6 ± 1.8 µl, RV-EDV -0.9 ± 2.3 µl/-1.0 ± 3.1 µl, LV-ESV -0.2 ± 1.3 µl/1.1 ± 0.6 µl, RV-ESV -1.7 ± 1.0 µl/-1.6 ± 1.0 µl, LV-EDM 1.6 ± 3.7 mg/0.1 ± 1.8 mg, RV-EDM 0.8 ± 1.6 mg/0.7 ± 1.0 mg. Using the CryoProbe standard deviations were smaller, except for the EDV.

The image quality of the CryoProbe ultra-high spatial resolution images (*Figure 6*) was even further enhanced compared to the high resolution images (*Figure 3*). Endo- and epicardial border delineation as well as the depiction of anatomic details of the papillary muscles and trabeculae were improved.

The partial volume effects for the very thin structure of the RV were estimated by calculating how many image voxels constitute the myocardium of the RV (mean volume 18.3 µl): 626, 2879, or 10266 voxels for the conventional, high, or ultra-high resolution protocols. With the improved spatial resolution afforded by the CP the RV wall (estimated wall thickness 0.40 mm) was covered by 3.5–5.8 pixels. For comparison, the RV was covered by only 1.7–2.6 pixels when using the RT coil with the lower resolution protocol. With the ultra-high spatial resolution protocol the RV was even covered by 2.9–9.3 pixels, which is beneficial for reducing partial volume effects.

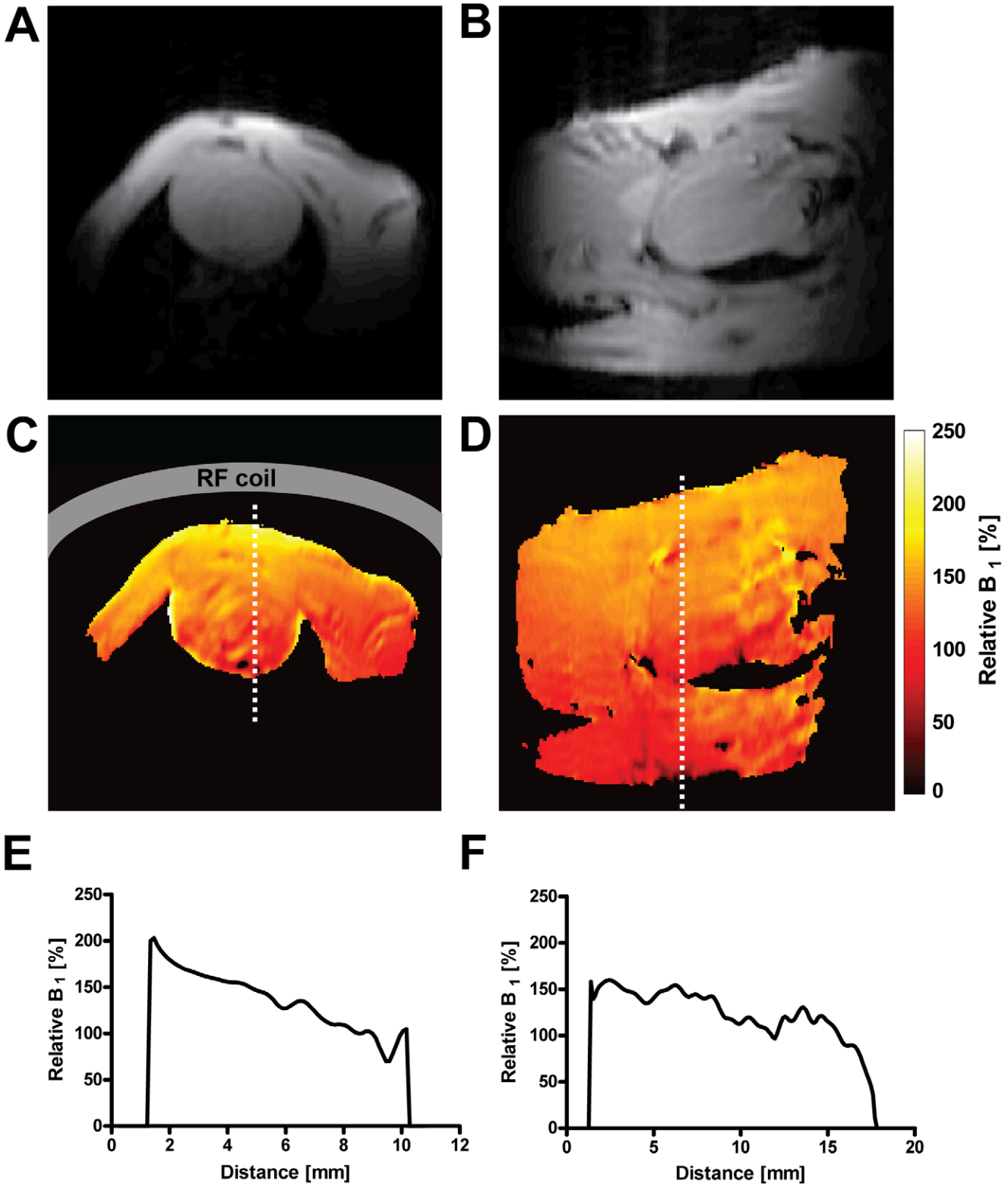

Figure 1. Relative B_1^+-maps of a short axis view (c) and a four chamber view (d) using the CryoProbe, with the corresponding MR images (a and b respectively) of identical image geometry. The coil is positioned on the upper side (anterior), schematically shown as a gray bar in (c). Compared to the B_1^+-maps (c,d), B_1^+-profile plots (e,f) allow for a more precise presentation of the spatial B_1^+-variation. These plots show the B_1^+ profile along a line crossing the heart (dotted line in (c) and (d) respectively). The B_1^+ decrease from anterior to posterior is approximately linear (c).

doi:10.1371/journal.pone.0042383.g001

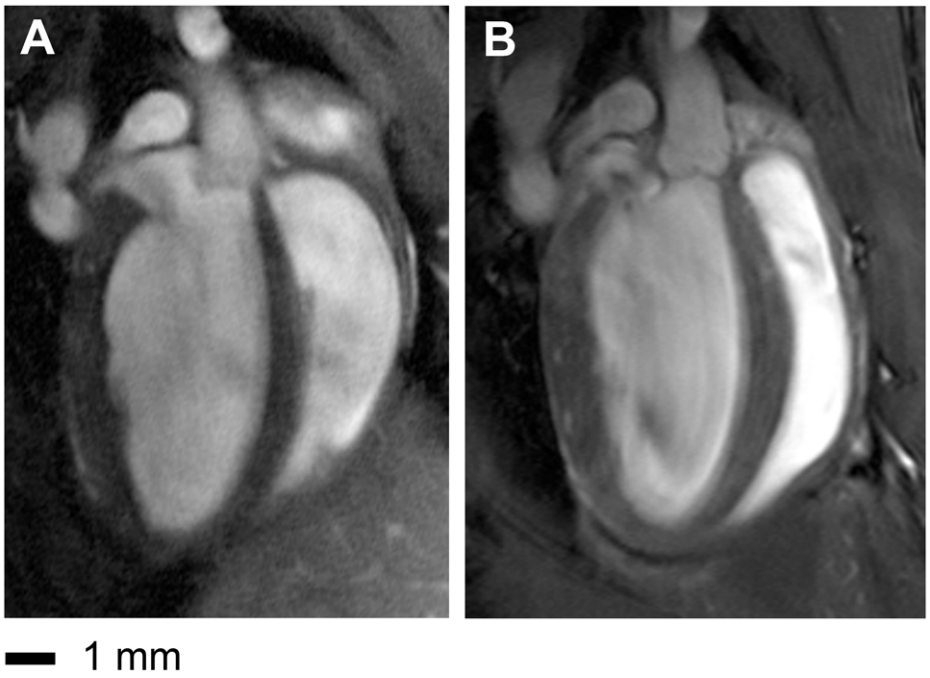

Figure 2. Comparison between high resolution (69×115×800 μm^3) images of a four chamber view acquired with the birdcage resonator in conjunction with a four channel mouse receive only cardiac surface coil array at room temperature (a) and the CryoProbe (b). Contrary to the room temperature coil image, the CryoProbe image accurately delineates the aortic valve, the left ventricular outflow tract including aortic vessel wall, as well as the lateral right ventricle blood myocardium border especially at the level of the apex.
doi:10.1371/journal.pone.0042383.g002

Discussion

In this study we demonstrated the feasibility of structural and functional CMR in mice employing a cryogenic RF surface coil. Image quality in terms of SNR and depiction of anatomic details was found to be superior using the CP compared to the standard cardiac four channel room temperature surface coil in conjunction with the volume resonator. Intraobserver variability improved for the assessment of cardiac volumes and masses and interobserver variability for ESV and EDM.

The B_1^+ decrease from anterior to inferior in the short axis view is approximately linear and less pronounced than that reported for phantom experiments by Baltes *et al* [16]. This may partially be due to the use of the double-oblique imaging slices, leading to the short axis view and four chamber view showing less of a B_1^+-gradient than one would expect in an axial slice and more than one would expect in a coronal slice.

B_1^+ values in the heart were found to be above 100%. This can be explained with the fact that the transmitter adjustment slice was placed in a strictly coronal orientation using a strictly axial reference image, while the heart orientation is oblique. Another limitation was that an entire slice was used for transmitter adjustment rather that a selected volume. Further optimization of the positioning of the RF-power adjustment slice and ideally a spatial limitation to a selected volume (through a modification of the adjustment procedure) might help to reduce this deviance and to further improve SNR and blood-myocardium contrast. Nevertheless, the B_1 characteristics afforded excellent image quality and facilitated cardiac chamber quantification.

The observed differences beween the shape of the right ventricle in the RT coil images and CP images can be explained with the different positioning of the animal, i.e. in the prone position for the RT coil and in supine position for the CP. Besides the natural prone position, also the supine position has been used for CMR studies of mice (e.g. [5,9,22]). An effect of the positioning on the functional parameters cannot be ruled out completely, but is unlikely since the end-diastolic and end-systolic volumes of the RV did not differ markedly in our study.

The demonstrated SNR improvements for images acquired with the CryoProbe compared to the RT-coil set-up is consistent with the published findings for MRI of the brain at the same field strength of 9.4 Tesla and with similar RF hardware [16]. For cardiac MRI the achievable SNR gain reported here exceeds that reported for brain (heart: 3.0 to 5.0, brain: 2.2 to 3.0). One possible reason for the differences in SNR gain in the present study is a different performance of the room-temperature coil that was used as reference. However differences in the CryoProbes cannot be excluded, notwithstanding same design.

The spatial variation in SNR across the myocardial segments of a short axis view can be explained with the proximity to the surface coil. A decrease in signal-amplitude with increasing distance is inherent to surface coils. Here, the surface coil characteristics explain that the region closest to the coil showed the highest SNR, and SNR clearly decreased with the distance from the coil.

A trend towards a SNR reduction along the base to apex line was observed, with the exception of the apical slice (CP only). The unexpected higher SNR at the apical slice observed for the CryoProbe was not found for the RT images. Hence partial volume effects, i.e. blood contaminations, can be excluded as a reason for this SNR increase. Moreover, the same SNR increase in slice 7 was found also for a region of interest in the skeletal muscle (located within the slice). This phenomenon is therefore not likely to have physiological causes, but conceivably may be caused by the two-element surface coil characteristics.

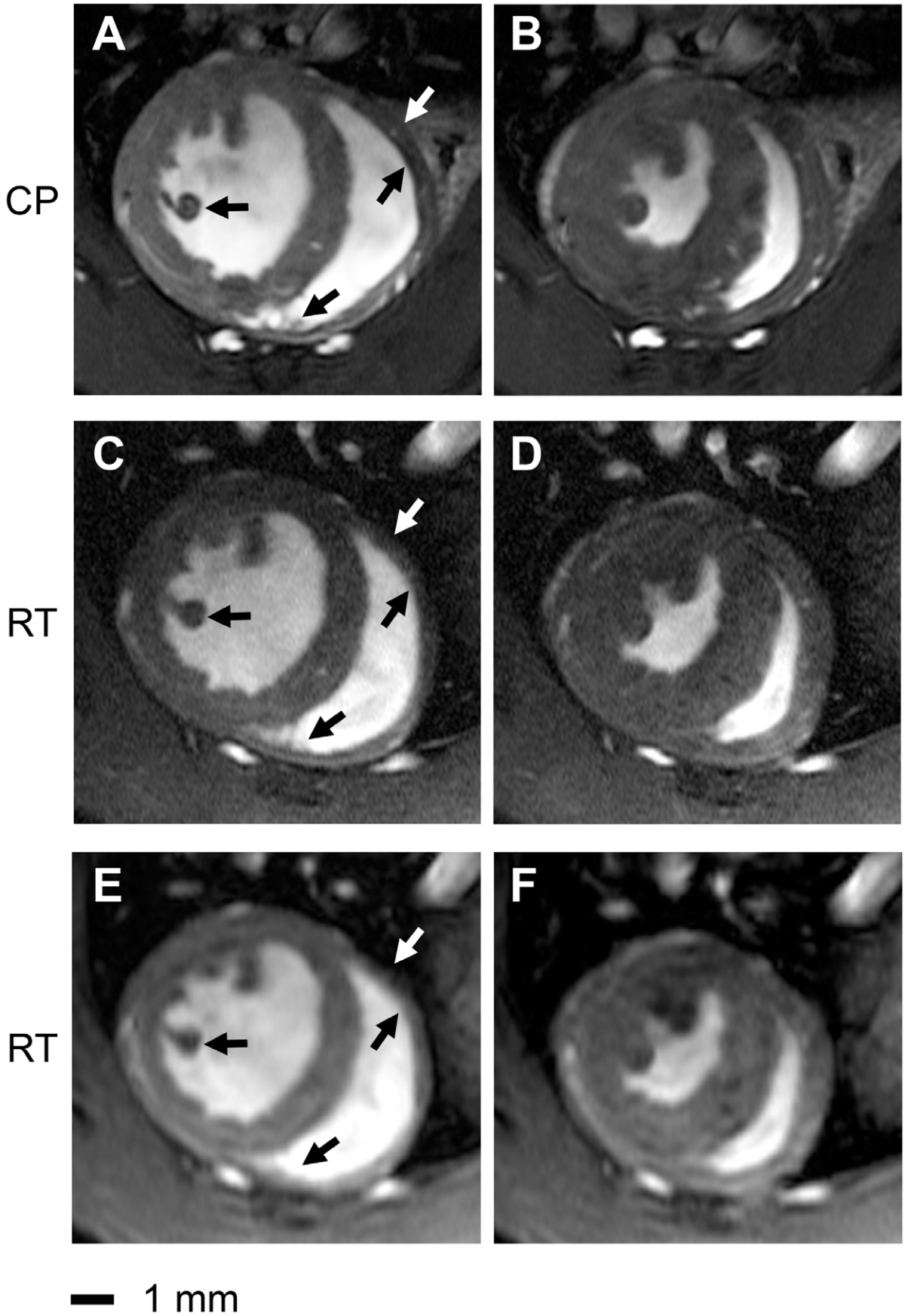
A
B
CP
C
D
RT
E
F
RT
1 mm

Figure 3. Comparison of end-diastole (left column) and end-systole (right column) short axis views acquired using a spatial resolution of 156×234×800 μm³ (a,b) and 69×115×800 μm³ (c,d,e,f). The depiction of anatomic details for left ventricular papillary muscles and right ventricular trabeculae is enhanced in the CryoProbe (CP) images (e,f) compared to the room temperature (RT) coil images (a,b,c,d) for both diastole and systole. Coronary arteries are more pronounced in the CryoProbe images. The lateral right endocardial boundary is better delineated in the CryoProbe images. The signal-to-noise ratio of the lower resolved images acquired with the RT-coil (47±9, a,b) is comparable to that of the higher resolved images acqured with the CryoProbe (54±7, e,f).
doi:10.1371/journal.pone.0042383.g003

The achieved gain in SNR by use of the CryoProbe facilitated higher spatial resolution CMR, while maintaining an SNR comparable to the lower resolution RT-coil images. While the high resolution protocol also yielded a better depiction of anatomical details in RT-coil images when compared with the respective lower resolved images, this came at the cost of significantly reduced SNR and poorer delineation of myocardial boundaries, particularly for the RV. The subjective criteria of

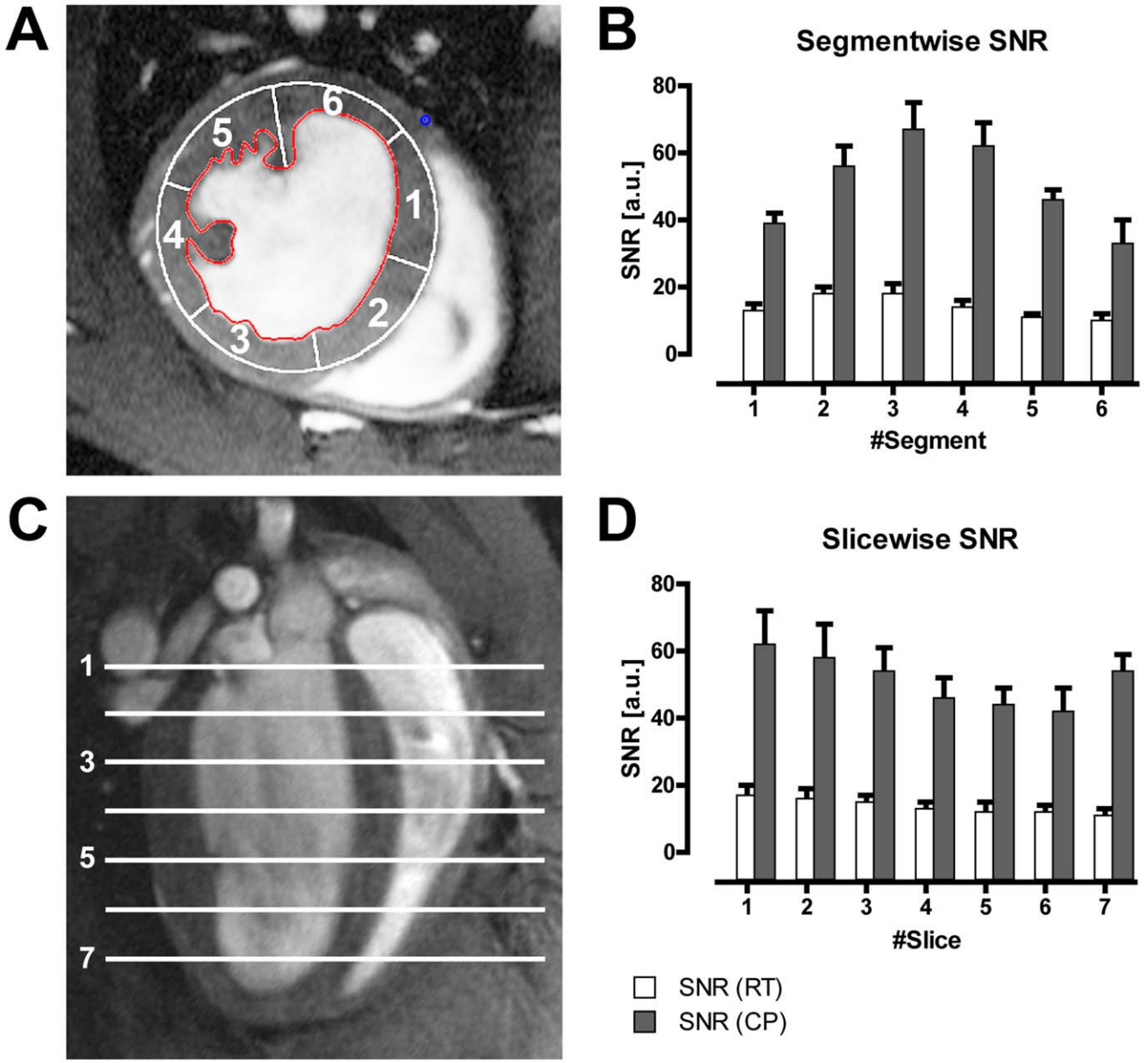

Figure 4. ***a,b:*** **Bar plot of mean LV myocardium signal-to-noise ratio (SNR) (b) measured in images acquired with the CryoProbe (CP) or room temperature coil (RT) for all mice in the different segments of a six-segment model (a).** The segments were numbered clockwise, starting at the inferoseptal segment. The region closest to the coil (segment 3) showed the highest SNR, and SNR decreased with distance from the coil. *c,d*: Bar plot of mean LV myocardium SNR (d) for all mice in the different slices (geometry shown in c). Slices were numbered from the basal slice to the apex. For the CryoProbe the apical slice showed an unexpected increase in SNR, in contrast to the decreasing trend from base to apex in the remaining 6 slices.
doi:10.1371/journal.pone.0042383.g004

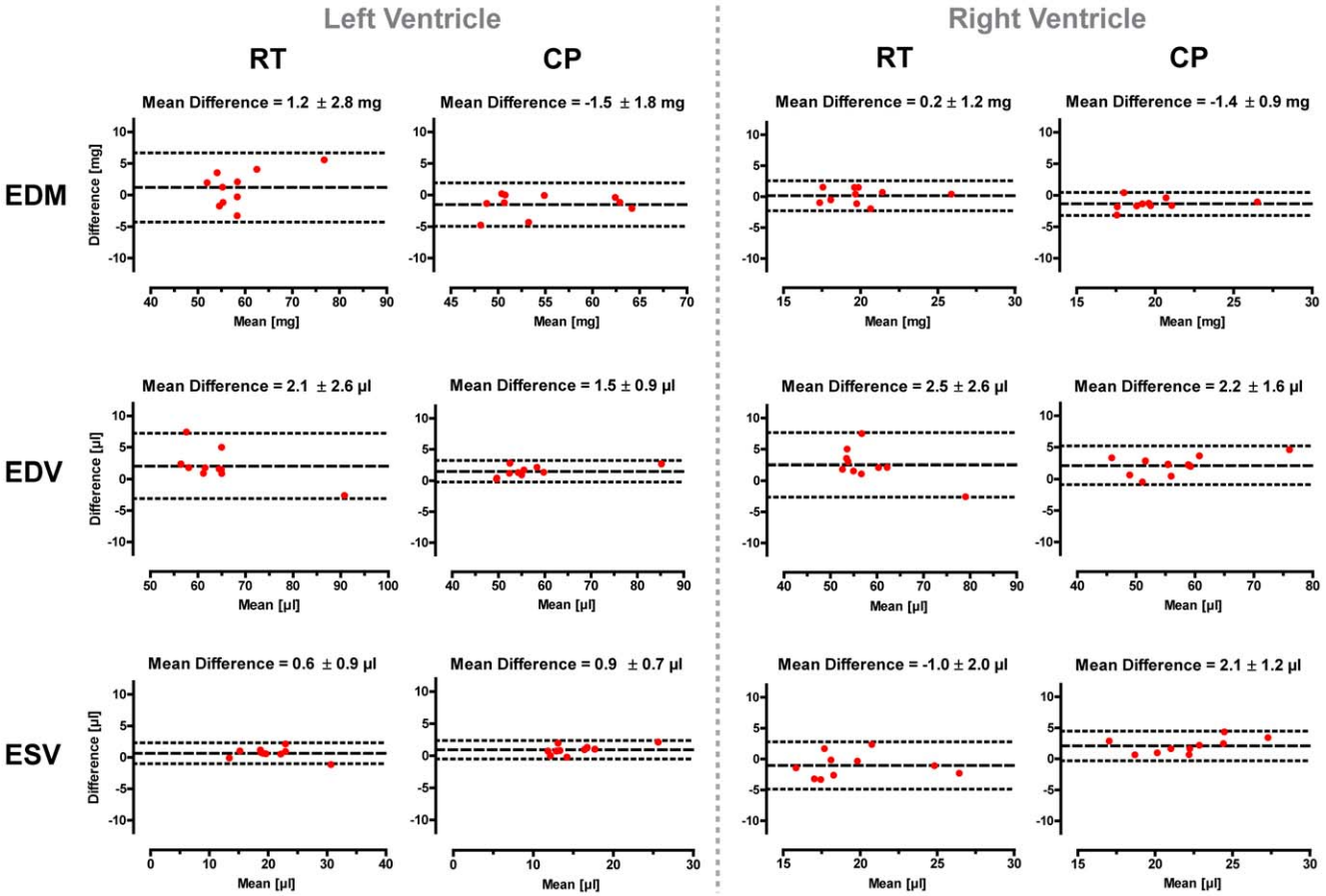

Figure 5. Bland-Altman plots of end-diastolic volumes (EDV), end-systolic volumes (ESV), and end-diastolic myocardial masses (EDM) for the left and right ventricle. For both ventricles and all three parameters the standard deviation of the differences was smaller for the CryoProbe than for the RT-coil. The LV-EDV and RV-ESV showed the largest impact, followed by the LV-EDM and the RV-EDM.
doi:10.1371/journal.pone.0042383.g005

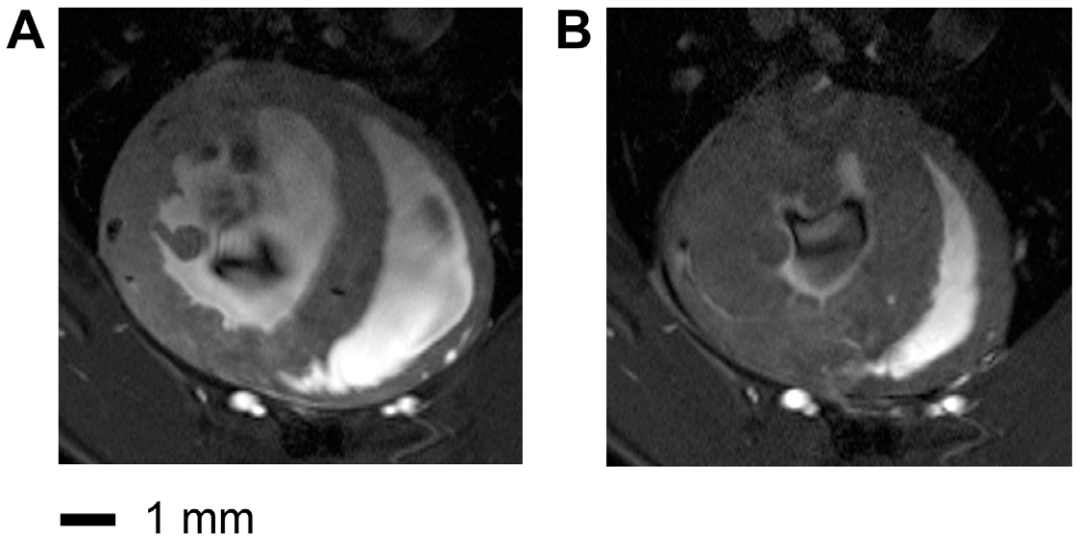

Figure 6. End-diastole (a) and end-systole (b) short axis views acquired using the CryoProbe together with a ultra-high spatial resolution of (43×138×300) µm^3. Endo- and epicardial border delineation as well as the depiction of anatomic details of the papillary muscles and trabeculae are improved versus the high resolution CryoProbe images (Figure 3 e,f) due to the enhanced spatial resolution used in the ultra-high spatial resolution protocol.
doi:10.1371/journal.pone.0042383.g006

enhanced image quality evident in the high resolution CP images was underpinned objectively by the results of the quantitative assessment of cardiac function and morphology. These encouraging results further support our subjective impression of excellent image quality in the high-resolution CryoProbe images and suggest that CMR-based assessment of cardiac function and morphology in mice for both left and right ventricle could benefit from the use of a cryogencally cooled RF coil.Furthermore, the high SNR of the CryoProbe allowed for pushing the limits of spatial resolution for *in-vivo* CMR of mice using a horizontal bore MR system even further to $43\times138\times300$ μm, resulting in superb delineation of endo- and epicardial borders, papillary muscles and trabeculae. Images of this quality for some selected slices of particular interest could complement whole heart coverage by means of the high resolution protocol. This work demonstrates the SNR benefits of the CryoProbe approach in healthy mice. This mandatory precursor was essential before extra variances due to gender and/or pathophysiological conditions are introduced. It is to be expected that the SNR gain shown here will not be altered significantly when moving towards pathological conditions. Realizing this opportunity we anticipate to put the proposed high spatial resolution CryoProbe approach to use for rapid characterization and phenotyping of mouse models of cardiovascular diseases.

In conclusion, cardiac morphology, cardiac chamber quantification and cardiac function assessement using a cryogenically cooled RF probe is feasible and affords SNR gains in the range of 3.0 to 5.0 compared to a conventional room temperature cardiac RF coil set-up. This SNR gain could potentially be invested in shortening the acquisition time. Yet, more relevant to CMR, the increased SNR enables a higher spatial resolution. This appears to facilitate a more accurate quantitative analysis, due to reduced intraobserver variability. In summary, the use of a cryogenically cooled RF probe represents a valuable means of enhancing the image quality in CMR of mice. This improvement holds the promise to be beneficial for cardiac MR research explorations into a variety of mouse models of cardiovascular diseases including the characterization of progression and regression of hypertension induced myocardial hypertrophy and identification of sex specific effects of cardiac damage and cardiac (dys) function.

Supporting Information

Figure S1 Short axis view CINE data set of 20 cardiac phases of the mouse heart acquired at 9.4 T using the CryoProbe together with the high spatial resolution protocol. End-diastolic (frame 1) and end-systolic (frame 11) cardiac phases are marked by a red and blue outline respectively. (TIF)

Author Contributions

Conceived and designed the experiments: BW AP MD TN HW JSM. Performed the experiments: BW MD AP. Analyzed the data: BW MD AE AP. Contributed reagents/materials/analysis tools: MD HW TN SW. Wrote the paper: AP MD BW SW TN HW.

References

1. Bovens SM, te Boekhorst BC, den Ouden K, van de Kolk KW, Nauerth A, et al. (2011) Evaluation of infarcted murine heart function: comparison of prospectively triggered with self-gated MRI. NMR Biomed 24: 307–315.
2. Epstein FH (2007) MR in mouse models of cardiac disease. NMR Biomed 20: 238–255.
3. Heijman E, Aben JP, Penners C, Niessen P, Guillaume R, et al. (2008) Evaluation of manual and automatic segmentation of the mouse heart from CINE MR images. J Magn Reson Imaging 27: 86–93.
4. Heijman E, de Graaf W, Niessen P, Nauerth A, van Eys G, et al. (2007) Comparison between prospective and retrospective triggering for mouse cardiac MRI. NMR Biomed 20: 439–447.
5. Hiba B, Richard N, Thibault H, Janier M (2007) Cardiac and respiratory self-gated cine MRI in the mouse: comparison between radial and rectilinear techniques at 7T. Magn Reson Med 58: 745–753.
6. Ratering D, Baltes C, Dorries C, Rudin M (2010) Accelerated cardiovascular magnetic resonance of the mouse heart using self-gated parallel imaging strategies does not compromise accuracy of structural and functional measures. J Cardiovasc Magn Reson 12: 43.
7. Schneider JE (2011) Assessment of global cardiac function. Methods Mol Biol 771: 387–405.
8. Schneider JE, Lanz T, Barnes H, Stork LA, Bohl S, et al. (2011) Accelerated cardiac magnetic resonance imaging in the mouse using an eight-channel array at 9.4 Tesla. Magn Reson Med 65: 60–70.
9. Sosnovik DE, Dai G, Nahrendorf M, Rosen BR, Seethamraju R (2007) Cardiac MRI in mice at 9.4 Tesla with a transmit-receive surface coil and a cardiac-tailored intensity-correction algorithm. J Magn Reson Imaging 26: 279–287.
10. Young AA, Barnes H, Davison D, Neubauer S, Schneider JE (2009) Fast left ventricular mass and volume assessment in mice with three-dimensional guide-point modeling. J Magn Reson Imaging 30: 514–520.
11. Wiesmann F, Frydrychowicz A, Rautenberg J, Illinger R, Rommel E, et al. (2002) Analysis of right ventricular function in healthy mice and a murine model of heart failure by in vivo MRI. Am J Physiol Heart Circ Physiol 283: H1065–1071.
12. Azaouagh A, Churzidse S, Konorza T, Erbel R (2011) Arrhythmogenic right ventricular cardiomyopathy/dysplasia: a review and update. Clin Res Cardiol 100: 383–394.
13. Urashima T, Zhao M, Wagner R, Fajardo G, Farahani S, et al. (2008) Molecular and physiological characterization of RV remodeling in a murine model of pulmonary stenosis. Am J Physiol Heart Circ Physiol 295: H1351-H1368.
14. Kirchhof P, Fabritz L, Zwiener M, Witt H, Schafers M, et al. (2006) Age- and training-dependent development of arrhythmogenic right ventricular cardiomyopathy in heterozygous plakoglobin-deficient mice. Circulation 114: 1799–1806.
15. Baltes C, Bosshard S, Mueggler T, Ratering D, Rudin M (2010) Increased blood oxygen level-dependent (BOLD) sensitivity in the mouse somatosensory cortex during electrical forepaw stimulation using a cryogenic radiofrequency probe. NMR Biomed.
16. Baltes C, Radzwill N, Bosshard S, Marek D, Rudin M (2009) Micro MRI of the mouse brain using a novel 400 MHz cryogenic quadrature RF probe. NMR Biomed 22: 834–842.
17. Ratering D, Baltes C, Nordmeyer-Massner J, Marek D, Rudin M (2008) Performance of a 200-MHz cryogenic RF probe designed for MRI and MRS of the murine brain. Magn Reson Med 59: 1440–1447.
18. Waiczies H, Millward JM, Lepore S, Infante-Duarte C, Pohlmann A, et al. (2012) Identification of Cellular Infiltrates during Early Stages of Brain Inflammation with Magnetic Resonance Microscopy. PLoS One 7: e32796.
19. Akoka S, Franconi F, Seguin F, Le Pape A (1993) Radiofrequency map of an NMR coil by imaging. Magn Reson Imaging 11: 437–441.
20. Insko EK, Bolinger L (1993) Mapping of the Radiofrequency Field. Journal of Magnetic Resonance, Series A 103: 82–85.
21. Cerqueira MD, Weissman NJ, Dilsizian V, Jacobs AK, Kaul S, et al. (2002) Standardized myocardial segmentation and nomenclature for tomographic imaging of the heart: a statement for healthcare professionals from the Cardiac Imaging Committee of the Council on Clinical Cardiology of the American Heart Association. Circulation 105: 539–542.
22. Ramirez MS, Esparza-Coss E, Bankson JA (2010) Multiple-mouse MRI with multiple arrays of receive coils. Magn Reson Med 63: 803–810.

Progress and promises of human cardiac magnetic resonance at ultrahigh fields: A physics perspective

http://dx.doi.org/10.1016/j.jmr.2012.11.015

Journal of Cardiovascular Magnetic Resonance

RESEARCH Open Access

Assessment of the right ventricle with cardiovascular magnetic resonance at 7 Tesla

Florian von Knobelsdorff-Brenkenhoff[1,2†], Valeriy Tkachenko[1,2], Lukas Winter[1], Jan Rieger[1], Christof Thalhammer[1], Fabian Hezel[1], Andreas Graessl[1], Matthias A Dieringer[1,2], Thoralf Niendorf[1,3] and Jeanette Schulz-Menger[1,2*]

Abstract

Background: Functional and morphologic assessment of the right ventricle (RV) is of clinical importance. Cardiovascular magnetic resonance (CMR) at 1.5T has become gold standard for RV chamber quantification and assessment of even small wall motion abnormalities, but tissue analysis is still hampered by limited spatial resolution. CMR at 7T promises increased resolution, but is technically challenging. We examined the feasibility of cine imaging at 7T to assess the RV.

Methods: Nine healthy volunteers underwent CMR at 7T using a 16-element TX/RX coil and acoustic cardiac gating. 1.5T served as gold standard. At 1.5T, steady-state free-precession (SSFP) cine imaging with voxel size (1.2x1.2x6) mm^3 was used; at 7T, fast gradient echo (FGRE) with voxel size (1.2x1.2x6) mm^3 and (1.3x1.3x4) mm^3 were applied. RV dimensions (RVEDV, RVESV), RV mass (RVM) and RV function (RVEF) were quantified in transverse slices. Overall image quality, image contrast and image homogeneity were assessed in transverse and sagittal views.

Results: All scans provided diagnostic image quality. Overall image quality and image contrast of transverse RV views were rated equally for SSFP at 1.5T and FGRE at 7T with voxel size (1.3x1.3x4)mm^3. FGRE at 7T provided significantly lower image homogeneity compared to SSFP at 1.5T. RVEDV, RVESV, RVEF and RVM did not differ significantly and agreed close between SSFP at 1.5T and FGRE at 7T (p=0.5850; p=0.5462; p=0.2789; p=0.0743). FGRE at 7T with voxel size (1.3x1.3x4) mm^3 tended to overestimate RV volumes compared to SSFP at 1.5T (mean difference of RVEDV 8.2±9.3ml) and to FGRE at 7T with voxel size (1.2x1.2x6) mm^3 (mean difference of RVEDV 9.3±8.6ml).

Conclusions: FGRE cine imaging of the RV at 7T was feasible and provided good image quality. RV dimensions and function were comparable to SSFP at 1.5T as gold standard.

Keywords: Magnetic resonance imaging, Right ventricle, Ultrahigh field, Cardiac

Background

Function, size and morphology of the right cardiac ventricle (RV) are known to be strong influencing factors on morbidity and mortality in various cardiac diseases, for instance congenital heart disease, pulmonary hypertension, myocardial infarction or arrythmogenic right ventricular cardiomyopathy (ARVC) [1-4]. However, their evaluation by using non-invasive imaging techniques is often a challenge, mainly attributable to the asymmetric and highly variable shape of the RV, the predominantly longitudinal systolic shortening, the small myocardial wall thickness and the location behind the sternum. Cardiovascular magnetic resonance (CMR), mainly using steady-state free-precession (SSFP) cine imaging at a field strength of 1.5Tesla (T), has evolved as the gold standard for the assessment of RV dimensions and function due to its ability to image in any plane, its excellent blood-tissue contrast, its capability to depict even small wall motion abnormalities and its proven reproducibility [4-7]. Nevertheless, expectations to characterize the myocardial tissue of the RV comparable to the LV including the differentiation of fibrosis, fat or edema, remained widely unaccomplished yet. As an example, the current task force criteria to assess ARVC include CMR to assess RV

* Correspondence: jeanette.schulz-menger@charite.de
†Equal contributors
[1]Berlin Ultrahigh Field Facility (B.U.F.F.), Max-Delbrueck Center for Molecular Medicine, Berlin, Germany
[2]Working Group on Cardiovascular Magnetic Resonance, Experimental and Clinical Research Center, a joint cooperation between the Charité Medical Faculty and the Max-Delbrueck Center for Molecular Medicine, HELIOS Klinikum Berlin Buch, Department of Cardiology and Nephrology, Berlin, Germany
Full list of author information is available at the end of the article

size and function, but emphasize that the evidence of fibro-fatty replacement within the RV wall is only obtained by endomyocardial biopsy [4]. Even the accuracy of CMR to quantify RV mass, which is known to be an important predictor of cardiovascular events, is uncertain due to the challenge of resolving the thin (2-5mm) RV free wall properly using protocols (typical voxel size of cine imaging 1.8x1.8x6mm^3) common in today's clinical [8-10]. To extend the information that is extractable from CMR, technological improvements that increase the spatial and temporal resolution as well as signal-to-noise ratio (SNR) are therefore desired. As field strength positively correlates with SNR, CMR at ultrahigh fields (7T) offers the potential to depict even microscopic structures and to facilitate targeted tissue characterization [11,12]. However, imaging at 7T comes with technical challenges, like increased B_0 heterogeneities, non-uniform B_1 distribution and increased radio frequency (RF) power deposition. Recently, the technical feasibility of cardiac cine imaging at 7T using fast gradient echo (FGRE) techniques has been demonstrated, and data demonstrating the ability for accurate LV chamber quantification at 7T were reported [13-16]. Moreover, dedicated transmit and receive coils as well as cardiac trigger techniques have been developed to meet the demands of CMR at 7T [17-21].

Aim of the present study was to extend the application of cine imaging at 7T to the assessment of RV size and function and to compare the results with the gold standard at 1.5T. This work is regarded as the first step toward a comprehensive assessment of RV function, size and morphology using CMR at 7T.

Methods

Subjects

Nine healthy volunteers (6 males; mean age 29±5 years, range 24–38 years; mean body mass index 22±2 kg/m^2, range 18-24kg/m^2) underwent CMR at 1.5T and at 7T. The status "healthy" was based on: i) uneventful medical history, ii) absence of any symptoms indicating cardiovascular dysfunction, iii) normal ECG, iv) normal cardiac dimensions and function on the CMR cine images of this study. The local ethics committee approved the study, and all subjects gave written informed consent to participate in the study.

MR and RF coil technology at 7T

A 7T whole body MR system (Siemens Healthcare, Erlangen, Germany) equipped with an Avanto (Siemens Healthcare, Erlangen, Germany) gradient system (slew rate: 200 T/m/s, max. gradient strength: 40mT/m) and an 8kW RF amplifier (Stolberg HF-Technik AG, Stolberg-Vicht, Germany) was used. A 16 channel transceiver coil array tailored for cardiac MR at 7.0 T [19,20] that uses loop elements and consists of two sections was applied: A planar posterior section located below the patient's chest and a modestly curved anterior section positioned on top of the patient's chest. Each section contains an identical arrangement of 8 TX/RX elements, connected to the MR system via a coil interface comprising 16 TX/RX switches and low-noise preamplifiers (Stark Contrasts, Erlangen, Germany). To drive each channel of the coil the output of the RF amplifier was split into 16 equal-intensity signals using a home-built 16x16 Butler matrix. The transmit phases of the individual coil elements were adjusted by using the 1st order circular polarized (cp) mode of the Butler matrix with an increment of 22.5 degrees between subsequent output channels in conjunction with −78° phase shifting coaxial cables for all posterior coil elements [20].

MR and RF coil technology at 1.5T

At 1.5T a Magnetom Avanto (Siemens Healthcare, Erlangen, Germany) system equipped with the same gradient coil used at 7.0 T was used. A TX body coil was used for transmission and a 12-channel RX body array coil was used for reception.

Cardiac gating

Since electrocardiography is corrupted by interference with electromagnetic fields and by magneto-hydrodynamic effects at 7T, acoustic cardiac triggering (ACT) was applied (EasyACT, MRI.TOOLS GmbH, Berlin, Germany). ACT registers the first heart tone of the phonocardiogram to synchronize data acquisition with cardiac motion [21]. ACT was used for retrospective gating at 7T and at 1.5T to ensure consistency throughout the study.

Slice positioning

One technician with profound experience performed all scans at 1.5T and 7.0T to ensure reproducibility and consistency. After acquisition of scout images, standard four- and two-chamber views as well as a long axis view of the RV were acquired. Next, a stack of transverse slices covering the entire RV was obtained twice using two voxel dimensions. These images served for RV volumetry and evaluation of image quality. Furthermore, a stack of sagittal slices covering the entire RV was acquired. These images only served for evaluation of image quality.

Imaging parameters

At 7T, cine images were acquired using 2D FGRE. Each slice was acquired in an end-expiratory breath-hold. Imaging parameters were: echo time TE=2.7ms, repetition time TR=5.6ms, nominal flip angle FA=32°, transmit reference voltage U_{ref} 400 V, peak voltage of sinc-pulse

(t=800 μs) U_{peak} 190V, voxel size (1.2x1.2x6)mm^3, no interslice gap, bandwidth 444Hz/pixel, 30 phases per heart cycle, parallel imaging (R=2, 32 calibration lines) in conjunction with GRAPPA reconstruction. For the transverse stack a second scan was performed using the same imaging parameters with the exception of the spatial resolution, which was adjusted to a voxel size of (1.3x1.3x4)mm^3. Prior to RV function assessment volume selective second order B_0-shimming was performed.

At 1.5T, a clinically established SSFP cine protocol was used. Imaging parameters were: TE=1.3ms, TR=3.0ms, FA=70°, voxel size (1.2x1.2x6)mm^3, no interslice gap, bandwidth 790Hz/pixel, 30 phases per heart cycle, parallel imaging (R=2, 32 calibration lines) in conjunction with GRAPPA reconstruction.

Image interpretation

The CMR images were read in consensus by two physicians (FvKB, VT) with very profound experience in CMR both at 7T and 1.5T [14,19,7]. The software CMR42® (Circle Cardiovascular Imaging, Calgary, Canada) was used. *Quantitatively*, RV end-diastolic volume (RVEDV), RV end-systolic volume (RVESV), RV ejection fraction (RVEF) and RV mass (RVM) were obtained by manually contouring endocardial borders in end-diastole and end-systole as well as epicardial borders in end-diastole. *Qualitatively*, each cine slice was scored in diastole and systole regarding overall image quality, homogeneity and contrast. The decision was based on anatomic border sharpness, visualization of subtle anatomic features and presence of artifacts. i) Overall image quality: 0=poor, non-diagnostic; 1=impaired image quality that may lead to misdiagnosis; 2=good; and 3=excellent. ii) Homogeneity: 0=inhomogeneous image or artifacts that may impair diagnostic quality; 1=homogeneous image, no artifact present. iii) Image contrast: 0=low or poor contrast between anatomical structures and blood pool; 1=sufficient contrast between anatomical structures and blood pool.

Statistical analysis

Continuous values (RVEDV, RVESV, RVEF, RVM) are displayed as median and range. Kruskal-Wallis tests were performed to evaluate differences between CMR settings (1.5T vs. 7T with voxel size (1.2x1.2x6)mm^3 vs. 7T with voxel size (1.3x1.3x4)mm^3). Bland-Altman analyses were performed to assess the pairwise agreement. For categorical data (image quality, contrast, homogeneity), relative frequencies are shown. Multinomial or logistic regression was used to evaluate differences between the different CMR settings. The regression analyses were based on generalized estimation equations with independence as working correlation matrix to account for multiple measurements per patient. A p-value of less than 0.05 was regarded as statistically significant. Calculations were done with SAS 9.2 (SAS Institute Inc., Cary, NC, USA).

Results

Evaluation of overall image quality, image contrast and homogeneity

Image quality was diagnostic in all CMR examinations at 1.5T and 7T, with no examination scored as "poor / non-diagnostic" (score 0). Figure 1 exemplarily depicts a four-chamber view, a RV long axis view and a mid-ventricular transverse slice of the RV obtained with FGRE at 7T together with SSFP images derived from 1.5T. Figure 2 provides an overview of the four-chamber views of all subjects derived from 7T. Additional movie files show cines of the RV long axis and the transverse slice acquired at 7T in one subject, and a composition of the four-chamber views of all study participants obtained at 7T (see Additional files 1, 2 and 3).

The results of the evaluation of overall image quality, image contrast and homogeneity are summarized in Figure 3:

Regarding *overall image quality*, SSFP at 1.5T and FGRE at 7T with voxel size (1.3x1.3x4)mm^3 provided a significantly higher proportion of "excellent image quality" (66.4% and 43.8%) compared to FGRE at 7T with voxel size (1.2x1.2x6)mm^3 (22.7%) in the transverse slice orientation in diastole ($p<0.0001$ and $p=0.0478$). For the sagittal slice orientation, SSFP cine images at 1.5T provided a significantly higher proportion of "excellent image quality" (75% in diastole and 87% in systole) compared to FGRE at 7T with voxel size (1.3x1.3x4)mm^3 (37% in diastole and 22% in systole) (each $p<0.0001$).

Regarding *image homogeneity*, SSFP at 1.5T provided significantly higher proportions of "homogeneous images" compared to the 7T acquisitions, both in transverse orientation in diastole ($p=0.0329$) and in systole ($p=0.0197$), and in sagittal orientation in diastole ($p=0.0002$) and systole ($p<0.0001$). The 7T groups did not differ significantly from each other.

Regarding *image contrast*, the various modalities were not found to differ significantly in transverse image orientation (diastole: $p=0.7290$; systole: $p=0.3170$), as well as in sagittal image orientation in diastole ($p=0.1182$). Only for systole in sagittal orientation, SSFP at 1.5T provided a higher proportion of images rated as "sufficient contrast" compared to FGRE at 7T with voxel size (1.3x1.3x4)mm^3 ($p=0.0463$).

RV chamber quantification

Median quantitative RV results are depicted in Table 1. No significant difference was found regarding RVEDV ($p=0.5850$), RVESV ($p=0.5462$), RVEF ($p=0.2789$) and

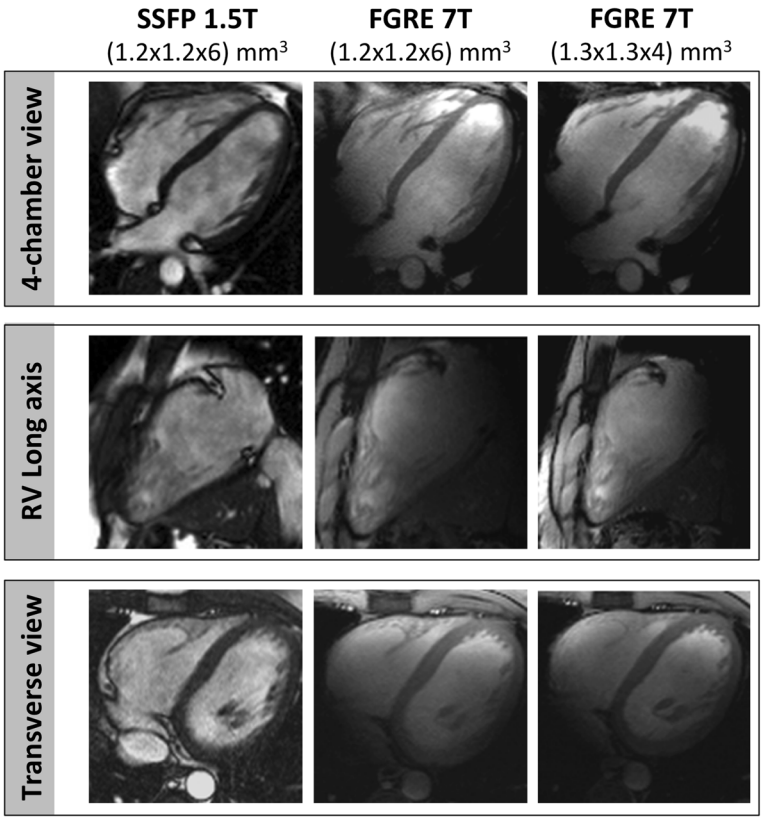

Figure 1 Cine imaging of the RV. Four-chamber view, RV long axis view and mid-ventricular transverse view obtained by SSFP at 1.5T with voxel size (1.2x1.2x6)mm^3*(left)*, by FGRE at 7T with voxel size (1.2x1.2x6)mm^3*(middle)* and by FGRE at 7T with voxel size (1.3x1.3x4)mm^3*(right)*.

RVM (p=0.0743) between SSFP at 1.5T and FGRE at 7T. Bland-Altman plots illustrating the agreement between the various approaches regarding REDV, RVESV, RVEF and RVM are shown in Figure 4. There was a tendency towards larger volumes with FGRE at 7T with voxel size (1.3x1.3x4)mm^3 both compared to SSFP at 1.5T (mean difference: RVEDV −8.2±9.3ml, RVESV −4.3±5.1ml) and FGRE at 7T with voxel size (1.2x1.2x6)mm^3 (mean difference: RVEDV −9.3±8.6ml, RVESV −6.0±4.5ml).

Discussion

The present results demonstrated that FGRE cine imaging of the RV at 7T using a dedicated 16-channel transceiver RF coil and acoustic cardiac gating provided good quality cine images of the RV to assess its size and function. The findings confirm preliminary experiences with the LV at 7T [14] and underline that cine imaging at 7T is feasible.

We know from studies of the LV with FGRE cine imaging at 1.5T and 7T that the step from 1.5T towards 7T improved the image quality of FGRE cine images, in particular in long axis acquisitions parallel to the blood flow [14]. The blood/myocardium contrast is known to be reduced with low blood flow, attributable to the inflow-dependent blood pool signal intensity in FGRE sequences [22]. The ultrahigh field strength has the potential to minimize this source of error due to different field strength dependent T_1 prolongation of blood and myocardium. Translated to the RV, this observation gains importance due to sometimes low blood flow between the RV trabeculae. In the present study of the RV, images in transverse orientation acquired with SSFP at 1.5T received the highest mean image score compared to the acquisitions at 7T. Notwithstanding, it is notable that our statistical analysis revealed that both field strengths did not differ significantly in overall image quality in systole in general, as well as in diastole if the enhanced spatial resolution (voxel size (1.3x1.3x4)mm^3) is regarded. This observation underlines the feasibility to obtain high-quality cine images of standard planes at 7T and forms the basement for accurate RV chamber quantification, which is predominantly done in transverse slices [6]. In contrast, the sagittal orientated slices exhibited significant differences in image quality between SSFP at 1.5T and FGRE at 7T, with SSFP at 1.5T being more often “excellent”. The observation that the image quality at 7T varied dependent on slice orientation can be attributed to the complex B_1 field pattern

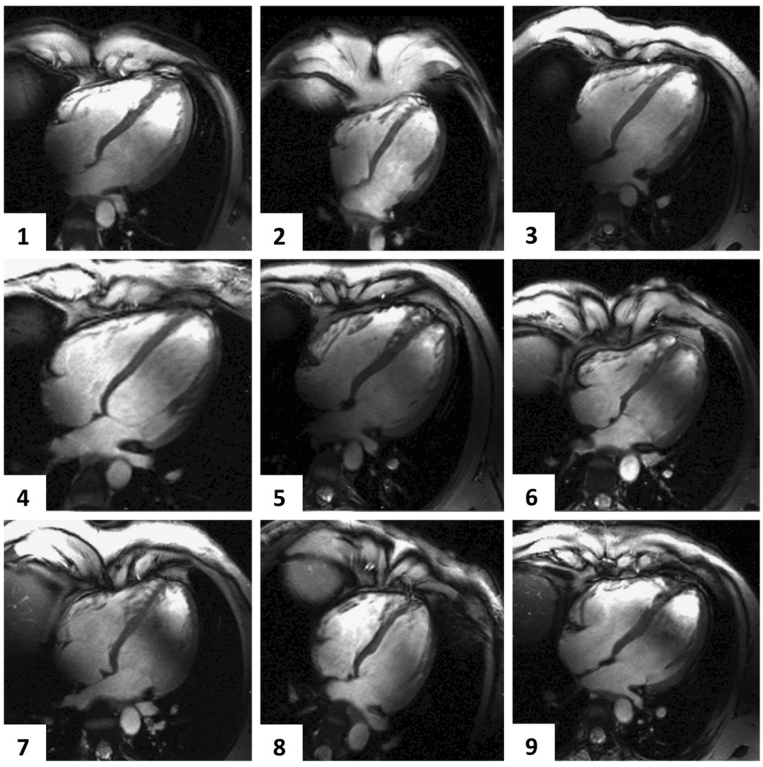

Figure 2 Cine imaging of the RV. Four-chamber views of all subjects obtained with 2D cine FGRE at 7T using a voxel size of (1.3x1.3x4) mm^3.

with various constructive and destructive interferences throughout the FOV. Depending on the volunteer and slice orientation, a specific field pattern is revealed. From a clinical perspective, sagittal views are currently mainly used to assess RV wall motion and morphology complementary to transverse slices. This comprehensive assessment is important for example in the diagnosis of ARVC, where regional akinesia, dyskinesia or asynchrony are relevant indicators [4]. Therefore, further technical improvements are necessary to enable patient and slice dependent transmit field shaping to provide stable image quality throughout a CMR examination at 7T.

It is a recognized limitation of this study that no SNR and blood/myocardium contrast-to-noise ratio (CNR) values are reported. A previous pilot study on cardiac chamber quantification at 1.5 T and 7.0 T showed that 2D cine FGRE imaging at 7.0 T provided SNR and blood/myocardium CNR that are superior to FGRE acquisitions at 1.5T using the same slice thickness [14]. Careful SNR and CNR validation demonstrated that SNR and CNR derived from 2D cine FGRE at 7T was found to be competitive with that derived from SSFP acquisitions at 1.5 T using standard clinical routine imaging parameter [14].

Regarding image contrast as assessed by visual evaluation, the present results underline that the combination of FGRE with ultrahigh field reaches a grade of contrast that is comparable to SSFP at 1.5T, similar to the results reported for the LV [14]. For the RV, this was true both for transverse and sagittal slice orientation and independent from the voxel size. Opposed to that, the acquisition of homogeneous images is still a challenge in ultrahigh field CMR. Both in sagittal and transverse direction, the results at 7T were inferior compared to 1.5T and a high proportion of 7T images were evident with poor homogeneity for both voxel sizes. Further improvements in subject specific and slice specific B_0- and B_1-shimming are therefore essential to fully exploit the potential of 7T [23,24].

Regarding the quantification of cardiac size and function, it has been shown for 1.5T and 3T that RV volumes are overestimated and mass underestimated when using SSFP instead of FGRE [22,10] - even though the absolute difference is relatively small with a mean RVEDV difference of about 4ml [22]. This difference is explained by the stronger contrast between myocardium and blood on the one side, and between myocardium and epicardial fat on the other side obtained with SSFP. This leads to an outward shift of the endocardial contour and an inward shift of the epicardial contour compared to FGRE. Furthermore, areas with slow flow, as within the apex, are often mistaken for myocardium when using FGRE. It is notable from the present results that the difference in RV quantification between SSFP and FGRE no longer

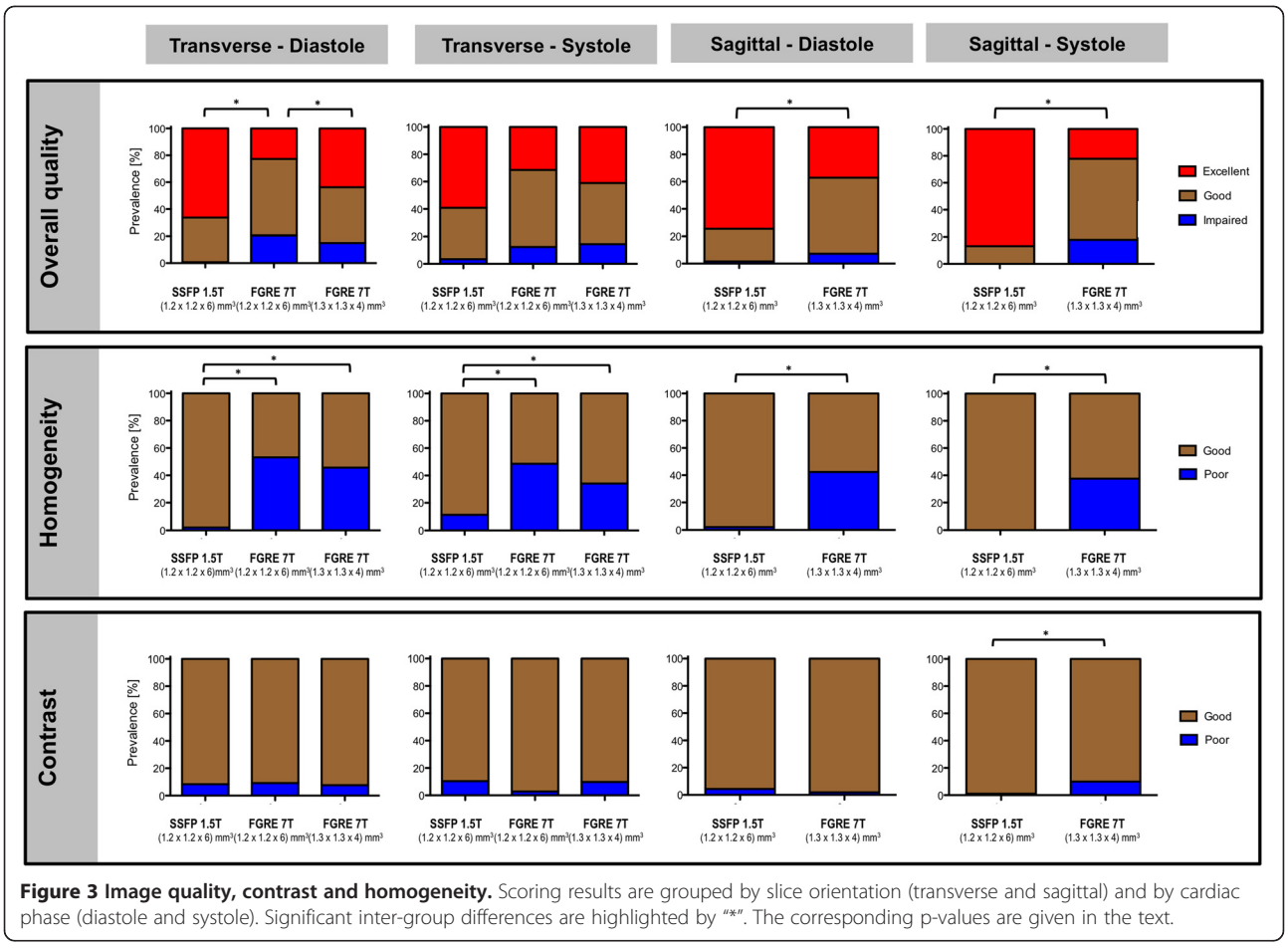

Figure 3 Image quality, contrast and homogeneity. Scoring results are grouped by slice orientation (transverse and sagittal) and by cardiac phase (diastole and systole). Significant inter-group differences are highlighted by "*". The corresponding p-values are given in the text.

Table 1 RV chamber quantification

	1.5T SSFP 1.2x1.2x6mm^3	7T FGRE 1.2x1.2x6mm^3	7T FGRE 1.3x1.3x4mm^3	p-value
RVEDV [ml]				0.5850
Median	146.2	138.6	152.1	
Min. - Max.	127.4 - 202.3	124-0 - 207.7	121.4 - 222.8	
RVESV [ml]				0.5462
Median	65.2	62.4	69.3	
Min. - Max.	57.4 - 91.1	53.7 - 93.5	54.6 - 103.6	
RVEF [%]				0.2789
Median	55.0	56.7	55	
Min. - Max.	54 - 57	54 - 58	54 - 58	
RVM [g]				0.0743
Median	35	36	33	
Min. - Max.	26 - 49	24 - 53	26 - 51	

Legend: RV end-diastolic volume (RVEDV), RV end-systolic volume (RVESV), RV ejection fraction (RVEF) and RV mass (RVM) are presented as median, min and max for each modality (1.5T SSFP, 7T FGRE with two voxel sizes). The p-values refer to the Kruskal-Wallis test including all three modalities. There was no significant difference regarding RVEDV, RVESV, RVEF and RVM.

existed when moving from 1.5T to 7T. This tendency matches the experiences we made for the LV at 7T [14]. The bias between the results obtained for FGRE imaging at 7T with voxel size (1.2x1.2x6)mm^{3}and SSFP at 1.5T (RVEDV 1.2±5.9ml, RVESV 1.7±2.5ml) was within the range of the inter-observer variability reported for SSFP examinations of the RV [22]. Hence, close agreement can be postulated. This finding underlines the accurate endocardial border delineation achievable by FGRE at 7T. Another interesting aspect of the present results was that FGRE at 7T by tendency provided larger volumes than SSFP 1.5T when we decreased the voxel size from (1.2x1.2x6)mm^3 to (1.3x1.3x4)mm^3. We explain this trend mainly by the observation that the higher spatial resolution led to a more detailed differentiation of the RV free wall that caused an outward shift of the manually contoured endocardial borders (Figure 5). This finding on the one hand has to be kept in mind when trying to translate normal values from 1.5T to 7T. On the other hand, it underscores the potential of CMR at 7T

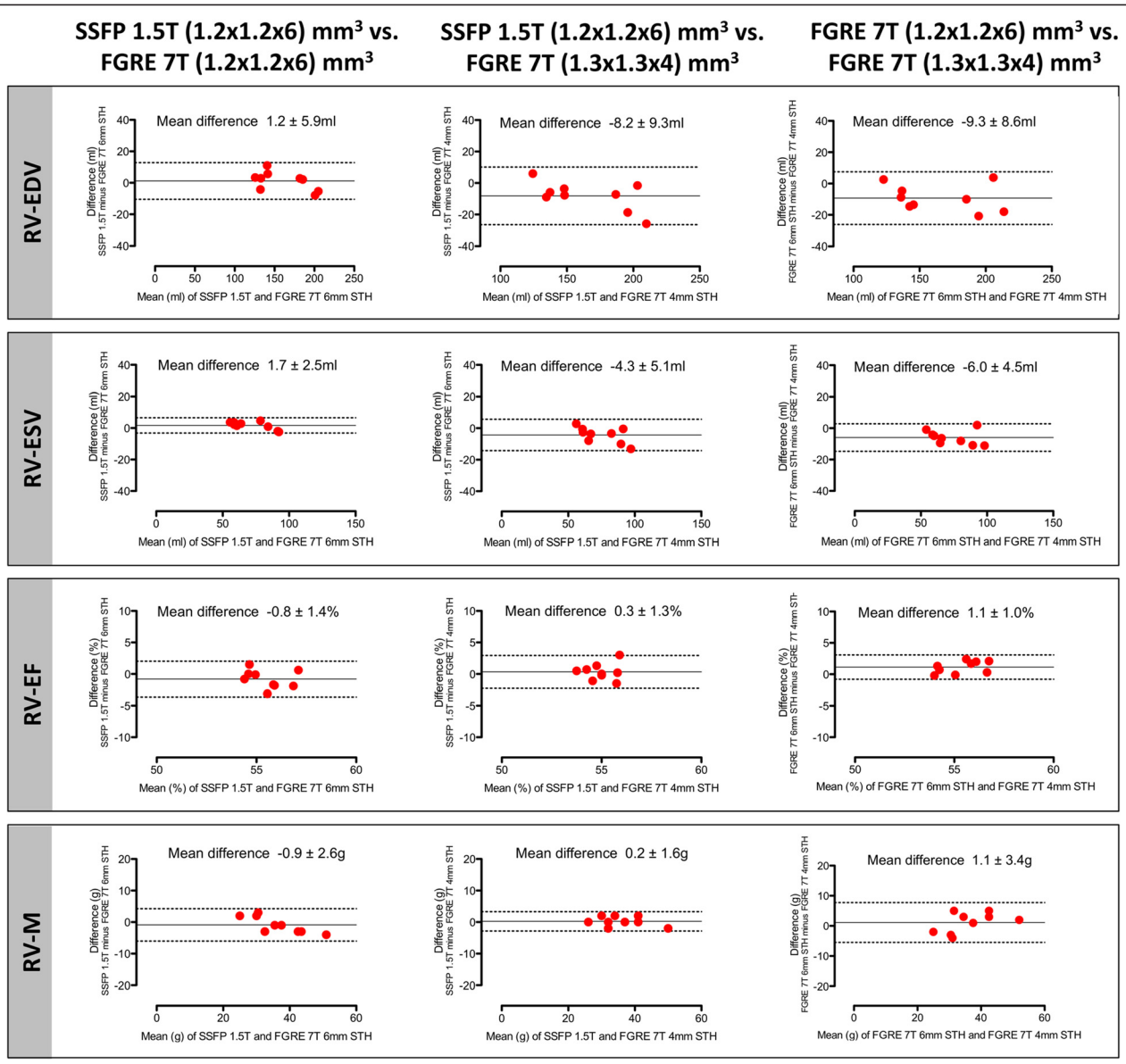

Figure 4 RV chamber quantification. Bland-Altman plots illustrating the agreement between RV volumes, ejection fraction and mass obtained by SSFP at 1.5T as the current gold standard and those derived from FGRE cine acquisitions with different spatial resolutions. [RV-EDV = right ventricular end-diastolic volume; RVESV = right ventricular end-systolic volume; RVEF = right ventricular ejection fraction; RVM = right ventricular mass].

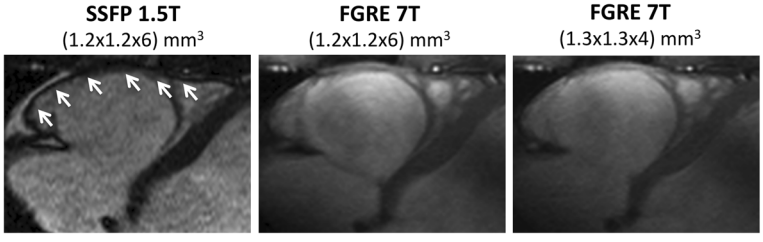

Figure 5 Blood-myocardium contrast of the RV free wall. Focused view on the RV free wall demonstrating that the border between blood and myocardium appears less dark and less sharp at 7T compared to 1.5T, which is further enhanced with decreasing voxel size. This potentially explains the tendency towards larger volume measurements at 7T with voxel size (1.3x1.3x4)mm^3 compared to 1.5T.

to have a more detailed look at the RV free wall. As it can be anticipated from Figure 3, some inter-subject variability of trabecular structure and compact layer thickness may exist. For instance, the measurement of the compact layer of the free RV wall as well of the remaining trabecular layer may provide new insights into the microstructure of the RV myocardium. Furthermore, the accurate quantification of RV mass based on properly spatially resolved cine images would strengthen its role as a cardiovascular risk marker. After this first evidence of the feasibility of RV cine imaging at 7T, such interesting aspects need further investigation in future studies with sample sizes large enough to provide adequate power.

Conclusions

In conclusion, the present study demonstrated that cine imaging of the RV is feasible at 7T using FGRE techniques. The achieved image quality was comparable to SSFP at 1.5T and allowed accurate myocardial border delineation for RV chamber quantification, which provided RV volumes, mass and function with close agreement to SSFP at 1.5T. This work is regarded as fundament and stimulator for further efforts to explore whether enhanced spatial resolution together with ultrahigh field strength can provide more detailed insights into the structure of the RV.

Additional files

Additional file 1: Long axis view of the right ventricle obtained by FGRE cine imaging at 7T with voxel size (1.3x1.3x4)mm^3 underlining the excellent blood/myocardium contrast even in the right ventricular apex.

Additional file 2: Transverse view of the right ventricle obtained by FGRE cine 7T with voxel size (1.3x1.3x4)mm^3 underlining the excellent resolution of the RV trabeculae.

Additional file 3: Cinematic four-chamber views of all subjects obtained with 2D cine FGRE at 7T using a voxel size of (1.3x1.3x4) mm^3.

Competing interests

The authors declare that they have no competing interests with the exception of Thoralf Niendorf and Jan Rieger, who are founder of MRI.TOOLS GmbH (Berlin, Germany).

Authors' contributions

FvKB and VT contributed to the study design, image acquisition, image interpretation, data storage, statistical data analysis and data interpretation and drafted the first version of the manuscript; LW and CT contributed to the image acquisition (in particular regarding coils) and data interpretation; JR contributed to the image acquisition (in particular regarding cardiac gating) and data interpretation; MD contributed to the image acquisition, image interpretation and data interpretation; TN and JSM contributed to the study design, image acquisition, image interpretation, data storage, statistical data analysis and data interpretation. All authors helped to draft the manuscript, and read and approved the final manuscript.

Acknowledgements

We thank the study nurses Antje Els and Elke Nickel-Szczech for coordinating and documenting the examinations, and Denise Kleindienst for assisting during CMR image acquisition. We thank Dr. Carsten Schwenke (scossis, Berlin, Germany) for supporting the statistical calculations.
FvKB and MD are supported by a research grant of the Else-Kröner Fresenius Stiftung (Bad Homburg, Germany). The study was supported by institutional grants of the Charité Medical Faculty Berlin and the Max-Delbrueck-Center for Molecular Medicine.

Author details

[1]Berlin Ultrahigh Field Facility (B.U.F.F.), Max-Delbrueck Center for Molecular Medicine, Berlin, Germany. [2]Working Group on Cardiovascular Magnetic Resonance, Experimental and Clinical Research Center, a joint cooperation between the Charité Medical Faculty and the Max-Delbrueck Center for Molecular Medicine, HELIOS Klinikum Berlin Buch, Department of Cardiology and Nephrology, Berlin, Germany. [3]Experimental and Clinical Research Center, a joint cooperation between the Charité Medical Faculty and the Max-Delbrueck Center for Molecular Medicine, Berlin, Germany.

Received: 17 October 2012 Accepted: 6 March 2013
Published: 14 March 2013

References

1. Hopkins WE. **Right ventricular performance in congenital heart disease: a physiologic and pathophysiologic perspective.** *Cardiol Clin.* 2012; **30:**205–18.
2. Galie N, Hoeper MM, Humbert M, Torbicki A, Vachiery JL, Barbera JA, Beghetti M, Corris P, Gaine S, Gibbs JS, Gomez-Sanchez MA, Jondeau G, Klepetko W, Opitz C, Peacock A, Rubin L, Zellweger M, Simonneau G. **Guidelines for the diagnosis and treatment of pulmonary hypertension: the Task Force for the Diagnosis and Treatment of Pulmonary Hypertension of the European Society of Cardiology (ESC) and the European Respiratory Society (ERS), endorsed by the International Society of Heart and Lung Transplantation (ISHLT).** *Eur Heart J.* 2009; **30:**2493–537.
3. Kumar A, Abdel-Aty H, Kriedemann I, Schulz-Menger J, Gross CM, Dietz R, Friedrich MG. **Contrast-enhanced cardiovascular magnetic resonance imaging of right ventricular infarction.** *J Am Coll Cardiol.* 2006; **48:**1969–76.
4. Marcus FI, McKenna WJ, Sherrill D, Basso C, Bauce B, Bluemke DA, Calkins H, Corrado D, Cox MG, Daubert JP, Fontaine G, Gear K, Hauer R, Nava A, Picard MH, Protonotarios N, Saffitz JE, Sanborn DM, Steinberg JS, Tandri H, Thiene G, Towbin JA, Tsatsopoulou A, Wichter T, Zareba W. **Diagnosis of arrhythmogenic right ventricular cardiomyopathy/dysplasia: proposed modification of the task force criteria.** *Circulation.* 2010; **121:**1533–41.
5. Kilner PJ, Geva T, Kaemmerer H, Trindade PT, Schwitter J, Webb GD. **Recommendations for cardiovascular magnetic resonance in adults with congenital heart disease from the respective working groups of the European Society of Cardiology.** *Eur Heart J.* 2010; **31:**794–805.
6. Alfakih K, Plein S, Bloomer T, Jones T, Ridgway J, Sivananthan M. **Comparison of right ventricular volume measurements between axial and short axis orientation using steady-state free precession magnetic resonance imaging.** *J Magn Rson Imaging.* 2003; **18:**25–32.
7. von Knobelsdorff-Brenkenhoff F, Bublak A, El-Mahmoud S, Wassmuth R, Opitz C, Schulz-Menger J. **Single-centre survey of the application of cardiovascular magnetic resonance in clinical routine.** *Eur Heart J Cardiovasc Imaging.* 2013; **14:**62–8.
8. Kawut SM, Barr RG, Lima JA, Praestgaard A, Johnson WC, Chahal H, Ogunyankin KO, Bristow MR, Kizer JR, Tandri H, Bluemke DA. **Right Ventricular Structure Is Associated With the Risk of Heart Failure and Cardiovascular Death: The Multi-Ethnic Study of Atherosclerosis (MESA)-Right Ventricle Study.** *Circulation.* 2012; **126:**1681–88.
9. Haddad F, Hunt SA, Rosenthal DN, Murphy DJ. **Right ventricular function in cardiovascular disease, part I: Anatomy, physiology, aging, and functional assessment of the right ventricle.** *Circulation.* 2008; **117:**1436–48.
10. Alfakih K, Plein S, Thiele H, Jones T, Ridgway JP, Sivananthan MU. **Normal human left and right ventricular dimensions for MRI as assessed by turbo gradient echo and steady-state free precession imaging sequences.** *J Magn Reson Imaging.* 2003; **17:**323–29.
11. Niendorf T, Sodickson DK, Krombach GA, Schulz-Menger J. **Toward cardiovascular MRI at 7 T: clinical needs, technical solutions and research promises.** *Eur Radiol.* 2010; **20:**2806–16.

12. Niendorf T, Graessl A, Thalhammer C, Dieringer MA, Kraus O, Santoro D, Fuchs K, Hezel F, Waiczies S, Ittermann B, Winter L. **Progress and promises of human cardiac magnetic resonance at ultrahigh fields: A physics perspective.** *J Magn Reson.* 2012. epub ahead of print.
13. Snyder CJ, DelaBarre L, Metzger GJ, van de Moortele PF, Akgun C, Ugurbil K, Vaughan JT. **Initial results of cardiac imaging at 7 Tesla.** *Magn Reson Med.* 2009; **61:**517–24.
14. von Knobelsdorff-Brenkenhoff F, Frauenrath T, Prothmann M, Dieringer MA, Hezel F, Renz W, Kretschel K, Niendorf T, Schulz-Menger J. **Cardiac chamber quantification using magnetic resonance imaging at 7 Tesla–a pilot study.** *Eur Radiol.* 2010; **20:**2844–52.
15. Brandts A, Westenberg JJ, Versluis MJ, Kroft LJ, Smith NB, Webb AG, de Roos A. **Quantitative assessment of left ventricular function in humans at 7 T.** *Magn Reson Med.* 2010; **64:**1471–77.
16. Suttie JJ, Delabarre L, Pitcher A, van de Moortele PF, Dass S, Snyder CJ, Francis JM, Metzger GJ, Weale P, Ugurbil K, Neubauer S, Robson M, Vaughan T. **7 Tesla (T) human cardiovascular magnetic resonance imaging using FLASH and SSFP to assess cardiac function: validation against 1.5 T and 3 T.** *NMR Biomed.* 2012; **25:**27–34.
17. Dieringer MA, Renz W, Lindel T, Seifert F, Frauenrath T, von Knobelsdorff-Brenkenhoff F, Waiczies H, Hoffmann W, Rieger J, Pfeiffer H, Ittermann B, Schulz-Menger J, Niendorf T. **Design and application of a four-channel transmit/receive surface coil for functional cardiac imaging at 7T.** *J Magn Reson Imaging.* 2011; **33:**736–41.
18. Grassl A, Winter L, Thalhammer C, Renz W, Kellman P, Martin C, von Knobelsdorff-Brenkenhoff F, Tkachenko V, Schulz-Menger J, Niendorf T. **Design, evaluation and application of an eight channel transmit/receive coil array for cardiac MRI at 7.0T.** *Eur J Radiol.* 2011. epub ahead of print.
19. Winter L, Kellman P, Renz W, Grassl A, Hezel F, Thalhammer C, von Knobelsdorff-Brenkenhoff F, Tkachenko V, Schulz-Menger J, Niendorf T. **Comparison of three multichannel transmit/receive radiofrequency coil configurations for anatomic and functional cardiac MRI at 7.0T: implications for clinical imaging.** *Eur Radiol.* 2012; **22:**2211–20.
20. Thalhammer C, Renz W, Winter L, Hezel F, Rieger J, Pfeiffer H, Graessl A, Seifert F, Hoffmann W, von Knobelsdorff-Brenkenhoff F, Tkachenko V, Schulz-Menger J, Kellman P, Niendorf T. **Two-Dimensional sixteen channel transmit/receive coil array for cardiac MRI at 7.0 T: Design, evaluation, and application.** *J Magn Reson Imaging.* 2012; **36:**847–57.
21. Frauenrath T, Hezel F, Renz W, D'Orth Tde G, Dieringer M, Von Knobelsdorff-Brenkenhoff F, Prothmann M, Menger JS, Niendorf T. **Acoustic cardiac triggering: a practical solution for synchronization and gating of cardiovascular magnetic resonance at 7 Tesla.** *J Cardiovasc Magn Reson.* 2010; **12:**67.
22. Grothues F, Boenigk H, Graessner J, Kanowski M, Klein HU. **Balanced steady-state free precession vs. segmented fast low-angle shot for the evaluation of ventricular volumes, mass, and function at 3 Tesla.** *J Magn Reson Imaging.* 2007; **26:**392–400.
23. Sengupta S, Welch EB, Zhao Y, Foxall D, Starewicz P, Anderson AW, Gore JC, Avison MJ. **Dynamic B0 shimming at 7 T.** *Magn Reson Imaging.* 2011; **29:**483–96.
24. Schar M, Vonken EJ, Stuber M. **Simultaneous B (0)- and B(1)+–map acquisition for fast localized shim, frequency, and RF power determination in the heart at 3 T.** *Magn Reson Med.* 2010; **63:**419–26.

doi:10.1186/1532-429X-15-23
Cite this article as: von Knobelsdorff-Brenkenhoff *et al.*: Assessment of the right ventricle with cardiovascular magnetic resonance at 7 Tesla. *Journal of Cardiovascular Magnetic Resonance* 2013 **15**:23.

Journal of Cardiovascular Magnetic Resonance

RESEARCH Open Access

Variability and homogeneity of cardiovascular magnetic resonance myocardial T2-mapping in volunteers compared to patients with edema

Ralf Wassmuth[1*], Marcel Prothmann[1], Wolfgang Utz[1], Matthias Dieringer[1], Florian von Knobelsdorff-Brenkenhoff[1], Andreas Greiser[2] and Jeanette Schulz-Menger[1]

Abstract

Background: The aim of the study was to test the reproducibility and variability of myocardial T2 mapping in relation to sequence type and spatial orientation in a large group of healthy volunteers. For control T2 mapping was also applied in patients with true edema. Cardiovascular magnetic resonance (CMR) T2-mapping has potential for the detection and quantification of myocardial edema. Clinical experience is limited so far. The variability and potential pitfalls in broad application are unknown.

Methods: Healthy volunteers (n = 73, 35 ± 13 years) and patients with edema (n = 28, 55 ± 17 years) underwent CMR at 1.5 T. Steady state free precession (SSFP) cine loops and T2-weighted spin echo images were obtained. In patients, additionally late gadolinium enhancement images were acquired. We obtained T2 maps in midventricular short axis (SAX) and four-chamber view (4CV) based on images with T2 preparation times of 0, 24, 55 ms and compared fast low angle shot (FLASH) and SSFP readout. 10 volunteers were scanned twice on separate days. Two observers analysed segmental and global T2 per slice.

Results: In volunteers global myocardial T2 systematically differed depending on image orientation and sequence (FLASH 52 ± 5 vs. SSFP 55 ± 5 ms in SAX and 57 ± 6 vs. 59 ± 6 ms in 4CV; $p < 0.0001$ for both). Anteroseptal and apical segments had higher T2 than inferior and basal segments (SAX: 59 ± 6 vs. 48 ± 5 ms for FLASH and 59 ± 7 vs. 52 ± 4 ms for SSFP; $p < 0.0001$ for both). 14 volunteers had segments with T2 ≥ 70 ms. Mean intraobserver variability was 1.07 ± 1.03 ms ($r = 0.94$); interobserver variability was 1.6 ± 1.5 ms ($r = 0.87$). The coefficient of variation for repeated scans was 7.6% for SAX and 6.6% for 4CV. Mapping revealed focally increased T2 (73 ± 9 vs. 51 ± 3 ms in remote myocardium; $p < 0.0001$) in all patients with edema.

Conclusions: Myocardial T2 mapping is technically feasible and highly reproducible. It can detect focal edema und differentiate it from normal myocardium. Increased T2 was found in some volunteers most likely due to partial volume and residual motion.

Background

In acute myocardial infarction or inflammation T2-weighted cardiovascular magnetic resonance (CMR) can detect myocardial edema in vivo [1-4]. Increased myocardial water content changes magnetic relaxation properties that influence the CMR signal [5,6]. This can be clinically helpful to differentiate acute from chronic myocardial lesions [7,8] and to detect even small acute myocardial damage very early [9,10]. T2-weighted short tau triple inversion recovery fast spin echo (STIR) can result in pronounced contrast between bright edema and hypointense normal myocardium [11]. However, T2-weighted imaging may suffer from signal loss in higher heart rates and arrhythmias as well as imperfect blood suppression in areas of slow blood flow hampering delineation of edema [12-14]. Therefore alternatives for more stable detection of edema and easier quantification are clinically warranted [15].

* Correspondence: ralf.wassmuth@charite.de
[1]Department of Cardiology and Nephrology, Working Group Cardiac MRI, Humboldt University Berlin, Charite Campus Buch Experimental and Clinical Research Center and HELIOS Klinikum Berlin Buch, Berlin, Germany
Full list of author information is available at the end of the article

CMR T2-mapping is a promising tool for characterizing myocardial edema [16-19]. While initial reports focused on the depiction of focal lesions the aim of this study was to assess the variability of myocardial T2 relaxation times in volunteers and patients and the influence of sequence type, spatial orientation and spatial resolution.

Methods

The local ethical committee approved the study. All participants were enrolled after informed consent was obtained.

The study complies with the declaration of Helsinki. The ethical committee of Charite Medical University approved the study on January 27th, 2011. The application number was EA1/276/10.

Volunteers

We scanned 73 healthy volunteers (13 female, 20–70 years, mean 35 ± 13 years, median 30 years, BMI 23 ± 3 kg/m2) without any cardiovascular disease, no symptoms of inflammation and a normal electrocardiogram. All participants were seen by a cardiologist. We discouraged alcohol intake one day before the scan to avoid inflammatory reaction [20]. Ten volunteers were scanned twice (time delay 469 ± 219 days, median 381 days) to assess interstudy variability.

Patients

We investigated a group of consecutive patients (n = 28; 8 females, age 55 ± 17 years, range 20–81 years) with acute myocardial damage. Edema was defined as a regional area of hyperintense signal on T2-weighted fast spin echo images corresponding to evidence of focal myocardial damage like wall motion abnormality or late gadolinium enhancement (LGE). The group comprises 20 patients with acute myocardial infarction (imaging 3 ± 1 days after admission), 5 patients with acute myocarditis (four male, median age 22 years, positive troponin and typical LGE lesions in all of them, CMR on 1 ± 1 day after admission), 2 postmenopausal female patients with Takotsubo cardiomyopathy (typical presentation and history, no scar, but transient apical ballooning) and 1 patient with cardiac sarcoidosis (acute admission with positive troponin, focal edema corresponding to typical LGE lesion).

CMR

Using a 1.5 T scanner (Magnetom Avanto, Siemens Erlangen, Germany, software version B17) with a 12-channel chest coil we obtained steady state free precession (SSFP) cine loops (repetition time 2.8 ms, echo time 1.2 ms, slice thickness 8 mm, flip angle 80 degrees, in-plane resolution 1.8 mm/pixel) during breathhold in three long and at least one midventricular short axis matching the slice position for mapping. T2-weighted STIR images (repetition time = 2 RR-intervals, echo time 58 ms, slice thickness 8 mm, in-plane resolution 1.3 × 1.3 mm/pixel, imaging in mid-diastole) were obtained in the same short axis as cine and additionally in long axis, if a focal abnormality was seen. In patients we additionally acquired fast low angle shot (FLASH) inversion recovery gradient echo LGE images in short and long axes (slice thickness 8 mm, in-plane resolution 1.8 × 1.4 mm/pixel) after 0.2 mmol/kg Gadolinium-DTPA.

For T2-mapping we applied a prototype sequence based on either FLASH or SSFP gradient echo [16] in one midventricular short axis (SAX) and four-chamber-view (4CV) matching the orientation of cine and STIR images. Slice thickness was 8 mm for all images. The pixel-wise map was based on three single shot images with preceding T2 preparation pulses employing T2 evolution times of 0, 24 and 55 ms (Figure 1). Read-out trajectory was centric for FLASH and linear for SSFP. A non-rigid motion correction was applied to reduce in-plane motion artefacts [17]. Pixel-wise curve fitting was done automatically as part of the inline imaging processing. Spatial resolution was 2.7 × 2.1 mm/pixel. Scan time was 12 heartbeats. The maximum acquisition window was 150 ms per single-shot image. Mid-diastole was chosen for image acquisition. In a subgroup of 24 volunteers additional SSFP-based maps with higher spatial resolution of 2.2 × 1.8 mm/pixel were acquired during

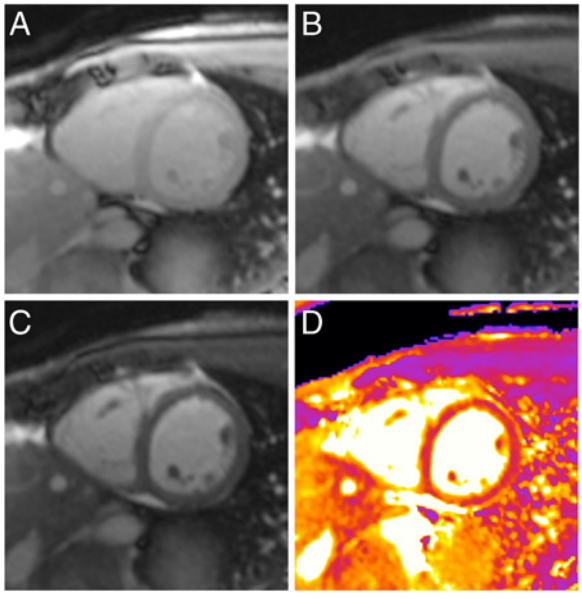

Figure 1 Raw data and resulting T2-map. T2 mapping in a healthy volunteer in midventricular short axis orientation. The color-coded map (**D**) is generated after motion correction and based on three images (**A-C**) with different T2 preparation times (**A**: 0 ms, **B**: 24 ms, **C**: 55 ms).

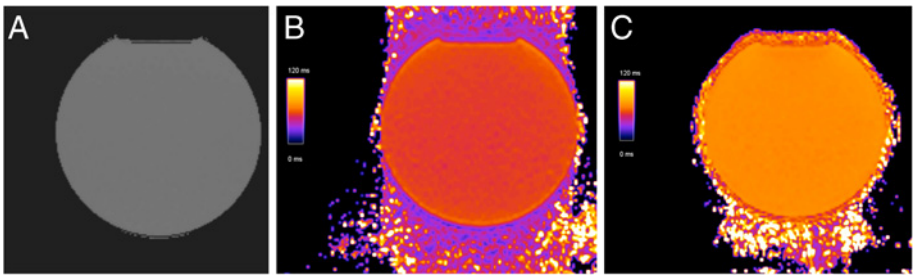

Figure 2 T2 measurements in a phantom. A multiecho spin echo sequence as a gold standard (**A**) resulted in T2 = 62.0 ± 0.5, FLASH T2 map (**B**) yielded T2 = 55.5 ± 1.0 ms and SSFP T2 map (**C**) resulted in T2 = 70.9 ± 0.8 ms.

the same scan. In patients image orientation was adjusted to the focal abnormality, e.g. in Takotsubo cardiomyopathy mapping was done in long axis. In 14/28 patients mapping data were acquired with the SSFP-based sequence only.

Phantom

We scanned a spherical phantom of 20 cm diameter filled with manganese chloride doped distilled water. The RR-interval was simulated to be 1000 ms. A 2D multi contrast spin echo sequence (repetition time = 2000 ms, 32 echo times equally spaced from 7 ms to 224 ms) in conjunction with a mono-exponential three-parameter-fit served as T2 reference measurement [21]. We additionally obtained measurements using the FLASH and SSFP sequences with identical parameters as used for imaging volunteers and patients.

Data analysis

For signal analysis we used Osirix (version 3.9.1 www.osirix-viewer.com) and QMASS (version 7, Medis, Leiden, The Netherlands) in all subjects. The endocardial and epicardial contours were manually drawn on the last corresponding T2-weighted raw image with the echo time of 55 ms. The myocardium was then segmented (manually in Osirix, automatically in QMass) into 6 segments according to the AHA segmentation scheme [22]. Contours were copied to the map, corrected when necessary and global and segmental T2-values were recorded. Two independent observers analysed all the volunteer data. Both do have considerable experience in CMR image analysis (> 15 years and > 3 years, respectively) and put much effort in avoiding inclusion of blood or fat while drawing regions of interest. Interstudy reproducibility was measured for SAX and 4CV. The coefficient of variation (CoV) was calculated as the ratio of the standard deviation of the interscan difference divided by the mean of the measurement. Anteroseptal enddiastolic myocardial wall thickness was measured on short axis and four-chamber-view cine frames and compared to T2-times in the same segment. To assess residual diastolic wall motion M-mode-like myocardial signal intensity projections over time were generated from 2D SSFP short axis and four-chamber -view cine images in selected patients using an in-house developed implementation in Matlab 7.1 (The Mathworks, Natick, MA).

The same investigator analyzed all SSFP volunteer maps twice. In patients areas of focal abnormality matching hyperintense signal in STIR and LGE were selected and compared to remote myocardium. We excluded hypointense infarction cores indicating microvascular obstruction [17].

Data are given as mean ± standard deviation unless indicated otherwise. We compared results from different sequences and orientations and repeated scans with paired student´s t-test and Pearson correlation coefficient r. P-values < 0.05 were considered significant. 95% confidence intervals (CI) were calculated. Bland-Altman -plots were obtained to analyse intra- and interobserver variability. Volunteer and patient data were compared using 95% tolerance intervals with 90% coverage. These tolerance intervals cover 90% of all observations of a normal distribution with 95% confidence when the mean and the standard deviation are known. Influencing factors were identified by sequence using the candidates age, gender, heart rate, body surface area, body mass index and the interaction terms in an analysis of variance with forward selection (criterion for selection p < 5%).

Table 1 Global myocardial T2 relaxation times (ms) in volunteers

		FLASH	SSFP	
SAX	Mean	52 ± 5	55 ± 5	p < 0.0001
	Range	41–62	46–69	
	CI (5–95%)	51–53	54–57	
4CV	Mean	57 ± 6	59 ± 6	p < 0.0001
	Range	46–74	51–80	
	CI (5–95%)	56–59	57–60	
		p < 0.0001	p < 0.0001	

CI denotes confidence interval, *SAX* = short axis, *4CV* = four-chamber view, *FLASH* = fast low angle shot, *SSFP* = steady state free precession.

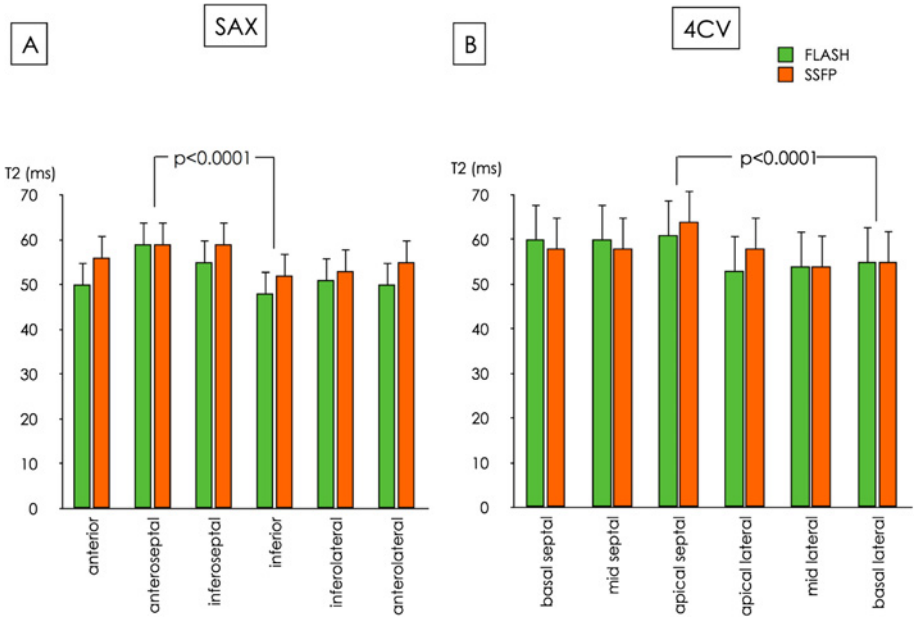

Figure 3 Spatial variation of T2 in volunteers. Segmental measurements reveal spatial variation of myocardial T2 in short axis (SAX) (**A**) and four-chamber view (4CV) (**B**). The Y-axis shows T2-times in ms. Note higher T2-values in anteroseptal and apical septal segments compared to inferior and basal septal segments.

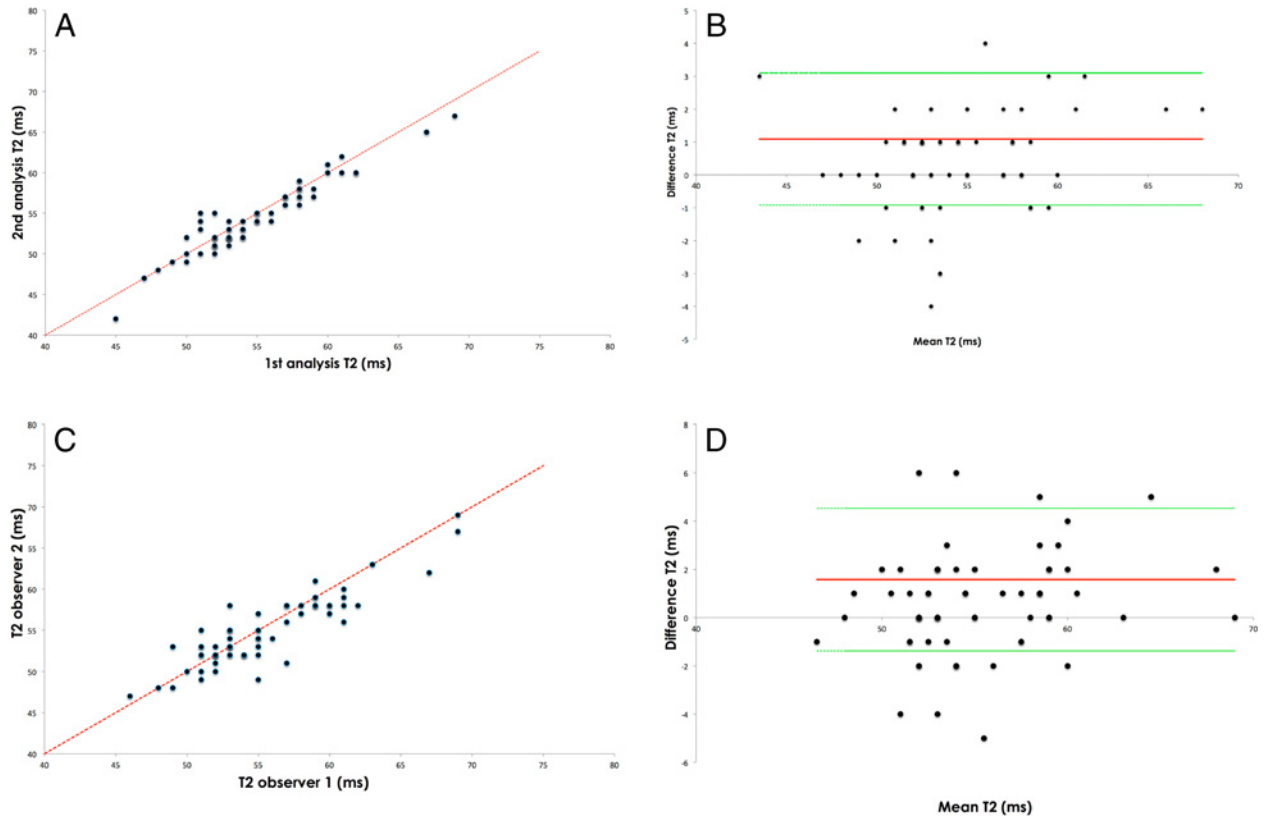

Figure 4 Intra- and interobserver variability in volunteers. Intra- (**A**) and (**B**) and interobserver (**C**) and (**D**) variability for global myocardial T2 in short axis based on the steady state free precession sequence in volunteers. Scatterplots (**A** and **C**) and Bland-Altman plots (**B**) and (**D**) are given. Red lines indicate bias. Green lines indicate the limits of agreement (1.96 x standard deviation). Due to overlap dots stand for more than 1 data point.

We compared the data on healthy volunteers and patients using a mixed linear model with compound symmetry as working correlation matrix to account for the multiple measurements of up to four sequences by subject. Gender and age (35 years or younger, more than 35 years) were included as covariates. We performed a multivariate analysis including wall thickness, diastolic motion and a combination thereof to assess the impact on myocardial T2.

Results

Phantom

Evaluation of multi contrast spin echo data in the phantom yielded T2 = 62.0 ± 0.5 ms. The T2-mapping variant using FLASH readout resulted in T2 = 55.5 ± 1.0 ms, whereas SSFP readout revealed T2 = 70.9 ± 0.8 ms (Figure 2).

Volunteers

Four volunteers were excluded from analysis due to pathological findings (pleural effusions, tachycardic atrial fibrillation and left ventricular hypertrophy). The remaining 69 formed the healthy study group.

Global T2 measurements in volunteers

In all subjects maps could be generated in diagnostic quality. Mean heart rate was 73 ± 10 bpm. Global myocardial T2 measurements are summarized in Table 1. Global T2-values did not correlate with heart rate (r = 0.002), age (r = 0.30), body surface area (r = 0.44) or body mass index (r = 0.36). SSFP-based mapping resulted in higher values for T2 than FLASH-based mapping (SAX: 55 ± 5 vs. 52 ± 5 ms; 4CV: 59 ± 6 vs. 57 ± 6 ms; $p < 0.0001$ for both). This was true for global (Table 1) and segmental measurements (Figure 3). Global T2-mapping resulted in higher values in 4CV-orientation than in short axis ($p < 0.0001$ for both sequences; Table 1).

Segmental T2 measurements in volunteers

With both sequences anteroseptal segments had higher T2-values than inferior segments in SAX (59 ± 6 vs. 48 ± 5 ms for FLASH and 59 ± 7 vs. 52 ± 4 ms for SSFP; $p < 0.0001$ for both, Figure 3). In 4CV the apical septal segment had higher T2 than the basal lateral segment for both FLASH (61 ± 8 vs. 55 ± 6 ms; $p < 0.0001$) and SSFP (64 ± 9 vs. 55 ± 6 ms; $p < 0.0001$; Figure 3). In SAX the mean absolute difference between a single segment and the whole slice was 4 ± 1 ms and 3 ± 2 ms for FLASH and SSFP, respectively. In 4CV the mean absolute difference between a single segment and a global measurement was 5 ± 2 ms for both, FLASH and SSFP.

Variability in volunteers

Intra- and inter-observer variability was low (Figure 4). The mean difference for T2 between repeated measurements in one observer was 1.07 ± 1.03 ms (r = 0.94). Mean difference for T2 between two observers was 1.6 ± 1.5 ms (r = 0.87). The CoV for repeated scans was 7.6% for SAX and 6.6% for 4CV. The results for myocardial T2 did not differ depending on the analysis software used.

Outliers among volunteers

Even among the normal volunteer group we found segmental and global T2-values equal to or higher than 70 ms (Figure 5) in 14 of 69 healthy subjects. On a segmental basis this occurred in 3/414 segments in FLASH and 7/414 segments in SSFP in short axis. In 4CV maps it occurred in 26/414 segments in FLASH and 29/414 in SSFP. In 13 out of 14 volunteers the apical septal segment was affected. In 4CV there were 4 volunteers each, who had global myocardial T2 ≥70 ms in FLASH or SSFP. There was no significant difference in age between those with and without T2 ≥70 ms (31 ± 12 vs. 38 ± 13 years; $p = 0.08$). Anteroseptal wall thickness as measured in enddiastolic cine frames (mean 3.5 mm, range 2–8 mm for 4CV) was inversely related to myocardial T2. The thinner the anteroseptal segment was, the higher was T2 (r = −0.6 for 4CV). The m-mode analysis revealed a mean residual diastolic motion of 2.3 mm (range 0.1 – 5.2 mm).

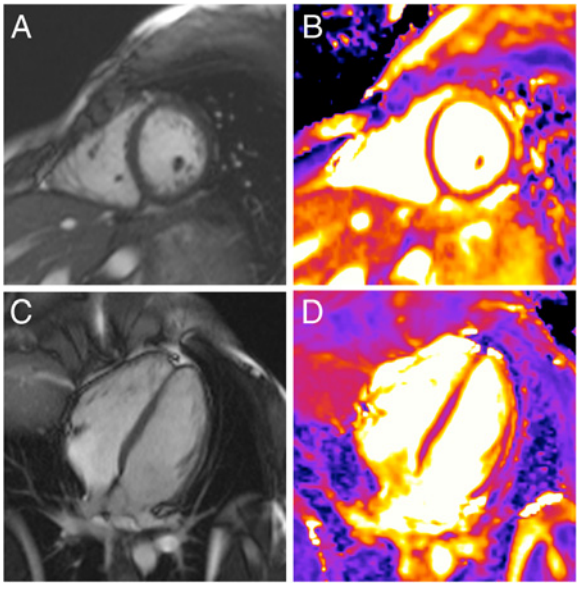

Figure 5 A healthy 22-year-old female volunteer with unusually high T2. Diastolic short axis (**A**) and four-chamber view (**C**) cine frames illustrate thin anterior and apical walls. T2-maps in short axis (**B**) and four-chamber view (**D**) reveal markedly elevated T2 in anterior and apical segments. Global myocardial T2 in short axis was 69 ms, anterior T2 was 77 ms.

More diastolic motion correlated with higher myocardial T2 (r = 0.37). In a multivariate analysis diastolic wall motion ($p < 0.001$) and the combination of wall thickness and motion ($p < 0.003$) significantly correlated with myocardial T2. Dichotomizing the volunteer group for age and gender reveals the larger range for myocardial T2 in younger and mainly female volunteers (Figure 6).

Mapping with improved spatial resolution did change results in individual subjects (Figure 7), but not for the whole group ($p = 0.3$) Even after improving spatial resolution 8 out of 24 volunteers had segmental myocardial T2 ≥70 ms on 4CV maps, while only one segment was affected in SAX. In 4CV this occurred in the apical septal segment in all but one case.

Measurements in patients

In all 28 patients with acute myocardial damage areas of increased T2 could be detected. Using SSFP-based mapping T2 of edema was 73 ± 9 ms on average (range 64–99 ms, 95% CI 70–76 ms), while T2 of remote

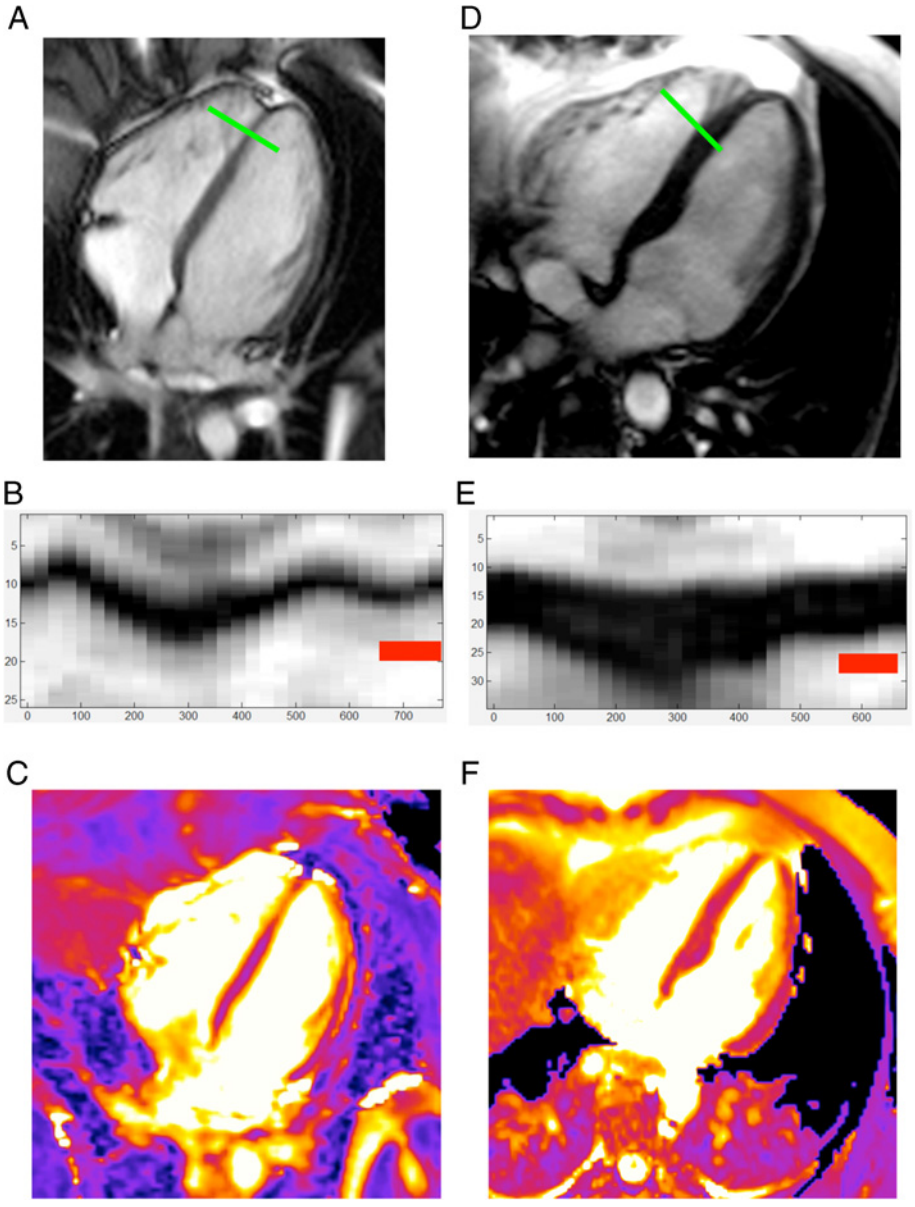

Figure 6 Wall thickness and diastolic motion influence myocardial T2. A young female volunteer has an apical septal wall thickness of 2 mm (**A**). In m-mode projections (**B**) and (**E**) the y-axis indicates distance in mm, the x-axis indicates time within the cardiac cycle in ms. The red bar represents the acquisition window. In this case M-mode projection reveals residual diastolic motion of 2.8 mm (**B**). Apical septal T2 was 80 ms (**C**). A 46-year-old male volunteer of had an apical-septal wall thickness of 7 mm (**D**), a diastolic wall motion of 1.3 mm (**E**) and a segmental T2 of 55 ms (**F**).

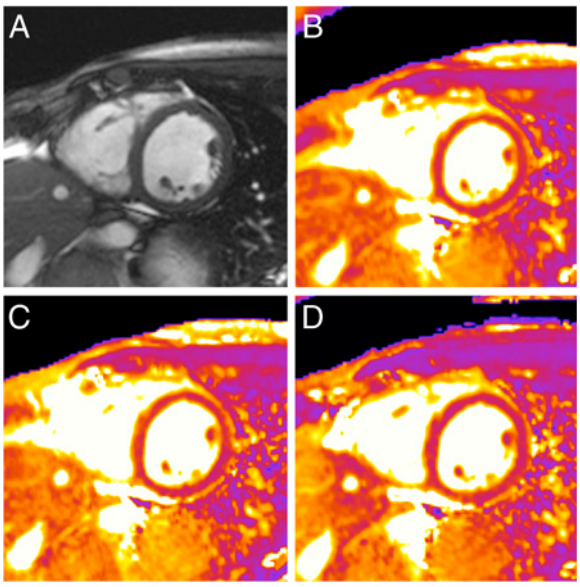

Figure 7 Influence of spatial resolution. T2-mapping in a healthy 43-year-old male with different spatial resolution. Corresponding cine frame in (**A**). While the map with an initial spatial resolution of 2.7 × 2.1 mm/pixel (**B**) suggests spots of increased T2 in the anteroseptal segment, these spots diminish with increasing spatial resolution to 2.2 × 1.8 mm/pixel (**C**) and improved motion correction on top (**D**). The acquisition window was 130 ms in (**D**). Anteroseptal T2 was 62 ms in (**B**), 58 ms in (**C**) and 51 ms in (**D**).

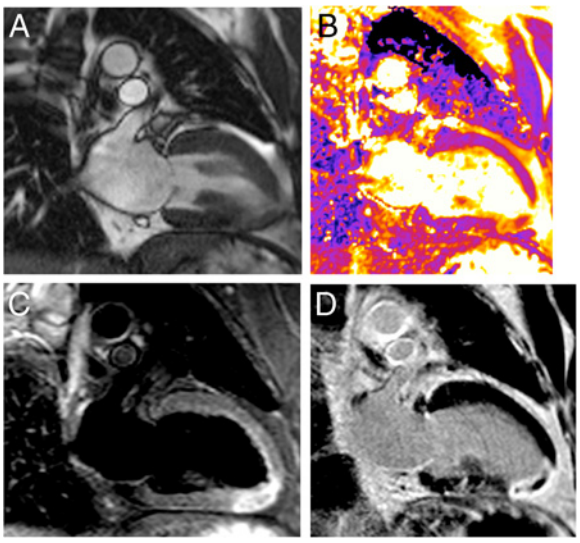

Figure 9 T2-mapping in acute myocardial infarction. CMR in a 47-year-old male patient 2 days after apical inferior infarction. The distal left anterior descending artery was occluded. All images shown here are in two-chamber-orientation. (**A**): systolic cine frame reveals apical-inferior wall motion abnormality. (**B**): T2-map shows an apical area of increased T2 reflected by orange color with a centre of lower T2 indicated by pink colour. (**C**): conventional T2-weighted STIR image shows focal area of hyperintense signal with a hypointense core. (**D**): Late gadolinium enhancement shows myocardial scar with core of microvascular obstruction.

myocardium was 51 ± 3 ms (range 44–57 ms, 95% CI 50–52 ms; Figure 8). T2 did not differ between ischemic (Figure 9) and nonischemic (Figure 10) edema.

Discussion

T2-mapping is technically feasible with low intra-, interobserver and inter-scan variability and does not depend on heart rate. Overall our mapping results with mean T2 around 55 ms for normal myocardium match previous experiences [6,16,23-27].

As far as T2 mapping in patients with acute myocardial damage is concerned we can confirm earlier small patient studies [17,19]. In patients with acute myocardial infarction or inflammation T2-mapping detects focal edema and reveals increased myocardial T2-values with

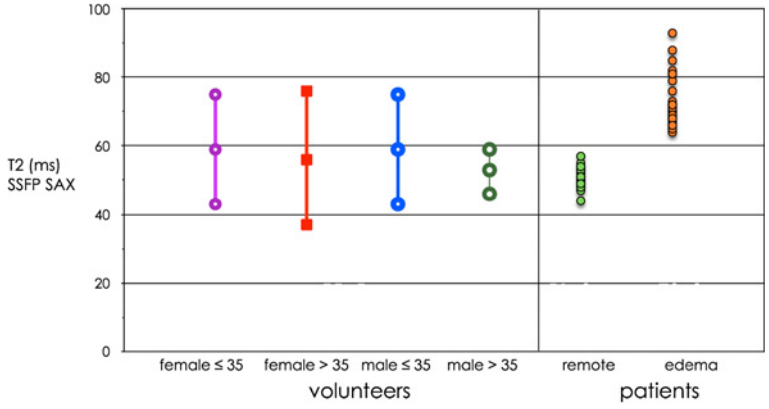

Figure 8 Comparison of global myocardial T2 in healthy volunteers (left) and focal edema in patients (right). Data are shown for SSFP-based mapping in short axis. Of note, in controls the bars do not represent mean ± standard deviation, but mean ± 95% tolerance interval with 90% coverage. For patients, individual data points are shown.

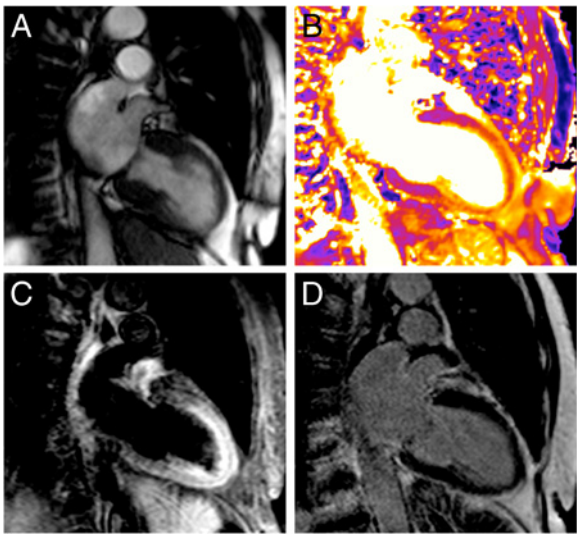

Figure 10 T2-mapping in Takotsubo cardiomyopathy. 81-year-old female presented with Takotsubo cardiomyopathy including transient ECG-changes and elevated troponin after a generalized seizure. CMR was done 3 days after the initial event. All images shown here are in two-chamber-orientation. Systolic cine frame reveals apical ballooning (**A**). T2 map indicates elevated apical myocardial T2 reflected by orange colour (**B**). Conventional T2-weighted STIR image shows increased myocardial signal intensity in the apex that might be difficult to differentiate from intraluminal blood signal in the case of slow flow (**C**). Late gadolinium enhancement excludes myocardial scar (**D**).

small variability. Our results for remote myocardium nicely match those for our elderly male volunteers.

Therefore it appears straightforward to characterize a clearly delineated pathologic lesion in clinical routine. However, it might be more challenging to exclude any lesion in a subject with no or mild disease.

Our systematic analysis in a large group of volunteers revealed, that SSFP-based T2-mapping resulted in slightly higher values than FLASH. In early phantom studies as well as our own experiment (Figure 2) mapping with FLASH showed good agreement with "true" T2 values [28]. Therefore SSFP tends to overestimate true T2 as demonstrated before [16,27]. On the other hand SSFP-based mapping offers more signal to noise [27] and suffers less from image artefacts than FLASH due to centric readout of FLASH-based mapping [16].

Partial volume and motion effects most likely explain higher global T2 in 4CV than in SAX as well as spatial inhomogeneity with higher T2 in anterior and anteroseptal segments. Wall thickness (i.e. thin walls) and residual diastolic motion were related to higher myocardial T2. Close observation of cine loops and analysis with m-mode-like projection confirm diastolic wall motion in particular in young volunteers with thin walls [29]. The low intra- and interobserver variability indicates that these outliers are not simply a problem of suboptimal contouring.

Inclusion of even small amounts of neighbouring entities like blood (T2 of about 200 ms) and pericardial fat (T2 of about 80 ms) can grossly influence the measurement of myocardial T2. Improving spatial resolution should minimize partial-volume effect, however this also prolongs the acquisition window increasing motion artefacts. We found T2-values of up to 80 ms even in our volunteer group, where as the T2 for edema associated with acute infarction has been reported to be 69 ± 6 ms [17]. Therefore care has to be taken not to generate false-positive findings of edema in subjects with thin and highly mobile walls. In patients with true edema this is less a problem due to increased wall thickness in the presence of edema [30].

For the future imaging at individually optimized time points within the cardiac cycle should be considered if cine imaging indicates abundant myocardial motion even in mid-diastole. Depending on individual wall motion across the cardiac cycle in cine loops systole or early diastole may be chosen. However, previous T1 mapping experiments in volunteers indicate that results might slightly differ between systole and diastole [31].

A clinical advantage for myocardial T2 mapping can be expected in particular in patients with pronounced apical wall motion abnormalities where conventional T2-weighted imaging can be challenging. A severe apical

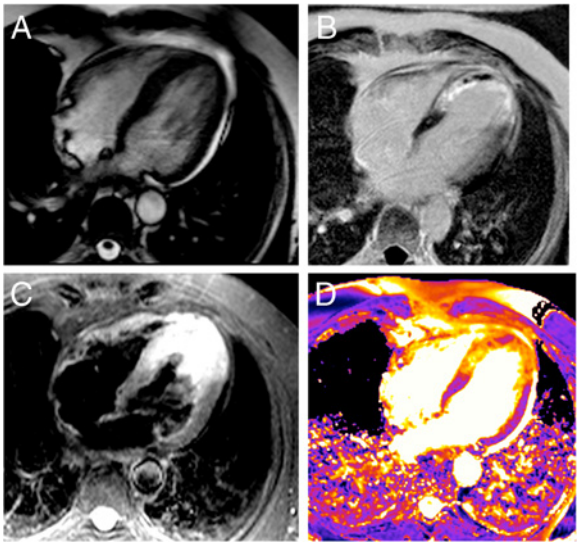

Figure 11 T2-mapping in acute apical infarction. The diastolic cine frame (**A**) reveals apical septal wall thickening in the area of edema. Late gadolinium enhancement shows apical infarction scar with microvascular obstruction (**B**). While conventional T2-weighted STIR image depicts both, edema and bright slow flowing blood within the lumen (**C**), T2 map correctly indicates edema color-coded in orange with an apical T2 of 91 ms (**D**). The microvascular obstruction corresponds to a T2 of 60 ms, color-coded in pink. Basal T2 was 54 ms.

wall motion abnormality may result in hyperintense intraluminal blood signal that is difficult to differentiate from bright signal within the wall that truly reflects edema. In these circumstances T2-mapping seems to offer additional options for clinical routine to confirm true edema while conventional T2-weighted spin echo remains inconclusive (Figure 11). In addition the breathhold time of the mapping sequence is by far shorter than that of a conventional fast spin echo sequence, which makes imaging easier for a heart failure patient. Conventional T2-weighted imaging is semi-quantitative at best requiring a reference structure. T2-mapping may open the way for a truly quantitative approach in assessing acute damage.

We enrolled patients with focal lesions only. Theoretically mapping offers the potential to quantify diffuse tissue damage that is less obvious on conventional CMR images. Future studies including patients with known diffuse disease might enlighten this phenomenon. We included two cases of typical Takotsubo cardiomyopathy and one case of sarcoidosis with typical late Gadolinium enhancement corresponding to focal edema. Edema has been previously described in both entities including a large multicentre study for Takotsubo cardiomyopathy [32-35].

Limitations

The power calculation took into account the differentiation of patients and volunteers as a whole group. The study and its sample size were not designed to reveal subtle differences among e.g. women of different decades of age. There is no dedicated gold standard for true edema. We assumed edema in myocardial areas where it made sense clinically based on concomitant late gadolinium enhancement or obvious wall motion abnormalities in patients with evidence of acute myocardial damage in laboratory results and electrocardiogram.

Conclusions

Myocardial T2 mapping is technically feasible and highly reproducible in a large number of normal volunteers. Differences in sequences and spatial resolution result in small differences in myocardial T2 values. Quantifying T2 easily detects focal myocardial edema and differentiates it from remote myocardium. T2 mapping may offer a more stable and truly quantitative alternative for edema detection in cases when conventional T2-weighted imaging fails. Mapping in thin and rapidly moving myocardial walls can result in overestimation of myocardial T2 and must not be confused with true edema.

Abbreviations

CMR: Cardiovascular magnetic resonance; STIR: Short tau triple inversion recovery; SSFP: Steady state free precession; FLASH: Fast low angle shot; SAX: Short axis; 4CV: Four-chamber view; CI: Confidence interval; LGE: Late gadolinium enhancement.

Competing interests

A Greiser is an employee of Siemens AG, Erlangen, Germany. The authors declare no other competing interests.

Authors' contributions

RW and JSM conceived of and designed the study. RW, MP, WU, MD, AG and FVK acquired, analysed and interpreted the data. RW wrote the manuscript with input from WU, FVK, MD and JSM. All authors read and approved the final manuscript.

Acknowledgements

We cordially thank all participating volunteers for their generous commitment. We gratefully acknowledge statistical support by Carsten Schwenke (scossis.com), technical advice by Saurabh Shah and the technical expertise of Denise Kleindienst, Kerstin Kretschel and Evi Polzin.

Author details

[1]Department of Cardiology and Nephrology, Working Group Cardiac MRI, Humboldt University Berlin, Charite Campus Buch Experimental and Clinical Research Center and HELIOS Klinikum Berlin Buch, Berlin, Germany. [2]Siemens AG Healthcare Sector, Erlangen, Germany.

Received: 26 November 2012 Accepted: 8 March 2013
Published: 27 March 2013

References

1. Abdel-Aty H, Boye P, Zagrosek A, Wassmuth R, Kumar A, Messroghli D, Bock P, Dietz R, Friedrich MG, Schulz-Menger J. **Diagnostic performance of cardiovascular magnetic resonance in patients with suspected acute myocarditis: comparison of different approaches.** *J Am Coll Cardiol.* 2005; **45:**1815–22.
2. Aletras AH, Tilak GS, Natanzon A, Hsu LY, Gonzalez FM, Hoyt RF Jr, Arai AE. **Retrospective determination of the area at risk for reperfused acute myocardial infarction with T2-weighted cardiac magnetic resonance imaging: histopathological and displacement encoding with stimulated echoes (DENSE) functional validations.** *Circulation.* 2006; **113:**1865–70.
3. Friedrich MG, Kim HW, Kim RJ. **T2-weighted imaging to assess post-infarct myocardium at risk.** *JACC Cardiovasc Imaging.* 2011; **4:**1014–21.
4. Lurz P, Eitel I, Adam J, Steiner J, Grothoff M, Desch S, Fuernau G, de Waha S, Sareban M, Luecke C, et al. **Diagnostic performance of CMR imaging compared with EMB in patients with suspected myocarditis.** *JACC Cardiovas Imaging.* 2012; **5:**513–24.
5. Scholz TD, Martins JB, Skorton DJ. **NMR relaxation times in acute myocardial infarction: relative influence of changes in tissue water and fat content.** *Magn Reson Med.* 1992; **23:**89–95.
6. Boxt LM, Hsu D, Katz J, Detweiler P, McLaughlin S, Kolb TJ, Spotnitz HM. **Estimation of myocardial water content using transverse relaxation time from dual spin-echo magnetic resonance imaging.** *Magn Reson Imaging.* 1993; **11:**375–83.
7. Abdel-Aty H, Zagrosek A, Schulz-Menger J, Taylor AJ, Messroghli D, Kumar A, Gross M, Dietz R, Friedrich MG. **Delayed enhancement and T2-weighted cardiovascular magnetic resonance imaging differentiate acute from chronic myocardial infarction.** *Circulation.* 2004; **109:**2411–16.
8. Ohlci D, Ridgway JP, Kuehne T, Berger F, Plein S, Sivananthan M, Messroghli DR. **Cardiovascular magnetic resonance of myocardial edema using a short inversion time inversion recovery (STIR) black-blood technique: diagnostic accuracy of visual and semi-quantitative assessment.** *J Cardiovasc Magn Reson.* 2012; **14:**22.
9. Abdel-Aty H, Cocker M, Meek C, Tyberg JV, Friedrich MG. **Edema as a very early marker for acute myocardial ischemia: a cardiovascular magnetic resonance study.** *J Am Coll Cardiol.* 2009; **53:**1194–201.
10. Cury RC, Shash K, Nagurney JT, Rosito G, Shapiro MD, Nomura CH, Abbara S, Bamberg F, Ferencik M, Schmidt EJ, et al. **Cardiac magnetic resonance with T2-weighted imaging improves detection of patients with acute coronary syndrome in the emergency department.** *Circulation.* 2008; **118:**837–44.
11. Abdel-Aty H, Simonetti O, Friedrich MG. **T2-weighted cardiovascular magnetic resonance imaging.** *J Magn Reson Imaging.* 2007; **26:**452–59.
12. Kellman P, Aletras AH, Mancini C, McVeigh ER, Arai AE. **T2-prepared SSFP improves diagnostic confidence in edema imaging in acute myocardial**

infarction compared to turbo spin echo. *Magn Reson Med.* 2007; **57:**891–97.
13. Walls MC, Verhaert D, Min JK, Raman SV. **Myocardial edema imaging in acute coronary syndromes.** *J Magn Reson Imaging.* 2011; **34:**1243–50.
14. Wince WB, Kim RJ. **Molecular imaging: T2-weighted CMR of the area at risk–a risky business?** *Nat Rev Cardiol.* 2010; **7:**547–49.
15. Ferreira VM, Piechnik SK, Dall'Armellina E, Karamitsos TD, Francis JM, Choudhury RP, Friedrich MG, Robson MD, Neubauer S. **Non-contrast T1-mapping detects acute myocardial edema with high diagnostic accuracy: a comparison to T2-weighted cardiovascular magnetic resonance.** *J Cardiovasc Magn Reson.* 2012; **14:**42.
16. Giri S, Chung YC, Merchant A, Mihai G, Rajagopalan S, Raman SV, Simonetti OP. **T2 quantification for improved detection of myocardial edema.** *J Cardiovasc Magn Reson.* 2009; **11:**56.
17. Verhaert D, Thavendiranathan P, Giri S, Mihai G, Rajagopalan S, Simonetti OP, Raman SV. **Direct T2 quantification of myocardial edema in acute ischemic injury.** *JACC Cardiovasc Imaging.* 2011; **4:**269–78.
18. Ugander M, Bagi PS, Oki AJ, Chen B, Hsu LY, Aletras AH, Shah S, Greiser A, Kellman P, Arai AE. **Myocardial edema as detected by Pre-contrast T1 and T2 CMR delineates area at risk associated with acute myocardial infarction.** *JACC Cardiovasc Imaging.* 2012; **5:**596–603.
19. Thavendiranathan P, Walls M, Giri S, Verhaert D, Rajagopalan S, Moore S, Simonetti OP, Raman SV. **Improved detection of myocardial involvement in acute inflammatory cardiomyopathies using T2 mapping.** *Circ Cardiovasc Imaging.* 2012; **5:**102–10.
20. Zagrosek A, Messroghli D, Schulz O, Dietz R, Schulz-Menger J. **Effect of binge drinking on the heart as assessed by cardiac magnetic resonance imaging.** *JAMA.* 2010; **304:**1328–30.
21. Poon CS, Henkelman RM. **Practical T2 quantitation for clinical applications.** *J Magn Reson Imaging.* 1992; **2:**541–53.
22. Cerqueira MD, Weissman NJ, Dilsizian V, Jacobs AK, Kaul S, Laskey WK, Pennell DJ, Rumberger JA, Ryan T, Verani MS. **Standardized myocardial segmentation and nomenclature for tomographic imaging of the heart: a statement for healthcare professionals from the Cardiac Imaging Committee of the Council on Clinical Cardiology of the American Heart Association.** *Circulation.* 2002; **105:**539–42.
23. Bottomley PA, Foster TH, Argersinger RE, Pfeifer LM. **A review of normal tissue hydrogen NMR relaxation times and relaxation mechanisms from 1–100 MHz: dependence on tissue type, NMR frequency, temperature, species, excision, and age.** *Med Phys.* 1984; **11:**425–48.
24. Blume U, Lockie T, Stehning C, Sinclair S, Uribe S, Razavi R, Schaeffter T. **Interleaved T(1) and T(2) relaxation time mapping for cardiac applications.** *J Magn Reson Imaging.* 2009; **29:**480–87.
25. Cobb JG, Paschal CB. **Improved in vivo measurement of myocardial transverse relaxation with 3 Tesla magnetic resonance imaging.** *J Magn Reson Imaging.* 2009; **30:**684–89.
26. He T, Gatehouse PD, Anderson LJ, Tanner M, Keegan J, Pennell DJ, Firmin DN. **Development of a novel optimized breathhold technique for myocardial T2 measurement in thalassemia.** *J Magn Reson Imaging.* 2006; **24:**580–85.
27. Huang TY, Liu YJ, Stemmer A, Poncelet BP. **T2 measurement of the human myocardium using a T2-prepared transient-state TrueFISP sequence.** *Magn Reson Med.* 2007; **57:**960–66.
28. Deichmann R, Adolf H, Noth U, Morrissey S, Schwarzbauer C, Haase A. **Fast T2-mapping with snapshot flash imaging.** *Magn Reson Imaging.* 1995; **13:**633–39.
29. Foll D, Jung B, Schilli E, Staehle F, Geibel A, Hennig J, Bode C, Markl M. **Magnetic resonance tissue phase mapping of myocardial motion: new insight in age and gender.** *Circ Cardiovasc Imaging.* 2010; **3:**54–64.
30. Zagrosek A, Wassmuth R, Abdel-Aty H, Rudolph A, Dietz R, Schulz-Menger J. **Relation between myocardial edema and myocardial mass during the acute and convalescent phase of myocarditis–a CMR study.** *J Cardiovasc Magn Reson.* 2008; **10:**19.
31. Kawel N, Nacif M, Zavodni A, Jones J, Liu S, Sibley CT, Bluemke DA. **T1 mapping of the myocardium: intra-individual assessment of the effect of field strength, cardiac cycle and variation by myocardial region.** *J Cardiovasc Magn Reson.* 2012; **14:**27.
32. Eitel I, von Knobelsdorff-Brenkenhoff F, Bernhardt P, Carbone I, Muellerleile K, Aldrovandi A, Francone M, Desch S, Gutberlet M, Strohm O, et al. **Clinical characteristics and cardiovascular magnetic resonance findings in stress (takotsubo) cardiomyopathy.** *JAMA.* 2011; **306:**277–86.
33. Neil C, Nguyen TH, Kucia A, Crouch B, Sverdlov A, Chirkov Y, Mahadavan G, Selvanayagam J, Dawson D, Beltrame J, et al. **Slowly resolving global myocardial inflammation/edema in Tako-Tsubo cardiomyopathy: evidence from T2-weighted cardiac MRI.** *Heart.* 2012; **98:**1278–84.
34. Srichai MB, Addrizzo-Harris DJ, Friedman K. **Cardiac sarcoidosis.** *J Am Coll Cardiol.* 2011; **58:**438.
35. Quarta G, Holdright DR, Plant GT, Harkness A, Hausenloy D, Hyare H, Moon JC. **Cardiovascular magnetic resonance in cardiac sarcoidosis with MR conditional pacemaker in situ.** *J Cardiovasc Magn Reason.* 2011; **13:**26.

doi:10.1186/1532-429X-15-27
Cite this article as: Wassmuth *et al.*: **Variability and homogeneity of cardiovascular magnetic resonance myocardial T2-mapping in volunteers compared to patients with edema.** *Journal of Cardiovascular Magnetic Resonance* 2013 **15**:27.

Journal of Cardiovascular Magnetic Resonance

RESEARCH Open Access

Myocardial T_1 and T_2 mapping at 3 T: reference values, influencing factors and implications

Florian von Knobelsdorff-Brenkenhoff[1,2*], Marcel Prothmann[1,2], Matthias A Dieringer[1,2], Ralf Wassmuth[1,2], Andreas Greiser[3], Carsten Schwenke[4], Thoralf Niendorf[1,5] and Jeanette Schulz-Menger[1,2]

Abstract

Background: Myocardial T_1 and T_2 mapping using cardiovascular magnetic resonance (CMR) are promising to improve tissue characterization and early disease detection. This study aimed at analyzing the feasibility of T_1 and T_2 mapping at 3 T and providing reference values.

Methods: Sixty healthy volunteers (30 males/females, each 20 from 20–39 years, 40–59 years, 60–80 years) underwent left-ventricular T_1 and T_2 mapping in 3 short-axis slices at 3 T. For T_2 mapping, 3 single-shot steady-state free precession (SSFP) images with different T_2 preparation times were acquired. For T_1 mapping, modified Look-Locker inversion recovery technique with 11 single shot SSFP images was used before and after injection of gadolinium contrast. T_1 and T_2 relaxation times were quantified for each slice and each myocardial segment.

Results: Mean T_2 and T_1 (pre-/post-contrast) times were: 44.1 ms/1157.1 ms/427.3 ms (base), 45.1 ms/1158.7 ms/411.2 ms (middle), 46.9 ms/1180.6 ms/399.7 ms (apex). T_2 and pre-contrast T_1 increased from base to apex, post-contrast T_1 decreased. Relevant inter-subject variability was apparent (scatter factor 1.08/1.05/1.11 for T_2/pre-contrast T_1/post-contrast T_1). T_2 and post-contrast T_1 were influenced by heart rate ($p < 0.0001$, $p = 0.0020$), pre-contrast T_1 by age ($p < 0.0001$). Inter- and intra-observer agreement of T_2 ($r = 0.95$; $r = 0.95$) and T_1 ($r = 0.91$; $r = 0.93$) were high. T_2 maps: 97.7% of all segments were diagnostic and 2.3% were excluded (susceptibility artifact). T_1 maps (pre-/post-contrast): 91.6%/93.9% were diagnostic, 8.4%/6.1% were excluded (predominantly susceptibility artifact 7.7%/3.2%).

Conclusions: Myocardial T_2 and T_1 reference values for the specific CMR setting are provided. The diagnostic impact of the high inter-subject variability of T_2 and T_1 relaxation times requires further investigation.

Keywords: Cardiovascular magnetic resonance, Heart, T_1, T_2, Mapping, 3 T

Background

Cardiovascular magnetic resonance (CMR) provides techniques for non-invasive myocardial tissue characterization. T_1 and T_2 mapping of the left ventricular myocardium, i.e. quantification of the myocardial T_1 and T_2 relaxation times, as well as the T_1-derived extracellular volume fraction have been demonstrated to add valuable information [1-6]. Most of the experience with myocardial mapping was gained at a magnetic field strength of 1.5 T. Parametric myocardial mapping at 3 T is conceptually appealing due to the signal gain inherent to higher fields, which may be exploited for improved spatial and temporal resolution [7]. Many of the previous studies focused on intra-individual comparison of diseased and remote myocardium. However, T_2 and T_1 reference values of all myocardial segments may be important to define small focal abnormalities and to identify diffuse tissue changes in the absence of healthy "remote" myocardium. For all these reasons this study scrutinizes myocardial T_1 and T_2 at 3 T in a large sample of healthy volunteers using state-of-the art mapping techniques.

* Correspondence: florian.von-knobelsdorff@charite.de
[1]Berlin Ultrahigh Field Facility, Max-Delbrueck Center for Molecular Medicine, Berlin, Germany
[2]Working Group on Cardiovascular Magnetic Resonance, Experimental and Clinical Research Center a joint cooperation between the Charité Medical Faculty and the Max-Delbrueck Center for Molecular Medicine HELIOS Klinikum Berlin Buch, Department of Cardiology and Nephrology, Lindenberger Weg 80, 13125, Berlin, Germany
Full list of author information is available at the end of the article

Methods

Study population

60 healthy volunteers were enrolled into the study (30 men/30 women, equally distributed within 3 age categories (Table 1)). The status "healthy" was based on: i) uneventful medical history, ii) absence of any symptoms indicating cardiovascular dysfunction, iii) normal ECG, iv) normal cardiac dimensions and function proven by cine CMR. v) normal myocardial tissue assessed by late enhancement (LGE). For each volunteer written informed consent was obtained prior to the study, after due approval by the ethical committee of the Charité Medical Faculty (EA2/077/10). All experiments were performed in compliance with the Helsinki Declaration.

CMR examination

All CMR exams were performed with a 3 T system (Magnetom Verio, Siemens Healthcare, Erlangen, Germany) using a 32-channel cardiac RF coil for signal reception, the integrated body RF coil for transmission, and ECG for cardiac gating. Subject-specific, volume-selective first- and second-order B_0-shimming based on field maps derived from double-gradient-echo acquisitions was performed to improve static field uniformity. The following CMR protocols were used (Figure 1).

Cine imaging

Steady-state free-precession (SSFP) cine images were obtained during repeated breath-holds in three long axes (horizontal, vertical, and 3-chamber) and in a stack of short axes (SAX) covering the left ventricle (LV) to assess wall motion and for cardiac chamber quantification. Imaging parameters were: repetition time (TR) 3.1 ms, echo time (TE) 1.3 ms, asymmetric echo with factor 0.29, flip angle (FA) 45°, field of view (FOV) (276 × 340) mm^2, matrix 156 × 192, slice thickness 6 mm, receiver bandwidth (BW) 704Hz/px, parallel imaging using GRAPPA reconstruction (R = 2), 30 cardiac phases.

Table 1 Characteristics of the volunteers

Parameter	Result
Number	60
Females/Males	30/30
Age [years]	48 ± 17
Age group 20–39 years	20 (10 Males/10 Females)
Age group 40–59 years	20 (10 Males/10 Females)
Age group 60–80 years	20 (10 Males/10 Females)
Height [cm]	173 ± 9
Weight [kg]	76 ± 14
Body mass index [kg/m^2]	25 ± 4
Body surface area [m^2]	1.9 ± 0.2
Systolic blood pressure [mm/Hg]	132 ± 12
Diastolic blood pressure [mm/Hg]	72 ± 11
Heart rate [min^{-1}]	70 ± 6
LV enddiastolic volume [ml]	143 ± 35
LV enddiastolic volume index [ml/cm]	0.8 ± 0.2
LV ejection fraction [%]	64 ± 5
LV mass [mg]	101 ± 26
LV mass index [mg/cm]	0.6 ±0.2

T_2 mapping

For T_2 mapping, data were acquired in basal, midventricular, and apical SAX planes using a T_2-prepared single-shot SSFP technique similar to the one described for 1.5 T [2]. For the application on a 3 T platform, the RF pulse length of the SSFP readout module was increased to reduce the SAR deposition and adiabatic T_2 preparation pulses were employed to improve the homogeneity of the T_2 weighting. Three SSFP images, each with different T_2 preparation time (TE_{T2P} = 0 ms, 24 ms, 55 ms) were acquired in end-diastole within one breathhold. Imaging parameters were: TR = 2.4 ms, TE = 1 ms, FA = 70°, FOV = (340 × 278) mm^2, matrix = 176 × 144, slice thickness = 6 mm, BW = 1093Hz/px, GRAPPA acceleration factor 2, linear phase encoding scheme. To correct for residual cardiac and respiratory motion between image sets, a non-rigid registration algorithm was used [8]. A pixel-wise myocardial T_2-map was generated using unsupervised curve-fitting based on a two-parameter equation [2]. The single shot SSFP readout and use of only three TE_{T2P} was chosen to balance accuracy and acquisition time (7 heart cycles) [2,9].

T_1 mapping

For T_1 mapping, data were acquired in basal, midventricular, and apical SAX planes before and 10 - minutes after administration of 0.2 mmol/kg i.v. gadobutrol (Gadovist®, Bayer Healthcare Germany). Data were obtained in end-diastole using a cardiac-gated, SSFP-based Modified Look-Locker Inversion Recovery (MOLLI) technique [10]. For the application at 3 T, the RF pulse length of the SSFP readout module was increased to reduce the SAR deposition. Imaging parameters were: TR = 2.6-2.7 ms, TE = 1.0-1.1 ms, FA = 35°, FOV = (270 × 360)mm^2, matrix = 156 × 208 to 168 × 224, slice thickness = 6 mm, BW = 1045-1028Hz/px, GRAPPA acceleration factor 2, linear phase-encoding ordering, minimum TI of 91 ms. To generate a pixel-wise myocardial T_1-map, single-shot SSFP images were acquired at different inversion times (pattern 3-3-5, [10]) and registered [8] prior to a non-linear least-square curve fitting using $S(TI) = A - B \exp(-TI/T1^*)$ with $T1 = T1 \times (B/A - 1)$, where A, B, and T1* are estimated by a three parameter fit [11]. In-plane voxel dimensions were kept isotropic to

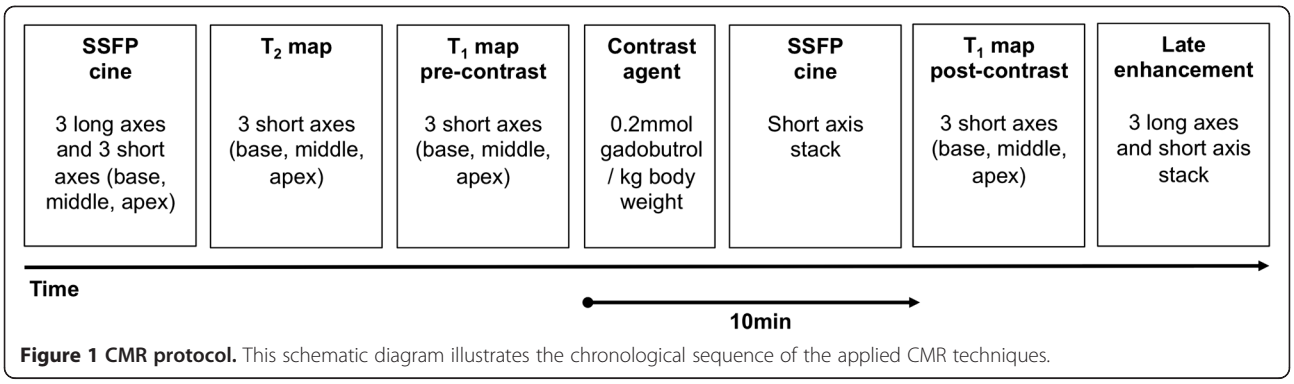

Figure 1 CMR protocol. This schematic diagram illustrates the chronological sequence of the applied CMR techniques.

ensure that partial volume effects are independent of slice rotation.

LGE imaging

LGE imaging was performed in the same planes as SSFP CINE imaging using a segmented inversion-recovery gradient-echo sequence beginning 15 minutes after contrast administration. The inversion time (TI) was repeatedly adjusted to appropriately null the myocardium during the length of LGE image acquisition. Imaging parameters were: TR = 10.5 ms, TE = 5.4 ms, FA = 30°, FOV (350 × 262) mm^2, matrix 256 × 162, slice thickness 6 mm, BW 140Hz/px, GRAPPA acceleration factor 2.

CMR image analysis

Image analysis was done using CMR[42] (Circle Cardiovascular Imaging, Calgary, Canada).

LV chamber quantification

SSFP cine images were visually evaluated regarding wall motion abnormalities. LV enddiastolic and endsystolic volume and LV mass were determined by manually contouring the endocardial and epicardial borders of the SAX in systole and diastole.

LGE assessment

The absence of LGE was determined qualitatively by visual assessment.

T_2 and T_1 mapping - qualitative assessment

Each single original image was assessed regarding artifacts caused by susceptibility effects, cardiac or respiratory motion. Each motion-corrected series was evaluated whether the images were correctly aligned. Each map was evaluated whether the original images were transformed to a reasonably appearing map. The presence of artifacts led to the exclusion of all affected myocardial segments. Two experienced readers assessed quality in consensus.

T_2 mapping - quantitative assessment

The LV myocardium was delineated by manually contouring the endocardial and epicardial border. We ensured that the region of interest (ROI) was definitely within the myocardium and did not include blood or epicardial fat based. An endocardial and epicardial contour was drawn in one original motion-corrected image. The trabeculated layer and the epicardial border were left out. In doubt, SSFP cine images were consulted. The contours were copied to the other images and adapted to fit in all of these. These final contours were copied to the map. The myocardial ROI was automatically segmented according to the AHA segment model [12]. Results are presented both per segment and averaged per slice.

T_1 mapping - quantitative assessment

T_1 values were recorded from pre-contrast and post-contrast T_1 maps applying the same procedure as for T_2.

T_2 and T_1 mapping - Observer dependency

Intra- and interobserver variability were tested in a subgroup of 20 randomly selected subjects (320 myocardial segments), where one observer measured T_2 and pre-contrast T_1 values of each LV segment twice with at least 3 months of time between the measurements. A second observer measured T_2 and pre-contrast T_1 values blinded to the other results.

Statistical analysis

Baseline characteristics are shown as means with standard deviation (SD) or absolute frequencies. Relaxation times are displayed as least-square means with 95% tolerance intervals (90% coverage) and were assessed by slice and by segment using mixed linear models on logarithmic transformed data to ensure normal distributed data. The following co-factors were included into each model to assess their impact on the relaxation times: age (categories), gender, heart rate (binary with split at median), blood pressure and excluded backwards if not significant. For T_1 and T_2, the scatter factor was

provided as back transformed SD, which allows a similar interpretation as the coefficient of variation for non-transformed data. All values presented were back transformed using the exponential to present the data on the original scale. Spearman's correlation coefficients were calculated to evaluate correlations between the co-factors, which may interfere with the modelling. A p-value of less than 0.05 was regarded as statistically significant. Calculations were performed using SAS 9.2 (SAS Institute Inc., Cary, NC, USA). Intra- and inter-observer dependency was assessed by Bland-Altman analysis and Pearson's correlation using Prism 5.0 (Graphpad Software, La Jolla, CA, USA).

Results

CMR

All 60 CMR scans were performed without major adverse events. The scans were incomplete in 4 subjects. T_2 maps were available for 58 subjects, pre-contrast T_1 maps for 59 subjects and post-contrast T_1 maps for 57 subjects.

T_2 mapping

From 922 segments, 901 (97.7%) were eligible for analysis (Figure 2). A full set of original data and corresponding maps is available as additional file (see Additional file 1). Twenty-one segments (2.3%) were excluded due to a susceptibility artifact (Figures 2 and 3) mainly in the inferior/inferolateral wall (18 out of 21; 85.7%). Exclusion of at least one segment affected 12 out of 58 subjects (20.7%).

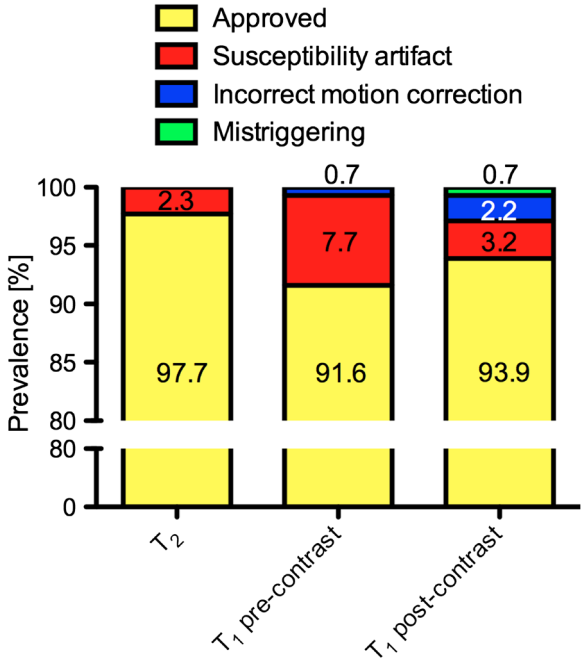

Figure 2 Quality assessment of T_2 and T_1 maps. The bar graphs show the prevalence of images approved as evaluable, as well as the frequency of susceptibility artifacts, incorrect motion correction, and mistriggering for each technique.

T_2 relaxation times per slice are shown in Table 2. Mean value was 44.1 ms (base), 45.1 ms (middle) and 46.9 ms (apex). All slices differed significantly ($p < 0.0001$) with increasing values from base to apex.

T_2 values for each myocardial segment are presented in Figure 4. Significant segment-to-segment differences were observed in the basal slice ($p = 0.0036$) with slightly lower values in the anterior wall compared to inferior. No significant segment-to-segment differences were found for the midventricular ($p = 0.5398$) and apical slices ($p = 0.1367$). The distribution of all individual T_2 results is illustrated in Figure 5. A relevant inter-subject variability was evident as indicated by a scatter factor of 1.08 (Figure 5 and Table 2).

Heart rate (ranging from 47 to 102 min^{-1}) was found to significantly influence T_2 measurements ($p < 0.0001$). A heart rate higher than the median (69.5 min^{-1}) was associated with lower T_2 values (base: 42.8 ms vs. 45.8 ms; middle: 43.9 ms vs. 46.5 ms; apex: 45.7 ms vs. 48.2 ms). Other tested cofactors including age and gender were not found to be significant.

Pre-contrast T_1 mapping

For pre-contrast T_1 mapping 938 segments were obtained. 859 (91.6%) were eligible for analysis (Figure 2). A full set of original data and corresponding maps is available as additional file (see Additional file 2). Seventy-two segments (7.7%) were excluded due to a susceptibility artifact and 7 segments (0.7%) due to incorrect motion correction (Figures 2, 6 and 7). In 63 out of 72 segments (87.5%) with susceptibility artifact, the inferior/inferolateral segments were affected. Exclusion of at least one segment affected 34 out of 59 subjects (57.6%).

T_1 relaxation times per slice are shown in Table 2. Mean value was 1157.1 ms (base), 1158.7 ms (middle) and 1180.6 ms (apex). Apical T_1 relaxation times were significantly larger than basal and midventricular (each $p < 0.0001$).

T_1 values for each myocardial segment are shown in Figure 4. A significant segment-to-segment difference was found for each slice (basal: $p < 0.0001$; mid: $p < 0.0001$; apex: $p = 0.0153$). T_1 of the anterior segment was lower than in the other segments. The distribution of all individual T_1 results is illustrated in Figure 5. A relevant inter-subject variability was found with a scatter factor of 1.05 (Figure 5, Table 2).

The age categories were found to significantly influence myocardial T_1 relaxation times ($p < 0.0001$). The difference was small between age category 20–39 years

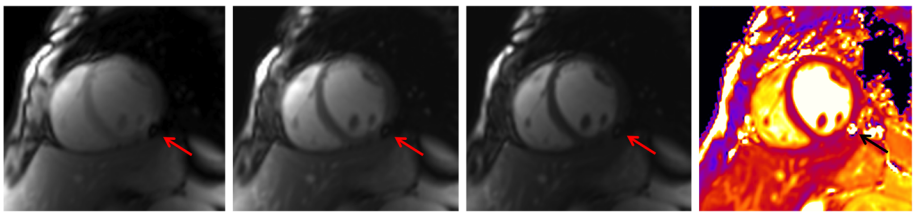

Figure 3 T_2 mapping artifact. Susceptibility artifact in the inferolateral wall of the midventricular plane (red arrow; the 3 grayscale images represent the T_2-prepared SSFP images with different T_2 preparation times). In the map (right image), the artifact is visible in the same area (black arrow).

and 40–59 years. A clear decrease of T_1 relaxation times was observed for subjects ≥ 60 years (Figure 8). Other tested cofactors including heart rate and gender were not found to be significant.

Post-contrast T_1 mapping

For post-contrast T_1 mapping 841 out of 896 segments (93.9%) were eligible for analysis (Figure 2). Twenty-nine segments (3.2%) were excluded due to a susceptibility artifact, which mainly affected the inferior/inferolateral segments (25 out of 29; 86.2%). Six segments (0.7%) were excluded due to mistriggering (all in one subject). Motion correction failed in one subject in all planes and in one subject in the apical plane leading to an exclusion of 20 segments (2.2%). Exclusion of at least one segment affected 18 out of 56 subjects (32.1%).

T_1 relaxation times per slice are shown in Table 2. Mean values of 427.3 ms (base), 411.2 ms (middle) and 399.7 ms (apex) were obtained. All slices differed significantly from each other (base vs. middle: $p < 0.0001$; base vs. apex $p < 0.0001$; middle vs. apex: $p = 0.0013$) with decreasing T_1 values from base to apex.

T_1 values for each myocardial segment are shown in Figure 4. No significant segment-to-segment differences were observed for each slice (basal: $p = 0.4918$; mid: $p = 0.4741$; apex: $p = 0.5629$). The distribution of all individual T_1 results is illustrated in Figure 5. Post-contrast T_1-maps revealed a relevant inter-subject variability reflected by a scatter factor of 1.11 (Figure 5, Table 2).

Heart rate was found to significantly influence the post-contrast T_1 relaxation time ($p = 0.0020$) with higher heart rates than the median (69.5 bpm) being associated with lower post-contrast T_1 relaxation times (base: 445.7 ms vs. 418.7 ms; middle: 430.1 ms vs. 405.3 ms; apex: 427.6 ms vs. 388.0 ms). Other tested cofactors including age and gender were not found to be significant.

For T_2 and pre-contrast T_1 mapping inter- and intra-observer analysis demonstrated close agreement (Table 3).

Discussion

This study examined myocardial T_1 and T_2 mapping techniques at 3 T in a large sample of healthy volunteers. The main findings are: i) T_2 and T_1 mapping achieve a high grade of diagnostic image quality, although susceptibility artifacts entailed the exclusion of a limited number of myocardial segments from the analysis. ii) Observer dependency of T_2 and T_1 relaxation time quantification was low. iii) Mean values and 95% tolerance interval of myocardial T_2 and T_1 relaxation times are presented per slice and per segment and can be used as reference values specific for this MR setting. iii) An inter-subject distribution of T_2 and T_1 values became apparent and may constitute a limitation to define appropriate cut-offs.

Table 2 Myocardial T_2 and T_1 relaxation times [in ms] for each plane (base, middle, apex)

	Position	Least square mean	95% Tolerance interval	Min-Max
T_2 [ms]	Base	44.1	39.3 – 49.5	36.2 – 53.3
	Middle	45.1	39.9 – 50.1	37.9 – 57.0
	Apex	46.9	40.8 – 53.8	39.1 – 59.1
T_1 pre-contrast [ms]	Base	1157.1	1074.5 – 1246.0	965.6 – 1340.8
	Middle	1158.7	1074.0 – 1250.1	1005.3 – 1295.9
	Apex	1180.6	1073.9 – 1297.9	1106.3 – 1393.9
T_1 post-contrast [ms]	Base	427.3	363.2 – 502.7	284.5 – 520.1
	Middle	411.2	349.9 – 483.2	282.5 – 513.2
	Apex	399.7	323.0 – 494.6	260.6 – 519.5

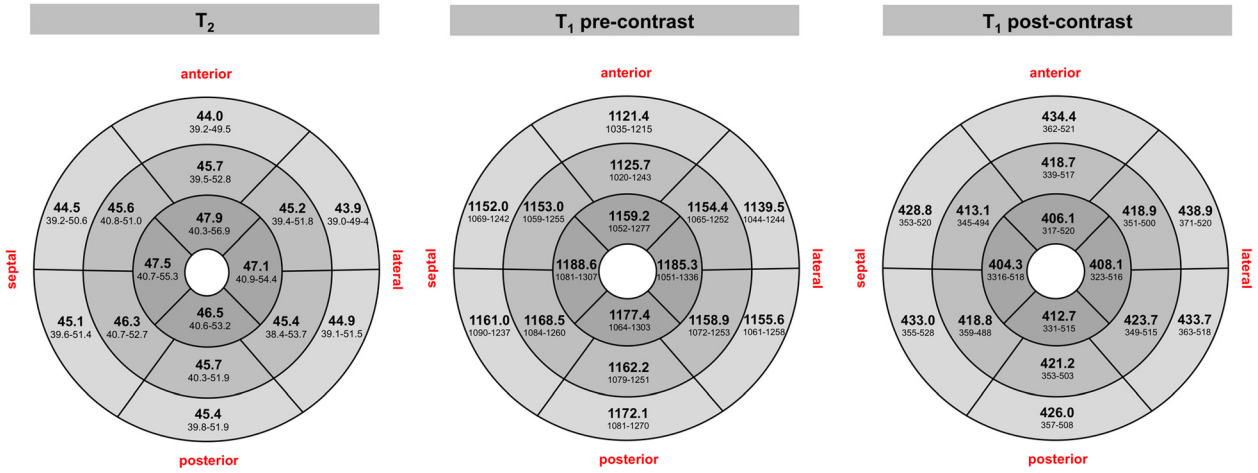

Figure 4 Mean T_2 and T_1 relaxation times. T_2 and T_1 relaxation times (ms) for each myocardial segment illustrated as a bulls eye plot that represents the 16 segments of the basal (outer ring), midventricular (middle ring) and apical (central ring) short-axis plane [12]. Results are given as least-square mean and 95% tolerance interval.

T_2 mapping

Previous studies with SSFP-based T_2 mapping at 1.5T did not report the exclusion of segments from analysis due to SSFP off-resonance or banding artifacts [2-4]. Hence, this challenge seems to surface at higher field strengths due to the increase in the peak-to-peak B_0 inhomogeneity across the heart. The use of an appropriately selected delta frequency may be an option to resolve some artifacts and deserves further systematic investigation. The artifacts mainly affected the inferolateral region, where pathologies like myocarditis may also exhibit their predominant lesion [13]. Despite that, the step from 1.5 T to 3 T for CMR is generally desired due to expected gains in signal, which may be exploited for improved spatial and temporal resolution. This potential promises to enable more detailed insights into cardiac tissue in order to facilitate the early detection of myocardial disease.

T_2 relaxation times derived from T_2-prepared SSFP imaging in this study are higher compared to a black-blood multi-echo spin-echo approach at 3 T, which provided a mean value of $T_2 = 39.6$m sin the septum [14]. Myocardial T_2 reported here was found to be lower versus a mean $T_2 = 52.2$ ms reported for T2 prepared SSFP imaging at 1.5 T [2]. Possible explanations are: i) differences in the pulse sequence design, ii) differences in the spatial resolution, with lower resolution being associated with more partial volume and potentially higher T_2 values, and iii) T_1 relaxation effects due to higher T_1 values at 3 T versus 1.5 T. Generally, myocardial T_2 reported in the literature varies substantially, ranging from about 50 ms to 58 ms at 1.5 T [2]. The heterogeneity of data underlines that the measured T_2 relaxation time is very sensitive to cofactors and emphasizes the need to generate reference values specific for each technique and imaging setting.

Our results showed that T_2 increased from base to apex, which is in accordance with a recent work using a similar mapping technique at 1.5 T [15]. The most probable cause is partial-volume effects that increase towards the apex owing to the curvature of the left ventricle. To encounter this limitation, some groups exclude the apical slice from mapping to omit measurement errors [6]. We tried to minimize this error by carefully drawing the contours in the middle of the myocardium while leaving out the endocardial portion of the myocardium, as well as by using an isotropic spatial resolution as high as possible.

Most of the previous studies reported T_2 values averaged over all myocardial segments or only for a midventricular slice. By averaging T_2 values over the whole slice or the whole heart, focal T_2 deviations may be overlooked. The present study is the largest study, which reports T_2 values for each myocardial segment and slice.

As reported for the global T_2 values, the segmental T_2 values increased from base to apex. In comparison, Markl et al. reported T_2 values from 50.5 ms to 51.6 ms in the basal slice and 54.3 ms to 56.1 ms in the apical slice at 1.5 T [15].

The inter-subject variability of absolute T_2 values was relatively large both per-slice and per-segment. This finding is in concordance with Thavendiranathan et al., who described T_2 values ranging from about 50 ms to 62 ms in healthy controls [4], and with Giri et al., who reported that the apical region showed the most pronounced inter-subject variability [2]. The high inter-subject variability can be considered as the main challenge

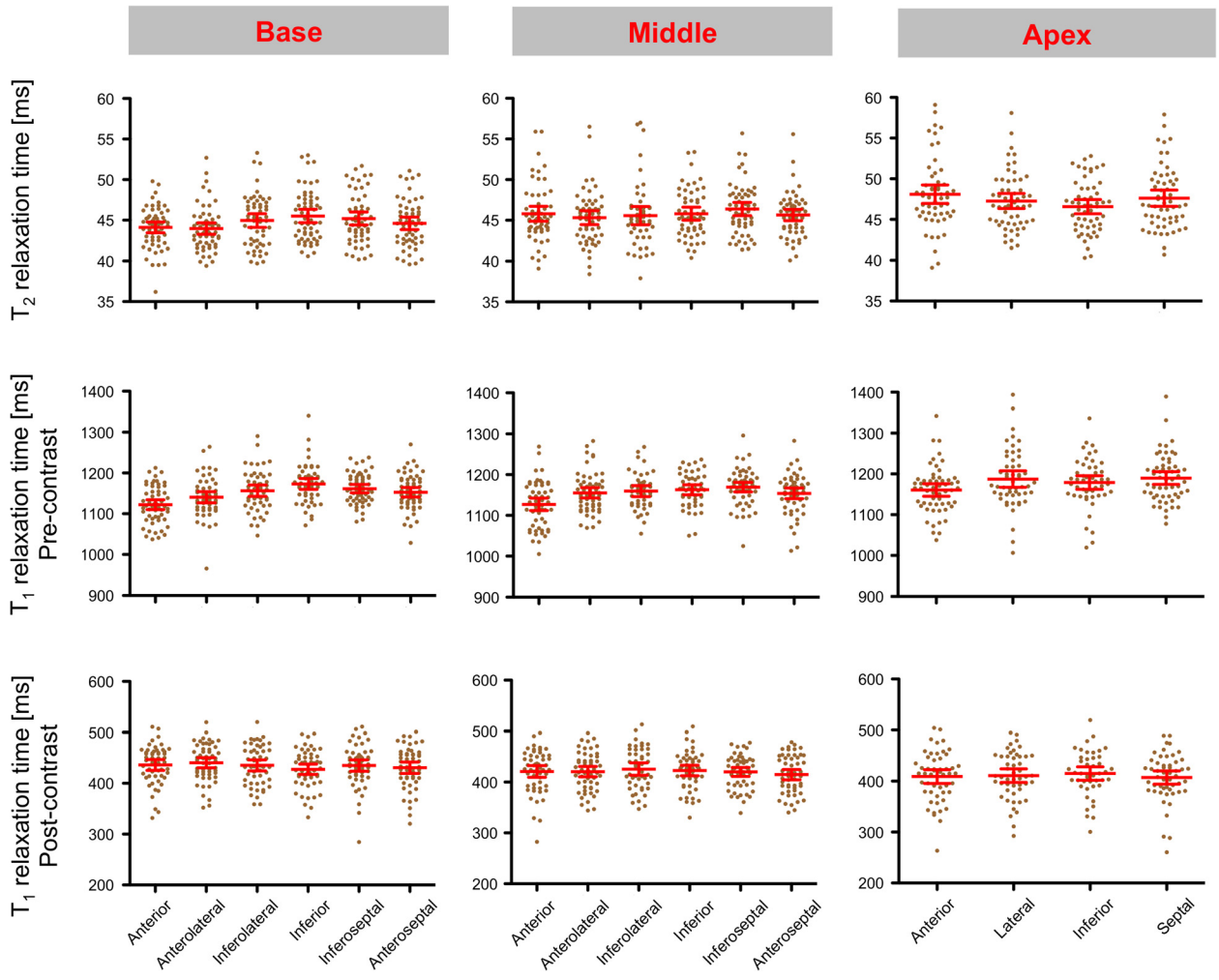

Figure 5 Individual T_2 and T_1 relaxation times. Distribution of all single individual T_2 and T_1 relaxation times in each myocardial segment. The red lines indicate the least-square mean and the 95% confidence interval.

of T_2 mapping, given that the difference in T_2 between healthy and injured myocardium has been reported to be relatively small, e.g. 13 ms/11 ms between infarct core/myocarditis and remote myocardium [3,4].

The association of heart rate and T_2 relaxation time is under discussion. Giri et al. reported that the variability between healthy subjects was unrelated to heart rate. Other studies reported lower T_2 values in patients with higher heart rate [1,4]. This may be attributed to the hypothesis that higher heart rates induce pronounced T_1 relaxation effects caused by incomplete T_1 relaxation, which may affect T_2 mapping using a SSFP-based approach. This finding is very relevant for clinical practice as subtle T_2 increases may disappear in acutely ill patients with higher heart rates.

T_1 mapping

T_1 mapping demonstrated diagnostic image quality for the vast majority of myocardial segments. However, a relevant number of myocardial segments had to be excluded due to technical challenges, which would lead to diagnostic uncertainty in a clinical scenario. Previous studies at 1.5 T and 3 T reported lower rates of artifact-related non-diagnostic segments [7,10,16,17]. The explicit source of the artifacts has not been reported in detail in most studies, which renders benchmarking against previous results challenging. A possible contributing factor might be that artifacts are often only visible in the original images - which are used for quality assessment - while they might be not apparent in the final maps. In our study, susceptibility artifacts in the inferolateral region were most frequent.

The pre-contrast T_1 values are in concordance with Piechnik et al., who reported T_1 = 1169 ms averaged over all myocardial segments [16]. At 3.0 T higher mid-ventricular T_1 values (T_1 = 1315 ms or T_1 = 1286 ms) were reported when using a T_1 mapping technique

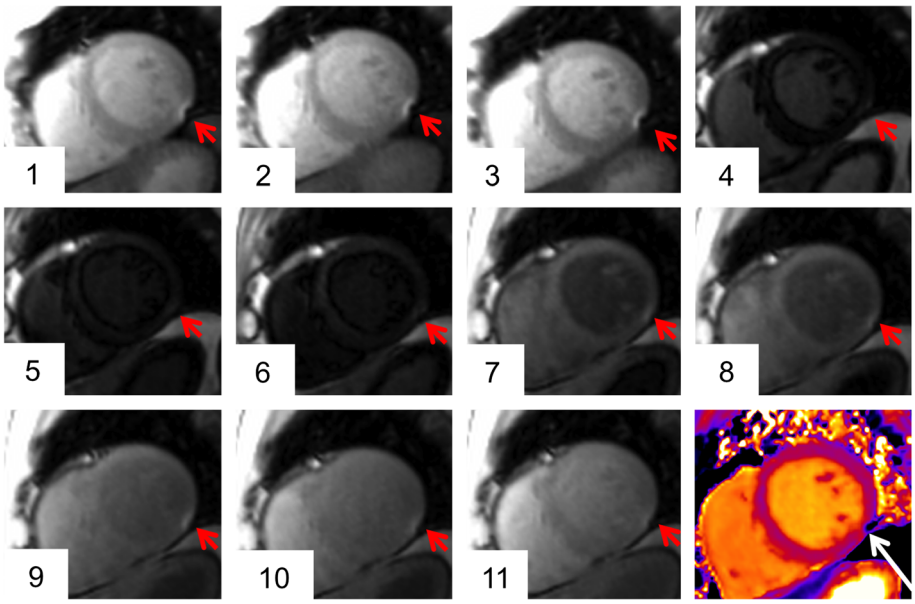

Figure 6 T_1 mapping artifact. Susceptibility artifact in the inferolateral wall of the midventricular plane (red arrow). The artifact was located at the border of the inferolateral and the inferior segment. In the corresponding map the artifact is hardly recognizable by visual assessment (white arrow).

similar to that used in this study [17,18]. These discrepancies underline that T_1 relaxation times are sensitive to many influencing factors.

The myocardial T_1 relaxation times reported here can be regarded as reference values specific only for this cohort, time point, mapping technique, type and dosage of contrast media. Further comparisons with other published results are difficult unless an identical study design is used. To provide a context, Lee et al. used 0.15 mmol Gadolinium DTPA and measured a mean T_1 of about 550 ms in one midventricular slice after 8.5 min in healthy human subjects at 3 T [17].

We observed that the pre-contrast T_1 times increased from base to apex, whereas the post-contrast T_1 values decreased from base to apex. Partial-volume effects owing to the curvature of the left ventricle can most probably explain this finding with blood signal being included into the voxel. While some completely exclude apical T_1 maps from analysis [6], we tried to minimize this error by excluding the endocardial portion of the myocardium and by choosing a high isotropic spatial resolution.

In agreement with Kawel et al. we did not observe significant segment-to-segment differences post-contrast [7]. However, pre-contrast T_1 values of the anterior segments were lower than T_1 observed for the other segments. Interestingly, Piechnik et al. observed the identical pattern with MOLLI at 3 T [16]. Kawel et al.

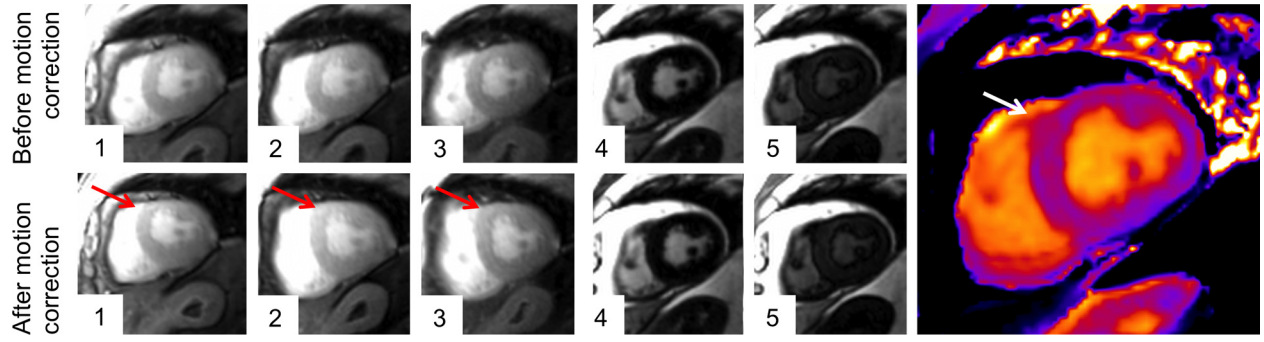

Figure 7 Failed motion correction during T_1 mapping. The original images (upper row) show the regular shape of the LV myocardium (the first five out of eleven images of the complete T_1 acquisition are depicted). The motion correction algorithm led to an outbound shift of the anterior and anteroseptal myocardial segment (red arrow in the bottom row). The corresponding map (right image) indicates an inhomogeneous T_1 distribution in this area (white arrow).

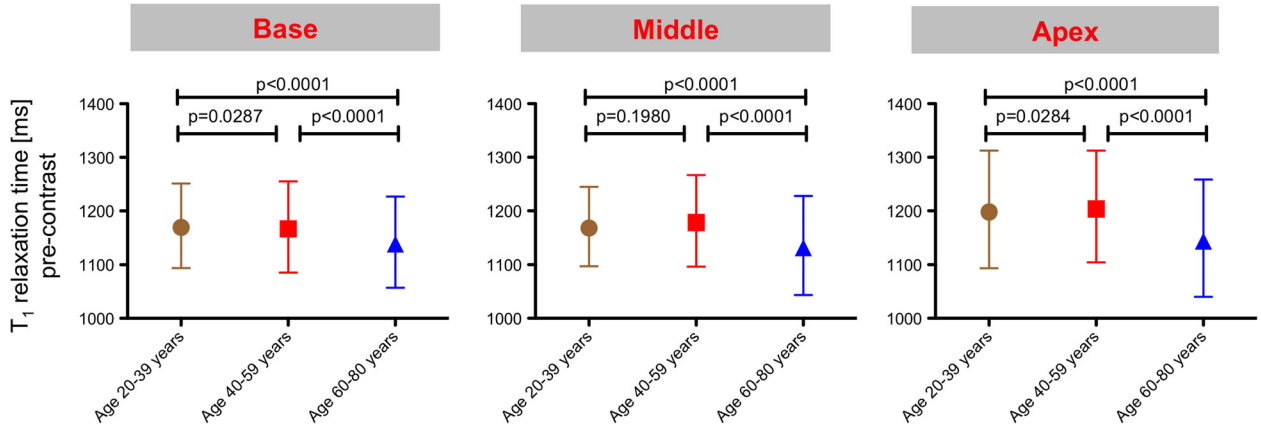

Figure 8 Age-dependency of T_1 times. Myocardial pre-contrast T_1 relaxation times grouped by age categories for each slice. Results are given as mean and 95% tolerance interval.

confirmed the presence of regional variability of pre-contrast T_1 values inspite of using a different classification into "septal" and "non-septal" myocardium [7]. Although absolute regional difference was small, this finding has to be considered in clinical CMR interpretation as the difference between healthy and abnormal tissue might be in a similar range.

The inter-subject variability of absolute T_1 values was notable both per-slice and per-segment, including extreme outliers. This finding is in concordance with other T_1 mapping studies reporting pre-contrast T_1 values at 1.5 T ranging from 862 ms to 1105 ms in healthy volunteers [19] and a coefficient of variation of 4.5% (pre-contrast) and 7.0% (post-contrast) [18]. The high inter-subject range may be the main challenge of T_1 mapping, given that the difference in T_1 times between healthy and injured myocardium has been reported to be relatively small depending on the underlying disease. Dall'Armellina et al. reported a mean pre-contrast T_1 value of 1257 ± 97 ms for acutely infarcted segments compared to 1196 ± 56 ms for normal unaffected segments at 3 T [20]. In other myocardial diseases like Fabry's disease or amyloidosis, pre-contrast T_1 may already be accurate enough to differentiate cardiac amyloid patients from normals [21].

Post-contrast T_1 in the present study was even more variable between subjects than pre-contrast T_1, attributable to the many factors with influence on the contrast kinetics (e.g. patient weight, hematocrit, renal function). Miller et al. recently demonstrated that even though isolated post-contrast T_1 measurement showed significant within-subject correlation with histological collagen volume fraction, the between-subject correlations were not significant. Hence, isolated post-contrast T_1 measurement seems to be insufficient for assessing extracellular volume fraction [22].

Aging was found to be associated with decreasing pre-contrast T_1 values. This is an interesting aspect that may reflect early age-dependent alterations of myocardial texture. Dall'Armellina et al. and Ugander et al. showed that pre-contrast T_1 times were increased in acute myocardial ischemia [20,23]. Dass et al. reported increase in pre-contrast T_1 in cardiomyopathies. Hence, the present reduction of pre-contrast T_1 with age may sound contradictory [24]. In contrast, in a rat model, diffuse myocardial fibrosis was associated with a non-significant trend towards lower pre-contrast T_1 values [25]. Therefore our data are stimulating to further analyze the value of pre-contrast T_1 mapping in non-ischemic heart disease in future.

Table 3 Intra- and inter-observer dependency of the segmental quantification of T_2 and pre-contrast T_1 relaxation times

Technique	Correlation coefficient r	Bland-Altman: Bias ± SD [ms]
T_2 – Intra-observer	0.95	0.0 ± 1.3
T_2 – Inter-observer	0.95	0.1 ± 1.1
T_1 – Intra-observer	0.93	4.6 ± 18.3
T_1 – Inter-observer	0.91	0.5 ± 20.2

Conclusion

In conclusion, myocardial T_2 and T_1 mapping at 3 T are feasible with a good diagnostic image quality, although susceptibility artifacts related to the magnetic field strength of 3 T triggered exclusion of myocardial segments from analysis. This study provides reference values for myocardial T_2 and T_1 relaxation times per slice and per segment for the specific MR setting, which were deduced from a large cohort of healthy volunteers.

With this approach a relatively high inter-subject distribution became apparent, which may constitute a relevant challenge for the definition of cut-offs that differentiate healthy from diseased myocardium in clinical practice.

Study limitations

i) As hematocrit was not measured in this study, its effect on T_2 and T_1 relaxation times could not be assessed. ii) Whereas observer variability to assess T_2 and T_1 relaxation times was low, the inter-scan variability was not assessed and deserves further investigation. iii) Regarding T_1 estimation by the applied MOLLI technique, there are known limitations to inversion efficiency [26] and to evaluation of magnitude based data. The inversion efficiency is also dependent on T_2. At the time the study was designed, an improved inversion pulse designed for myocardial T_1 mapping tailored for myocardial T_2 was not available yet. The limitations of evaluating T_1 based on magnitude images are described in a recent publication [27]. By the time the study was designed, the proposed phase-sensitive recon was not yet available on our system.

Additional files

Additional file 1: T_2-mapping. A full set of T_2-weighted SSFP single shot images with 3 different T_2 preparation times and the corresponding T_2 maps from the basal, midventricular and apical slice.

Additional file 2: T_1-mapping. A full set of T_1-weighted SSFP single-shot images and the corresponding pre-contrast T_1 maps from the basal, midventricular and apical slice.

Competing interests

The co-author A. Greiser is employee of Siemens Healthcare, Germany. The other authors declare that they have no competing interests.

Authors' contributions

FvKB defined the design of the study, headed its coordination, acquired the image data, read the images, assisted in statistical analysis and drafted the manuscript. MP contributed to the analysis and interpretation of the data and was involved in drafting the manuscript. MD made contributions to acquisition of data and was involved in drafting the manuscript. RW and AG made substantial contributions to the analysis and interpretation of the data and were involved in drafting the manuscript. CS participated in the design of the study, performed the statistical analysis and was involved in drafting the manuscript. TN made substantial contributions to the acquisition, analysis and interpretation of the data and was involved in drafting the manuscript. JSM defined the design of the study, headed its coordination, assisted in statistical analysis and interpretation of the data, and drafted the manuscript. All authors read and approved the final manuscript.

Acknowledgements

The authors wish to acknowledge the technicians Kerstin Kretschel, Evelyn Polzin, Denise Kleindienst and Franziska Neumann for assisting in acquiring the CMR data, and the study nurses Elke Nickel-Szczech and Antje Els for assisting in the organization of the CMR scans.
This project was supported by a grant of the Else Kröner-Fresenius Stiftung (Bad Homburg, Germany).

Author details

[1]Berlin Ultrahigh Field Facility, Max-Delbrueck Center for Molecular Medicine, Berlin, Germany. [2]Working Group on Cardiovascular Magnetic Resonance, Experimental and Clinical Research Center a joint cooperation between the Charité Medical Faculty and the Max-Delbrueck Center for Molecular Medicine HELIOS Klinikum Berlin Buch, Department of Cardiology and Nephrology, Lindenberger Weg 80, 13125, Berlin, Germany. [3]Siemens Healthcare, Erlangen, Germany. [4]Scossis, Berlin, Germany. [5]Experimental and Clinical Research Center, a joint cooperation between the Charité Medical Faculty and the Max-Delbrueck Center for Molecular Medicine, Berlin, Germany.

Received: 13 February 2013 Accepted: 3 June 2013
Published: 18 June 2013

References

1. Messroghli DR, Niendorf T, Schulz-Menger J, Dietz R, Friedrich MG. **T1 mapping in patients with acute myocardial infarction.** *J Cardiovasc Magn Reson.* 2003; **5:**353–9.
2. Giri S, Chung YC, Merchant A, Mihai G, Rajagopalan S, Raman SV, Simonetti OP. **T2 quantification for improved detection of myocardial edema.** *J Cardiovasc Magn Reson.* 2009; **11:**56.
3. Verhaert D, Thavendiranathan P, Giri S, Mihai G, Rajagopalan S, Simonetti OP, Raman SV. **Direct T2 quantification of myocardial edema in acute ischemic injury.** *JACC Cardiovasc Imaging.* 2011; **4:**269–78.
4. Thavendiranathan P, Walls M, Giri S, Verhaert D, Rajagopalan S, Moore S, Simonetti OP, Raman SV. **Improved detection of myocardial involvement in acute inflammatory cardiomyopathies using T2 mapping.** *Circ Cardiovasc Imaging.* 2012; **5:**102–10.
5. Flett AS, Hayward MP, Ashworth MT, Hansen MS, Taylor AM, Elliott PM, McGregor C, Moon JC. **Equilibrium contrast cardiovascular magnetic resonance for the measurement of diffuse myocardial fibrosis: preliminary validation in humans.** *Circulation.* 2010; **122:**138–44.
6. Wong TC, Piehler K, Meier CG, Testa SM, Klock AM, Aneizi AA, Shakesprere J, Kellman P, Shroff SG, Schwartzman DS, Mulukutla SR, Simon MA, Schelbert EB. **Association between extracellular matrix expansion quantified by cardiovascular magnetic resonance and short-term mortality.** *Circulation.* 2012; **126:**1206–16.
7. Kawel N, Nacif M, Zavodni A, Jones J, Liu S, Sibley CT, Bluemke DA. **T1 mapping of the myocardium: Intra-individual assessment of the effect of field strength, cardiac cycle and variation by myocardial region.** *J Cardiovasc Magn Reson.* 2012; **14:**27.
8. Xue H, Shah S, Greiser A, Guetter C, Littmann A, Jolly MP, Arai AE, Zuehlsdorff S, Guehring J, Kellman P. **Motion correction for myocardial T1 mapping using image registration with synthetic image estimation.** *Magn Reson Med.* 2012; **67:**1644–55.
9. MacFall JR, Riederer SJ, Wang HZ. **An analysis of noise propagation in computed T2, pseudodensity, and synthetic spin-echo images.** *MedPhys.* 1986; **13:**285–92.
10. Messroghli DR, Greiser A, Frohlich M, Dietz R, Schulz-Menger J. **Optimization and validation of a fully-integrated pulse sequence for modified look-locker inversion-recovery (MOLLI) T1 mapping of the heart.** *J Magn Reson Imaging.* 2007; **26:**1081–6.
11. Messroghli DR, Radjenovic A, Kozerke S, Higgins DM, Sivananthan MU, Ridgway JP. **Modified Look-Locker inversion recovery (MOLLI) for high-resolution T1 mapping of the heart.** *Magn Reson Med.* 2004; **52:**141–6.
12. Cerqueira MD, Weissman NJ, Dilsizian V, Jacobs AK, Kaul S, Laskey WK, Pennell DJ, Rumberger JA, Ryan T, Verani MS. **Standardized myocardial segmentation and nomenclature for tomographic imaging of the heart: a statement for healthcare professionals from the Cardiac Imaging Committee of the Council on Clinical Cardiology of the American Heart Association.** *Circulation.* 2002; **105:**539–42.
13. Abdel-Aty H, Boye P, Zagrosek A, Wassmuth R, Kumar A, Messroghli D, Bock P, Dietz R, Friedrich MG, Schulz-Menger J. **Diagnostic performance of cardiovascular magnetic resonance in patients with suspected acute myocarditis: comparison of different approaches.** *J Am Coll Cardiol.* 2005; **45:**1815–22.
14. Guo H, Au WY, Cheung JS, Kim D, Jensen JH, Khong PL, Chan Q, Chan KC, Tosti C, Tang H, Brown TR, Lam WW, Ha SY, Brittenham GM, Wu EX.

Myocardial T2 quantitation in patients with iron overload at 3 Tesla. *J Magn Reson Imaging.* 2009; **30:**394–400.
15. Markl M, Rustogi R, Galizia M, Goyal A, Collins J, Usman A, Jung B, Foell D, Carr J. **Myocardial T2-mapping and velocity mapping: Changes in regional left ventricular structure and function after heart transplantation.** *Magn Res Med.* 2012. epub ahead of print.
16. Piechnik SK, Ferreira VM, Dall'Armellina E, Cochlin LE, Greiser A, Neubauer S, Robson MD. **Shortened Modified Look-Locker Inversion recovery (ShMOLLI) for clinical myocardial T1-mapping at 1.5 and 3 T within a 9 heartbeat breathhold.** *J Cardiovasc Magn Reson.* 2010; **12:**69.
17. Lee JJ, Liu S, Nacif MS, Ugander M, Han J, Kawel N, Sibley CT, Kellman P, Arai AE, Bluemke DA. **Myocardial T1 and extracellular volume fraction mapping at 3 tesla.** *J Cardiovasc Magn Reson.* 2011; **13:**75.
18. Kawel N, Nacif M, Zavodni A, Jones J, Liu S, Sibley CT, Bluemke DA. **T1 mapping of the myocardium: intra-individual assessment of post-contrast T1 time evolution and extracellular volume fraction at 3T for Gd-DTPA and Gd-BOPTA.** *J Cardiovasc Magn Reson.* 2012; **14:**26.
19. Messroghli DR, Plein S, Higgins DM, Walters K, Jones TR, Ridgway JP, Sivananthan MU. **Human myocardium: single-breath-hold MR T1 mapping with high spatial resolution–reproducibility study.** *Radiology.* 2006; **238:**1004–12.
20. Dall'Armellina E, Piechnik SK, Ferreira VM, Si QL, Robson MD, Francis JM, Cuculi F, Kharbanda RK, Banning AP, Choudhury RP, Karamitsos TD, Neubauer S. **Cardiovascular magnetic resonance by non contrast T1-mapping allows assessment of severity of injury in acute myocardial infarction.** *J Cardiovasc Magn Reson.* 2012; **14:**15.
21. Karamitsos TD, Piechnik SK, Banypersad SM, Fontana M, Ntusi NB, Ferreira VM, Whelan CJ, Myerson SG, Robson MD, Hawkins PN, Neubauer S, Moon JC. **Noncontrast t1 mapping for the diagnosis of cardiac amyloidosis.** *JACC Cardiovasc Imaging.* 2013; **6:**488–97.
22. Miller CA, Naish J, Bishop P, Coutts G, Clark D, Zhao S, Ray SG, Yonan N, Williams SG, Flett AS, Moon JC, Greiser A, Parker GJ, Schmitt M. **Comprehensive validation of cardiovascular magnetic resonance techniques for the assessment of myocardial extracellular volume.** *Circ Cardiovasc Imaging.* 2013; **6:**373–83.
23. Ugander M, Bagi PS, Oki AJ, Chen B, Hsu LY, Aletras AH, Shah S, Greiser A, Kellman P, Arai AE. **Myocardial edema as detected by pre-contrast T1 and T2 CMR delineates area at risk associated with acute myocardial infarction.** *JACC Cardiovasc Imaging.* 2012; **5:**596–603.
24. Dass S, Suttie JJ, Piechnik SK, Ferreira VM, Holloway CJ, Banerjee R, Mahmod M, Cochlin L, Karamitsos TD, Robson MD, Watkins H, Neubauer S. **Myocardial tissue characterization using magnetic resonance noncontrast t1 mapping in hypertrophic and dilated cardiomyopathy.** *Circ Cardiovasc Imaging.* 2012; **5:**726–33.
25. Messroghli DR, Nordmeyer S, Dietrich T, Dirsch O, Kaschina E, Savvatis K, Oh-I D, Klein C, Berger F, Kuehne T. **Assessment of diffuse myocardial fibrosis in rats using small-animal Look-Locker inversion recovery T1 mapping.** *Circ Cardiovasc Imaging.* 2011; **4:**636–40.
26. Kingsley PB, Ogg RJ, Reddick WE, Steen RG. **Correction of errors caused by imperfect inversion pulses in MR imaging measurement of T1 relaxation times.** *Magn Reson Imaging.* 1998; **16:**1049–55.
27. Xue H, Greiser A, Zuehlsdorff S, Jolly MP, Guehring J, Arai AE, Kellman P. **Phase-sensitive inversion recovery for myocardial T1 mapping with motion correction and parametric fitting.** *Magn Reson Med.* 2013; **69:**1408–20.

doi:10.1186/1532-429X-15-53
Cite this article as: von Knobelsdorff-Brenkenhoff *et al.*: Myocardial T_1 and T_2 mapping at 3 T: reference values, influencing factors and implications. *Journal of Cardiovascular Magnetic Resonance* 2013 **15**:53.

Modular 32-Channel Transceiver Coil Array for Cardiac MRI at 7.0T

http://dx.doi.org/10.1002/mrm.24903

Isometric Handgrip Exercise During Cardiovascular Magnetic Resonance Imaging: Set-up and Cardiovascular Effects

http://dx.doi.org/10.1002/jmri.23924

OPEN ACCESS Freely available online

PLOS ONE

Characterization of Phase-Based Methods Used for Transmission Field Uniformity Mapping: A Magnetic Resonance Study at 3.0 T and 7.0 T

Flavio Carinci[1,2], Davide Santoro[1]*, Federico von Samson-Himmelstjerna[1,3,4], Tomasz Dawid Lindel[1,5], Matthias Alexander Dieringer[1,6], Thoralf Niendorf[1,6]

1 Berlin Ultrahigh Field Facility (BUFF), Max Delbrück Center for Molecular Medicine (MDC), Berlin, Germany, **2** Research Center Magnetic Resonance Bavaria (MRB), Würzburg, Germany, **3** Center for Stroke Research Berlin (CSB), Charitè Universitätsmedizin, Berlin, Germany, **4** Institute for Medical Image Computing, Fraunhofer MEVIS, Bremen, Germany, **5** Department of Medical Metrology, Physikalisch Technische Bundesanstalt (PTB), Berlin, Germany, **6** Experimental and Clinical Research Center (ECRC), a joint cooperation between the Charité Medical Faculty and the Max Delbrück Center for Molecular Medicine (MDC), Berlin, Germany

Abstract

Knowledge of the transmission field (B_1^+) of radio-frequency coils is crucial for high field ($B_0 = 3.0$ T) and ultrahigh field ($B_0 \geq 7.0$ T) magnetic resonance applications to overcome constraints dictated by electrodynamics in the short wavelength regime with the ultimate goal to improve the image quality. For this purpose B_1^+ mapping methods are used, which are commonly magnitude-based. In this study an analysis of five phase-based methods for three-dimensional mapping of the B_1^+ field is presented. The five methods are implemented in a 3D gradient-echo technique. Each method makes use of different RF-pulses (composite or off-resonance pulses) to encode the effective intensity of the B_1^+ field into the phase of the magnetization. The different RF-pulses result in different trajectories of the magnetization, different use of the transverse magnetization and different sensitivities to B_1^+ inhomogeneities and frequency offsets, as demonstrated by numerical simulations. The characterization of the five methods also includes phantom experiments and *in vivo* studies of the human brain at 3.0 T and at 7.0 T. It is shown how the characteristics of each method affect the quality of the B_1^+ maps. Implications for *in vivo* B_1^+ mapping at 3.0 T and 7.0 T are discussed.

Citation: Carinci F, Santoro D, von Samson-Himmelstjerna F, Lindel TD, Dieringer MA, et al. (2013) Characterization of Phase-Based Methods Used for Transmission Field Uniformity Mapping: A Magnetic Resonance Study at 3.0 T and 7.0 T. PLoS ONE 8(3): e57982. doi:10.1371/journal.pone.0057982

Editor: Essa Yacoub, University of Minnesota, United States of America

Received October 4, 2012; **Accepted** January 30, 2013; **Published** March 5, 2013

Funding: This study was funded through institutional funding by the Max Delbrück Centrum for Molecular Medicine. The funders had no role in study design, data collection and analysis, decision to publish, or preparation of the manuscript.

Competing Interests: The authors have declared that no competing interests exist.

* E-mail: davide.santoro.73@gmail.com

Introduction

Non-uniformities of the transmission radio-frequency (RF) field (B_1^+) constitute an adverse factor for high field ($B_0 = 3.0$ T) and ultrahigh field ($B_0 \geq 7.0$ T) magnetic resonance (MR), which may render diagnostics challenging. This practical impediment is pronounced when imaging techniques sensitive to the excitation flip angle (FA) are applied. The knowledge of the B_1^+ field distribution is essential to correct for B_1^+ non-uniformities of single channel or multi-channel transmit (TX) RF-coils. To trim or shim the B_1^+ field, multiple channel transmission has been pioneered [1–3]. For this purpose, multi transmit arrays are used, which require B_1^+ mapping routines to calibrate each individual RF coil element. This procedure can be time consuming when using TX arrays comprising many transmit elements. Consequently accurate and fast B_1^+ distribution mapping is the key for ultrahigh field clinical applications.

B_1^+ mapping approaches commonly used are mainly magnitude-based and are generally confined to the ratios or the fit of signal intensity images [4–11]. For this purpose sets of images are acquired using either two flip angles [4–6], identical flip angles but different repetition times (TR) [7], variable flip angles [8,9] or also signals from spin-echoes and stimulated-echoes [10], as well as signals from gradient-echoes and stimulated-echoes [11]. For most of these magnitude-based approaches the quantitative B_1^+ evaluation may be influenced by saturation effects given by T_1 relaxation. This problem can be overcome with the use of long repetition times (TR), which, however, would result in prolonged acquisition times. Alternatively, phase-based methods have been proposed as they are insensitive to T_1 relaxation. They were also found to be more accurate than magnitude-based methods, especially at low flip angle regimes [12].

Realizing the advantages of phase-based methods for B_1^+ mapping, this work characterizes five of these methods: **A)** an optimized version for high field proton MRI [13] of the low flip angle method proposed by Mugler [14,15] here named "*Optimized low-flip-angle method*", **B)** the phase sensitive method of Morrell [16] here named "*Phase-sensitive method*", **C)** the phase-based method of Santoro [17,18], applied to high field proton MRI [19] here named "*ΦFA-CUP method*", **D)** the Bloch-Siegert shift method of Sacolick [20–22] here named "*Bloch-Siegert method*" and **E)** the orthogonal pulses method proposed by Chang [23] here named "*Orthogonal-pulses method*". These phase-based methods share in common the use of a composite or off-resonance RF-pulse to encode the spatial B_1^+ magnitude information into the phase of the magnetization vector (**M**). Each method uses a different scheme of

the RF-phases, generating a different evolution of **M**. The sensitivity to B_1^+ variations and frequency offsets is examined using numerical simulations of the Bloch equations. Phantom experiments and human brain imaging studies are conducted at 3.0 T and 7.0 T to scrutinize each method. This includes the assessment of repetition times achievable, according to specific absorption rate (SAR) levels, as well as the susceptibility to off-resonance effects. For a balanced comparison, all methods are used in conjunction with the same reading module.

Materials and Methods

Theory

The B_1^+ mapping methods analyzed in this work make use of a *complex* RF-pulse envelope (a rectangular composite pulse or an off-resonance Fermi pulse) for excitation, with separately controlled amplitude and phase (Fig. 1). Each pulse achieves a different trajectory of the magnetization **M**, depending on the combination of amplitude and phase of the RF-pulse. The trajectories of **M** for the five pulses are depicted in Fig. 2 for the ideal case where $\Delta B_0 = 0$. The presence of B_0 inhomogeneities, or other sources of frequency offsets, results in deviations from the ideal trajectory.

All the five trajectories can be represented by a different polygon lying on the surface of a unitary sphere. Each of them is characterized by a different number of sides and it is traversed a different number of times: **A** – ***Optimized low-flip-angle method***) a squared trajectory which is traversed for one and a half turns [13–15], **B** – ***Phase-sensitive method***) a rectangular trajectory which is traversed for a half turn [16], **C** – ***ΦFA-CUP method***) an off-origin loop trajectory which is traversed for a single turn [17–19], **D** – ***Bloch-Siegert method***) an initial excitation followed by an off-resonance pulse (which is equivalent to traversing a small circular trajectory for several turns) [20–22] and **E** – ***Orthogonal-pulses method***) a square trajectory which is traversed for a half turn [23].

At the end of each RF-pulse, the local magnetization presents a phase accrual depending on the local B_1^+ intensity and frequency offset experienced, as shown in the curves of Fig. 3. The theoretical description of this effect has been already reported in [16,18,20,23], and is briefly resumed here.

For methods **A**, **B**, **C** and **E** the RF-pulse can be divided into sub-pulses of flip-angle α and RF-phase Φ, denoted with α_Φ. Each sub-pulse α_Φ represents a rotation about a different axis, due to their different RF-phase. The magnetization accumulates a phase shift which is proportional to the local B_1^+ field intensity because of the non-commutativity of rotations about different axes.

Method **D,** after the initial excitation, uses an off-resonance RF-pulse. In this case the RF-phase varies linearly within the pulse and the magnetization accumulates a phase shift proportional to the local B_1^+ field intensity, due to the well-known Bloch-Siegert shift effect [24].

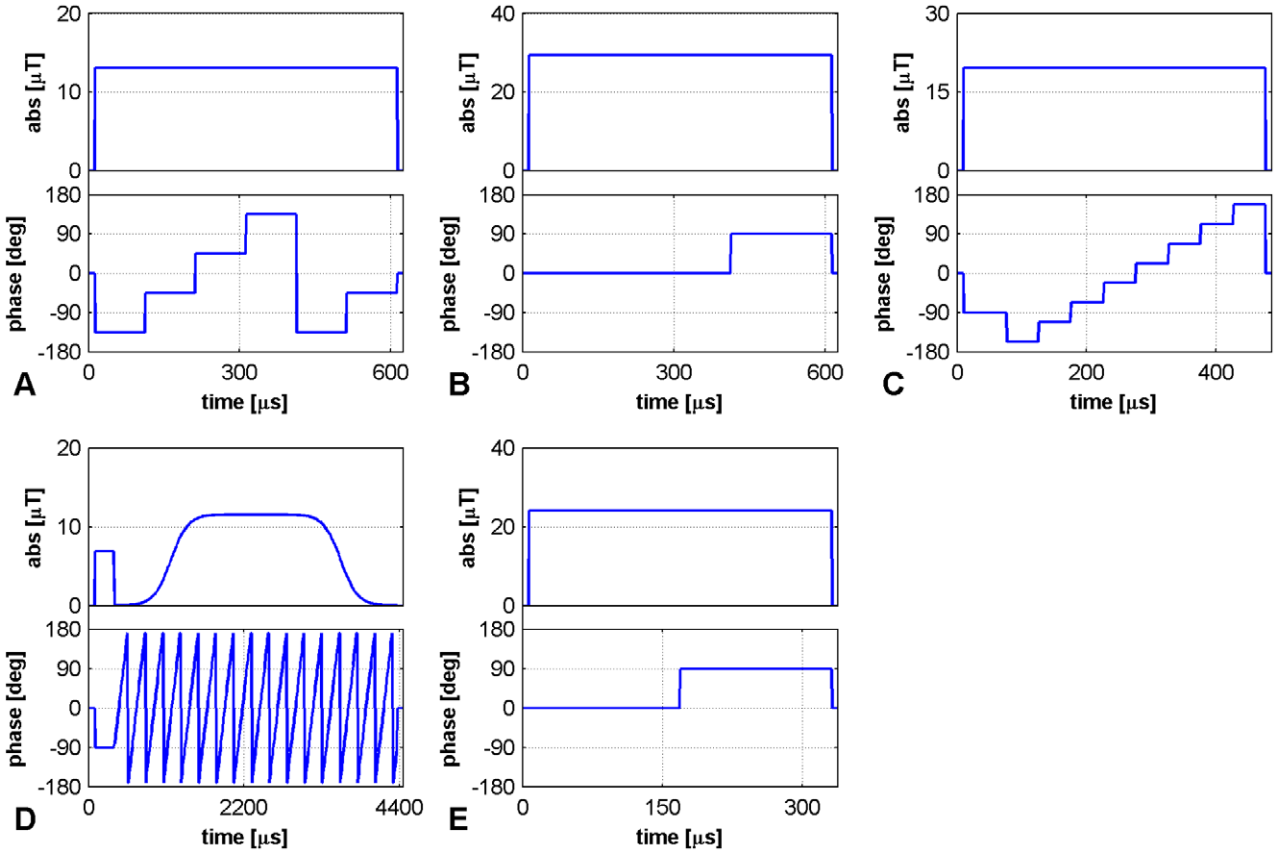

Figure 1. RF-pulse envelopes for phase-based B_1^+ mapping. Diagrams of the composite pulses used for all methods: **A –** *Optimized low-flip-angle method*, **B –** *Phase-sensitive method*, **C –** *ΦFA-CUP method*, **D –** *Bloch-Siegert method*, **E –** *Orthogonal-pulses method*. Pulse timing, intensity of the B_1^+ field (in μT) and RF-phases (in degrees) are sketched. The parameters used are: **A)** $\alpha = 20^\circ$ and duration of 600 μs; **B)** $\alpha = 90^\circ$ and duration of 600 μs; **C)** *p0* $= 20^\circ$, $\alpha = 15^\circ$ and duration of 400 μs (plus the duration of the *p0* pulse); **D)** *p0* $= 20^\circ$, $\alpha = 425^\circ$ and duration of 4000 μs (plus the duration of the *p0* pulse); **E)** $\alpha = 60^\circ$ and duration of 325 μs.
doi:10.1371/journal.pone.0057982.g001

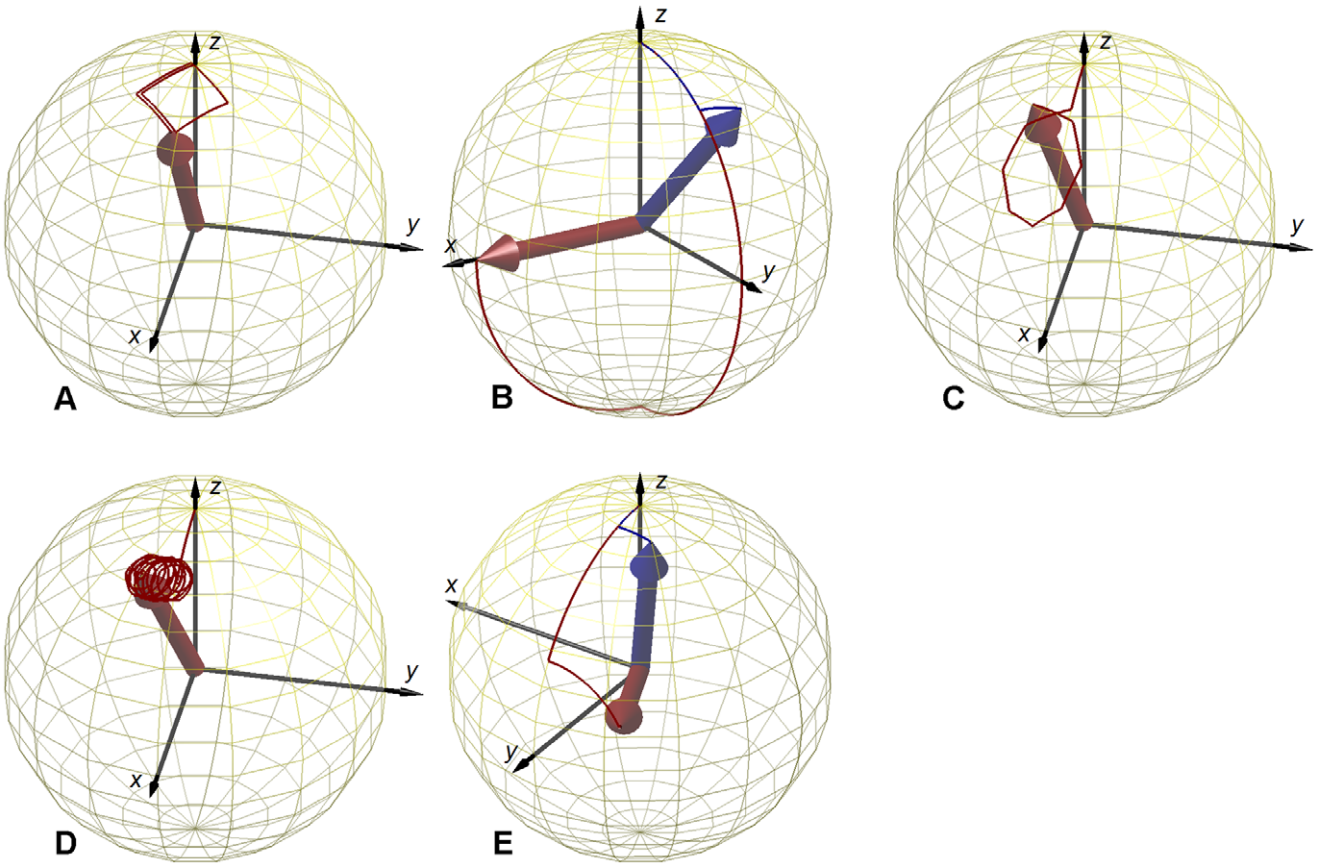

Figure 2. Trajectories of the magnetization during RF-excitation. Evolution of **M** in a unitary sphere during the RF-pulses of Fig.1 (red lines), under ideal conditions ($\Delta B_0 = 0$) for all methods: **A –** *Optimized low-flip-angle method*, **B –** *Phase-sensitive method*, **C –** *ΦFA-CUP method*, **D –** *Bloch-Siegert method*, **E –** *Orthogonal-pulses method*. **A)** a squared trajectory is traversed for one and a half turns; **B)** for small flip angles a rectangular trajectory is traversed for half turn (blue line: $\alpha = 18^\circ$), the flip angle originally proposed moves **M** into the transverse plane (red line: $\alpha = 90^\circ$); **C)** an intial pulse moves **M** far from the origin, then an octagonal loop is traversed for one turn only; **D)** an initial excitation is followed by an off-resonance pulse, which is equivalent to traversing a circular trajectory for several turns; **E)** for small flip angles a square trajectory is traversed for half turn (blue line: $\alpha = 12^\circ$), the flip angle originally proposed moves **M** close to the transverse plane (red line: $\alpha = 60^\circ$).
doi:10.1371/journal.pone.0057982.g002

To cancel phase contributions due to sources other than B_1^+, such as the receive coil sensitivity (B_1^-), the acquisition of two phase images, obtained with opposite senses of rotation of the magnetization (opposite RF-phase schemes), is required for all methods. The subtraction of the images preserves the B_1^+ information, while removing all other time-independent phase contributions.

A – Optimized low-flip-angle method. Excitation is performed by the application of the non-selective composite pulse: $[\alpha_{-135}\ \alpha_{-45}\ \alpha_{45}\ \alpha_{135}\ \alpha_{-135}\ \alpha_{-45}]$ (Fig. 1A). The pulse moves the magnetization vector about a square, of side length α, through 1.5 turns (Fig. 2A) [13]. A second image must be acquired using a corresponding pulse that moves the magnetization in the opposite sense of rotation: $[\alpha_{-45}\alpha_{-135}\alpha_{135}\alpha_{45}\alpha_{-45}\alpha_{-135}]$.

B – Phase-sensitive method. Excitation is performed by the application of the non-selective composite pulse: $[2\alpha_0\ \alpha_{90}]$ (Fig. 1B). For a small flip angle α the pulse moves the magnetization vector along a rectangular trajectory, with one side of length 2α and the other of length α, through 0.5 turns (Fig. 2B - blue line). The method is originally proposed using a nominal flip angle $\alpha = 90^\circ$ (which performs the trajectory in Fig. 2B - red line) [16]. A second image must be acquired with the first sub-pulse reversed in sign: $[2\alpha_{180}\ \alpha_{90}]$.

C – ΦFA-CUP method. Excitation is performed by the application of the non-selective composite pulse: $[p0_{-90}\ \alpha_{-157.5}\ \alpha_{-112.5}\ \alpha_{-67.5}\ \alpha_{-22.5}\ \alpha_{+22.5}\ \alpha_{+67.5}\ \alpha_{+112.5}\ \alpha_{+157.5}]$ (Fig. 1C). The magnetization vector is moved away from the origin by the first sub-pulse, named *p0*. The phase accrual is achieved by traversing for 1.0 turn an octagonal trajectory of side α shifted from the origin. The use of the first pulse *p0* separates the excitation from the phase accrual in order to optimize the sensitivity to B_1^+ variations [17,19]. A second image must be acquired with the composite pulse: $[p0_{+90}\ \alpha_{+157.5}\ \alpha_{+112.5}\ \alpha_{+67.5}\ \alpha_{+22.5}\ \alpha_{-22.5}\ \alpha_{-67.5}\ \alpha_{-112.5}\ \alpha_{-157.5}]$.

D – Bloch-Siegert method. This method makes use of an off-resonance pulse of frequency shift $\Delta\omega_{RF}$ applied immediately after an excitation: $[p0_{-90}\ \alpha_{-90,\Delta\omega}]$ (Fig. 1D). The off-resonance pulse moves the magnetization about a circular trajectory traversed several times (Fig. 2D). The number of loops is given by the duration of the pulse multiplied by the off-resonance frequency. The off-resonance pulse can be seen as a pulse in which the RF phase Φ is continuously varied during its duration τ, according to $\Phi = \Delta\omega_{RF}.\tau$. A second image must be acquired using the opposite frequency shift:

$-\Delta\omega_{RF}$. The method is originally proposed using an off-resonance Fermi pulse of frequency shift $\Delta\omega_{RF} = 4$ kHz and duration of 8 ms [20]. However it has been widely shown [21,22]

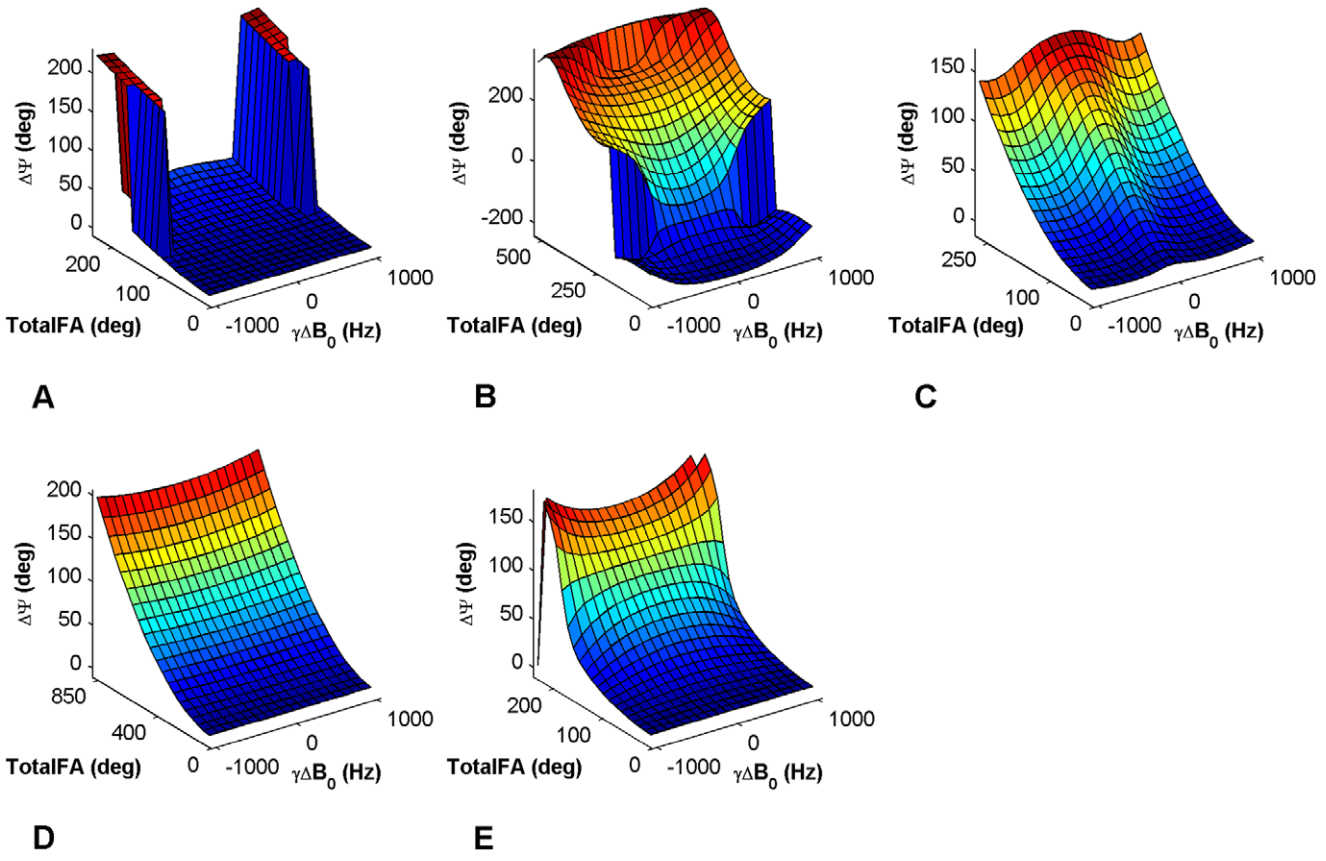

Figure 3. Curves of sensitivity to B_1^+ and B_0 inhomogeneities. Phase accrual curves of the five methods plotted versus the *TotalFA* of the RF-pulses and a frequency offset distribution -1 kHz $\leq \Delta B_0 \leq 1$ kHz. The frequency offset range is the same for all methods, while the *TotalFA* ranges differ, as well as the phase accrual Ψ. These curves were derived from simulations (using the same parameters as in Fig. 1) and used for the 2D interpolation to obtain the B_1^+ maps. Methods: **A –** *Optimized low-flip-angle method*, **B –** *Phase-sensitive method*, **C –** *ΦFA-CUP method*, **D –** *Bloch-Siegert method*, **E –** *Orthogonal-pulses method*.
doi:10.1371/journal.pone.0057982.g003

that different values of the pulse duration and frequency shift, as well as different pulse shapes, can be used to optimize this method. Here we used a Fermi pulse of frequency shift $\Delta\omega_{RF} = 4$ kHz and duration of 4 ms.

E – Orthogonal-pulses method. Excitation is performed by the application of the non-selective composite pulse: $[\alpha_0\ \alpha_{90}]$ (Fig. 1E). For a small flip angle α the pulse moves the magnetization vector along a square trajectory, with side of length α, through 0.5 turns (Fig. 2E – blue line). The method is originally proposed using a nominal flip angle $\alpha = 60^\circ$ (which performs the trajectory in Fig. 2E - red line) [23]. A second image must be acquired with the phases of the two sub-pulses swapped: $[\alpha_{90}\ \alpha_0]$.

Numerical Simulations

MATLAB (MathWorks Inc, Natick, USA) software was used to calculate the dynamics of the magnetization during the excitation pulses, by means of numerical simulations of the Bloch equations. A range of values of the frequency offset (-1 kHz $\leq \Delta B_0 \leq 1$ kHz, with an increment of 50 Hz) and of the B_1^+ intensity (rescaling the flip angle from 0 to 2 times the nominal value, with an increment of 0.05) was used. The sensitivity of the different methods to the local variations of the B_1^+ field and of the frequency offset is expressed by the variable Ψ (Fig. 3), which is defined as the subtraction of the phase accruals obtained from the two complementary scans required by each method. The intensity of the B_1^+ is expressed in terms of the total flip angle (*TotalFA*) used by each pulse, which results from the total duration and amplitude of the RF applied, regardless of its RF-phase scheme.

At high field strengths the *TotalFA* represents a crucial parameter, as the SAR levels limit the lowest achievable TR. This is especially the case for the methods used in this work, which require values of *TotalFA* of the order of several tens to a few hundred degrees. In order to quantify the efficiency (ε) of each method to convert the employed RF-power into a phase accrual Ψ the following variable was defined and calculated:

$$\varepsilon(TotalFA,\Delta B_o) = \frac{\Psi(TotalFA,\Delta B_o) - \Psi(0,0)}{TotalFA^2}\tau_{RF} \propto \frac{\Delta\Psi}{\mathrm{RSAR}} \quad (1)$$

where τ_{RF} is the total duration of the pulse.

MR Hardware

Phantom studies and *in vivo* experiments of the human brain were performed at magnetic field strengths of 3.0 T and 7.0 T. For this purpose, methods A-E were implemented on a clinical 3.0 T MR-scanner (TIM Verio, Siemens Healthcare, Erlangen, Germany) and a whole body 7.0 T MR-scanner (Magnetom, Siemens Healthcare, Erlangen Germany), using a dedicated sequence development environment (IDEA, Siemens Healthcare, Erlangen, Germany). At 3.0 T a transmit/receive (TX/RX) birdcage coil (Siemens Healthcare, Erlangen, Germany) operating in the circular polarized (CP) mode was used (diameter = 27 cm,

length = 31 cm). At 7.0 T a TX/RX birdcage coil (Siemens Healthcare, Erlangen, Germany) operating in the CP mode was used (diameter = 34 cm, length = 38 cm).

Implementation of the B_1^+ Mapping Techniques

The implementation comprises a standard 3D gradient-echo sequence, where the excitation is performed for each method by the non-selective RF-pulses sketched in Fig. 1 and described in the Theory section.

To reduce bulk motion effects the two images required by each method were acquired interleavedly. To examine and correct for variations in the main magnetic field (B_0) across the object ΔB_0 maps were acquired. For this purpose a secondary gradient-echo readout was added to the sequence; the ΔB_0 maps (Fig. 4) were obtained from the subtraction of the two phase images acquired at different echo times (TE) [25].

B_1^+ maps (Figs. 5–8) were calculated for each method from the measured phase accrual Ψ and the ΔB_0 map, using the corresponding curve of sensitivity of Fig. 3 as a lookup table and performing a linear 2D interpolation.

For comparison, a standard 3D gradient-echo technique was used to acquire three-dimensional B_1^+ maps using the double-angle method (DAM) [4]. This required the acquisition of two magnitude images with nominal flip angles of $\alpha = 60^\circ$ and $2\alpha = 120^\circ$ together with repetition times of $TR > 5T_1$ [5].

Specific Absorption Rate Adjustment

Each method uses a different RF-power level. Since the SAR represents the limiting factor for the minimum achievable TR at high field strengths for all methods, the RF-pulse amplitudes (i.e. the nominal B_1^+) were individually adjusted for each method in order to accomplish identical SAR levels, given a common repetition time. This corresponds to truncating the sensitivity curves of Fig. 3 to a *TotalFA* value which guarantees identical SAR levels for all methods. The TRs were adjusted in *in vivo* experiments - according to the volunteer weight - to achieve a nominal SAR level of 2.4 W/kg. This value corresponds to 75% of the SAR limit for the normal and first level operating modes for head imaging, as given by the IEC guidelines [26].

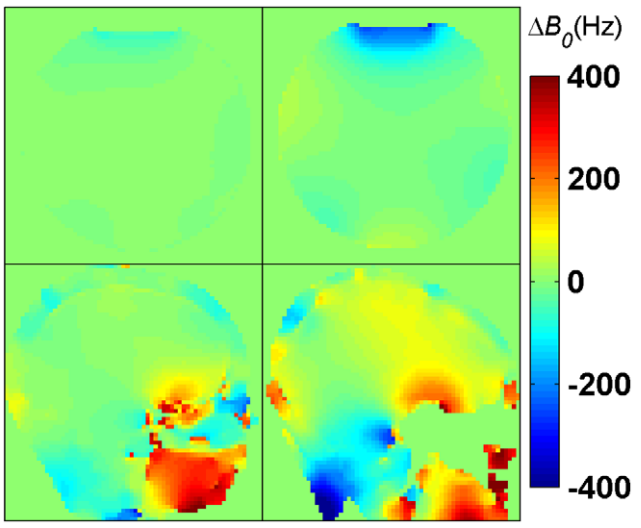

Figure 4. ΔB_0 maps in phantom and *in vivo* at 3.0 T and 7.0 T. Top: central axial partition of the 3D ΔB_0 maps obtained at 3.0 T (top-left) and at 7.0 T (top-right) in phantom with $\Delta TE = 2.5$ ms; strong B_0 offsets are visible at the air-water interface in the upper part of the phantom. Bottom: central sagittal partition of the 3D ΔB_0 maps of the human brain obtained at 3.0 T (bottom-left) with $\Delta TE = 2.46$ ms and at 7.0 T (bottom-right) with $\Delta TE = 3.06$ ms; strong B_0 offsets are visible in the sphenoid sinuses area and, at 7.0 T, in the neck region. All maps are in hertz.
doi:10.1371/journal.pone.0057982.g004

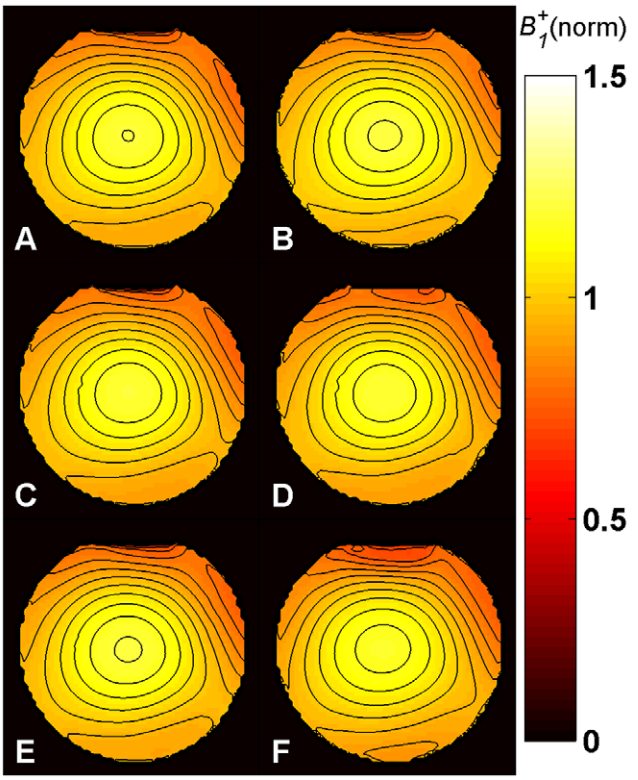

Figure 5. B_1^+ maps in phantom at 3.0 T. Central axial partition of the 3D B_1^+ maps obtained with methods **A**-**E** in phantom at 3.0 T using a birdcage TX/RX coil. Identical repetition times (TR = 30 ms) and SAR levels were used for all methods. The same partition of the B_1^+ map acquired for comparison with the DAM with TR = 500 ms is also shown (**F**). All maps are normalized to their nominal B_1^+ given in Table 1 in μT. The typical central spot of the birdcage TX/RX coil is visible. The contour plots (with contour increment of 0.05) show that the B_1^+ distributions obtained from the phase-based methods are consistent with the DAM. Methods: **A** – *Optimized low-flip-angle method*, **B** – *Phase-sensitive method*, **C** – *ΦFA-CUP method*, **D** – *Bloch-Siegert method*, **E** – *Orthogonal-pulses method*, **F** – *Double Angle method*.
doi:10.1371/journal.pone.0057982.g005

The nominal values of α, *TotalFA* and B_1^+ for the five methods are reported in Table 1, together with the duration of the RF-pulses and the repetition times. The nominal B_1^+ values are calculated starting from the reference voltage necessary to obtain a 1 ms rectangular π-pulse, and adjusted according to the duration τ and the *TotalFA* of the pulses of the five methods. The reported B_1^+ intensity represents the average value within the pulse. Identical parameters were used for both phantom and *in vivo* experiments.

Phantom Studies

A synopsis of the imaging parameters used for phantom studies at 3.0 T and 7.0 T is shown in Table 1. The basic imaging parameters were kept constant for all methods, including: field of view FOV = (200×200×200) mm^3, matrix size of 32×32×16 (plus zero-filling interpolation) and receiver bandwidth BW = 800 Hz/pixel. The echo times were set to the minimum possible value,

Table 1. Nominal values of the initial excitation angle (*p*0), flip angle of each sub-pulse (α), total flip angle (*TotalFA*), B_1+ intensity, total duration of the RF-pulses, echo times (TE) and repetition times (TR) for the experiments performed in phantom and *in vivo*, at 3.0 T and 7.0 T, with methods A–E.

Method	*p0*	α	*TotalFA*	Total Duration	B_1^+ intensity	TE	TR [ms] at 3.0 T	TR [ms] at 7.0 T
	[deg]	[deg]	[deg]	[μs]	[μT]	[ms]	phantom/*in vivo*	phantom/*in vivo*
A	-	20	120	600	13.0	1.55	30/30	110/110
B	-	40	120	600	13.0	1.42	30/30	110/110
C	20	15	140	490	14.6	1.47	30/30	110/110
D	20	250	270	4250	4.14	5.21	30/30	110/110
E	-	45	90	325	18.1	1.25	30/30	110/110
DAM	-	60	60	300	13.0	2.00	500/6000	500/6000
		120	120	600	13.0		500/6000	500/6000

Also the parameters for the comparison with the DAM are listed. The echo times are calculated relatively to the center of the first sub-pulse for each method.
doi:10.1371/journal.pone.0057982.t001

which depends on the pulse duration of each method. For ΔB_0 mapping an inter-echo time of $\Delta TE = 2.5$ ms was used. TRs needed to be prolonged at 7.0 T, in order to accomplish identical SAR levels as at 3.0 T.

A spherical phantom (18 cm diameter), filled with water and doped with 50 mM Na and 20 mM $CuSO_4$, was prepared. This setup provides sufficient RF-loading and short T_1 relaxation time

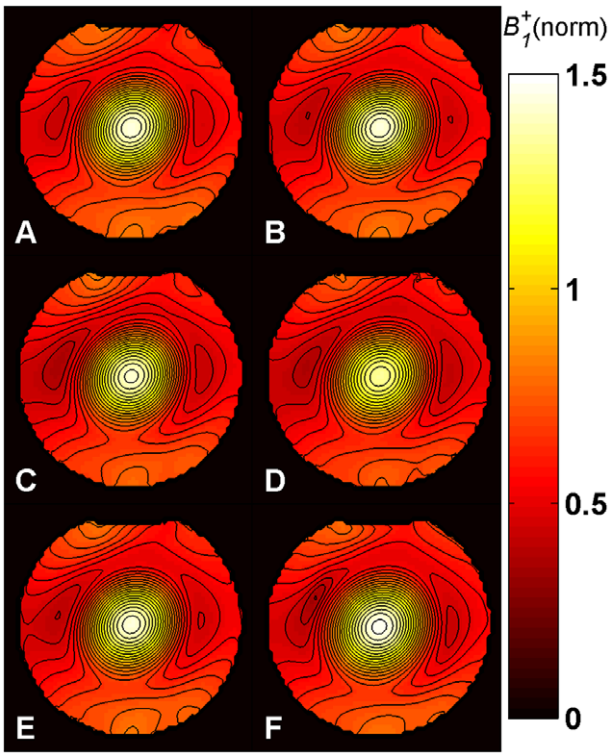

Figure 6. B_1^+ maps in phantom at 7.0 T. Central axial partition of the 3D B_1^+ maps obtained with methods **A**-**E** in phantom at 7.0 T using a birdcage TX/RX coil. Identical repetition times (TR = 110 ms) and SAR levels were used for all methods. The same partition of the B_1^+ map acquired for comparison with the DAM with TR = 500 ms is also shown (**F**). All maps are normalized to their nominal B_1^+ given in Table 1 in μT. The typical central spot of the birdcage TX/RX coil and the destructive interference patterns around it are visible. The contour plots (with contour increment of 0.05) show that the B_1^+ distributions obtained from the phase-based methods are consistent with the DAM. Methods: **A** – *Optimized low-flip-angle method*, **B** – *Phase-sensitive method*, **C** – *ΦFA-CUP method*, **D** – *Bloch-Siegert method*, **E** – *Orthogonal-pulses method*, **F** – *Double Angle method*.
doi:10.1371/journal.pone.0057982.g006

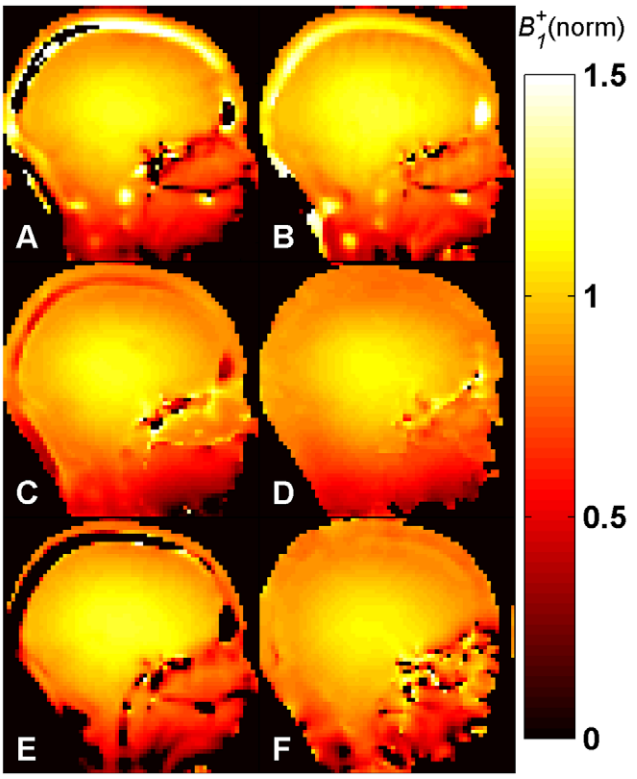

Figure 7. B_1^+ maps *in vivo* at 3.0 T. Central sagittal partition of the 3D B_1^+ maps of the human brain obtained with methods A-E *in vivo* at 3.0 T using a birdcage TX/RX coil. Identical repetition times (TR = 30 ms) and SAR levels were used for all methods. The central slice of the B_1^+ map acquired for comparison with the 2D DAM, with TR = 6000 ms, is also shown (**F**). All maps are normalized to their nominal B_1^+ given in Table 1 in μT. Methods: **A** – *Optimized low-flip-angle method*, **B** – *Phase-sensitive method*, **C** – *ΦFA-CUP method*, **D** – *Bloch-Siegert method*, **E** – *Orthogonal-pulses method*, **F** – *Double Angle method*.
doi:10.1371/journal.pone.0057982.g007

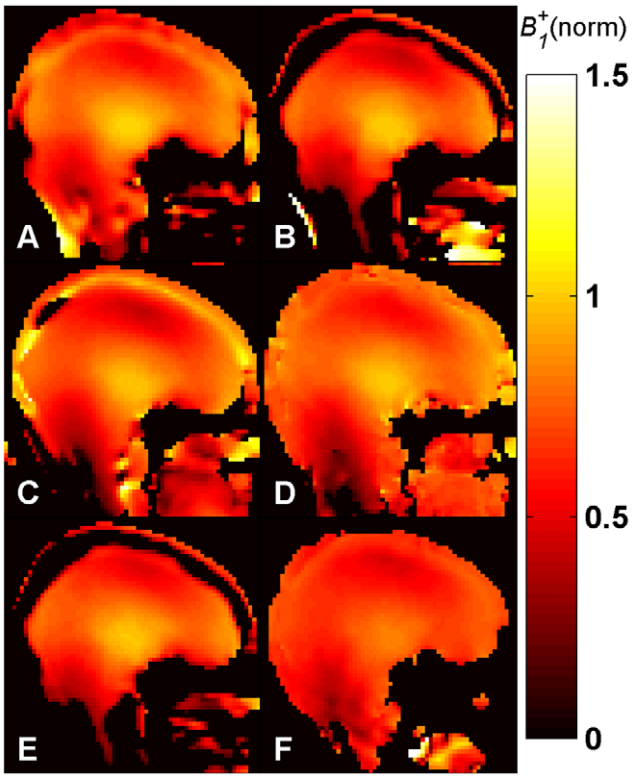

Figure 8. B_1^+ maps *in vivo* at 7.0 T. Central sagittal partition of the 3D B_1^+ maps of the human brain obtained with methods A-E *in vivo* at 7.0 T using a birdcage TX/RX coil. Identical repetition times (TR = 110 ms) and SAR levels were used for all methods. The central slice of the B_1^+ map acquired for comparison with the 2D DAM, with TR = 6000 ms, is also shown (**F**). All maps are normalized to their nominal B_1^+ given in Table 1 in μT. Methods: **A** – *Optimized low-flip-angle method*, **B** – *Phase-sensitive method*, **C** – *ΦFA-CUP method*, **D** – *Bloch-Siegert method*, **E** – *Orthogonal-pulses method*, **F** – *Double Angle method*.
doi:10.1371/journal.pone.0057982.g008

(at 3.0 T: $T_1 \approx 70$ ms, $T_2 \approx 40$ ms). The latter affords reasonable scan time for the DAM approach.

Ethics Statement

For the *in vivo* feasibility study, two healthy subjects without any known history of neurovascular disease were included after due approval by the local ethical committee (registration number DE/CA73/5550/09, Landesamt für Arbeitsschutz, Gesundheitsschutz und technische Sicherheit, Berlin, Germany). Informed written consent was obtained from each volunteer prior to the study.

In vivo Studies

Human brain imaging was performed at 3.0 T and 7.0 T in healthy subjects using the five phase-based methods (**A-E**) and the DAM. FOV was adjusted to $(230\times230\times176)$ mm^3 at 3.0 T and $(210\times210\times160)$ mm^3 at 7.0 T, in order to cover the whole brain with 16 sagittal partitions using a matrix size of $32\times32\times16$ (plus zero-fill interpolation). The inter echo time for the ΔB_0 map was set to $\Delta TE = 2.46$ ms at 3.0 T and $\Delta TE = 3.06$ ms at 7.0 T, to make sure that fat and water are in phase for both TEs.

For the DAM approach only a central partition of the brain was acquired, since covering the whole brain would have required several hours of scan time: a constraint that is dictated by the T_1 of the brain (gray matter: $T_1 \approx 1800$ ms, white matter $T_1 \approx 1000$ ms at 3.0 T [27]), so that the repetition time was set to TR = 6000 ms.

Results

Numerical Simulations

The results derived from the simulations are shown in Figs. 2 and 3. The trajectories of **M** during excitation (Fig. 2) are used to qualitatively estimate the use of transverse magnetization. The curves displayed in Fig. 3 represent the sensitivities to B_1^+ variations (expressed as the *TotalFA*) and frequency offsets (ΔB_0 in Hz). The frequency offset range is identical for all the curves, while the total flip angle ranges vary (*TotalFA* axis), as well as the phase accrual ranges (Ψ axis). Efficiency ε is used to combine the flip angle range and phase accrual characteristics in a single variable that supports a balanced comparison. The values of ε were calculated for each method at the center of the sensitivity curves using Eq. 1.

A – Optimized low-flip-angle method. This method revealed the lowest B_1^+ sensitivity among all methods, with $\varepsilon = 0.44$ μs/deg. Its sensitivity curve presents a rather flat dependency upon frequency offsets. A discontinuity is observed for some combinations of ΔB_0 and *TotalFA* (Fig. 3A). In terms of usage of the transverse magnetization its composite pulse is equivalent to an excitation of $\sqrt{2}\alpha$ (Fig. 2A).

B – Phase-sensitive method. This method shows the highest B_1^+ sensitivity, with $\varepsilon = 1.91$ μs/deg. For frequency offsets exceeding a range of approximately ± 500 Hz the phase accrual Ψ experiences a discontinuity (Fig. 3B). A folding, leading to non-unique phase information which could not be decoded into the B_1^+ value, can also be observed outside of this range. This method employs the highest transverse magnetization, as the composite pulse is equivalent to a 90° excitation, when $\alpha = 90°$ (Fig. 2B).

C – ΦFA-CUP method. This method has a high B_1^+ sensitivity, with $\varepsilon = 1.52$ μs/deg. The dependency upon frequency offsets is more pronounced than in method **A**. This method does not present the discontinuities observed for methods **A** and **B** (Fig. 3C). The use of transverse magnetization is equal to *p0* (Fig. 2C). Its value can be chosen equal to the Ernst angle in order to optimize the signal, without affecting the B_1^+ sensitivity. This is not possible for methods **A** and **B**.

D – Bloch-Siegert method. This method exhibits a low B_1^+ sensitivity, with $\varepsilon = 0.66$ μs/deg, because it requires a much larger *TotalFA* compared to the other methods. This results also in a longer pulse duration, which manifests itself in a TE prolongation. The sensitivity curve of this method presents a rather modest dependency upon frequency offsets (Fig. 3D). The use of transverse magnetization depends only on the initial excitation *p0* (Fig. 2D), and can therefore be controlled, like for method **C**.

E – Orthogonal-pulses method. This method presents an intermediate B_1^+ sensitivity, with $\varepsilon = 0.82$ μs/deg. Its sensitivity curve shows a non-negligible dependency upon frequency offsets. A reduced B_1^+ sensitivity was observed for small flip angles versus the high flip angle regime (Fig. 3E). In terms of usage of the transverse magnetization the composite pulse used is equivalent to a flip angle larger than α (at small flip angles it is equal to $\sqrt{2}\alpha$, like for method **A**) (Fig. 2E).

Phantom Studies

The results derived from phantom experiments at 3.0 T and 7.0 T are shown in Figs. 5 and 6. All maps present the typical behavior of a birdcage resonator, where B_1^+ is higher at the center. At 7.0 T, due to destructive interference patterns, some areas around the center present a lower intensity.

The B_1^+ maps obtained with methods **A**-**E** (Figs. 5–6, A–E) are compared to the DAM approach (Figs. 5–6, F).

B_0 inhomogeneities can be observed at the air-water interface from the ΔB_0 maps shown in Fig. 4 (top), especially at 7.0 T. However, the fit performed using the sensitivity curves provides a very good estimation of B_1^+ in these regions. Even for the *phase-sensitive method* (**B**), the Φ*FA-CUP method* (**C**) and the *orthogonal-pulses method* (**E**) which are most sensitive to frequency offsets. This is confirmed by the contour plots in Figs. 5 and 6. Compared to the DAM no B_1^+ distortion can be observed in these areas.

All methods revealed sufficient signal, as the T_1 of the phantom was short enough ($T_1 \approx 70$ ms) to allow recovery of the magnetization.

In vivo Studies

The results of the human brain studies at 3.0 T and 7.0 T are summarized in Figs. 7 and 8. The results obtained with methods **A**–**E** (Figs. 7–8, A–E) for brain regions are in agreement with the DAM (Figs. 7–8, F). The typical B_1^+ peak of a birdcage coil can be observed at the center of the brain both at 3.0 T and 7.0 T. At 7.0 T a region of signal void due to destructive interference is visible in the area of the cerebellum. It should be noted that all methods except the *Bloch-Siegert method* (**D**) present some regions where the B_1^+ estimation is not correct, both at 3.0 T and at 7.0 T. This is due to the 3.5 ppm chemical shift between fat and water (corresponding to a resonance frequency difference of 150 Hz/T). The individual phases of water and fat signals are affected by the presence of B_1^+ inhomogeneities and frequency offsets, as demonstrated by the sensitivity curves (Fig. 3). Since the signal from each pixel is given by the complex sum of these two components, the resulting phase is decoded into a wrong B_1^+ value during the fitting. In fact, the ΔB_0 maps shown in Fig. 4 (bottom) do not account for this effect, as they were acquired with fat and water in phase. Due to air-tissue interfaces, strong B_0 offsets were observed in the sphenoid sinuses area, extending into the interior of the brain. The correction fit performs correctly in this region.

At 7.0 T the *Bloch-Siegert method* (**D**) shows SNR loss in the regions with short T_2^*, such as the areas nearby the bones.

Discussion

In this work five phase-based methods used for B_1^+ mapping have been examined carefully at magnetic field strengths of 3.0 T and 7.0 T. The characteristics of each method were analyzed by means of numerical simulations, phantom studies and *in vivo* experiments.

Although all methods have in common the use of a *complex* RF-pulse (composite or off-resonance pulse) for excitation, in conjunction with the same gradient-echo readout scheme, it is shown here that the five methods exhibit different sensitivities to B_1^+ inhomogeneities and frequency offsets. Furthermore they make different use of transverse magnetization and hence reveal different SNR, depending on the TR/T_1 ratio. For these reasons, the quality of the B_1^+ maps obtained from each method depends on the specific experimental conditions (T_1, T_2^*, frequency offset and dynamic range of B_1^+ in the region of interest) and on the parameters settings (TR, TE, flip angles and duration of the RF-pulse).

In this work, a fixed TR and an identical SAR level were used for all methods to compare their performances under fast imaging conditions. This approach was chosen deliberately since SAR limits dictate the minimum TR achievable, especially at high and ultrahigh magnetic field strengths. Within these limits all phase-based methods support short TR, since full relaxation of the longitudinal magnetization is not required prior to each excitation. Due to this SAR restriction the feasibility of using short TRs varies for each method, and depends primarily on the characteristics for the small nominal flip angle regime. The main challenge in the small flip angle regime is achieving enough B_1^+ sensitivity, given by the phase accrual. In order to quantify the ability of each method to convert the employed RF-power into the B_1^+ information, efficiency, which is defined as the specific phase accrual per unit SAR, was examined carefully. The *phase-sensitive method* (**B**) showed the best efficiency, followed by the Φ*FA-CUP method* (**C**), the *orthogonal-pulses method* (**E**), the *Bloch-Siegert method* (**D**) and the *optimized low-flip-angle method* (**A**). According to our results, the use of very short TRs in conjunction with methods which have a low efficiency results in highly noise-corrupted B_1^+ maps [28].

Another important characteristic for the quality of the resulting B_1^+ maps is represented by the consumption of longitudinal magnetization. Since the SNR of phase images is directly proportional to that of magnitude images, the amount of longitudinal magnetization available at each repetition should support the phase measurements with enough signal, in order to provide reliable phase images. In this regard, the Φ*FA-CUP method* (**C**) and the *Bloch-Siegert method* (**D**) are superior to the others. In fact the pulses used by these two methods include an initial excitation which is independent from the B_1^+ sensitization. To optimize the SNR this initial excitation can be set to the Ernst-angle. According to the simulations the *phase-sensitive method* (**B**), which provides the highest efficiency, uses the largest transversal magnetization and may be affected by a severe SNR drop when the TR/T_1 ratio is too small [28]. The large use of transverse magnetization could be useful if another reading module, such as EPI, is used. However this approach bears the risk to result in geometric distortion artifacts, due to magnetic field inhomogeneities, which pose a significant challenge [29], especially at 7.0 T.

It should be noted that B_1^+ mapping is not a problem limited to proton MRI. For instance the *phase-sensitive method* (**B**) has been applied to ^{23}Na MRI [30], where the low MRI signal and the short relaxation time T_1 require a large use of transverse magnetization, without incurring in saturation effects. On the other hand, the *optimized low-flip-angle method* (**A**) and the Φ*FA-CUP method* (**C**) were originally proposed for low field MRI using hyperpolarized ^{3}He [14,17,18], were the frequency offsets are not significant, and the longitudinal magnetization needs to be preserved.

For all methods, except the *Bloch-Siegert method* (**D**), the knowledge of ΔB_0 is required to perform a correct fitting to obtain the B_1^+ magnitude. This may require additional scan time. However, the acquisition of a second echo is feasible and affords the ΔB_0 mapping with no extra scan time. In any case, localized B_0 shimming would further improve the results. For these methods the presence of the fat-water chemical shift may affect the estimation of B_1^+, as the ΔB_0 maps do not account for this effect. In this case a fat-water separation approach could be eventually applied to remove artifacts.

All the five methods revealed that the sensitivity change induced by frequency offsets (ΔB_0 direction) would be reduced for shorter pulse durations. Also the frequency offsets, at which the discontinuities observed for the *optimized low-flip-angle method* (**A**) and the *phase-sensitive method* (**B**) occur, could be shifted away from the chosen range of ± 1 kHz, as they are inversely proportional to the pulse duration. On the downside this approach would hamper the efficiency ε (Eq. 1), since the SAR is increased for shorter RF-pluses due to the increase in the peak power necessary to achieve the same flip angle.

Among the methods used here, the *Bloch-Siegert method* (**D**) was found to be the least sensitive to ΔB_0 offsets and chemical shift effects, due to its flat sensitivity curve in the frequency offset direction.

Unlike all the other methods, the *Bloch-Siegert method* (**D**) supports also 2D mapping. This can be beneficial when time constraints do not allow for a full 3D acquisition; for example for B_1^+ mapping of the heart, where scan time constraints dictated by cardiac and respiratory motion need to be managed carefully. On the other hand the *Bloch-Siegert method* (**D**) presents a smaller efficiency than the *phase-sensitive method* (**B**), the Φ*FA-CUP method* (**C**) and the *orthogonal-pulses method* (**E**), and requires the longest pulse duration among all the methods. This feature results in SNR degradation for short T_2^* regions, such as interfaces with strong susceptibility gradients.

As our work is focused on the excitation pulse, results are derived using a standard 3D gradient-echo sequence, a Cartesian *k*-space sampling scheme and a single channel TX/RX coil. However, all the methods are inherently compatible with other 3D-imaging modules and *k*-space sampling schemes, as long as the phase information is preserved. Therefore all the methods can be accelerated using multi-echo techniques, or *k*-space undersampling techniques. This can be useful for B_1^+ mapping applications in other organs, including cardiac or abdominal MRI where physiological motion constraints dictate the viable window of data acquisition.

Conclusion

The B_1^+ mapping techniques examined here provided characteristics which underline the capabilities of phase-based methods, including the scan time advantage over conventional magnitude-based B_1^+ mapping methods. All presented methods can be adjusted to provide enough B_1^+ sensitivity without exceeding the clinical SAR limits. However, some characteristics, such as the sensitivity to B_1^+ inhomogeneities and frequency offsets and the consumption of longitudinal magnetization, are different for each method. This has an impact on the performance, depending on the specific experimental conditions.

Author Contributions

Conceived and designed the experiments: FC DS. Performed the experiments: FC DS FVS. Analyzed the data: FC DS. Contributed reagents/materials/analysis tools: FC DS FVS TDL MAD TN. Wrote the paper: FC DS TN.

References

1. Zhu Y (2004) Parallel excitation with an array of transmit coils. Magn Reson Med 51: 775–784.
2. Ullmann P, Junge S, Wick M, Seifert F, Ruhm W, et al. (2005) Experimental analysis of parallel excitation using dedicated coil setups and simultaneous RF transmission on multiple channels. Magn Reson Med 54: 994–1001.
3. Katscher U, Bornert P, Leussler C, van den Brink JS (2003) Transmit SENSE. Magn Reson Med 49: 144–150.
4. Insko EK, Bolinger L (1993) Mapping of the radiofrequency field. J Magn Reson A 103: 83–85.
5. Stollberger R, Wach P (1996) Imaging of the active B1 field in vivo. Magn Reson Med 35: 246–251.
6. Cunningham CH, Pauly JM, Nayak KS (2006) Saturated double-angle method for rapid B1+ mapping. Magn Reson Med 55: 1326–1333.
7. Yarnykh VL (2007) Actual flip-angle imaging in the pulsed steady state: a method for rapid three-dimensional mapping of the transmitted radiofrequency field. Magn Reson Med 57: 192–200.
8. Klose U (1992) Mapping of the radio frequency magnetic field with a MR snapshot FLASH technique. Med Phys 19: 1099–1104.
9. Dowell NG, Tofts PS (2007) Fast, accurate, and precise mapping of the RF field in vivo using the 180 degrees signal null. Magn Reson Med 58: 622–630.
10. Akoka S, Franconi F, Seguin F, Le Pape A (1993) Radiofrequency map of an NMR coil by imaging. Magn Reson Imaging 11: 437–441.
11. Stanisz GJ, Odrobina EE, Pun J, Escaravage M, Graham SJ, et al. (2005) T1, T2 relaxation and magnetization transfer in tissue at 3T. Magn Reson Med 54: 507–512.
12. Morrell GR, Schabel MC (2010) An analysis of the accuracy of magnetic resonance flip angle measurement methods. Phys Med Biol 55: 6157–6174.
13. Storey P, Wiggins GC, Santoro D, Sodickson DK (2009) Optimization of a low-flip-angle phase-based 3D B1 mapping technique for high field applications. In Proceedings of the 17th Annual Meeting of ISMRM, Honolulu, USA: 374.
14. Mugler JPI, Miller GW, Altes TA, de Lange EE, Brookeman JR (2005) A Low-Flip-Angle, Phase-Based Method for Accurately Calibrating the Transmitter in Hyperpolarized-Gas MRI. In Proceedings of the 13th Annual Meeting of ISMRM, Miami Beach, USA: 789.
15. Mugler JPI, Miller GW (2007) Rapid 3D Mapping of the B1 Field Using a Low-Flip-Angle, Phase-Based Method with Improved Sensitivity. In Proceedings of the 15th Annual Meeting of ISMRM, Berlin, Germany: 351.
16. Morrell GR (2008) A phase-sensitive method of flip angle mapping. Magn Reson Med 60: 889–894.
17. Santoro D, Rivoire J, Meise FM, Terekhov MV, Schreiber WG (2009) Optimized Sensitivity for 3D Mapping of the B1 Field Using a Phase-Based Method. In Proceedings of the 17th Annual Meeting of ISMRM, Honolulu, USA: 2611.
18. Santoro D, Rivoire J, Meise F, Terekhov M, Salhi Z, et al. (2011) Three-dimensional mapping of the B1 field using an optimized phase-based method: application to hyperpolarized 3He in lungs. Magn Reson Med 65: 1166–1172.
19. Santoro D, Lindel T, Dieringer M, Renz W, Niendorf T (2010) ΦFA CUP: PHase based Flip Angle Calibration Using the P0 pulse for proton MRI at 7T. In Proceedings of the 18th Annual Meeting of ISMRM, Stockholm, Sweden: 4943.
20. Sacolick LI, Wiesinger F, Hancu I, Vogel MW (2010) B1 mapping by Bloch-Siegert shift. Magn Reson Med 63: 1315–1322.
21. Saranathan M, Khalighi MM, Kerr AB, Rutt B (2011) Fast 3D B1+ mapping using an optimized, asymmetric Bloch-Siegert method. In Proceedings of the 19th Annual Meeting of ISMRM, Montreal, Canada: 577.
22. Khalighi MM, Rutt BK, Saranathan M, Kerr AB (2011) RF Pulse Optimization for Bloch-Siegert B1+ Mapping. In Proceedings of the 19th Annual Meeting of ISMRM, Montreal, Canada: 4431.
23. Chang YV (2012) Rapid B1 mapping using orthogonal, equal-amplitude radio-frequency pulses. Magn Reson Med 67: 718–723.
24. Bloch F, Siegert A (1940) Magnetic resonance for nonrotating fields. Phys Rev 57: 522–527.
25. Park HW, Kim YH, Cho ZH (1988) Fast gradient-echo chemical-shift imaging. Magn Reson Med 7: 340–345.
26. IEC-60601-2-33 (2010) Medical electrical equipment - Part 2–33: Particular requirements for the basic safety and essential performance of magnetic resonance equipment for medical diagnosis. Edition 30.
27. Nehrke K, Bornert P (2012) DREAM-a novel approach for robust, ultrafast, multislice B(1) mapping. Magn Reson Med.
28. Carinci F, Santoro D, von Samson Himmelstjerna F, Lindel T, Dieringer M, et al. (2011) Characterization of four phase-based methods for 3D B_1^+ mapping at 3T and 7T. In Proceedings of the 28th annual meeting of the ESMRMB, Leipzig, Germany: 46.
29. Yang QX, Wang J, Smith MB, Meadowcroft M, Sun X, et al. (2004) Reduction of magnetic field inhomogeneity artifacts in echo planar imaging with SENSE and GESEPI at high field. Magn Reson Med 52: 1418–1423.
30. Allen SP, Morrell GR, Peterson B, Park D, Gold GE, et al. (2011) Phase-sensitive sodium B1 mapping. Magn Reson Med 65: 1125–1130.

Rapid Parametric Mapping of the Longitudinal Relaxation Time T_1 Using Two-Dimensional Variable Flip Angle Magnetic Resonance Imaging at 1.5 Tesla, 3 Tesla, and 7 Tesla

Matthias A. Dieringer[1,2], Michael Deimling[1,3], Davide Santoro[1], Jens Wuerfel[4,5], Vince I. Madai[6], Jan Sobesky[6], Florian von Knobelsdorff-Brenkenhoff[1,2], Jeanette Schulz-Menger[1,2], Thoralf Niendorf[1,7]

[1] *Berlin Ultrahigh Field Facility (B.U.F.F.), Max-Delbrueck Center for Molecular Medicine, Berlin, Germany*
[2] *Working Group on Cardiovascular Magnetic Resonance, Experimental and Clinical Research Center, a joint cooperation between the Charité Medical Faculty and the Max-Delbrueck Center for Molecular Medicine, HELIOS Clinics Berlin Buch, Department of Cardiology and Nephrology, Berlin, Germany*
[3] *Siemens Healthcare, Erlangen, Germany*
[4] *Institute of Neuroradiology, University Medicine Goettingen, Germany*
[5] *NeuroCure Clinical Research Center, Charité University Medicine Berlin, Germany*
[6] *Clinic for Neurology & Center for Stroke Research Berlin, Charité Medical Faculty Berlin, Berlin, Germany*
[7] *Experimental and Clinical Research Center, a joint cooperation between the Charité Medical Faculty and the Max-Delbrueck Center for Molecular Medicine, Berlin, Germany*

Corresponding author:
Matthias A. Dieringer
E-mail: Matthias.dieringer@charite.de

Short running title: Rapid 2D T_1 mapping at 1.5T, 3T, and 7T

Keywords: magnetic resonance imaging, relaxation time mapping, brain imaging, variable flip angle, multiple sclerosis, stroke

Abstract

Introduction: Visual but subjective reading of longitudinal relaxation time (T_1) weighted magnetic resonance images is commonly used for the detection of brain pathologies. For this non-quantitative measure, diagnostic quality depends on hardware configuration, imaging parameters, radio frequency transmission field (B_1^+) uniformity, as well as observer experience. Parametric quantification of the tissue T_1 relaxation parameter offsets the propensity for these effects, but is typically time consuming. For this reason, this study examines the feasibility of rapid 2D T_1 quantification using a variable flip angles (VFA) approach at magnetic field strengths of 1.5 Tesla, 3 Tesla, and 7 Tesla. These efforts include validation in phantom experiments and application for brain T_1 mapping.

Methods: T_1 quantification included simulations of the Bloch equations to correct for slice profile imperfections, and a correction for B_1^+. Fast gradient echo acquisitions were conducted using three adjusted flip angles for the proposed T_1 quantification approach that was benchmarked against slice profile uncorrected 2D VFA and an inversion-recovery spin-echo based reference method. Brain T_1 mapping was performed in six healthy subjects, one multiple sclerosis patient, and one stroke patient.

Results: Phantom experiments showed a mean T_1 estimation error of (-63±1.5)% for slice profile uncorrected 2D VFA and (0.2±1.4)% for the proposed approach compared to the reference method. Scan time for single slice T_1 mapping including B_1^+ mapping could be reduced to 5 seconds using an in-plane resolution of (2x2)mm^2, which equals a scan time reduction of more than 99% compared to the reference method.

Conclusion: Our results demonstrate that rapid 2D T_1 quantification using a variable flip angle approach is feasible at 1.5T/3T/7T. It represents a valuable alternative for rapid T_1 mapping due to the gain in speed versus conventional approaches. This progress may serve to enhance the capabilities of parametric MR based lesion detection and brain tissue characterization.

Introduction

Magnetic resonance imaging (MRI) offers capabilities for non-invasive tissue characterization for a broad range of MRI applications including neuroinflammatory diseases and stroke [1,2,3,4,5]. At high and ultrahigh magnetic field strengths, brain parenchyma can be depicted with higher spatial resolution, which improves morphological conspicuity and facilitates improved characterization of multiple sclerosis (MS) plaques [6,7,8], enhances differential diagnosis of orphan neuorinflammatory diseases [9,10,11] and stroke [12]. Visual assessment of T_1 weighted techniques [13,14,15] is a common standard in today's clinical brain imaging

practice, although the diagnostic efficacy of cerebral lesion detection depends on the severity of focal or regional (patho-)physiological changes, on the imaging technique and pulse sequence design/timing used, on the impact of hardware configuration, as well as on the observer experience. Notwithstanding the ubiquity and success of clinical T_1 weighted imaging, quantification of brain parenchymal T_1 values is of great research interest and of substantial clinical relevance [16,17,18] but comes with the caveat of typically being rather time consuming.

T_1 quantification techniques using variable flip angles (VFA), such as *driven equilibrium single pulse observation of T_1* (DESPOT1, [19]) have been proposed for fast three dimensional T_1 mapping of the brain. DESPOT1 includes at least two radio frequency (RF) spoiled gradient echo (FLASH [20]) measurements using different flip angles from which T_1 maps with full brain coverage can be achieved in approximately 10 minutes scan time [21]. Not all clinical indications necessarily require whole brain coverage, but might rather benefit from fast 2D zonal imaging covering particular brain regions or lesions using a high in-plane spatial resolution together with a limited number of slices. Consequently, targeting rapid 2D mapping approaches is conceptually appealing for clinical T_1 quantification of brain tissue. However, commonly used non-ideal radiofrequency (RF) pulses evoke an inhomogeneous slice excitation leading to deformed slice profiles [22]. Slice profile deformation presents an extra challenge for VFA based T_1 mapping and bears the potential to deem T_1 quantification inaccurate. Recognizing the constraints of conventional 2D VFA and the opportunities of 2D T_1 mapping, this study examines the feasibility and fidelity of rapid slice profile corrected 2D VFA T_1 mapping. To meet this goal, numerical simulations of the Bloch equations are used, which account for non-ideal RF pulse shapes and RF transmission field (B_1^+) non-uniformities. The applicability of this approach is demonstrated in phantom experiments at 1.5T, 3T and 7T. *In vivo* feasibility studies including healthy subjects, MS and stroke patients are conducted as a precursor to a broader clinical study. The merits and limitations of the proposed 2D VFA T_1 mapping variant are discussed and implications for clinical imaging are considered.

Methods

Theory

Fast radio frequency (RF) spoiled gradient echo (FLASH) measurements using at least two flip angles allow for the quantification of the longitudinal relaxation time T_1 [19]. The commonly accepted equation that governs FLASH signal intensity S(α) in the steady state is [23]

$$S(\alpha) = M_0 \frac{(1-E_1)\sin(\alpha)}{1-E_1\cos(\alpha)} e^{-\frac{TE}{T_2^*}}, \text{ with } E_1 = e^{-\frac{TR}{T_1}}, \quad \text{(Eq. 1)}$$

where M_0 is the proton density, TR is the repetition time, TE is the echo time, α is the flip angle, and T_2^* is the effective transversal relaxation time. Rearrangement of equation 1 yields [24]

$$\frac{S(\alpha)}{\sin(\alpha)} = E_1 \frac{S(\alpha)}{\tan(\alpha)} + M_0(1-E_1)e^{-\frac{TE}{T_2^*}} \quad \text{(Eq. 2)}$$

Arranging S(α)/sin(α) over S(α)/tan(α) allows for extraction of T_1 from a linear fit T_1=-TR/ln(m), where m is the slope between measurement points.

Bloch equation simulations

Equation 1 and 2 hold true for excitations that exhibit a uniform flip angle over the entire target area. In 2D acquisitions, however, non-ideal RF pulse shapes lead to deformations of the slice profile altering the resulting signal intensities. To assess the extent of slice profile deformation and its impact on variable flip angle T_1 quantification, a Matlab (TheMathworks, Natick, MA, USA) environment was developed allowing for simulations according to the Bloch equations and emulation of a FLASH sequence. A bandwidth truncated sinc RF pulse (bandwidth=1kHz, duration=2ms, time-bandwidth-product=2) used for FLASH imaging was extracted from the sequence development environment of the "integrated development environment for (MR) applications" (IDEA, Siemens Healthcare, Erlangen, Germany) and fed into the simulation. One-dimensional magnetization vector profiles along the slice selection direction were generated in the steady state for given flip angles.

T_1 quantification: Simulated versus experimental signals

Using mathematical integration of the simulated slice profiles for different flip angles, theoretically achievable signal intensities were calculated. An iterative least squares minimization function matched these theoretical signal intensities to measured FLASH MR signal intensities by varying T_1 between 1ms and 10000ms starting at T_1=1000ms and adapting the scaling factor M_0. Pixel-by-pixel application of this method facilitated T_1 mapping.

The simulation environment allowed inclusion of afore acquired B_1^+ data that were derived from RF transmission field mapping.

Three flip angles approach
Further to the conventional approach that uses two flip angles we propose the application of three flip angles for VFA based T_1 quantification. The first flip angle α_1 was chosen to achieve the maximum signal intensity determined by Bloch simulations using the specific target T_1. To determine the remaining two flip angles, α_2 and α_3 were varied from 1° to 90° including all possible combinations. Gaussian noise was added to the corresponding signal and T_1 evaluations using the proposed approach were performed for all flip angle combinations. Flip angle sets resulting in minimal T_1 differences between the theoretical T_1 value and the estimated T_1 value were regarded as adjusted flip angles and were henceforth used as nominal flip angles for the phantom experiments and for the *in vivo* studies.
In the first step, these one-time calculations were performed for T_1 of a manganese chloride doped water phantom (T_1=1000ms) described below. In the second step, approximated mean T_1 values found in the literature for gray and white matter at different field strengths (T_1=950ms at 1.5T [25,26,27,28], T_1=1250ms at 3T [25,27,29,30,31], and T_1=1650ms at 7T [27]) were targeted.

Monte Carlo simulations
To assess T_1 dependent accuracy (defined as deviation of mean T_1 value from nominal T_1 value) and precision index (defined as standard deviation of T_1 divided by mean T_1) of the proposed mapping method and to compare the three flip angles approach with the two flip angles approach, Monte Carlo simulations of the proposed corrected 2D VFA fitting algorithm were performed for T_1 values of 1ms to 3000ms using a 1ms increment. Gaussian noise was added to the signal intensities so that a SNR margin of 100 between the highest of all three signals and the standard deviation of the noise was achieved. 10000 simulation experiments were conducted for each T_1 using the adjusted flip angle set for the respective T_1 values.

RF transmission field (B_1^+) mapping
As VFA methods rely on a priori knowledge of the exact flip angle in the region of interest, correction for RF transmission field (B_1^+) non-uniformities is essential. B_1^+ mapping was done using a Bloch-Siegert [32] implementation for phase based B_1^+ mapping [33] using TR≈100ms, Fermi pulse flip angle=400° (nominal B_1^+=4.35µT), and a Fermi pulse off-center frequency=4kHz. Spatial resolution was adapted to the respective T_1 mapping protocol. The sequence employed double gradient echo acquisitions with different echo times adapted to the corresponding fat/water frequency shift for each field strength to enable B_0-mapping [34]. Calculation of transmission field distribution normalized to the nominal B_1^+ was done offline using Bloch simulations in Matlab that also considered B_0 off-resonances.

MR hardware
Measurements were performed on 1.5T/3T/7T whole body MRI systems (Avanto/Verio/Magnetom 7T, Siemens Healthcare, Erlangen, Germany) running identical software versions. At 1.5T and 3T a 12 channel (Siemens Healthcare, Erlangen, Germany) head coil was used for signal reception (Rx) while at 7T a 24 channel Rx coil (Nova Medical, Andover, MA, USA) was employed. For transmission (Tx), the integrated body coil was used at 1.5T and 3T while the head coil's Tx channel was used at 7T.

Validation in Phantom Experiments
An oval brain like shaped water based phantom (diameter=10cm, length=20cm, T_1=960ms, T_2=100ms, measured at 1.5T) was built to mimic mean gray and white matter T_1 values at 1.5T. Manganese chloride was used to adjust T_1, sodium chloride was used to adjust the conductivity to that of brain tissue [35].
To assess the capability of the Bloch simulations to accurately emulate slice excitation, the simulated magnetization vector profiles were compared to excitation profiles measured exemplarily at α=30° at 3.0 T employing a modified FLASH sequence with the readout gradient along the slice selection direction.
Signal intensities over different flip angles calculated from Bloch simulations using the actual sequence configuration were compared to signal intensities derived from standard FLASH measurements (TE/TR=2.5/5ms; α=2°-90°, voxel size=(2x2x5)mm³).
A two-dimensional inversion recovery (IR) prepared technique (voxel size: (2x2x5)mm³, non-selective adiabatic hyperbolic secant inversion, echo spacing=5.5ms, TR=10 s, α=90°, turbo factor=5, GRAPPA acceleration factor=2, 8 inversion times of TI=60/120/240/480/750/1000/3000/5000ms, scan time=16min) in conjunction with a spin-echo readout served as a reference for T_1 quantification. T_1 was calculated offline in Matlab using a non-linear least squares three-parameter fit.

To validate the feasibility and accuracy of the corrected 2D VFA T_1 mapping method accounting for slice profile deformations, 2D FLASH images (TE/TR=2.5/5ms, scan time=3.5s) using a set of three adjusted flip angles were acquired. B_1^+-maps were used to account for B_1^+ non-uniformities.
T_1 of the phantom was quantified for all field strengths (1.5T, 3T, and 7T). For this purpose, a region of interest covering the entire cross-section of a central coronal slice of the phantom was used. Mean T_1 values and standard deviations were calculated for this ROI. To elucidate the impact of the signal change due to slice profile deformation on the 2D quantification of T_1, conventional B_1^+-corrected VFA T_1 evaluation used for 3D acquisitions that did not consider slice profiles were performed using two flip angles (2°/13°) suggested by the 3D approach [36]. For reasons of brevity, the expression "uncorrected 2D VFA" is used for this approach in the following. The proposed 2D B_1^+ corrected VFA T_1 mapping approach that includes extra slice profile deformation versus the conventional approach is called "corrected 2D VFA".

Ethics Statement
For the *in vivo* feasibility study, 6 healthy subjects (mean age: 28±2 years, 2 females) without any known history of brain disease, one MS patient (age: 46 years, female), and one stroke patient (24 years, male) underwent MR imaging after due approval by the ethical committees (registration number DE/CA73/5550/09, Landesamt für Arbeitsschutz, Gesundheitsschutz und technische Sicherheit, Berlin, Germany and registration number DRKS00003193, 7 Tesla Ultra-High Field Project 7UP, WHO International). Informed written consent was obtained from each volunteer and patient prior to the study.

In vivo studies in healthy subjects and patients
Axial 2D brain images were obtained (FLASH, TE/TR=2.5ms/5ms, scan time=3.5s) using flip angle triples, which were adjusted to mitigate saturation and noise induced errors. Gray matter (GM) and white matter (WM) were segmented by thresholding a combination of T_1 weighted images and T_1 maps derived from the reference T_1 measurement. The resulting gray matter and white matter masks were applied to the uncorrected 2D VFA approach and to the proposed corrected 2D VFA. The IR-SE based T_1 quantification reference method described for the phantom measurements was also used for the volunteer study. Mean T_1 and standard deviations were calculated for the reference method and for slice profile deformation corrected 2D VFA. For volunteer studies, a spatial resolution of (2x2x5)mm³ was used for data acquisition, which was interpolated to (1x1x5)mm³ during reconstruction to improve visual appearance. For patient studies, the spatial resolution was adjusted to (1.6x1.6x4)mm³ during the acquisitions and interpolated to (0.8x0.8x4)mm³ in the reconstruction.

Results
Determination of adjusted flip angles using Bloch simulations
Optimum flip angles for T_1 quantification of the phantom were calculated to be 3°/11°/30° at 1.5T, 3°/11°/28° at 3T, and 3°/11°/26° at 7T. Adjusted flip angles for T_1 quantification *in vivo* were found to be 3°/11°/26° at 1.5T, 3°/9°/22° at 3T, and 3°/8°/25° at 7T.

Monte Carlo simulations
Figure 1a shows results derived from Monte Carlo simulation of the proposed corrected 2D VFA approach for T_1 relaxation times ranging from 0-3 s. T_1 precision decreases with increasing T_1, while accuracy remains unaffected. If a two flip angle approach is used as a reference, the T_1 precision index was improved for the three flip angles approach by 9% for T_1 values ranging from 100ms to 300ms, by 13% for T_1 values ranging from 300ms to 1000ms, and by 12% for T_1 values ranging from 1000ms to 3000ms.

Validation in phantom experiments
Bloch simulated and measured excitation slice profiles derived from the phantom are depicted in Figure 1b for an excitation pulse of α=30°. Simulation and measurement agree very well. The saturation dependent slice profile deformation is characterized by the RF pulse shape, TR, T_1 and the flip angle. The slice profile deformation and B_1^+ non-uniformity induced discrepancy between theoretical and measured signal curves for FLASH is demonstrated in Figure 1c. While theoretical signal intensities using Eq. 2 deviated substantially from the measurements, the signal curve derived from the B_1^+ corrected simulations including slice profile considerations perfectly matched the experimental data. The flip angle providing maximum signal was found to be 11° (considering slice profile deformations), which is almost twice the theoretical Ernst angle of 6°.
B_1^+ maps of the phantom at 1.5T, 3T, and 7T are shown in Figure 2a. As expected, the B_1^+ homogeneity decreases with increasing field strength. At 1.5T, T_1 quantification using the inversion recovery approach as a reference yielded T_1=(963±7)ms for the cross-sectional ROI of the phantom. At 3T, the reference T_1 value was found to be (1022±10)ms. For the same phantom, T_1=(1002±10)ms was obtained at 7T as illustrated in Figure

2b. Conventional, only B_1^+ corrected 2D VFA T_1 mapping using Eq. 2 substantially underestimated T_1 and yielded T_1=(372±28)ms at 1.5T, T_1=(376±23)ms at 3T, and T_1=(357±60)ms at 7T as demonstrated in Figure 2b. The inhomogeneous T_1 map at 7T also underlines that a solitary B_1^+ correction is not sufficient to compensate for the non-linear flip angle dependent signal changes. In comparison, slice profile deformation and B_1^+ corrected 2D VFA provided T_1=(966±67)ms at 1.5T, T_1=(1010±47)ms at 3T and T_1=(1017±89)ms at 7T as illustrated in Figure 2b, which matches the reference data fairly well. The proposed slice profile corrected 2D VFA approach yielded a mean deviation of T_1 from the reference value as low as (0.2±1.4) % averaged over all field strengths (Figure 2c). In comparison, an error in T_1 quantification of (-63±1.5) % was observed for the 2D VFA technique without slice profile deformation correction as shown in Figure 2c.
All measurements, including T_1 reference measurements, showed inconsistent results in the neck of the water bottle at 7T, because this region was outside of the covered volume of the local transmission coil.

Volunteer and Patient Studies
T_1 mapping performed in healthy volunteers at 1.5T, 3T, and 7T using the IR-SE reference measurement, the uncorrected 2D VFA, and the corrected 2D VFA are depicted in Figure 3. T_1 values for gray matter and white matter are illustrated in Table 1.
At 1.5T, flip angles were 3°/11°/26° for the proposed corrected 2D VFA and 2°/13° for uncorrected 2D VFA. The absolute mean difference between IR reference and uncorrected 2D VFA was 60% for gray matter and 56% for white matter. The absolute mean difference between IR reference and corrected 2D VFA was 11% for gray matter and 17% for white matter.
At 3T, flip angles were 2°/12° for uncorrected 2D VFA and 3°/9°/22° for the proposed corrected 2D VFA. The absolute mean difference between IR reference and uncorrected 2D VFA was 68% for gray matter and 59% for white matter. The absolute mean difference between IR reference and corrected 2D VFA was 11% for gray matter and 6% for white matter.
At 7T, flip angles were 2°/11° for uncorrected 2D VFA and 3°/8°/25° for the proposed corrected 2D VFA. The absolute mean difference between IR reference and uncorrected 2D VFA was 61% for gray matter and 57% for white matter. The absolute mean difference between IR reference and corrected 2D VFA was 22% for gray matter and 44% for white matter.
The acquisition time for the IR-SE reference measurement was 16 minutes for each slice at each field strength. For corrected 2D VFA T_1 mapping, acquisition time including B_1^+ mapping was 18s for each slice.
The T_1 measurement of the MS patient at 7T revealed (2758±615)ms in three periventricular lesions vs. (1842±62)ms in the surrounding white matter (Fig. 4a). T_1 in the subcortical lesion of the stroke patient was (2554±316)ms vs. (951±74)ms of the surrounding white matter at 3T (Fig. 4b).

Discussion
This study demonstrates the feasibility of rapid 2D T_1 quantification using variable flip angles in phantom experiments and *in vivo* at magnetic field strengths of 1.5T, 3T and 7T. For this purpose, implications of RF transmission field non-uniformities, as well as excitation slice profile deformations due to non-ideal RF pulses were carefully considered. For correction of slice profile deformation induced errors, Bloch simulations were employed. Corrected 2D VFA T_1 mapping was found to be accurate when compared to reference inversion recovery acquisitions in phantom studies at all tested field strengths. For T_1 mapping of the brain, mean T_1 values measured by corrected 2D VFA show a fairly good agreement with the reference measurement at 1.5T and 3T for both gray and white matter. T_1 relaxation times found for corrected 2D VFA at 7T were larger than that derived from IR-SE. The applicability and efficacy of the proposed procedure to calculate adjusted flip angles in order to mitigate noise induced errors was confirmed by our simulations and experimental data.
The inclusion of B_1^+ maps made 2D VFA T_1 mapping immune to non-uniformities in the B_1^+ transmission field, which are pronounced at high and ultrahigh field strengths. Magnitude based B_1^+ mapping methods such as double angle [37,38,39,40] or the use of inversion recovery prepared extra scans [21,41] have been presented previously to correct for flip angle inaccuracies. However, most of these techniques rely on equilibrium magnetization before each acquisition or need extra calibration routines and therefore add extra scan time. Flash-EPI hybrid sequences employing adiabatic pulses [42] were proposed to potentially provide means for overcoming B_1^+ inhomogeneities while maintaining reasonable scan time. However, SAR constraints dictate flip angle limits and adiabatic pulses demand longer echo times especially at higher magnetic fields, which lead to partial dephasing of the magnetization. The phase based B_1^+ mapping technique used here is fast and reliable, even in low signal regions [33] of the brain. The rapid data acquisition reduces motion sensitivity in B_1^+ mapping, which is ultimately beneficial for in vivo T_1 quantification.
The reference method was already accelerated by using parallel imaging with an effective reduction factor of R=2 together with a spin echo turbo factor of 5 and a reduced phase field of view. The corrected 2D VFA

implementation used for the volunteers offers a scan time advantage factor of approximately 570 versus the unaccelerated inversion recovery reference method. Obviously, corrected 2D VFA supports modest accelerations, which would further enhance the speed advantage over the reference. Notwithstanding the utility of the reference method that relied on equilibrium magnetization before each inversion pulse for T_1 quantification, the potential to shorten scan times is limited. As T_1 of brain tissue increases with field strength, the equilibrium condition of TR > 5 x T_1 requires even longer TRs, which further increase scan time. Unlike the reference method, moving to higher magnetic fields does not add a scan time penalty to corrected 2D VFA. Even more, the lack of inversion pulses in 2D VFA reduces magnetization transfer effects and RF power deposition.

Our results demonstrate severe T_1 quantification errors due to slice profile deformations in the uncorrected 2D VFA T_1 mapping using commonly accepted signal equations. This underscores that theoretical signal predictions only hold true for ideal rectangular slice profiles assuming uniform excitation over the entire slice or volume. Slice selection RF pulses are however bandwidth limited and lead to a spatially non-uniform flip angle distribution in slice selection direction. This evokes T_1-, TR-, and flip angle dependent saturation phenomena that create distorted slice profiles. Consequently, it is essential to correct for slice deformations before T_1 values derived from 2D VFA acquisitions can be considered accurate.

The match of T_1 values derived from IR-SE reference measurements with T_1 values derived from the corrected 2D VFA at all tested field strengths suggests that the sequence related deviations were successfully addressed by our 2D VFA implementation. In-vivo T_1 maps obtained with the two methods, however, revealed some residual differences. This underscores the challenges of parametric mapping when moving from phantoms to *in vivo*, where tissue characteristics become relevant and play a role for T_1 quantification. It is to be expected that magnetization transfer weighting, weighting of T_1 relaxation components, and T_2 relaxation components in mixed tissue is different for different T_1 mapping techniques, which ultimately leads to different mean T_1 values. Therefore, it is challenging to establish normal values for tissue that are valid across all T_1 quantification techniques. The broad variety of reference T_1 values found in the literature supports this statement [25,26,27,28,29,30,31]. We also performed simulations using a three pool model of mixed white matter tissue (myelin, myelinated axons, and mixed water pools) together with volume fractions reported for adults [43]. The difference in mean T_1 between the IR-SE reference and the proposed corrected 2D VFA was found to be 15%. In our measurements, the linear trend of increasing T_1 with increasing field strength could not be shown for the corrected 2D VFA method at 7T. However, for all field strength the discrepancy between the reference measurement and corrected 2D VFA T_1 mapping (mean deviation of 18%) was reduced versus the discrepancy between the reference and uncorrected 2D VFA T_1 mapping (mean deviation of 63%).

Admittedly, it may take several excitations before the magnetization reaches steady state in gradient echo techniques, which depends on the RF pulse shape, T_1 relaxation time, TR, and the flip angle used. For this reason, we integrated 200 dummy pulses for T_1 mapping to approximate steady state. This approach resulted in total scan times of approximately 18s for single slice 2D VFA T_1 mapping in the phantom and in healthy volunteers (spatial resolution=2x2x5mm³) including all three flip angles and including B_1^+ mapping. For the patient measurements, a clinically acceptable scan time of 30 s was achieved for single slice T_1 mapping (spatial resolution=1.6x1.6x4mm³). As all variable flip angle T_1 quantification techniques rely on the steady state approximation, fast moving blood might not allow the steady state to form, alter the signal, and thus bear the potential to deem blood T_1 quantification inaccurate.

In order to maintain consistent scan protocols throughout all field strengths, we used an echo time of 2.5ms and a repetition time of 5ms due to specific absorption rate (SAR) considerations at 7T. It is a recognized limitation that this approach is suboptimal at 1.5T and 3T. Here, shortening of TR would further reduce scan time. Moreover, RF Pulse shapes, gradient strengths and slew rates, receiver bandwidth, and spatial resolution can be adapted to use the full range of the system's specification at 1.5T, 3T and 7T. The repetition times and scan times reported here for B_0 and B_1^+ mapping were limited by SAR constraints at 7T and of course can be further shortened at 1.5T and 3T. Implementation of these changes affords T_1 mapping for a single slice in 5s including B_1^+ mapping. To reduce the computational effort, an accelerated algorithm for T_1 quantification was implemented in Matlab, which enables generation of T_1 maps using a matrix size of 256x256 pixels in less than three seconds.

The proposed approach for the calculation of adjusted flip angles to reduce T_1 quantification errors in 2D VFA T_1 mapping by balancing dynamic range and SNR does not yet account for B_1^+ inhomogeneities or RF transmitter mis-calibrations, which can be hardware-, setup-, subject-, and also organ specific. Therefore, the proposed approach requires proper RF transmitter adjustment – a procedure which is included in the pre-scan calibration of clinical scanners - in order to get as close as possible to the adjusted flip angles. The choice of flip angles depends on the grade of slice profile deformation and therefore varies with the RF pulse shape. Our simulations and experiments focused on a bandwidth truncated sinc RF pulse with a bandwidth of 1kHz and a

duration of 2ms. For other RF excitation pulses, adjusted flip angles might be different and require a onetime pre-calculation before used for T_1 mapping. In contrast to the theoretical assumptions based on signal equations, the deformation of the slice profile in 2D gradient echo acquisitions shifts the suggested flip angles to larger values. Consequently, these flip angles may be limited by SAR constraints, especially at high and ultrahigh field strengths. Bandwidth reduced RF pulses allow higher flip angles, however at the cost of a non-uniform slice excitation. Notwithstanding the possible limitations discussed here, the proposed 2D VFA T_1 mapping approach is capable to deal with and correct for slice profile distortions and showed reliability even at high field strengths. The single slice approach presented in this work can be extended to multi-slice T_1 mapping. As the effective slice thickness increases with increasing slice profile distortion, cross-talk between slices has to be mitigated by application of interleaved data acquisition or a sufficient inter-slice distance.
SNR constraints of 2D VFA T_1 mapping remain a concern for tissue characterization using parametric mapping of relaxation times. Here our B_1^+ corrected approach is promising, since it was found to support the use of many-element surface receiver coils that can provide SNR improvements and speed gain [44,45].

Conclusion

Corrected 2D VFA T_1 mapping represents a valuable alternative for rapid T_1 mapping due to the speed gain versus conventional approaches. This progress may serve to enhance the capabilities of parametric MR based lesion detection and brain tissue characterization. The benefits of such improvements would be in positive alignment with the needs of explorations that are designed to examine the potential of high and ultrahigh field MRI for the assessment of neurodegenerative and neuroinflammatory diseases including differential diagnosis of orphan diseases.

Acknowledgements

The authors wish to thank M. Klassen from the Robarts Research Institute, Western University, Canada, P. Ehses from the Max Planck Institute for Biological Cybernetics, Tübingen, Germany, and B. Hargreaves from Stanford University, USA, for providing Matlab code.

References

1. Polman CH, Reingold SC, Banwell B, Clanet M, Cohen JA, et al. (2011) Diagnostic criteria for multiple sclerosis: 2010 revisions to the McDonald criteria. Ann Neurol 69: 292-302.
2. Inglese M (2006) Multiple sclerosis: new insights and trends. AJNR Am J Neuroradiol 27: 954-957.
3. Ge Y (2006) Multiple sclerosis: the role of MR imaging. AJNR Am J Neuroradiol 27: 1165-1176.
4. Sobesky J (2012) Refining the mismatch concept in acute stroke: lessons learned from PET and MRI. J Cereb Blood Flow Metab 32: 1416-1425.
5. Wardlaw JM, Smith EE, Biessels GJ, Cordonnier C, Fazekas F, et al. (2013) Neuroimaging standards for research into small vessel disease and its contribution to ageing and neurodegeneration. Lancet Neurol 12: 822-838.
6. de Graaf WL, Kilsdonk ID, Lopez-Soriano A, Zwanenburg JJ, Visser F, et al. (2013) Clinical application of multi-contrast 7-T MR imaging in multiple sclerosis: increased lesion detection compared to 3 T confined to grey matter. Eur Radiol 23: 528-540.
7. Sinnecker T, Mittelstaedt P, Dorr J, Pfueller CF, Harms L, et al. (2012) Multiple sclerosis lesions and irreversible brain tissue damage: a comparative ultrahigh-field strength magnetic resonance imaging study. Arch Neurol 69: 739-745.
8. Tallantyre EC, Brookes MJ, Dixon JE, Morgan PS, Evangelou N, et al. (2008) Demonstrating the perivascular distribution of MS lesions in vivo with 7-Tesla MRI. Neurology 70: 2076-2078.
9. Sinnecker T, Dorr J, Pfueller CF, Harms L, Ruprecht K, et al. (2012) Distinct lesion morphology at 7-T MRI differentiates neuromyelitis optica from multiple sclerosis. Neurology 79: 708-714.
10. Wuerfel J, Sinnecker T, Ringelstein EB, Jarius S, Schwindt W, et al. (2012) Lesion morphology at 7 Tesla MRI differentiates Susac syndrome from multiple sclerosis. Mult Scler 18: 1592-1599.
11. Susac JO, Murtagh FR, Egan RA, Berger JR, Bakshi R, et al. (2003) MRI findings in Susac's syndrome. Neurology 61: 1783-1787.
12. Madai VI, von Samson-Himmelstjerna FC, Bauer M, Stengl KL, Mutke MA, et al. (2012) Ultrahigh-field MRI in human ischemic stroke--a 7 tesla study. PLoS One 7: e37631.
13. Brant-Zawadzki M, Gillan GD, Nitz WR (1992) MP RAGE: a three-dimensional, T1-weighted, gradient-echo sequence--initial experience in the brain. Radiology 182: 769-775.
14. Redpath TW, Smith FW (1994) Technical note: use of a double inversion recovery pulse sequence to image selectively grey or white brain matter. Br J Radiol 67: 1258-1263.

15. Hajnal JV, Bryant DJ, Kasuboski L, Pattany PM, De Coene B, et al. (1992) Use of fluid attenuated inversion recovery (FLAIR) pulse sequences in MRI of the brain. J Comput Assist Tomogr 16: 841-844.
16. Vrenken H, Geurts JJ, Knol DL, van Dijk LN, Dattola V, et al. (2006) Whole-brain T1 mapping in multiple sclerosis: global changes of normal-appearing gray and white matter. Radiology 240: 811-820.
17. Jurcoane A, Wagner M, Schmidt C, Mayer C, Gracien RM, et al. (2013) Within-lesion differences in quantitative MRI parameters predict contrast enhancement in multiple sclerosis. J Magn Reson Imaging.
18. Parry A, Clare S, Jenkinson M, Smith S, Palace J, et al. (2002) White matter and lesion T1 relaxation times increase in parallel and correlate with disability in multiple sclerosis. J Neurol 249: 1279-1286.
19. Homer J, Beevers M (1985) Driven-equilibrium single-pulse observation of T1 relaxation. A re-evaluation of a rapid 'new' method for determining NMR spin-lattice relaxation times. J Magn Reson 63: 287-297.
20. Haase A, Frahm J, Matthaei D, Hanicke W, Merboldt KD (1986) FLASH imaging: rapid NMR imaging using low flip-angle pulses. J Magn Reson 67: 258–266.
21. Deoni SC (2007) High-resolution T1 mapping of the brain at 3T with driven equilibrium single pulse observation of T1 with high-speed incorporation of RF field inhomogeneities (DESPOT1-HIFI). J Magn Reson Imaging 26: 1106-1111.
22. Parker GJ, Barker GJ, Tofts PS (2001) Accurate multislice gradient echo T(1) measurement in the presence of non-ideal RF pulse shape and RF field nonuniformity. Magn Reson Med 45: 838-845.
23. Frahm J, Haase A, Matthaei D (1986) Rapid three-dimensional MR imaging using the FLASH technique. J Comput Assist Tomogr 10: 363-368.
24. Fram EK, Herfkens RJ, Johnson GA, Glover GH, Karis JP, et al. (1987) Rapid calculation of T1 using variable flip angle gradient refocused imaging. Magn Reson Imaging 5: 201-208.
25. Stanisz GJ, Odrobina EE, Pun J, Escaravage M, Graham SJ, et al. (2005) T1, T2 relaxation and magnetization transfer in tissue at 3T. Magn Reson Med 54: 507-512.
26. Sled JG, Pike GB (2001) Quantitative imaging of magnetization transfer exchange and relaxation properties in vivo using MRI. Magn Reson Med 46: 923-931.
27. Rooney WD, Johnson G, Li X, Cohen ER, Kim SG, et al. (2007) Magnetic field and tissue dependencies of human brain longitudinal 1H2O relaxation in vivo. Magn Reson Med 57: 308-318.
28. Henderson E, McKinnon G, Lee TY, Rutt BK (1999) A fast 3D look-locker method for volumetric T1 mapping. Magn Reson Imaging 17: 1163-1171.
29. Wansapura JP, Holland SK, Dunn RS, Ball WS, Jr. (1999) NMR relaxation times in the human brain at 3.0 tesla. J Magn Reson Imaging 9: 531-538.
30. Gelman N, Ewing JR, Gorell JM, Spickler EM, Solomon EG (2001) Interregional variation of longitudinal relaxation rates in human brain at 3.0 T: relation to estimated iron and water contents. Magn Reson Med 45: 71-79.
31. Ethofer T, Mader I, Seeger U, Helms G, Erb M, et al. (2003) Comparison of longitudinal metabolite relaxation times in different regions of the human brain at 1.5 and 3 Tesla. Magn Reson Med 50: 1296-1301.
32. Sacolick LI, Wiesinger F, Hancu I, Vogel MW (2010) B1 mapping by Bloch-Siegert shift. Magn Reson Med 63: 1315-1322.
33. Carinci F, Santoro D, von Samson-Himmelstjerna F, Lindel TD, Dieringer MA, et al. (2013) Characterization of phase-based methods used for transmission field uniformity mapping: a magnetic resonance study at 3.0 T and 7.0 T. PLoS One 8: e57982.
34. Schneider E, Glover G (1991) Rapid in vivo proton shimming. Magn Reson Med 18: 335-347.
35. Loader B, Gregory A, Bownds D, Johnson Y. Non-toxic phantoms for SAR measurements (30 MHz to 6 GHz). 32nd Annual Meeting of the Bioelectromagnetics Society; 2010; Seoul, Korea. The Bioelectromagnetics Society. pp. 94.
36. Deoni SC, Peters TM, Rutt BK (2004) Determination of optimal angles for variable nutation proton magnetic spin-lattice, T1, and spin-spin, T2, relaxation times measurement. Magn Reson Med 51: 194-199.
37. Akoka S, Franconi F, Seguin F, Le Pape A (1993) Radiofrequency map of an NMR coil by imaging. Magn Reson Imaging 11: 437-441.
38. Insko EK, Bolinger L (1993) Mapping of the radiofrequency field. J Magn Reson A 103: 82-85.
39. Andreisek G, White LM, Yang Y, Robinson E, Cheng HL, et al. (2009) Delayed gadolinium-enhanced MR imaging of articular cartilage: three-dimensional T1 mapping with variable flip angles and B1 correction. Radiology 252: 865-873.
40. Cheng HL, Wright GA (2006) Rapid high-resolution T(1) mapping by variable flip angles: accurate and precise measurements in the presence of radiofrequency field inhomogeneity. Magn Reson Med 55: 566-574.

41. Venkatesan R, Lin W, Haacke EM (1998) Accurate determination of spin-density and T1 in the presence of RF-field inhomogeneities and flip-angle miscalibration. Magn Reson Med 40: 592-602.
42. Tannus A, Garwood M (1997) Adiabatic pulses. NMR Biomed 10: 423-434.
43. Lancaster JL, Andrews T, Hardies LJ, Dodd S, Fox PT (2003) Three-pool model of white matter. J Magn Reson Imaging 17: 1-10.
44. Zhu Y, Hardy CJ, Sodickson DK, Giaquinto RO, Dumoulin CL, et al. (2004) Highly parallel volumetric imaging with a 32-element RF coil array. Magn Reson Med 52: 869-877.
45. Niendorf T, Sodickson DK (2006) Parallel imaging in cardiovascular MRI: methods and applications. NMR Biomed 19: 325-341.

Tables

		T_1 [ms]		
		1.5T	**3T**	**7T**
white matter	IR reference	678±10	911±15	1284±22
	uncorrected 2D VFA	298±14	377±25	554±21
	corrected 2D VFA	791±21	969±85	1855±141
gray matter	IR reference	1154±82	1615±149	2065±69
	uncorrected 2D VFA	465±40	518±42	804±48
	corrected 2D VFA	1282±78	1433±80	2524±137

Table 1: T_1 values for gray matter and white matter in healthy volunteers at 1.5T, 3T, and 7T derived from IR-SE reference measurement, uncorrected 2D VFA, and corrected 2D VFA.

Figures

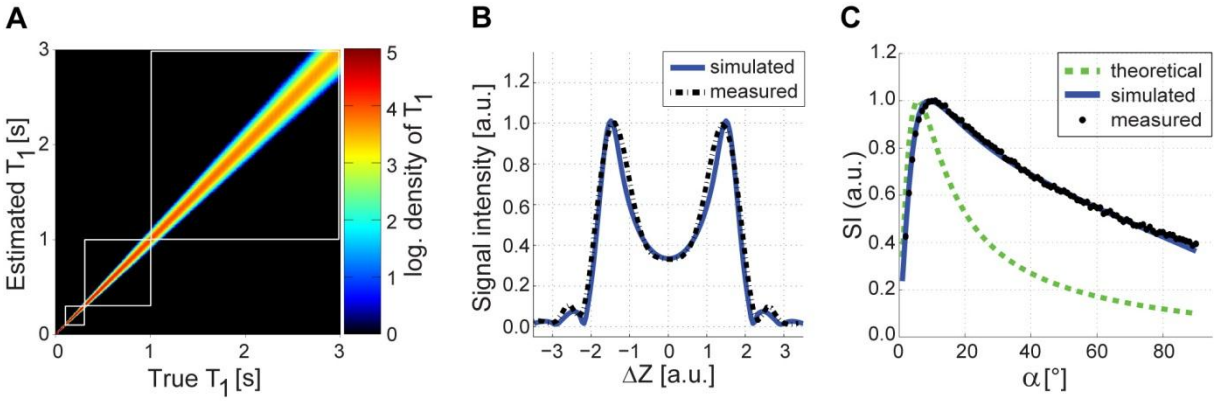

Figure 1: Monte Carlo simulation and impact of slice profile deformation on FLASH signal.

(a) Simulated density distribution (logarithmic) of true T_1 values versus estimated T_1 values derived from corrected 2D VFA using three flip angles. For each T_1 value, 10000 experiments were performed. The use of three flip angles improved the T_1 precision index by 11% compared using only two flip angles. **(b)** Bloch simulated (blue solid line) and measured (black dashed line) slice profiles (signal relevant component) in the steady state of a FLASH sequence show good agreement. The slice profile substantially deviates from an ideal rectangular slice profile. **(c)** Theoretical (green dashed line), Bloch simulated (blue solid line), and measured (black dots) signal intensities for FLASH as a function of the flip angle (at T_1=1000ms). The Bloch simulated signal intensities agree very well with the phantom measurements.

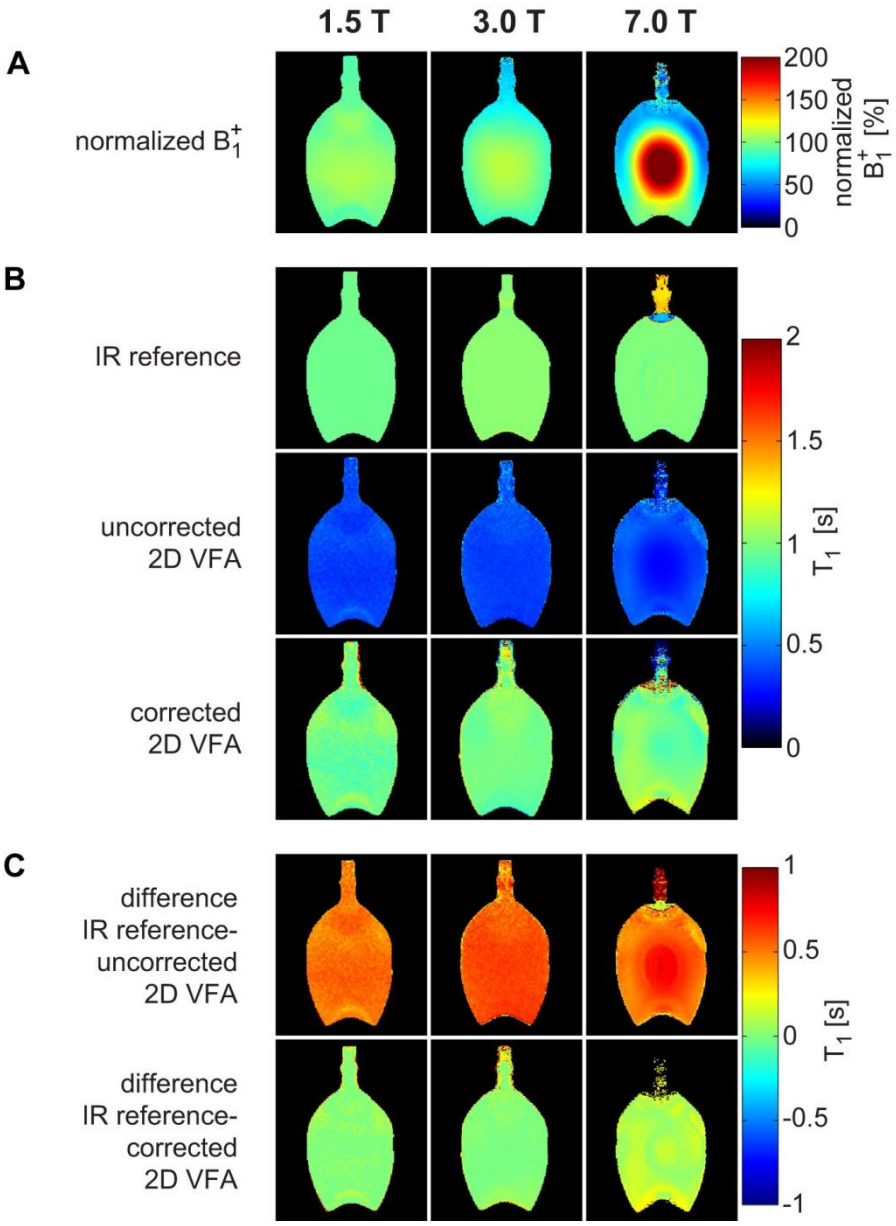

Figure 2: Normalized B_1^+ maps and T_1 maps of the water phantom at 1.5T, 3T, and 7T.

(a) Measured B_1^+ normalized to the nominal B_1^+ (4,35µT) in percent. **(b, top row)** T_1 derived from the inversion recovery reference method (T_1=(963±7)ms at 1.5T, T_1=(1022±10)ms at 3T, T_1=(1002±10)ms at 7T). **(b, center row)** Uncorrected 2D VFA approach that does only consider B_1^+ but not slice profile deformations. Adjusted flip angles (α_1=2°, α_2=13°) were used. This approach revealed a T_1 underestimation of -63.0±1.5% averaged over all field strengths (T_1=(372±28)ms at 1.5T, T_1=(376±23)ms at 3T, T_1=(357±60)ms at 7T) compared to the reference measurement. **(b, bottom row)** With the proposed B_1^+ corrected and slice profile distortion corrected 2D VFA measured a T_1 deviation of only 0.2±1.4% averaged over all field strengths (T_1=(966±67)ms at 1.5T, T_1=(1010±47)ms at 3T, T_1=(1017±89)ms at 7T) compared to the reference measurement. **(c, top row)** Difference map between uncorrected 2D VFA and IR reference. **(c, bottom row)** Difference map between corrected 2D VFA and IR reference.

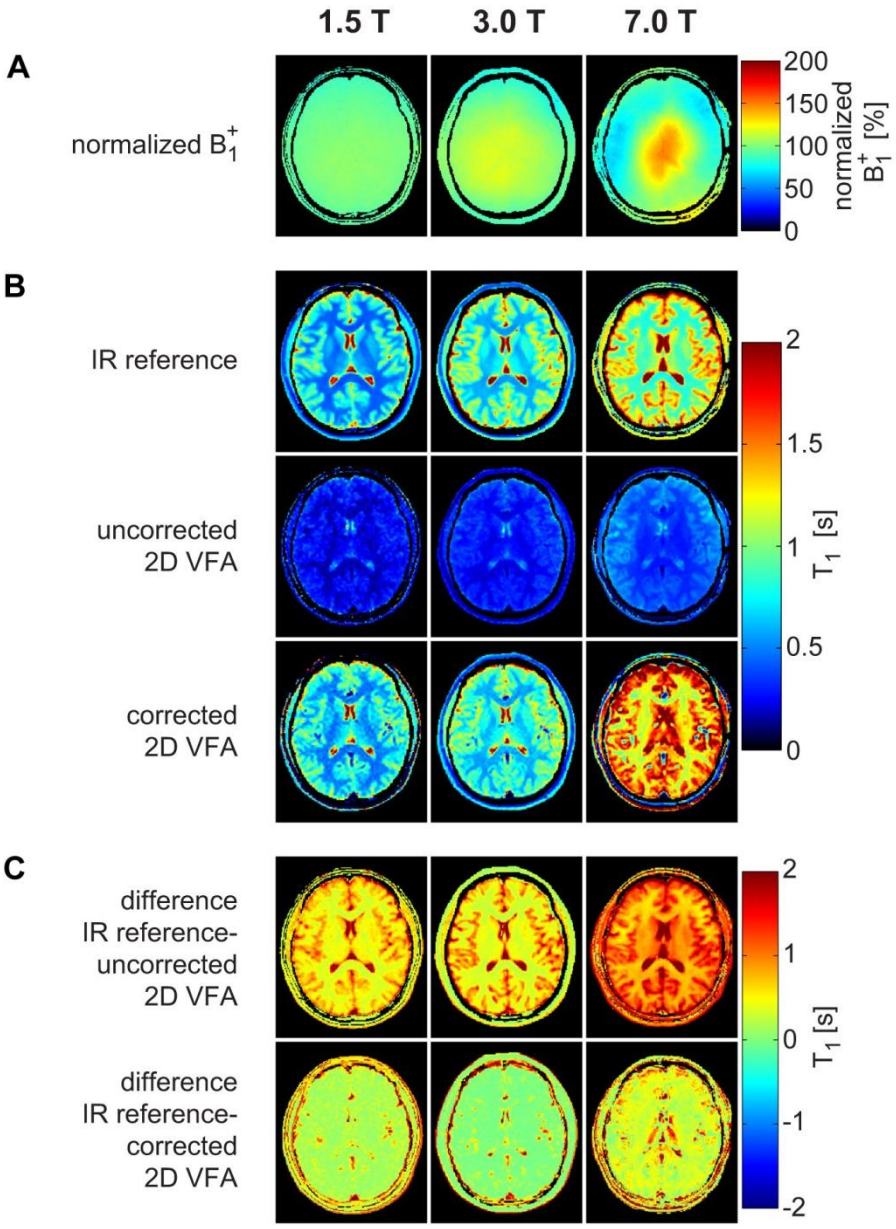

Figure 3: B_1^+ mapping and T_1 mapping in healthy volunteers at 1.5T, 3T, and 7T.

Exemplary normalized B_1^+ maps **(a)** and T_1 maps **(b)** of a healthy brain using the inversion recovery reference measurement, the uncorrected 2D VFA, and the proposed corrected 2D VFA approach at 1.5T, 3T, and 7T. The difference maps between IR reference and uncorrected/corrected 2D VFA are illustrated in **(c)**.

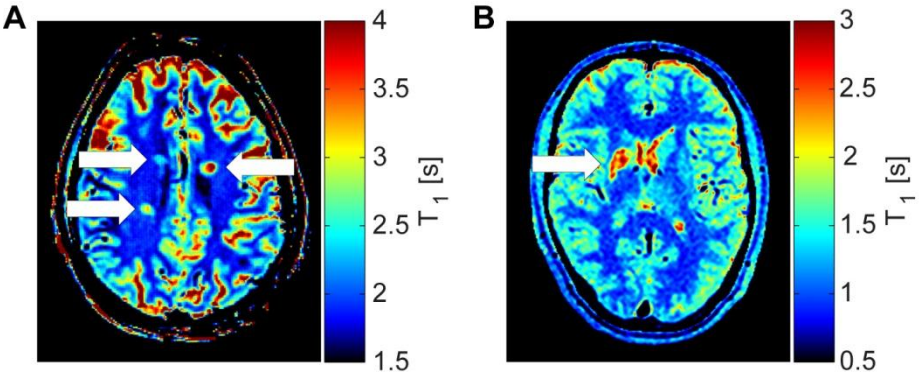

Figure 4: Patient measurements using the corrected 2D VFA method.

(a) T_1-map of a multiple sclerosis patient at 7T using the corrected 2D VFA method. The map shows three periventricular lesions (white arrows). Mean T_1 of the lesions was (2758±615)ms vs. (1842±62)ms in the surrounding white matter. **(b)** Corrected 2D VFA T_1-map of a stroke patient derived from 3T acquisitions showing a subcortical lesion (white arrow). The stroke occurred five months before measurement. T_1 of the lesion was (2554±316)ms vs. (951±74)ms in the surrounding white matter.

Mein Lebenslauf wird aus datenschutzrechtlichen Gründen in der elektronischen Version meiner Arbeit nicht veröffentlicht.

Publikationsliste

Artikel in wissenschaftlichen Fachzeitschriften (Peer-Review)

1. P.D. Gatehouse, M.P. Rolf, M.J. Graves, M.B. Hofman, J. Totman, B. Werner, R.A. Quest, Y. Liu, J. von Spiczak, **M. Dieringer**, D.N. Firmin, A. van Rossum, M. Lombardi, J. Schwitter, J. Schulz-Menger, and P.J. Kilner, *Flow measurement by cardiovascular magnetic resonance: a multi-centre multi-vendor study of background phase offset errors that can compromise the accuracy of derived regurgitant or shunt flow measurements.* J Cardiovasc Magn Reson, 2010. 12: p. 5.

2. T. Frauenrath, F. Hezel, W. Renz, T.d.O. de Geyer, **M. Dieringer**, F.V. Knobelsdorff-Brenkenhoff, M. Prothmann, J. Schulz-Menger, and T. Niendorf, *Acoustic cardiac triggering: a practical solution for synchronization and gating of cardiovascular magnetic resonance at 7 Tesla.* J Cardiovasc Magn Reson, 2010. 12(1): p. 67.

3. F. von Knobelsdorff-Brenkenhoff, T. Frauenrath, M. Prothmann, **M.A. Dieringer**, F. Hezel, W. Renz, K. Kretschel, T. Niendorf, and J. Schulz-Menger, *Cardiac chamber quantification using magnetic resonance imaging at 7 Tesla--a pilot study.* Eur Radiol, 2010. 20(12): p. 2844-52.

4. **M.A. Dieringer**, W. Renz, T. Lindel, F. Seifert, T. Frauenrath, F. von Knobelsdorff-Brenkenhoff, H. Waiczies, W. Hoffmann, J. Rieger, H. Pfeiffer, B. Ittermann, J. Schulz-Menger, and T. Niendorf, *Design and application of a four-channel transmit/receive surface coil for functional cardiac imaging at 7T.* J Magn Reson Imaging, 2011. 33(3): p. 736-41.

5. F. von Knobelsdorff-Brenkenhoff, **M.A. Dieringer**, A. Greiser, and J. Schulz-Menger, *In vitro assessment of heart valve bioprostheses by cardiovascular magnetic resonance: four-dimensional mapping of flow patterns and orifice area planimetry.* Eur J Cardiothorac Surg, 2011. 40(3): p. 736-42.

6. T. Frauenrath, K. Fuchs, **M.A. Dieringer**, C. Ozerdem, N. Patel, W. Renz, A. Greiser, T. Elgeti, and T. Niendorf, *Detailing the use of magnetohydrodynamic effects for synchronization of MRI with the cardiac cycle: a feasibility study.* J Magn Reson Imaging, 2012. 36(2): p. 364-72.

7. **M.A. Dieringer**, J. Hentschel, T. de Quadros, F. von Knobelsdorff-Brenkenhoff, W. Hoffmann, T. Niendorf, and J. Schulz-Menger, *Design, construction, and evaluation of a dynamic MR compatible cardiac left ventricle model.* Med Phys, 2012. 39(8): p. 4800-6.

8. B. Wagenhaus, A. Pohlmann, **M.A. Dieringer**, A. Els, H. Waiczies, S. Waiczies, J. Schulz-Menger, and T. Niendorf, *Functional and morphological cardiac magnetic resonance imaging of mice using a cryogenic quadrature radiofrequency coil.* PLoS One, 2012. 7(8): p. e42383.

9. T. Niendorf, A. Graessl, C. Thalhammer, **M.A. Dieringer**, O. Kraus, D. Santoro, K. Fuchs, F. Hezel, S. Waiczies, B. Ittermann, and L. Winter, *Progress and promises of human cardiac magnetic resonance at ultrahigh fields: a physics perspective.* J Magn Reson, 2013. 229: p. 208-22.

10. F. von Knobelsdorff-Brenkenhoff, V. Tkachenko, L. Winter, J. Rieger, C. Thalhammer, F. Hezel, A. Graessl, **M.A. Dieringer**, T. Niendorf, and J. Schulz-Menger, *Assessment of the right ventricle with cardiovascular magnetic resonance at 7 Tesla.* J Cardiovasc Magn Reson, 2013. 15: p. 23.

11. R. Wassmuth, M. Prothmann, W. Utz, **M. Dieringer**, F. von Knobelsdorff-Brenkenhoff, A. Greiser, and J. Schulz-Menger, *Variability and homogeneity of cardiovascular magnetic resonance myocardial T2-mapping in volunteers compared to patients with edema.* J Cardiovasc Magn Reson, 2013. 15: p. 27.

12. F. von Knobelsdorff-Brenkenhoff, M. Prothmann, **M.A. Dieringer**, R. Wassmuth, A. Greiser, C. Schwenke, T. Niendorf, and J. Schulz-Menger, *Myocardial T1 and T2 mapping at 3 T: reference values, influencing factors and implications.* J Cardiovasc Magn Reson, 2013. 15(1): p. 53.

13. F. von Knobelsdorff-Brenkenhoff, **M.A. Dieringer**, K. Fuchs, F. Hezel, T. Niendorf, and J. Schulz-Menger, *Isometric handgrip exercise during cardiovascular magnetic resonance imaging: set-up and cardiovascular effects.* J Magn Reson Imaging, 2013. 37(6): p. 1342-50.

14. A. Graessl, W. Renz, F. Hezel, **M.A. Dieringer**, L. Winter, C. Oezerdem, J. Rieger, P. Kellman, D. Santoro, T.D. Lindel, T. Frauenrath, H. Pfeiffer, and T. Niendorf, *Modular 32-channel transceiver coil array for cardiac MRI at 7.0T.* Magn Reson Med, 2013 (epub ahead of print).

15. F. Carinci, D. Santoro, F. von Samson-Himmelstjerna, T.D. Lindel, **M.A. Dieringer**, and T. Niendorf, *Characterization of phase-based methods used for transmission field uniformity mapping: a magnetic resonance study at 3.0 T and 7.0 T.* PLoS One, 2013. 8(3): p. e57982.

16. **M.A. Dieringer**, M. Deimling, D. Santoro, J. Wuerfel, V.I. Madai, J. Sobesky, F. von Knobelsdorff-Brenkenhoff, T. Niendorf, and J. Schulz-Menger, *Rapid Parametric Mapping of the Longitudinal Relaxation Time T1 Using Two-Dimensional Variable Flip Angle Magnetic Resonance Imaging at 1.5 Tesla, 3 Tesla, and 7 Tesla.* PLoS One, in press.

Vorträge und Poster (wissenschaftliche Kongresse)

1. F. von Knobelsdorff-Brenkenhoff, **M.A. Dieringer**, A. Greiser, and J. Schulz-Menger. *Evaluation of bioprostheses in aortic position using cardiovascular magnetic resonance - in-vivo and in-vitro studies*. in *Scientific Meeting of the American Heart Association*. 2008. New Orleans, USA.

2. P.D. Gatehouse, M.P. Rolf, M.J. Graves, J. Totman, J.v. Spiczaki, M. Santarelli, Y. Liu, R.A. Quest, **M.A. Dieringer**, M. Lombardi, J. Schwitter, J. Schulz-Menger, D.N. Firmin, M.B. Hofman, and P.J. Kilner. *Evidence across CMR sites and systems of background velocity offset errors requiring correction before accurate measurement of regurgitant and shunt flow*. in *12th Annual SCMR Scientific Sessions*. 2009. Orlando, USA. p. O96.

3. W. Renz, T. Lindel, F. Seifert, **M.A. Dieringer**, W. Hoffmann, J. Schulz-Menger, and B. Ittermann. *A 4 channel TX/RX decoupled loop array for cardiac/body imaging at 7T*. in *ESMRMB*. 2009. Antalya, Turkey. p. 476.

4. F. von Knobelsdorff-Brenkenhoff, A. Rudolph, A. Greiser, **M.A. Dieringer**, S. Bohl, R. Wassmuth, E.E. Buschmann, H. abdel-Aty, R. Dietz, and J. Schulz-Menger. *Kardiovaskuläre Magnetresonanztomographie zur Evaluierung von Bioprothesen in Aortenposition – In-vivo und in-vitro Studien*. in *75th Annual Meeting of the German Cardiac Society*. 2009. Mannheim, Germany: Deutsche Gesellschaft für Kardiologie. p. V18.

5. **M.A. Dieringer**, F. Hezel, W. Renz, P. Boye, B. Ittermann, F. Seifert, T. Lindel, and T. Niendorf. *Single Breath-hold High Spatial Resolution Abdominal Imaging and T2* Mapping at 7.0 T*. in *ISMRM*. 2010. Stockholm, Sweden. p. 2616.

6. **M.A. Dieringer**, W. Renz, T. Lindel, F. Seifert, T. Frauenrath, H. Waiczies, F. von Knobelsdorff-Brenkenhoff, D. Santoro, W. Hoffmann, B. Ittermann, and T. Niendorf. *4CH TX/RX Surface Coil for 7T: Design, Optimization and Application for Cardiac Function Imaging*. in *ISMRM*. 2010. Stockholm, Sweden. p. 3583.

7. T. Frauenrath, F. Hezel, W. Renz, F. von Knobelsdorff-Brenkenhoff, T. de Geyer d'Orth, M. Prothmann, **M.A. Dieringer**, K. Kretschel, J. Schulz-Menger, and T. Niendorf. *Cardiac imaging at 7.0T: Comparison of pulse oximetry, electrocardiogram and phonocardiogram triggered 2D CINE for left ventricular function assessment*. in *ISMRM*. 2010. Stockholm, Sweden. p. 5008.

8. T. Frauenrath, W. Renz, N. Patel, F. Hezel, **M.A. Dieringer**, J. Schulz-Menger, and T. Niendorf. *Cardiac imaging at 7.0 T: comparison of pulse oximetry, electrocardiogram and phonocardiogram triggered 2D-CINE for LV-function assessment*. in *13th Annual SCMR Scientific Sessions*. 2010. Phoenix, USA. p. O15.

9. W. Renz, T. Lindel, **M.A. Dieringer**, F. Seifert, J. Schulz-Menger, T. Niendorf, and B. Ittermann. *A 8 Channel TX/RX Decoupled Loop Array for Cardiac/body Imaging at 7T* in *ISMRM*. 2010. Stockholm, Sweden. p. 3806.

10. D. Santoro, T. Lindel, **M.A. Dieringer**, W. Renz, and T. Niendorf. *ΦFA CUP: PHase Based Flip Angle Calibration Using the P0 Pulse for Proton MRI at 7T*. in *ISMRM*. 2010. Stockholm, Sweden. p. 4943.

11. F. von Knobelsdorff-Brenkenhoff, T. Frauenrath, M. Prothmann, **M.A. Dieringer**, F. Hezel, W. Renz, K. Kretschel, T. Niendorf, and J. Schulz-Menger. *Accurate Left Ventricular Chamber Quantification Is Feasible Using Cardiovascular Magnetic Resonance at 7T*. in *ISMRM*. 2010. Stockholm, Sweden. p. 590.

12. F. Carinci, F. von Samson-Himmelstjerna, D. Santoro, T. Lindel, **M.A. Dieringer**, F. Seifert, J. Sobesky, and T. Niendorf. *Comparison of four Phase Based Methods for the B1+ Mapping at 7T*. in *ISMRM*. 2011. Montreal, Canada. p. 4418.

13. **M.A. Dieringer**, M. Deimling, D. Santoro, F. Carinci, J. Schulz-Menger, and T. Niendorf. *Implications of 2D Slice Profile Deformations for Rapid Myocardial T1/T2 Quantification using DESPOT*. in *ISMRM*. 2011. Montreal, Canada. p. 3411.

14. **M.A. Dieringer**, A. Greiser, and J. Schulz-Menger. *Influence of slice thickness on MR flow quantification in turbulent jets*. in *14th Annual SCMR Scientific Sessions*. 2011. Nice, France. p. 363.

15. T. Frauenrath, **M.A. Dieringer**, N. Patel, C. Özerdem, J. Hentschel, W. Renz, and T. Niendorf. *From Artifact to Merit: Cardiac Gated MRI at 7T and 3T Using Magneto-Hydrodynamic Effects for Synchronization*. in *ISMRM*. 2011. Montreal, Canada. p. 644.

16. F. von Knobelsdorff-Brenkenhoff, **M.A. Dieringer**, A. Greiser, and J. Schulz-Menger. *In-vitro Analyse von Flussmuster und Öffnungsfläche verschiedener Bioherzklappen mittels kardiovaskulärer Magnetresonanztomographie*. in *77th Annual Meeting of the German Cardiac Society*. 2011. Mannheim, Germany: Deutsche Gesellschaft für Kardiologie. p. 708.

17. L. Winter, C. Thalhammer, **M.A. Dieringer**, C. Özerdem, J. Rieger, F. Hezel, W. Renz, and T. Niendorf. *Anatomic & Functional Cardiac MR at 7T: A Comparison of 4, 8 & 16-Element Transceive RF Coil Designs*. in *ISMRM*. 2011. Montreal, Canada. p. 276.

18. **M.A. Dieringer**, T. de Quadros, J. Hentschel, W. Hoffmann, T. Niendorf, and J. Schulz-Menger. *Design, Implementation, Application and Evaluation of a MR Compatible Left Ventricle Model*. in *ISMRM*. 2012. Melbourne, Australia. p. 1241.

19. **M.A. Dieringer**, M. Deimling, F. von Knobelsdorff-Brenkenhoff, A. Greiser, J. Schulz-Menger, and T. Niendorf. *Correction of Slice Profile Deformations and Estimation of Optimal Flip Angles to Enable Accurate T1/T2 Mapping Using 2D Variable Flip Angle Techniques* in *ISMRM*. 2012. Melbourne, Australia. p. 2487.

20. T. Frauenrath, K. Fuchs, F. Hezel, **M.A. Dieringer**, J. Rieger, and T. Niendorf. *Improved Cardiac Triggering by Combining Multiple Physiological Signals: A Cardiac MR Feasibility Study at 7.0 T*. in *ISMRM*. 2012. Melbourne, Australia. p. 0090.

21. T. Frauenrath, H. Pfeiffer, F. Hezel, **M.A. Dieringer**, L. Winter, A. Graessel, D. Santoro, C. Oezerdem, W. Renz, A. Greiser, and T. Niendorf. *Lessons Learned from Cardiac MRI at 7.0 T: LV Function Assessment at 3.0 T Using Local Multi-Channel Transceiver Coil Arrays*. in *ISMRM*. 2012. Melbourne, Australia. p. 2803.

22. A. Greiser, H. Xue, P. Schmitt, **M. Dieringer**, F. von Knobelsdorff-Brenkenhoff, T. Niendorf, J. Schulz-Menger, and E. Mueller. *Cardiac Motion-Corrected Inversion Prepared Real-Time ("TIRT") Cine TrueFISP Imaging for Rapid Myocardial T1 Estimation*. in *ISMRM*. 2012. Melbourne, Australia. p. 3851.

23. T.D. Lindel, A. Greiser, P. Waxmann, M. Dietterle, F. Seifert, U. Fontius, W. Renz, **M.A. Dieringer**, T. Frauenrath, J. Schulz-Menger, T. Niendorf, and B. Ittermann. *Cardiac CINE MRI at 7 T Using a Transmit Array*. in *ISMRM*. 2012. Melbourne, Australia. p. 1227.

24. D. Santoro, F. von Samson-Himmelstjerna, F. Carinci, F. Hezel, **M. Dieringer**, and T. Niendorf. *Cardiac Triggered B1+ Mapping Using Bloch Siegert in the Heart at 3T*. in *ISMRM*. 2012. Melbourne, Australia. p. 3840.

25. V. Tkachenko, F. von Knobelsdorff-Brenkenhoff, D. Kleindienst, L. Winter, J. Rieger, T. Frauenrath, **M.A. Dieringer**, D. Santoro, T. Niendorf, and J. Schulz-Menger. *Cardiovasular MR at 7Tesla: Assessment of the Right Ventricle*. in *ISMRM*. 2012. Melbourne, Australia. p. 1128.

26. F. von Knobelsdorff-Brenkenhoff, **M.A. Dieringer**, K. Fuchs, F. Hezel, W. Renz, T. Niendorf, and J. Schulz-Menger. *Physiological stress during cardiovascular magnetic resonance - handgrip exercise induced hemodynamic effects*. in *15th Annual SCMR Scientific Sessions*. 2012. Orlando, USA. p. 229.

27. F. von Knobelsdorff-Brenkenhoff, **M.A. Dieringer**, A. Greiser, T. Niendorf, and J. Schulz-Menger. *Myokardiale Gewebeanalyse mittels Multiparametrischem Mapping bei 3 Tesla*. in *78th Annual Meeting of the German Cardiac Society*. 2012. Mannheim, Germany: Deutsche Gesellschaft für Kardiologie. p. V144.

28. B. Wagenhaus, A. Pohlmann, **M.A. Dieringer**, and T. Niendorf. *High Spatial Resolution Functional Cardiac MRI in Mice Using a Cryogenic RF Probe*. in *ISMRM*. 2012. Melbourne, Australia. p. 3811.

29. **M.A. Dieringer**. *Ultrahochfeld-Magnetresonanztomographie (UHF-MRT)*. in *Deutsche Gesellschaft für Medizinische Physik (DGMP) und Berufsverband der Physiker in der Medizin für Berlin-Brandenburg (BPMB)*. 2012. Berlin, Germany. p. N/A.

30. B. Dieringer, A. Pohlmann, **M.A. Dieringer**, K. Fuchs, A. Els, H. Waiczies, S. Waiczies, J. Schulz-Menger, and T. Niendorf. *Feasibility and benefit of using a cryogenic radiofrequency coil for functional cardiac magnetic resonance imaging of mice at 9.4 T*. in *16th Annual SCMR Scientific Sessions*. 2013. San Francisco, USA. p. W39.

31. **M.A. Dieringer**, M. Deimling, K. Fuchs, L. Winter, O. Kraus, F. von Knobelsdorff-Brenkenhoff, J. Schulz-Menger, and T. Niendorf. *Blood/myocardium contrast-to-noise ratio for cardiac morphology and function imaging increases with field strength*. in *EuroCMR*. 2013. Florence, Italy. p. 1045.

32. **M.A. Dieringer**, M. Deimling, J. Wuerfel, V.I. Madai, J. Sobesky, F. von Knobelsdorff-Brenkenhoff, J. Schulz-Menger, and T. Niendorf. *Rapid 2D T1 Brain Mapping in Healthy Volunteers, MS Patients, and Stroke Patients at 1.5T, 3T, and 7T using Variable Flip Angles*. in *ESMRMB*. 2013. Toulouse, France. p. 122.

33. **M.A. Dieringer**, M. Prothmann, F. von Knobelsdorff-Brenkenhoff, A. Greiser, C. Eichhorn, T. Niendorf, and J. Schulz-Menger. *Fusion of T1-Mapping and Semi Quantitative Perfusion (T1Per-Fusion) Imaging Provides Additional Insight Into Myocardial Tissue Viability*. in *ISMRM*. 2013. Salt Lake City, USA. p. 4512.

34. K. Fuchs, F. Hezel, L. Winter, C. Oezerdem, A. Graessl, **M.A. Dieringer**, O. Kraus, and T. Niendorf. *Feasibility of Cardiac Fast Spin Echo Imaging at 7.0 T Using a Two-Dimensional 16 Channel Array of Bowtie Transceivers*. in *ISMRM*. 2013. Salt Lake City, USA. p. 1412.

35. A. Greiser, A. Rudolph, **M.A. Dieringer**, J. Traber, E. Polzin, E. Mueller, and J. Schulz-Menger. *Optimization and Standardization of TI-Selection in Contrast Enhanced Viability Imaging by Automated Analysis of Rapid Quantitative T1 Mapping*. in *ISMRM*. 2013. Salt Lake City, USA. p. 1370.

36. O. Kraus, **M.A. Dieringer**, F. Hezel, L. Winter, A. Graessl, C. Oezerdem, and T. Niendorf. *2D CINE SSFP Imaging at 7.0T Using 8-Channel Bowtie Antenna Transceiver Arrays: A Cardiac MR Feasibility Study*. in *ISMRM*. 2013. Salt Lake City, USA. p. 0580.

37. E.M. Tovar Martinez, K. Fuchs, F. Hezel, **M.A. Dieringer**, J. Wuerfel, and T. Niendorf. *Assessment of Multiple Sclerosis at 7.0 T Using High Spatial Resolution, Fluid Attenuated Inversion Recovery Prepared Susceptibility Weighted Fast Spin Echo Imaging*. in *ISMRM*. 2013. Salt Lake City, USA. p. 0928.

38. F. von Knobelsdorff-Brenkenhoff, **M.A. Dieringer**, M. Prothmann, A. Greiser, T. Niendorf, and J. Schulz-Menger. *Segment-based myocardial T1 and T2 mapping at 3T: feasibility and normal values*. in *16th Annual SCMR Scientific Sessions*. 2013. San Francisco, USA. p. 37.

39. **M.A. Dieringer**, J. Schulz-Menger, and T. Niendorf. *Rapid 2D variable flip angle (VFA) T1 mapping using sharp slice profiles*. in *ISMRM*. 2014. Milan, Italy. p. -- (accepted abstract).

40. L. Grosse, J. Traber, U.I. Grieben, W. Utz, **M.A. Dieringer**, P. Kellman, S. Spuler, and J. Schulz-Menger. *Cardiac involvement of the systemic disorder myotonic dystrophy type II - detection by CMR*. in *17th Annual SCMR Scientific Sessions*. 2014. New Orleans, USA. p. 390.

41. O. Kraus, L. Winter, **M.A. Dieringer**, A. Graessel, J. Rieger, C. Oezerdem, F. Hezel, A. Kuehne, P. Waxmann, H. Pfeiffer, and T. Niendorf. *Local Coil versus Conventional Body Coil Transmission for Cardiac MR: B1+ Efficiency Improvements and Enhanced Blood Myocardium Contrast for 2D CINE SSFP Imaging at 3T*. in *ISMRM*. 2014. Milan, Italy. p. -- (accepted abstract).

42. J. Traber, L. Wurche, **M.A. Dieringer**, W. Utz, A. Greiser, N. Jin, P. Barckow, and J. Schulz-Menger. *Real-time flow assessment: From model to patients*. in *17th Annual SCMR Scientific Sessions*. 2014. New Orleans, USA. p. 386.

43. J. Traber, L. Wurche, **M.A. Dieringer**, W. Utz, A. Greiser, N. Jin, P. Barckow, and J. Schulz-Menger. *Validation of real-time flow MRI: From phantom to patients with atrial fibrillation*. in *80th Annual Meeting of the German Cardiac Society*. 2014. Mannheim, Germany: Deutsche Gesellschaft für Kardiologie. p. -- (accepted abstract).

44. F. von Knobelsdorff-Brenkenhoff, M. Prothmann, **M.A. Dieringer**, R. Wassmuth, A. Rudolph, W. Utz, J. Traber, A. Greiser, T. Niendorf, and J. Schulz-Menger. *Differentiation of acute and chronic myocardial infarction using T2-weighted imaging, late enhancement and T1 and T2 mapping - a pilot study at 3T*. in *17th Annual SCMR Scientific Sessions*. 2014. New Orleans, USA. p. 222.

45. C. Martin, M.C. Ku, S. Lepore, H. Waiczies, A. Pohlmann, J. Hentschel, **M.A. Dieringer**, T. Niendorf, and S. Waiczies. *Quantification of Dendritic Cells entering the Lymph Nodes in Mice using 19-F MRI*. in *ISMRM*. 2014. Milan, Italy. p. -- (accepted abstract).

46. P. Dusek, V.I. Madai, **M.A. Dieringer**, F. Hezel, T. Niendorf, J. Sobesky, M. Radoslav, and J. Wuerfel. *Effect of embedding media on post-mortem MRI of formalin-fixed brain tissue at 7.0 T*. in *ISMRM*. 2014. Milan, Italy. p. -- (accepted abstract).

Danksagung

Ich danke Prof. Dr. Jeanette Schulz-Menger für die Möglichkeit zur Promotion, für die sehr spannende und lehrreiche Zeit, für die fachliche und die mentale Unterstützung und für die zahlreichen anregenden Gespräche. Weiter danke ich der gesamten Arbeitsgruppe AG kardiale MRT sowie der gesamten Arbeitsgruppe der „Berlin Ultrahigh Field Facility (B.U.F.F)“ unter der Leitung von Prof. Dr. Thoralf Niendorf für die Unterstützung auf allen Ebenen, ohne die diese Arbeit nicht möglich gewesen wäre.

Michael Deimling möchte ich für die fachliche Mentorenschaft danken, für die vielen Anregungen und Gedankenexperimente.

Weiter danke ich allen nicht namentlich genannten Kooperationspartnern aus Forschung, Klinik und Industrie für die gute Zusammenarbeit und die zahlreichen spannenden Projekte, die angestoßen wurden.

Bei meiner Familie bedanke ich mich für die emotionale Unterstützung. Ganz besonderer Dank gilt meiner Frau und meiner Tochter, die mir sehr viel Kraft gegeben haben und denen ich diese Dissertation widme.